

ÉCOLE DOCTORALE MATHÉMATIQUES, SCIENCES DE L'INFORMATION ET DE
L'INGÉNIEUR – ED269

ICUBE

THÈSE

présentée par :

Anil Kemal GÜN

soutenue le : 15 Novembre 2024

pour obtenir le grade de : **Docteur de l'université de Strasbourg**

Discipline/ Spécialité : Mécanique des fluides

**Two-phase flow modeling for the
simulation of loss-of-coolant accidents
in nuclear reactors**

THÈSE dirigée par :

M. HOARAU Yannick
M. GONCALVES Eric

Professeur, Université de Strasbourg, ICUBE
Professeur, ENSMA, Institut Pprime

RAPPORTEURS :

Mme MATHIS Hélène
M. CORRE Christophe

Professeure, Université de Montpellier, IMAG
Professeur, École Centrale de Lyon, LMFA

EXAMINATEUR :

M. HELLUY Philippe

Professeur, Université de Strasbourg, IRMA

Remerciements

First and foremost, I extend my deepest appreciation to my advisors, Prof. Yannick Hoarau and Prof. Eric Goncalves, for their invaluable guidance, insightful feedback, and unwavering support. Their expertise and mentorship greatly helped me throughout this study and contributed significantly to its successful completion.

I am also deeply grateful to the members of my thesis committee, Prof. Philippe Helluy, Prof. Hélène Mathis, and Prof. Christophe Corre, for their constructive feedback and valuable contributions. Their comments and suggestions have played a crucial role in enhancing the quality of this work.

Many thanks go to Asst. Prof. Abderahmane Marouf and my colleagues for their invaluable advice and for helping me prepare for my final oral defense.

The scholarship awarded by the Ministry of National Education of the Republic of Türkiye provided an invaluable opportunity for academic enrichment and professional development, for which I express my sincere gratitude.

I extend my heartfelt thanks to my family for their patience, unconditional support, and encouragement throughout this journey. I am also grateful to my friends and colleagues for their motivation and understanding, which helped me stay focused and resilient.

Résumé étendu

Le flux multiphasique est un phénomène complexe rencontré dans divers processus naturels et industriels, où plusieurs phases coexistent et interagissent au sein d'un système. Ces phases incluent généralement des combinaisons de gaz, de liquides et de solides, chacune avec des propriétés physiques et des comportements distincts. Comprendre et modéliser les écoulements multiphasiques est crucial dans de nombreux domaines, tels que le génie chimique, le génie pétrolier, la sûreté nucléaire et le génie environnemental. L'accent principal de ces travaux portera sur les écoulements gaz-liquide.

Les écoulements gaz-liquide sont répandus dans un large éventail de domaines, englobant à la fois des phénomènes naturels et des systèmes conçus par l'homme, ce qui rend leur étude essentielle en raison de leur inévitabilité dans ces contextes. Une compréhension approfondie de leur comportement permet aux ingénieurs de favoriser ou de réduire leur occurrence et de prévoir leurs effets sur les performances des systèmes. Cela est particulièrement crucial dans l'industrie nucléaire, où les analyses de sécurité exigent une compréhension complète des écoulements gaz-liquide pour garantir un fonctionnement sûr et efficace. Cette étude se concentrera spécifiquement sur les écoulements diphasiques gaz-liquide, en examinant leur dynamique, les techniques de modélisation, et leurs applications. La compréhension de ces écoulements est essentielle pour améliorer la sécurité et l'efficacité dans diverses applications industrielles, en particulier dans le contexte de la sécurité nucléaire.

Un accident de perte de réfrigérant (LOCA) est l'un des scénarios accidentels pouvant affecter un réacteur à eau pressurisée (REP). Bien qu'il existe de nombreux autres scénarios accidentels possibles dans les REP, nous nous concentrerons sur le LOCA comme principale application de ce travail. Les LOCA sont des accidents postulés à la base de conception qui provoquent des fractures dans la barrière de pression du réfrigérant du réacteur et entraînent une perte de réfrigérant à un débit supérieur à la capacité du système de reconstitution du réacteur. Comme la fracture dans les tuyaux peut être petite ou grande, dès que la fuite est détectée, la réaction en chaîne dans le cœur est arrêtée au moyen de barres de contrôle absorbant les neutrons. Ensuite, la perte de réfrigérant causée par le LOCA est compensée par des systèmes d'injection de sécurité, qui assurent l'élimination à long terme de la chaleur résiduelle. Si les systèmes de sécurité répondent et parviennent à éliminer la chaleur en temps voulu, il n'y aura pas de problème avec le cœur du réacteur et les crayons combustibles, et presque aucune radioactivité ne sera libérée, de sorte que le LOCA reste un accident à la base de conception. Cependant, en cas de défaillance des systèmes de sécurité ou de tout autre dysfonctionnement, une dépressurisation soudaine se produit, l'eau commence à bouillir, la chaleur augmente dans le cœur, et l'oxydation du gainage du combustible par la vapeur du réfrigérant entraîne la détérioration du cœur et la fusion totale ou partielle des crayons combustibles. Dans ce cas, le LOCA cesse d'être un accident à la base de conception et devient l'initiateur d'un accident grave.

Un domaine clé de la thermique nucléaire est la modélisation de la réponse des réacteurs à eau sous pression lors d'un accident de perte de réfrigérant, un type de défaillance fréquent. Dans ces scénarios, deux processus physiques principaux sont impliqués : le déplacement

des ondes de pression et le transfert de masse. Comprendre ces interactions est crucial pour prédire avec précision le comportement du système. Ainsi, les modèles numériques sont censés fournir des informations détaillées sur les forces mécaniques exercées sur le combustible nucléaire et d'autres composants du réacteur. Dans l'analyse numérique, le scénario théorique considère souvent un accident de perte de réfrigérant se produisant principalement dans la branche froide du circuit primaire. Une rupture soudaine dans la tuyauterie du circuit primaire déclenche une dépressurisation rapide du système. Pendant cette dépressurisation, le réfrigérant à haute pression du circuit primaire rencontre l'environnement à basse pression de la structure de confinement, générant potentiellement une onde de raréfaction qui se propage dans le circuit primaire et la cuve du réacteur. Initialement, l'onde de dépressurisation se propage comme un écoulement monophasique liquide, mais en quelques millisecondes, elle passe à un régime d'écoulement diphasique.

Un état métastable se réfère à une condition où une substance reste dans un état intermédiaire temporairement avant de passer à une phase plus stable. Dans les réacteurs à eau pressurisée, le fluide caloporteur, qui est de l'eau, est généralement maintenu à haute pression pour rester à l'état liquide, même à des températures supérieures à son point d'ébullition normal. Dans des conditions normales de fonctionnement, ce fluide caloporteur est dans un état monophasique liquide et non dans un état métastable. Lors d'un accident de perte de réfrigérant, la situation change radicalement. Un LOCA implique une rupture soudaine dans le circuit primaire du réacteur, entraînant une chute rapide de la pression. Lorsque le fluide caloporteur à haute pression est exposé à un environnement de basse pression, il subit une dépressurisation rapide. Cette chute de pression soudaine crée des conditions où l'eau ne peut plus rester à l'état liquide monophasique et commence à passer à un domaine d'écoulement diphasique liquide-vapeur. Pendant cette période de transition, le fluide caloporteur peut entrer dans un état métastable. Il s'agit d'une phase intermédiaire où l'eau liquide surchauffée existe à une combinaison de pression et de température où elle devrait idéalement bouillir, mais n'est pas encore complètement passée à l'état de vapeur. Le retard avant le passage complet au domaine d'écoulement diphasique correspond à l'état métastable. Pendant cette courte période, le fluide caloporteur maintient temporairement sa forme liquide malgré les conditions favorisant un changement de phase. Comprendre cet état métastable transitoire est crucial car il affecte le comportement du fluide caloporteur et la dynamique thermohydraulique du réacteur. À mesure que le fluide caloporteur passe à l'écoulement diphasique, il génère une onde de raréfaction qui se propage dans le système de refroidissement du réacteur. Cette onde influence les dynamiques de pression et d'écoulement à l'intérieur du réacteur, affectant les forces mécaniques sur les composants du réacteur et la réponse globale du système pendant le LOCA. Une modélisation précise de cette transition, y compris l'état métastable, est essentielle pour prédire le comportement du réacteur en cas d'accident et assurer l'efficacité des systèmes de sécurité conçus pour atténuer les conséquences d'un LOCA.

Dans les sections initiales de la thèse, le cadre mathématique sous-jacent aux modèles d'écoulement diphasique est introduit. Contrairement aux écoulements monophasiques, les écoulements diphasiques impliquent le mouvement simultané de deux phases distinctes, généralement un gaz et un liquide, qui interagissent de manière complexe. Ces interactions nécessitent des techniques de modélisation sophistiquées pour capturer la dynamique entre les phases, qui possèdent des propriétés différentes telles que la densité, la vitesse et la température. L'un des principaux défis de la modélisation des écoulements diphasiques est de représenter avec précision l'interface entre les phases. Cette interface peut être nette ou diffuse, selon l'approche de modélisation adoptée. Les méthodes d'interface nette maintiennent une frontière distincte entre les phases, nécessitant un suivi précis de la position et de la forme

de l'interface, tandis que les méthodes d'interface diffuse permettent une transition plus graduelle entre les phases, ce qui simplifie le traitement numérique mais introduit d'autres complexités. Diverses procédures de moyennage—moyennage temporel, moyennage spatial et moyennage d'ensemble—sont également explorées, lesquelles sont fondamentales pour dériver des modèles macroscopiques à partir des équations microscopiques. Sur ces bases, la dérivation des modèles d'écoulement diphasique à partir des modèles monophasiques est introduite via le moyennage d'ensemble. Ce processus implique la transformation des équations de conservation de la masse, de la quantité de mouvement et de l'énergie, avec une attention particulière portée aux conditions de saut interfaciaux, essentielles pour capturer les discontinuités aux frontières des phases. La discussion inclut également un examen du problème de Riemann et de la méthode de Godunov, qui sont des outils essentiels pour résoudre les systèmes hyperboliques de lois de conservation. Le problème de Riemann fournit un cadre pour comprendre comment les discontinuités évoluent dans le temps, ce qui est particulièrement pertinent pour modéliser des phénomènes tels que les ondes de choc et les ondes de raréfaction dans les systèmes diphasiques compressibles. La méthode de Godunov, une technique numérique pour résoudre ces systèmes, est mise en avant pour sa robustesse dans le traitement des discontinuités sans introduire d'oscillations non physiques, en faisant un pilier de la dynamique des fluides numérique pour les écoulements diphasiques.

Bien qu'il existe différentes méthodes de modélisation pour l'écoulement diphasique dans la littérature, nous allons ici présenter différents modèles basés sur le modèle de Baer–Nunziato. La base de cette méthode est liée à la manière dont le non-équilibre est traité. La forme complète non-équilibre des modèles d'équations d'écoulement multiphasique, dans laquelle chaque phase possède sa propre vitesse, pression et température, est la plus générale. Dans les cas où l'écoulement se compose de 2 phases, le modèle le plus général consiste en 7 équations différentielles partielles. Ces 7 équations comprennent les équations de bilan de masse, de quantité de mouvement et d'énergie pour chaque phase, ainsi que l'équation de la fraction volumique. Dans la littérature, ce modèle est souvent appelé le modèle à sept équations. À partir de ce point, il est possible de dériver différents modèles réduits en ajoutant des hypothèses d'équilibre entre les phases, jusqu'au modèle d'équilibre homogène où l'on suppose que les deux phases ont la même vitesse, pression, température et potentiel chimique.

Dans cette étude, deux modèles différents ont été implémentés dans le solveur numérique : le modèle à six équations avec une seule vitesse et le modèle à quatre équations. Le modèle à six équations est un modèle d'équilibre de vitesse relâché, dérivé du modèle à sept équations de Baer–Nunziato sous la condition d'équilibre cinétique instantané. Ce modèle comprend une équation d'advection pour la fraction volumique d'une phase, des équations distinctes de masse et d'énergie totale pour chaque phase, ainsi qu'une équation de quantité de mouvement pour le mélange. Les effets de non-équilibre mécanique, thermique et chimique sont préservés dans le modèle à six équations, qui suppose un équilibre de vitesse immédiat entre les deux phases. Un modèle à quatre équations est utilisé pour représenter un écoulement diphasique en équilibre cinétique, mécanique et thermique. Ce modèle est dérivé du modèle diphasique à sept équations de Baer–Nunziato, sous les conditions d'équilibre de vitesse, de pression et de température. Il comprend une équation de masse pour chaque phase, ainsi que des équations de quantité de mouvement et d'énergie pour le mélange. Une exigence fondamentale pour décrire complètement et fermer un système physique est l'utilisation d'une équation d'état qui corrèle la température, la pression, l'énergie interne et la densité. Pour les deux modèles, une équation d'état de gaz raidi a été choisie à cette fin. La méthode des étapes fractionnaires a été utilisée pour résoudre les modèles à 6 équations et à 4 équations. Dans la première étape, la partie homogène du système est résolue sans

le terme source. La solution obtenue de cette étape initiale est ensuite utilisée dans l'étape de relaxation suivante. La partie homogène du système est résolue en utilisant le solveur de Riemann approximatif Harten-Lax-van Leer Contact (HLLC).

Les deux modèles ont d'abord été implémentés dans un solveur spécialement conçu, puis validés à l'aide de différents cas de test. Tout d'abord, le processus de dépressurisation dans une conduite contenant du CO_2 a été testé en utilisant ces deux modèles. Le test a été mené selon deux scénarios distincts : dans le premier scénario, le transfert de masse n'a pas été activé, comme le montrent les Figure 1 et Figure 2, tandis que dans le second scénario, le transfert de masse a été activé, comme le montrent les Figure 3 et Figure 4. Dans les deux scénarios, les résultats des deux modèles sont cohérents avec les données de référence.

Par la suite, le cas de test proposé par Riegel, également connu sous le nom d'expérience Canon, a fait l'objet d'analyses numériques pour trois procédures de relaxation chimique différentes. Les résultats obtenus avec le solveur ont été comparés à ceux de différents modèles présents dans la littérature (HRM), et un bon accord a été observé. Cependant, tant les résultats obtenus que ceux utilisés pour la comparaison dans la littérature ont prédit une vaporisation plus précoce que l'expérience (environ 200 ms plus tôt), comme le montrent la Figure 5 et la Figure 6. Néanmoins, même dans ce scénario complexe, les résultats obtenus avec les deux modèles ont globalement permis d'expliquer les résultats expérimentaux.

Le montage expérimental suivant a également été conçu par Riegel, également connu sous le nom d'expérience Super-Canon. Contrairement à l'expérience précédente, les valeurs de température et de pression sont plus élevées. La principale raison de ces changements de pression et de température était de représenter les conditions de la boucle primaire d'un réacteur à eau pressurisée. Une pression de 150 bars et une température de 300°C ont été choisies pour représenter un scénario de perte de réfrigérant dans le circuit primaire d'un REP. Des analyses numériques ont été effectuées pour trois procédures de relaxation chimique différentes, et les résultats obtenus avec le solveur ont été comparés à ceux de différents modèles présents dans la littérature (modèle à 5 équations). Les mêmes phénomènes observés dans le cas précédent sont également présents ici, ce qui signifie que la vaporisation numérique est prédite plus tôt que dans l'expérience, comme le montrent la Figure 7 et la Figure 8. Étant donné la large gamme de pressions et de températures dans ce cas, l'équation d'état de gaz raidi semble trop simpliste pour capturer avec précision le comportement thermodynamique de l'eau. Cependant, le fait que les résultats obtenus soient très similaires à ceux de la littérature montre que les modèles actuels sont capables de simuler le phénomène de vaporisation éclair, même dans des scénarios numériques complexes et difficiles.

Dans la section finale de l'étude, le modèle à six équations avec une seule vitesse et relaxation arbitraire, est analysé et implémenté. Contrairement au modèle à six équations précédent, ce nouveau modèle permet de traiter les processus de relaxation thermique et chimique de manière instantanée ou arbitraire. Plus précisément, la relaxation thermique est considérée sous des conditions d'équilibre de pression, tandis que la relaxation chimique est abordée sous des conditions d'équilibre de pression et de température. Il est à noter que le modèle peut également prendre en compte la relaxation chimique sous des contraintes thermiques. En conséquence, le modèle nécessite le modèle à cinq équations avec relaxation de pression (p-relaxed) et le modèle à quatre équations avec relaxation de pression et de température (pT-relaxed) pour effectuer la procédure de relaxation. Par la suite, en appliquant certaines hypothèses simplificatrices, des solutions analytiques semi-exactes de type exponentiel sont dérivées pour décrire les processus de relaxation. En termes d'efficacité computationnelle, ce modèle présente des avantages par rapport au précédent modèle à six équations, car il ne nécessite pas de procédure itérative pour déterminer les propriétés d'équilibre.

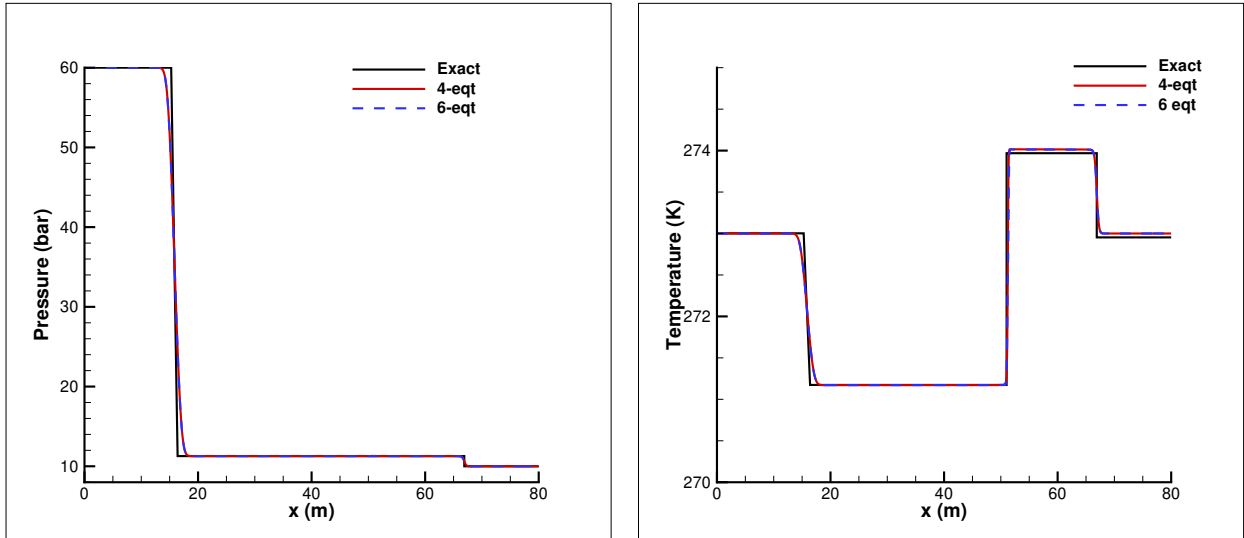


Figure 1: Résultats de la dépressurisation d'un conduit de CO_2 en utilisant le modèle à 6 équations (pointillés bleus) et le modèle à 4 équations (ligne rouge continue) : profils de pression (à gauche) et de température (à droite), à $t = 0.08$ s, sans transfert de masse.

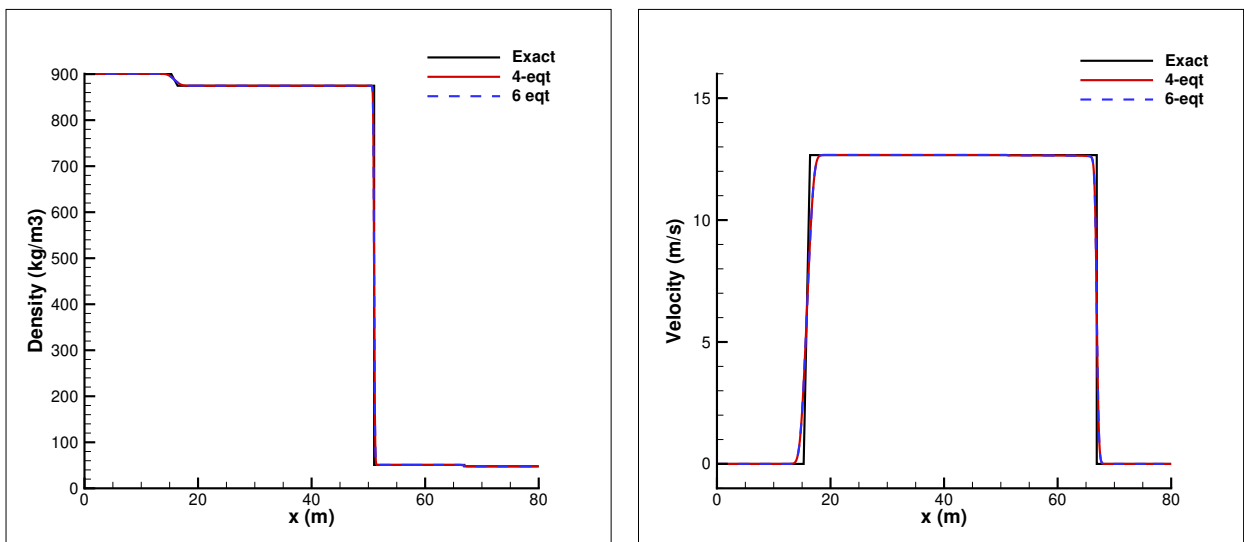


Figure 2: Résultats de la dépressurisation d'un conduit de CO_2 en utilisant le modèle à 6 équations (pointillés bleus) et le modèle à 4 équations (ligne rouge continue) : profils de densité (à gauche) et de vitesse (à droite), à $t = 0.08$ s, sans transfert de masse.

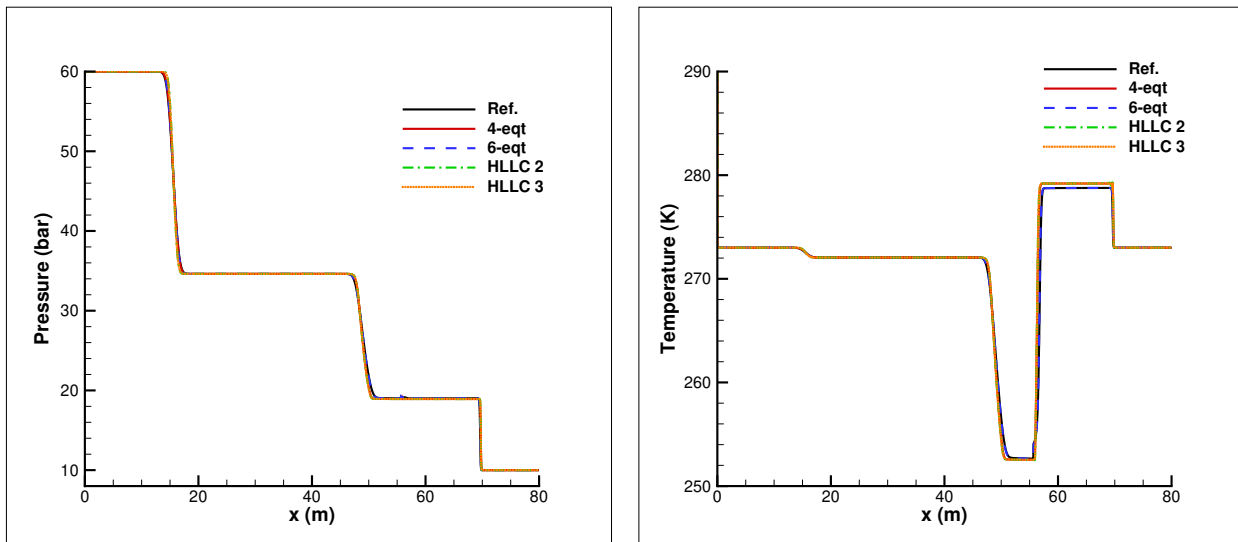


Figure 3: Résultats de la dépressurisation d'un conduit de CO_2 en utilisant le modèle à 6 équations (pointillés bleus) et le modèle à 4 équations (ligne rouge continue), ainsi que les résultats HLLC du second ordre (tiret-point vert) et du troisième ordre (pointillés orange) : profils de pression (à gauche) et de température (à droite), à $t = 0.08$ s, avec transfert de masse.

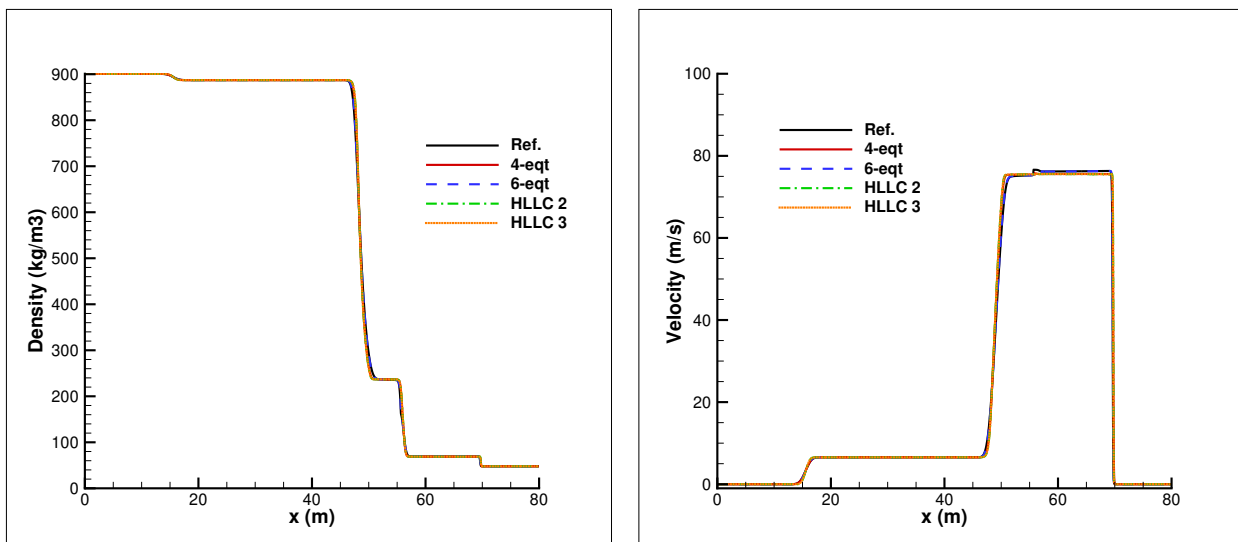


Figure 4: Résultats de la dépressurisation d'un conduit de CO_2 en utilisant le modèle à 6 équations (pointillés bleus) et le modèle à 4 équations (ligne rouge continue), ainsi que les résultats HLLC du second ordre (tiret-point vert) et du troisième ordre (pointillés orange) : profils de densité (à gauche) et de vitesse (à droite), à $t = 0.08$ s, avec transfert de masse.

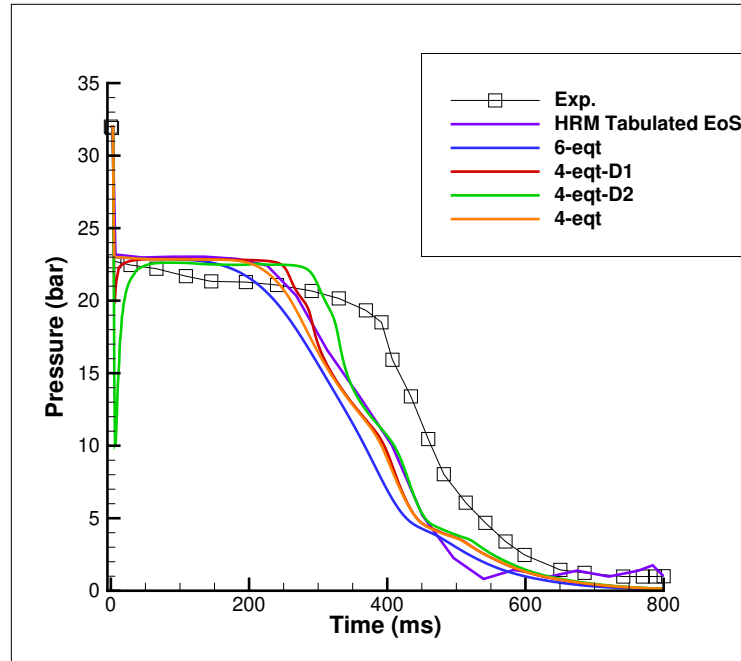


Figure 5: Comparaison des profils de pression à l'emplacement P1 (3,899 m en amont de la brèche) de l'expérience Canon : résultats expérimentaux (Exp., marqueurs carrés noirs), modèle à 6 équations (6-eqt, ligne bleue continue), modèle à 4 équations (4-eqt, ligne orange continue), modèle à 4 équations avec transfert de masse non instantané (4-eqt-D1/D2, lignes rouge/verte continues) issu du solveur, et résultats de l'EoS tabulé HRM (HRM Tabulated EoS, ligne violette continue) obtenus de la littérature par [Lepareux \(1994\)](#).

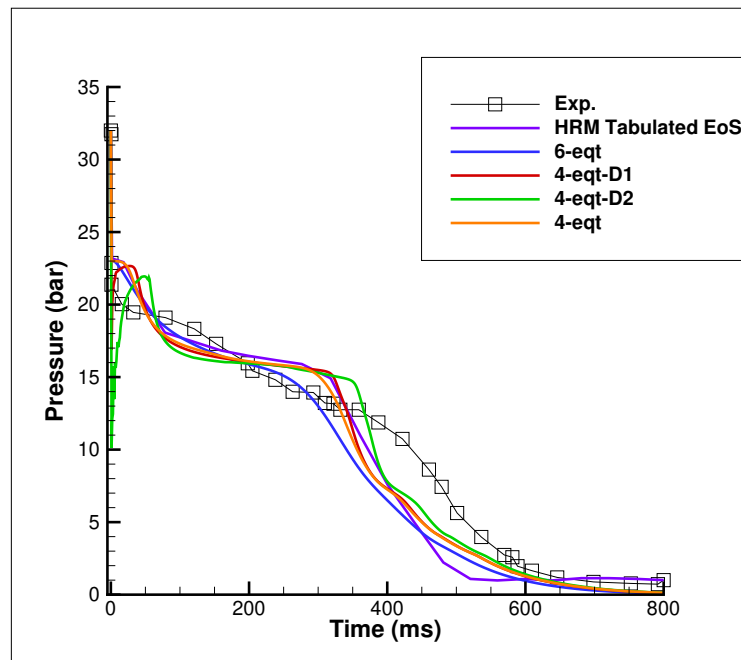


Figure 6: Comparaison des profils de pression à l'emplacement P5 (0,504 m en amont de la brèche) de l'expérience Canon : résultats expérimentaux (Exp., marqueurs carrés noirs), modèle à 6 équations (6-eqt, ligne bleue continue), modèle à 4 équations (4-eqt, ligne orange continue), modèle à 4 équations avec transfert de masse non instantané (4-eqt-D1/D2, lignes rouge/verte continues) issu du solveur, et résultats de l'EoS tabulé HRM (HRM Tabulated EoS, ligne violette continue) obtenus de la littérature par [Lepareux \(1994\)](#).

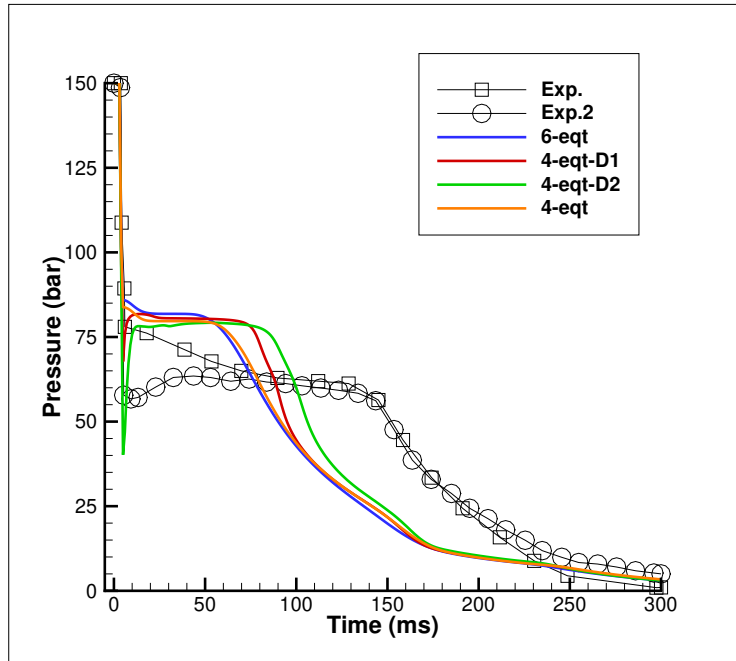


Figure 7: Comparaison des profils de pression à l'emplacement P1 (3,899 m en amont de la brèche) de l'expérience Super-Canon : résultats expérimentaux (Exp., marqueurs carrés noirs), deuxième résultat expérimental (Exp.2, marqueurs cercles noirs), modèle à 6 équations (6-eqt, ligne bleue continue), modèle à 4 équations (4-eqt, ligne orange continue), modèle à 4 équations avec transfert de masse non instantané (4-eqt-D1/D2, lignes rouge/verte continues).

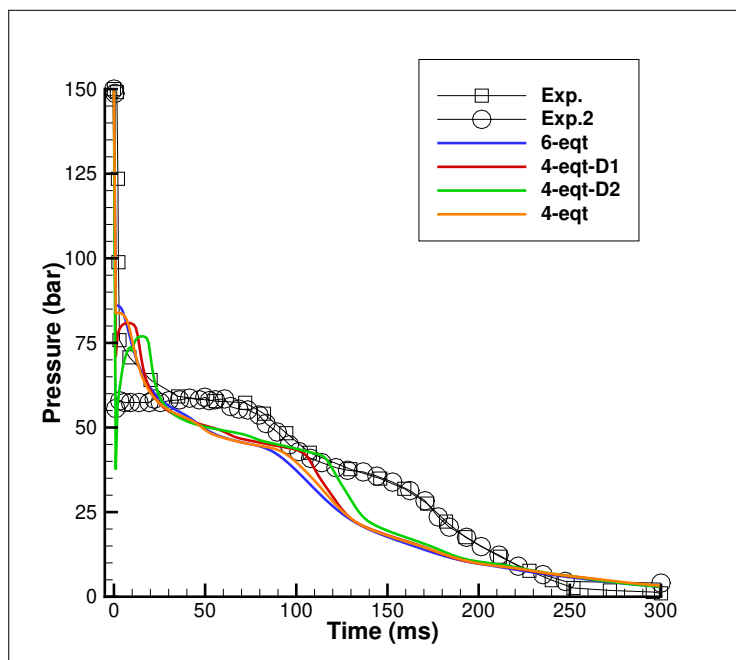


Figure 8: Comparaison des profils de pression à l'emplacement P5 (0,504 m en amont de la brèche) de l'expérience Super-Canon : résultats expérimentaux (Exp., marqueurs carrés noirs), deuxième résultat expérimental (Exp.2, marqueurs cercles noirs), modèle à 6 équations (6-eqt, ligne bleue continue), modèle à 4 équations (4-eqt, ligne orange continue), modèle à 4 équations avec transfert de masse non instantané (4-eqt-D1/D2, lignes rouge/verte continues).

Le modèle a été validé sur différents cas de test, tels que le tube à choc et la double raréfaction. Les résultats sont en bon accord avec les solutions de référence. De plus, le modèle a été testé sur l'expérience de Bartak, qui examine la dépressurisation rapide de l'eau surchauffée et la formation dynamique de bulles de vapeur en son sein. Cette étude est particulièrement pertinente pour comprendre des scénarios tels que les accidents de perte de réfrigérant primaire dans les réacteurs nucléaires à eau pressurisée. Ces événements se caractérisent par la rupture soudaine des canalisations de réfrigérant primaire, entraînant une onde de dépressurisation qui se propage dans le système. La pression dans cette onde peut chuter de manière significative en dessous de la pression de saturation correspondant à la température initiale du réfrigérant, conduisant à un état métastable avant que la nucléation et la formation de bulles de vapeur ne se produisent. Comme on peut le voir sur la Figure 9, les résultats sont qualitativement en accord avec les données expérimentales dans le cas d'un transfert de masse arbitraire. Cela démontre la capacité du modèle numérique à prédire avec précision la formation d'un état surchauffé métastable, où la pression chute en dessous de la pression de saturation correspondant à la température, suivie d'une vaporisation ultérieure.

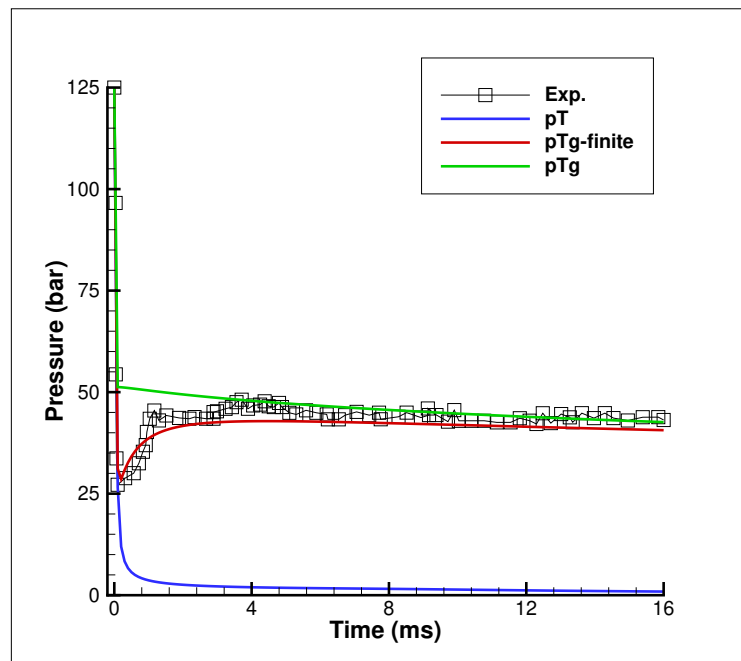


Figure 9: Comparaison des profils de pression à l'emplacement P1 (0,048 m en amont de la brèche) de l'expérience de Bartak : résultats expérimentaux (Exp., marqueurs carrés noirs), relaxation mécanique et thermique instantanée (pT, ligne bleue continue), relaxation mécanique, thermique et chimique à vitesse finie (pTg-finite, ligne rouge continue), et relaxation mécanique, thermique et chimique instantanée (pTg, ligne verte continue).

Abstract

Multiphase flow is a complex phenomenon encountered in various natural and industrial processes, where multiple phases coexist and interact within a system. These phases typically include combinations of gases, liquids, and solids, each with distinct physical properties and behaviors. Understanding and modeling multiphase flows is crucial in many fields, such as chemical engineering, petroleum engineering, nuclear safety, and environmental engineering. This work will primarily focus on gas-liquid flows, which are prevalent in a wide range of domains, encompassing both natural phenomena and man-made systems. Understanding these flows is essential for improving safety and efficiency in various industrial applications, particularly in the context of nuclear safety.

A Loss of Coolant Accident (LOCA) is one of the accidental scenarios that can affect a pressurized water reactor. Although there are many other potential accident scenarios in nuclear reactors, we will focus on the LOCA as the main application of this work. In these scenarios, two main physical processes are involved: pressure wave propagation and mass transfer. Understanding these interactions is crucial for accurately predicting system behavior. Therefore, numerical models are designed to provide detailed information on the mechanical forces exerted on nuclear fuel and other reactor components. In numerical analysis, the theoretical scenario often considers a LOCA occurring mainly in the cold leg of the primary circuit. A sudden rupture in the primary circuit piping triggers rapid depressurization of the system. During this depressurization, the high-pressure coolant from the primary circuit encounters the low-pressure environment of the containment structure, potentially generating a rarefaction wave that propagates through the primary circuit and the reactor vessel. Initially, the depressurization wave propagates as a single-phase liquid flow, but within milliseconds, it transitions to a two-phase flow regime.

A LOCA involves a sudden rupture of the reactor's primary circuit, leading to a rapid pressure drop. When the high-pressure coolant is exposed to a low-pressure environment, it undergoes rapid depressurization. This sudden pressure drop creates conditions where the water can no longer remain in a single-phase liquid state and begins to transition into a two-phase liquid-vapor flow regime. During this transition period, the coolant may enter a metastable state. This is an intermediate phase where superheated liquid water exists at a combination of pressure and temperature where it should ideally boil, but has not yet fully transitioned to vapor. The delay before the complete transition to the two-phase regime corresponds to the metastable state. During this short period, the coolant temporarily maintains its liquid form despite conditions favoring a phase change. Understanding this transient metastable state is crucial, as it affects the coolant's behavior and the thermo-hydraulic dynamics of the reactor. Accurate modeling of this transition, including the metastable state, is essential for predicting reactor behavior in the event of an accident and ensuring the effectiveness of safety systems designed to mitigate the consequences of a LOCA.

In the initial sections of the thesis, the mathematical framework underlying two-phase flow models is introduced. Unlike single-phase flows, two-phase flows involve the simultane-

ous movement of two distinct phases, typically a gas and a liquid, which interact in complex ways. These interactions require sophisticated modeling techniques to capture the dynamics between the phases. Various averaging procedures—temporal averaging, spatial averaging, and ensemble averaging—are also explored, as they are fundamental for deriving macroscopic models from microscopic equations. Based on this, the derivation of two-phase flow models from single-phase models is introduced via ensemble averaging. The discussion also includes a review of the Riemann problem and the Godunov method, which are essential tools for solving hyperbolic systems of conservation laws.

In the first part of the study, two different models were implemented in the custom numerical solver: the six-equation model with a single velocity and the four-equation model. The six-equation model is a relaxed velocity equilibrium model, derived from the Baer-Nunziato seven-equation model under the condition of instantaneous kinetic equilibrium. A four-equation model is used to represent two-phase flow in kinetic, mechanical, and thermal equilibrium. Both models were first implemented and then validated using different test cases.

In the final section of the study, the six-equation model with a single velocity and arbitrary-rate relaxation is analyzed and implemented in the custom solver. Unlike the previous six-equation model, this new model allows thermal and chemical relaxation processes to be treated instantaneously or arbitrarily. In terms of computational efficiency, this model has advantages over the previous one, as it does not require iterative procedures to determine equilibrium properties. The model was validated using different test cases and showed particularly strong agreement with reference solutions in scenarios where a metastable state exists.

Contents

1	Introduction	1
1.1	Industrial Context	1
1.2	Multiphase Flow	7
1.3	Plan of the thesis	9
2	Mathematical framework of two-phase flow models	11
2.1	Averaging procedure in two-phase flow	14
2.1.1	Single phase flow	15
2.1.2	Ensemble averaging procedure	16
2.1.3	Closure problem	21
2.2	Theory of conservation laws	22
2.3	Riemann Problem	24
2.4	Categorisation of two-phase flow models	25
2.4.1	The seven-equation model	28
2.4.2	The six-equation model	30
2.4.3	The five-equation model	32
2.4.4	The four-equation model	33
2.4.5	The three-equation model	33
2.4.6	Additional significant models	34
2.5	Godunov's method	37
2.6	Summary	39
3	Thermodynamic metastability	41
3.1	Pure substance phase diagram	41
3.2	Equation of state	45
3.3	Phase Stability and Metastable States	48
3.4	Summary	51
4	Numerical solver	53
4.1	Navier-Stokes Multi-Block solver	53
4.2	Three equation model	54
4.3	Four equation model	55
4.3.1	Numerics	56
4.3.2	Harten-Lax-van Leer-Contact Riemann solver	57
4.3.3	High order extensions	58
4.4	Validation test cases	59
4.5	Summary	66

5	Comparative Study: 4-Equation vs. 6-Equation Models	69
5.1	Governing Equations	69
5.2	Numerical solution method	73
5.3	Relaxation procedure	75
5.3.1	Mechanical relaxation	76
5.3.2	Thermal relaxation	77
5.3.3	Chemical relaxation	78
5.4	Validation test cases	80
5.5	Summary	97
6	Six-equation model with arbitrary-rate relaxation	99
6.1	Single velocity six-equation model	99
6.2	Numerical solution method	101
6.3	Relaxation procedure	103
6.3.1	Mechanical relaxation procedure	103
6.3.2	Thermal relaxation procedure	105
6.3.3	Chemical relaxation procedure	108
6.4	Validation test cases	110
6.5	Summary	132
7	General conclusion and perspectives	135
7.1	General conclusion	135
7.2	Perspectives	137
A	Error Analysis for Canon Experiment	139
B	Error Analysis for Super-Canon Experiment	143
C	Error Analysis for Edwards O'Brien Experiment	146

List of Tables

1.1	Operable nuclear power plants provided by Nuc.	3
1.2	Main objectives and measures of defence-in-depth approach.	4
2.1	The variables in the generic conservation equations and jump equations.	16
4.1	EoS parameters for liquid and vapor phases in the Canon experiment.	63
4.2	Initial conditions for the Canon experiment.	66
5.1	EoS parameters for liquid and vapor phases in the shock CO ₂ test.	81
5.2	EoS parameters for liquid and vapor for the Super-Canon experiment.	93
5.3	Initial conditions for the Super-Canon experiment.	96
6.1	EoS parameters for liquid and vapor phases in the shock tube test by Chiapolino et al. (2017)	111
6.2	EoS parameters for liquid and vapor phases in Case 2.	117
6.3	Initial conditions for the Edwards and O'Brien experiment.	121
6.4	EoS parameters for liquid and vapor phases for the Edwards and O'Brien experiment.	122
6.5	EoS parameters for liquid and vapor phases for the case 4.	126
6.6	Initial conditions for the case 4.	126
6.7	EoS parameters for liquid and vapor phases for the Bartak experiment.	131

List of Figures

1	Résultats de la dépressurisation d'un conduit de CO ₂ en utilisant le modèle à 6 équations (pointillés bleus) et le modèle à 4 équations (ligne rouge continue) : profils de pression (à gauche) et de température (à droite), à $t = 0.08$ s, sans transfert de masse.	vii
2	Résultats de la dépressurisation d'un conduit de CO ₂ en utilisant le modèle à 6 équations (pointillés bleus) et le modèle à 4 équations (ligne rouge continue) : profils de densité (à gauche) et de vitesse (à droite), à $t = 0.08$ s, sans transfert de masse.	vii
3	Résultats de la dépressurisation d'un conduit de CO ₂ en utilisant le modèle à 6 équations (pointillés bleus) et le modèle à 4 équations (ligne rouge continue), ainsi que les résultats HLLC du second ordre (tiret-point vert) et du troisième ordre (pointillés orange) : profils de pression (à gauche) et de température (à droite), à $t = 0.08$ s, avec transfert de masse.	viii
4	Résultats de la dépressurisation d'un conduit de CO ₂ en utilisant le modèle à 6 équations (pointillés bleus) et le modèle à 4 équations (ligne rouge continue), ainsi que les résultats HLLC du second ordre (tiret-point vert) et du troisième ordre (pointillés orange) : profils de densité (à gauche) et de vitesse (à droite), à $t = 0.08$ s, avec transfert de masse.	viii
5	Comparaison des profils de pression à l'emplacement P1 (3,899 m en amont de la brèche) de l'expérience Canon : résultats expérimentaux (Exp., marqueurs carrés noirs), modèle à 6 équations (6-eqt, ligne bleue continue), modèle à 4 équations (4-eqt, ligne orange continue), modèle à 4 équations avec transfert de masse non instantané (4-eqt-D1/D2, lignes rouge/verte continues) issu du solveur, et résultats de l'EoS tabulé HRM (HRM Tabulated EoS, ligne violette continue) obtenus de la littérature par Lepareux (1994)	ix
6	Comparaison des profils de pression à l'emplacement P5 (0,504 m en amont de la brèche) de l'expérience Canon : résultats expérimentaux (Exp., marqueurs carrés noirs), modèle à 6 équations (6-eqt, ligne bleue continue), modèle à 4 équations (4-eqt, ligne orange continue), modèle à 4 équations avec transfert de masse non instantané (4-eqt-D1/D2, lignes rouge/verte continues) issu du solveur, et résultats de l'EoS tabulé HRM (HRM Tabulated EoS, ligne violette continue) obtenus de la littérature par Lepareux (1994)	ix
7	Comparaison des profils de pression à l'emplacement P1 (3,899 m en amont de la brèche) de l'expérience Super-Canon : résultats expérimentaux (Exp., marqueurs carrés noirs), deuxième résultat expérimental (Exp.2, marqueurs cercles noirs), modèle à 6 équations (6-eqt, ligne bleue continue), modèle à 4 équations (4-eqt, ligne orange continue), modèle à 4 équations avec transfert de masse non instantané (4-eqt-D1/D2, lignes rouge/verte continues).	x

8	Comparaison des profils de pression à l'emplacement P5 (0,504 m en amont de la brèche) de l'expérience Super-Canon : résultats expérimentaux (Exp., marqueurs carrés noirs), deuxième résultat expérimental (Exp.2, marqueurs cercles noirs), modèle à 6 équations (6-eqt, ligne bleue continue), modèle à 4 équations (4-eqt, ligne orange continue), modèle à 4 équations avec transfert de masse non instantané (4-eqt-D1/D2, lignes rouge/verte continues).	x
9	Comparaison des profils de pression à l'emplacement P1 (0,048 m en amont de la brèche) de l'expérience de Bartak : résultats expérimentaux (Exp., marqueurs carrés noirs), relaxation mécanique et thermique instantanée (pT, ligne bleue continue), relaxation mécanique, thermique et chimique à vitesse finie (pTg-finite, ligne rouge continue), et relaxation mécanique, thermique et chimique instantanée (pTg, ligne verte continue).	xi
1.1	Schematic of a Pressurized Water Reactor (PWR).	3
1.2	Flow patterns in vertical (left) and horizontal (right) pipe by da Silva (2008)	8
2.1	The general solution to the Riemann problem for the one-dimensional Euler equations encompasses scenarios where the nonlinear wave can develop as either a rarefaction wave or a shock wave Toh (2024)	25
2.2	Categorization of the two-phase fluid model where considering instantaneous relaxation in zero or more of the variables p (pressure), T (temperature), μ (chemical potential), and v (velocity). Parallel edges signify the same relaxation processes, and each circle denotes a distinct model. Yellow circles represent the <i>homogeneous models</i> which assumes that phases move at the same velocity Linga and Flåtten (2019)	26
2.3	Representation of data as piecewise constants in the finite volume Godunov scheme by Núñez-De La Rosa (2015)	39
3.1	$T - v$ diagram of pure water by Çengel et al. (2019)	42
3.2	$T - v$ diagram of pure substance by Çengel et al. (2019)	43
3.3	(a) $p - T$ and (b) $p - v - T$ diagrams for pure water by Çengel et al. (2019)	44
3.4	Stability, metastability, and unstability concepts.	49
3.5	Spinodal lines and metastable regions on a P-v diagram by Kim et al. (2021) . A-B represents the stable liquid phase, B-C represents the metastable superheated liquid phase, C-D-E indicates the unstable region, D-E shows the metastable supersaturated vapor phase, F-G depicts the stable vapor phase.	50
4.1	Representation of data as piecewise linear in the finite volume MUSCL scheme by Núñez-De La Rosa (2015)	59
4.2	Void ratio and mixture density profiles along the tube, case 1, $t=80 \mu\text{s}$	61
4.3	Mixture pressure and velocity profiles along the tube, case 1, $t=80 \mu\text{s}$	61
4.4	Void ratio and mixture density profiles along the tube, case 2, $t=3.2 \text{ ms}$	62
4.5	Mixture pressure and velocity profiles along the tube, case 2, $t=3.2 \text{ ms}$	62
4.6	Results of CO_2 pipe depressurization for pressure, and density, case 3, at $t=0.08 \text{ s}$, without mass transfer.	64
4.7	Results of CO_2 pipe depressurization for temperature, case 3, at $t=0.08 \text{ s}$, without mass transfer.	64
4.8	Results of CO_2 pipe depressurization for pressure, and density with high order scheme, case 3, at $t=0.08 \text{ s}$, without mass transfer.	65
4.9	Results of CO_2 pipe depressurization for pressure, and density, case 3, at $t=0.08 \text{ s}$, with mass transfer.	65

4.10	Schematic of experiment facility by Hurisse and Quibel (2022)	66
4.11	Void ratio vs time at P_T location, case 4, at $t=800$ ms.	66
4.12	Pressure vs time at P1 location, case 4, at $t=800$ ms.	67
4.13	Pressure vs time at P5 location, case 4, at $t=800$ ms.	67
5.1	Comparison of convergence studies for CO_2 pipe depressurization using 6-equation model: pressure (left) and temperature (right) profiles, using the HLLC scheme with 1000, 2000, 4000, and 5000 nodes, case 1, at $t = 0.08$ s, without mass transfer.	82
5.2	Comparison of convergence studies for CO_2 pipe depressurization using 4-equation model: density (left) and velocity (right) profiles, using the HLLC scheme with 1000, 2000, 4000, and 5000 nodes, case 1, at $t = 0.08$ s, without mass transfer.	82
5.3	Results of CO_2 pipe depressurization using the 6-equation model (blue dashed) and 4-equation model (red solid): pressure (left) and temperature (right) profiles, case 1, at $t = 0.08$ s, without mass transfer. CPU time: 235 s (6-equation) vs 127 s (4-equation)	83
5.4	Results of CO_2 pipe depressurization using the 6-equation model (blue dashed) and 4-equation model (red solid): density (left) and velocity (right) profiles, case 1, at $t = 0.08$ s, without mass transfer.	83
5.5	Comparison of convergence studies for CO_2 pipe depressurization using 6-equation model: pressure (left) and temperature (right) profiles, using the HLLC scheme with 1000, 2000, 4000, and 5000 nodes, case 1, at $t = 0.08$ s, with mass transfer.	84
5.6	Comparison of convergence studies for CO_2 pipe depressurization using 4-equation model: density (left) and velocity (right) profiles, using the HLLC scheme with 1000, 2000, 4000, and 5000 nodes, case 1, at $t = 0.08$ s, with mass transfer.	84
5.7	Results of CO_2 pipe depressurization using the 6-equation model (blue dashed) and 4-equation model (red solid), along with HLLC second-order (green dash-dot) and third-order (orange dotted) results: pressure (left) and temperature (right) profiles, case 1, at $t = 0.08$ s, with mass transfer. CPU times: 265 s (6-equation), 141 s (4-equation), 149 s (HLLC 2), and 168 s (HLLC 3).	85
5.8	Results of CO_2 pipe depressurization using the 6-equation model (blue dashed) and 4-equation model (red solid), along with HLLC second-order (green dash-dot) and third-order (orange dotted) results: density (left) and velocity (right) profiles, case 1, at $t = 0.08$ s, with mass transfer.	85
5.9	Comparison of convergence studies for void ratio at PT location (2.887 m upstream from the breach): 6-equation model (left) and 4-equation model (right), using the HLLC scheme with 500, 1000, and 1500 nodes, case 2.	87
5.10	Comparison of convergence studies for pressure at P1 location (3.899 m upstream from the breach): 6-equation model (left) and 4-equation model (right), using the HLLC scheme with 500, 1000, and 1500 nodes, case 2.	87
5.11	Comparison of convergence studies for pressure at P2 location (3.033 m upstream from the breach): 6-equation model (left) and 4-equation model (right), using the HLLC scheme with 500, 1000, and 1500 nodes, case 2.	88
5.12	Comparison of convergence studies for pressure at P3 location (2.471 m upstream from the breach): 6-equation model (left) and 4-equation model (right), using the HLLC scheme with 500, 1000, and 1500 nodes, case 2.	88

5.13	Comparison of convergence studies for pressure at P4 location (3.033 m upstream from the breach): 6-equation model (left) and 4-equation model (right), using the HLLC scheme with 500, 1000, and 1500 nodes, case 2. . . .	89
5.14	Comparison of convergence studies for pressure at P5 location (2.471 m upstream from the breach): 6-equation model (left) and 4-equation model (right), using the HLLC scheme with 500, 1000, and 1500 nodes, case 2. . . .	89
5.15	Comparison of void ratio profiles at location PT (2.887 m upstream from the breach) in the Canon experiment: experimental results (Exp., black square markers), 6-equation model (6-eqt, blue solid line), 4-equation model (4-eqt, orange solid line), 4-equation model with non-instantaneous mass transfer (4-eqt-D1/D2, red/green solid line) from the solver, and HRM Tabulated EoS results (HRM Tabulated EoS, purple solid line) obtained from the literature by Lepareux (1994) , case 2.	90
5.16	Comparison of pressure profiles at location P1 (3.899 m upstream from the breach) from the Canon experiment: experimental results (Exp., black square markers), 6-equation model (6-eqt, blue solid line), 4-equation model (4-eqt, orange solid line), 4-equation model with non-instantaneous mass transfer (4-eqt-D1/D2, red/green solid line) from the solver, and HRM Tabulated EoS results (HRM Tabulated EoS, purple solid line) obtained from the literature by Lepareux (1994) , case 2.	90
5.17	Comparison of pressure profiles at location P2 (3.033 m upstream from the breach) from the Canon experiment: experimental results (Exp., black square markers), 6-equation model (6-eqt, blue solid line), 4-equation model (4-eqt, orange solid line), 4-equation model with non-instantaneous mass transfer (4-eqt-D1/D2, red/green solid line), case 2.	91
5.18	Comparison of pressure profiles at location P3 (2.471 m upstream from the breach) from the Canon experiment: experimental results (Exp., black square markers), 6-equation model (6-eqt, blue solid line), 4-equation model (4-eqt, orange solid line), 4-equation model with non-instantaneous mass transfer (4-eqt-D1/D2, red/green solid line), case 2.	91
5.19	Comparison of pressure profiles at location P4 (1.6965 m upstream from the breach) from the Canon experiment: experimental results (Exp., black square markers), 6-equation model (6-eqt, blue solid line), 4-equation model (4-eqt, orange solid line), 4-equation model with non-instantaneous mass transfer (4-eqt-D1/D2, red/green solid line), case 2.	92
5.20	Comparison of pressure profiles at location P5 (0.504 m upstream from the breach) from the Canon experiment: experimental results (Exp., black square markers), 6-equation model (6-eqt, blue solid line), 4-equation model (4-eqt, orange solid line), 4-equation model with non-instantaneous mass transfer (4-eqt-D1/D2, red/green solid line) from the solver, and HRM Tabulated EoS results (HRM Tabulated EoS, purple solid line) obtained from the literature by Lepareux (1994) , case 2.	92
5.21	Comparison of pressure profiles at location P1 (3.899 m upstream from the breach) from the Super-Canon experiment: experimental results (Exp., black square markers), 6-equation model (6-eqt, blue solid line), 4-equation model (4-eqt, orange solid line), 4-equation model with non-instantaneous mass transfer (4-eqt-D1/D2, red/green solid line) from the solver, and 5-equation model results (5-eqt, purple solid line) obtained from the literature by Daude et al. (2014) , case 3.	94

5.22	Comparison of pressure profiles at location P1 (3.899 m upstream from the breach) from the Super-Canon experiment: experimental results (Exp., black square markers), second experimental result (Exp.2, black circle marker), 6-equation model (6-eqt, blue solid line), 4-equation model (4-eqt, orange solid line), 4-equation model with non-instantaneous mass transfer (4-eqt-D1/D2, red/green solid line), case 3.	94
5.23	Comparison of pressure profiles at location P5 (0.504 m) from the Super-Canon experiment: experimental results (Exp., black square markers), 6-equation model (6-eqt, blue solid line), 4-equation model (4-eqt, orange solid line), 4-equation model with non-instantaneous mass transfer (4-eqt-D1/D2, red/green solid line) from the solver, and 5-equation model results (5-eqt, purple solid line) obtained from the literature by Daude et al. (2014) , case 3.	95
5.24	Comparison of pressure profiles at location P5 (0.504 m upstream from the breach) from the Super-Canon experiment: experimental results (Exp., black square markers), second experimental result (Exp.2, black circle marker), 6-equation model (6-eqt, blue solid line), 4-equation model (4-eqt, orange solid line), 4-equation model with non-instantaneous mass transfer (4-eqt-D1/D2, red/green solid line), case 3.	95
5.25	Comparison of void ratio profiles at location PT (2.887 m upstream from the breach) in the Super-Canon experiment: experimental results (Exp., black square markers), 6-equation model (6-eqt, blue solid line), 4-equation model (4-eqt, orange solid line), 4-equation model with non-instantaneous mass transfer (4-eqt-D1/D2, red/green solid line) from the solver, and 5-equation model results (5-eqt, purple solid line) obtained from the literature by Daude et al. (2014) , case 3.	96
6.1	Comparison of convergence studies for density: (left) without mass transfer and (right) with mass transfer, using the HLLC scheme with 200, 500, and 1000 nodes, case 1, $t = 0.8ms$	112
6.2	Comparison of convergence studies for pressure: (left) without mass transfer and (right) with mass transfer, using the HLLC scheme with 200, 500, and 1000 nodes, case 1, $t = 0.8ms$	113
6.3	Comparison of convergence studies for temperature: (left) without mass transfer and (right) with mass transfer, using the HLLC scheme with 200, 500, and 1000 nodes, case 1, $t = 0.8ms$	113
6.4	Comparison of pressure profiles using 1000 nodes with HLLC first, second, and third order: (left) without mass transfer and (right) with mass transfer, case 1, $t = 0.8 ms$	114
6.5	Comparison of density profiles using 1000 nodes with HLLC first, second, and third order: (left) without mass transfer and (right) with mass transfer, case 1, $t = 0.8 ms$	114
6.6	Comparison of the density profiles from the solver results with the reference solution: (left) without mass transfer and (right) with mass transfer, case 1, $t = 0.8ms$	115
6.7	Comparison of the pressure profiles from the solver results with the reference solution: (left) without mass transfer and (right) with mass transfer, case 1, $t = 0.8ms$	115
6.8	Comparison of the temperature profiles from the solver results with the reference solution: (left) without mass transfer and (right) with mass transfer, case 1, $t = 0.8ms$	116

6.9	Comparison of the liquid mass fraction profiles from the solver results with the reference solution: (left) without mass transfer and (right) with mass transfer, case 1, $t = 0.8ms$	116
6.10	Comparison of convergence studies for pressure: (left) without mass transfer and (right) with mass transfer, using the HLLC scheme with 1000, 2000, 4000, and 5000 nodes, case 2, $t = 3.2ms$	118
6.11	Comparison of convergence studies for velocity: (left) without mass transfer and (right) with mass transfer, using the HLLC scheme with 1000, 2000, 4000, and 5000 nodes, case 2, $t = 3.2ms$	118
6.12	Pressure profiles for different relaxation methods: instantaneous mechanical relaxation (p-relax, black solid line), instantaneous mechanical relaxation and finite-rate thermal relaxation (pT-finite, blue dashed line), instantaneous mechanical and thermal relaxation (pT, blue solid line), instantaneous mechanical and thermal relaxation with finite-rate chemical relaxation (pTg-finite, red dashed line), and instantaneous mechanical, thermal, and chemical relaxation (pTg, red solid line), case 2, $t = 3.2$ ms.	119
6.13	Velocity profiles for different relaxation methods: instantaneous mechanical relaxation (p-relax, black solid line), instantaneous mechanical relaxation and finite-rate thermal relaxation (pT-finite, blue dashed line), instantaneous mechanical and thermal relaxation (pT, blue solid line), instantaneous mechanical and thermal relaxation with finite-rate chemical relaxation (pTg-finite, red dashed line), and instantaneous mechanical, thermal, and chemical relaxation (pTg, red solid line), case 2, $t = 3.2$ ms.	119
6.14	Void ratio profiles for different relaxation methods: instantaneous mechanical relaxation (p-relax, black solid line), instantaneous mechanical relaxation and finite-rate thermal relaxation (pT-finite, blue dashed line), instantaneous mechanical and thermal relaxation (pT, blue solid line), instantaneous mechanical and thermal relaxation with finite-rate chemical relaxation (pTg-finite, red dashed line), and instantaneous mechanical, thermal, and chemical relaxation (pTg, red solid line), case 2, $t = 3.2$ ms.	120
6.15	Vapor mass fraction profiles for different relaxation methods: instantaneous mechanical relaxation (p-relax, black solid line), instantaneous mechanical relaxation and finite-rate thermal relaxation (pT-finite, blue dashed line), instantaneous mechanical and thermal relaxation (pT, blue solid line), instantaneous mechanical and thermal relaxation with finite-rate chemical relaxation (pTg-finite, red dashed line), and instantaneous mechanical, thermal, and chemical relaxation (pTg, red solid line), case 2, $t = 3.2$ ms.	120
6.16	Schematic of experiment facility for the Edwards and O'Brien.	121
6.17	Comparison of void ratio profiles at location G5 (2.627 m upstream from the breach) from the Edwards O'Brien experiment: experimental results (Exp., black square markers), instantaneous mechanical and thermal relaxation (pT, blue solid line), instantaneous mechanical, thermal, and finite-rate chemical relaxation (pTg-finite, red solid line), and instantaneous mechanical, thermal, and chemical relaxation (pTg, green dashed line), case 3.	123
6.18	Comparison of void ratio profiles at location G5 (2.627 m upstream from the breach) from the Edwards O'Brien experiment: experimental results (Exp., black square markers), pTg-finite results (pTg-finite, red solid line) from the solver, and RELAP5 results (RELAP5, blue dashed line) obtained from the literature by Sun et al. (2021) , case 3.	123

6.19	Comparison of pressure profiles at location G5 (2.627 m upstream from the breach) from the Edwards O'Brien experiment: experimental results (Exp., black square markers), instantaneous mechanical and thermal relaxation (pT, blue solid line), instantaneous mechanical, thermal, and finite-rate chemical relaxation (pTg-finite, red solid line), and instantaneous mechanical, thermal, and chemical relaxation (pTg, green dashed line), case 3.	124
6.20	Comparison of pressure profiles at location G5 (2.627 m upstream from the breach) from the Edwards O'Brien experiment: experimental results (Exp., black square markers), pTg-finite results (pTg-finite, red solid line) from the solver, and RELAP5 results (RELAP5, blue dashed line) obtained from the literature by Sun et al. (2021) , case 3.	124
6.21	Comparison of pressure profiles at location G7 (4.017 m upstream from the breach) from the Edwards O'Brien experiment: experimental results (Exp., black square markers), instantaneous mechanical and thermal relaxation (pT, blue solid line), instantaneous mechanical, thermal, and finite-rate chemical relaxation (pTg-finite, red solid line), and instantaneous mechanical, thermal, and chemical relaxation (pTg, green dashed line), case 3.	125
6.22	Comparison of pressure profiles at location G7 (4.017 m upstream from the breach) from the Edwards O'Brien experiment: experimental results (Exp., black square markers), pTg-finite results (pTg-finite, red solid line) from the solver, and RELAP5 results (RELAP5, blue dashed line) obtained from the literature by Sun et al. (2021) , case 3.	125
6.23	Schematic of experiment facility for the Canon.	126
6.24	Comparison of void ratio profiles at location PT (2.887 m upstream from the breach) from the Canon experiment: experimental results (Exp., black square markers), instantaneous mechanical, thermal, and finite-rate chemical relaxation (pTg-finite, red solid line), and instantaneous mechanical, thermal, and chemical relaxation (pTg, green solid line) from the solver, and HRM Tabulated EoS results (HRM Tabulated EoS, purple solid line) obtained from the literature by Lepareux (1994) case 4.	127
6.25	Comparison of pressure profiles at location P1 (3.899 m upstream from the breach) from the Canon experiment: experimental results (Exp., black square markers), instantaneous mechanical and thermal relaxation (pT, blue solid line), instantaneous mechanical, thermal, and finite-rate chemical relaxation (pTg-finite, red solid line), and instantaneous mechanical, thermal, and chemical relaxation (pTg, green solid line) from the solver, and HRM Tabulated EoS results (HRM Tabulated EoS, purple solid line) obtained from the literature by Lepareux (1994) case 4.	127
6.26	Comparison of pressure profiles at location P2 (3.033 m upstream from the breach) from the Canon experiment: experimental results (Exp., black square markers), instantaneous mechanical and thermal relaxation (pT, blue solid line), instantaneous mechanical, thermal, and finite-rate chemical relaxation (pTg-finite, red solid line), and instantaneous mechanical, thermal, and chemical relaxation (pTg, green solid line), case 4.	128

6.27	Comparison of pressure profiles at location P3 (2.471 m upstream from the breach) from the Canon experiment: experimental results (Exp., black square markers), instantaneous mechanical and thermal relaxation (pT, blue solid line), instantaneous mechanical, thermal, and finite-rate chemical relaxation (pTg-finite, red solid line), and instantaneous mechanical, thermal, and chemical relaxation (pTg, green solid line), case 4.	128
6.28	Comparison of pressure profiles at location P4 (1.6965 m upstream from the breach) from the Canon experiment: experimental results (Exp., black square markers), instantaneous mechanical and thermal relaxation (pT, blue solid line), instantaneous mechanical, thermal, and finite-rate chemical relaxation (pTg-finite, red solid line), and instantaneous mechanical, thermal, and chemical relaxation (pTg, green solid line), case 4.	129
6.29	Comparison of pressure profiles at location P5 (0.504 m upstream from the breach) from the Canon experiment: experimental results (Exp., black square markers), instantaneous mechanical and thermal relaxation (pT, blue solid line), instantaneous mechanical, thermal, and finite-rate chemical relaxation (pTg-finite, red solid line), and instantaneous mechanical, thermal, and chemical relaxation (pTg, green solid line) from the solver, and HRM Tabulated EoS results (HRM Tabulated EoS, purple solid line) obtained from the literature by Lepareux (1994) case 4.	129
6.30	Schematic of experiment facility for the Bartak experiment.	131
6.31	Comparison of pressure profiles at location P1 (0.048 m upstream from the breach) from the Bartak experiment: experimental results (Exp., black square markers), instantaneous mechanical and thermal relaxation (pT, blue solid line), instantaneous mechanical, thermal, and finite-rate chemical relaxation (pTg-finite, red solid line), and instantaneous mechanical, thermal, and chemical relaxation (pTg, green solid line), case 5.	132
A.1	Overview of the error analysis for the Canon experiment across various numerical models at the P1 location.	141
A.2	Overview of the error analysis for the Canon experiment across various numerical models at the P5 location.	142
B.1	Overview of the error analysis for the Super-Canon experiment across various numerical models at the P1 location.	143
B.1	Overview of the error analysis for the Super-Canon experiment across various numerical models at the P1 location (continued).	144
B.2	Overview of the error analysis for the Super-Canon experiment across various numerical models at the P5 location.	144
B.2	Overview of the error analysis for the Super-Canon experiment across various numerical models at the P5 location (continued).	145
C.1	Overview of the error analysis for the Edwards O'Brien experiment at the G5 location.	147
C.1	Overview of the error analysis for the Edwards O'Brien experiment at the G5 location (continued).	148
C.2	Overview of the error analysis for the Edwards O'Brien experiment at the G7 location.	148
C.2	Overview of the error analysis for the Edwards O'Brien experiment at the G7 location (continued).	149

Chapter 1

Introduction

1.1 Industrial Context

Nuclear-based electricity generation, which has been a topic of safety debates since its inception, accounted for about 10% of the total energy supply as of 2023, according to the [IAE](#). The United States leads with the highest nuclear share of electricity generation, producing 780 TWh, while France has the highest percentage of its electricity generated from nuclear power, at 65%. In addition, nuclear technology has many application areas such as medical applications, food and agriculture, and imaging [Molins \(2001\)](#), [Chandra \(2011\)](#). As with all other electricity generation methods, nuclear-based electricity generation has its own advantages and disadvantages [Irvine \(2011\)](#). The advantages of nuclear energy can be listed as follows:

- **High power output:** Nuclear power plants generate significant amounts of energy relative to other power sources, which makes them excellent providers of electricity. Additionally, thanks to this feature, nuclear power is a strong candidate to take the place of current base load electricity sources such as coal power plants that considerably increase air pollution.
- **Carbon-free electricity:** Nuclear power facilities operate without emitting any air pollution or carbon dioxide, in contrast to conventional fossil fuel generation sources, which release significant volumes of carbon dioxide into the environment [OECD and Nuclear Energy Agency \(2007\)](#). However, it should not be forgotten that there is an indirect carbon emission as different energy sources are used during the production and enrichment of uranium.
- **Small land footprint:** Regarding the first advantage listed, nuclear power plants occupy significantly less physical area to generate the same amount of electricity compared to other common renewable energy plants.
- **Reliable energy source:** Nuclear power has a greater capacity factor than other conventional methods, making it a reliable source. According to the data of the U.S. Department of Energy for 2023, more than 93% of the time throughout the year, nuclear power facilities are operating at their maximum capacity [5Fa](#). In addition, nuclear-based energy production is more independent than other methods in terms of the unit price of raw materials, which is very important in terms of transmitting electricity to the industry and citizens of the countries in extraordinary situations (epidemic, war, etc.) in a way that will be less affected by the global markets.

Despite the various advantages mentioned above, many people still have a negative opinion of nuclear energy. Disadvantages and concerns about nuclear energy can be listed as:

- **Production of radioactive waste:** As it is known, after the chain reaction in the reactor, very hot and radioactive waste is produced. Radioactive waste is dangerous to the majority of life forms and the environment so governmental organizations regulate radioactive waste to safeguard public health and the environment [OECD and Nuclear Energy Agency \(2007\)](#). However, it should not be forgotten that this radioactive waste is classified and prevented from causing pollution by being buried near the surface or underground.
- **High investment cost:** While operating nuclear power plants do not spend a lot of money, their initial costs are quite high compared to other power plants due to their international security measures and complex systems [Wealer et al. \(2021\)](#).
- **Nuclear proliferation:** Another important prejudice against nuclear among the public is the possibility of the proliferation of nuclear weapons and technology [Sagan \(2011\)](#). Although international agreements try to prevent the proliferation of nuclear weapons, it is assumed that countries that have nuclear power plants but do not have nuclear weapons have the potential to ignore these agreements and use them for the interests of their own countries.
- **Nuclear Accidents:** Although experts have made serious improvements regarding the safety measures of nuclear power plants ever since the initial commercial nuclear power plant was successfully linked to the electrical grid and began supplying power to the network, it is a fact that nuclear accidents such as Fukushima-Daiichi and Chernobyl, which happened in the recent past, will not be easily erased from the public memory.

Although there are many different types of reactors and studies are carried out on 4th generation reactors, the most used nuclear reactor type today is the Pressurized Water Reactor (PWR) with 310 reactors worldwide. Approximately 60 reactors are currently under construction worldwide, with an additional 110 reactors planned. Türkiye is also preparing to open its first nuclear power plant, Akkuyu-1, in 2025. Different types of reactors and their main features can be seen in Table 1.1.

Pressurized water reactors were initially designed for use in submarines. Westinghouse Bettis Laboratories and Knolls Atomic Power Laboratory carried out the research and development work. This initial research and development work led to the creation of a commercial PWR for use in nuclear power plants. A number of industrial PWR providers eventually appeared in the USA, Germany, France, Russia, and Japan. Many PWRs were put into service over the last three decades, resulting in thousands of reactor years of operation. A schematic of the PWR is shown in Figure 1.1.

As widely recognized, nuclear power plants have remained a topic of significant debate and controversy, largely due to the wide range of concerns expressed by the public since their initial introduction and use in energy production. Over the years, experts have worked and continue to work to improve the safety of NPPs and ease public opinion. This subpart first outlines the safety guidelines followed by NPPs in order to avoid incidents and accidents and lessen their effects. Nuclear power plants offer a "defense-in-depth" approach to ensure maximum safety, consisting of multiple safety systems that complement the inherent characteristics of the reactor core. The defense-in-depth approach enables an NPP to be designed, manufactured, and operated not only during normal operation but also by calculating certain accident probabilities. Thus, the facility has a number of security measures that protect

Reactor type	Main countries	Number	GWe	Fuel
Pressurized water reactor (PWR)	USA, France, Japan, Russia, China	310	296.5	enriched UO_2
Boiling water reactor (BWR)	USA, Japan, Sweden	60	60.9	enriched UO_2
Pressurized heavy water reactor (PHWR)	Canada, India	48	25.0	natural UO_2
Light water graphite reactor (LWGR)	Russia	10	6.5	enriched UO_2
Advanced gas-cooled reactor (AGR)	UK	8	4.7	natural U, enriched UO_2
Fast neutron reactor (FNR)	Russia	2	1.4	PuO_2 and UO_2
High temperature gas-cooled reactor (HTGR)	China	1	0.2	enriched UO_2
TOTAL		439	395.3	

Table 1.1: Operable nuclear power plants provided by Nuc.

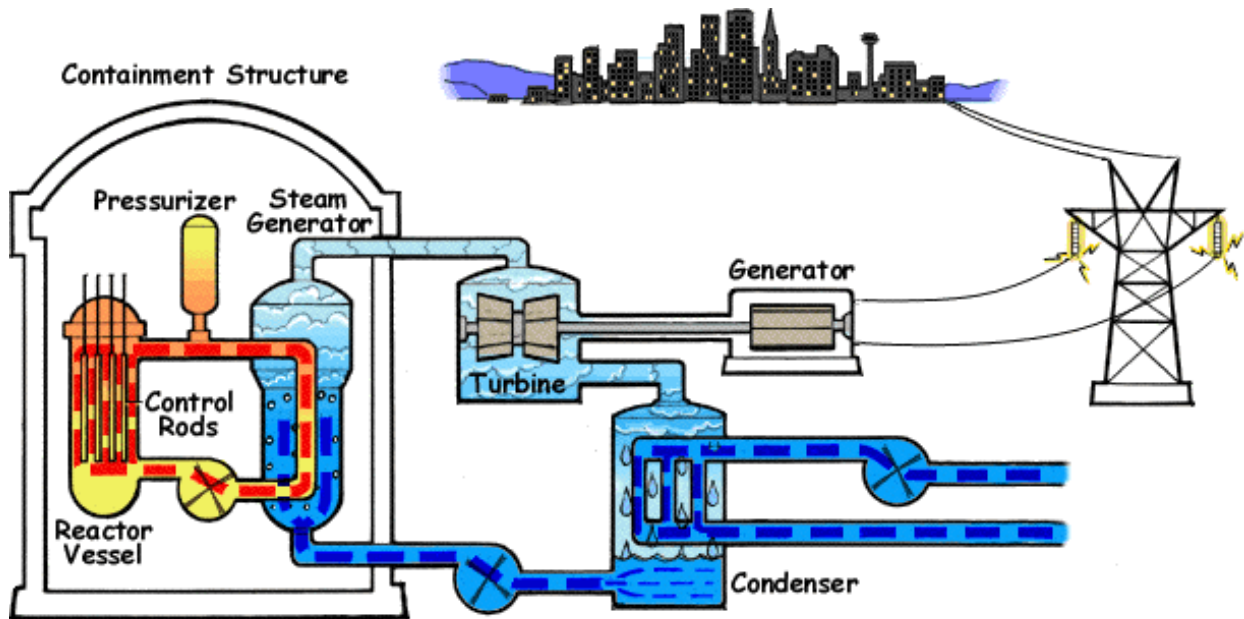


Figure 1.1: Schematic of a Pressurized Water Reactor (PWR).

against natural disasters, human error, and equipment failures. The chain fission reaction that takes place in a nuclear reactor emits high-energy particles that require the protection of people and the environment [Bodansky \(2004\)](#). This situation creates 3 main problems that manufacturers and operators need to solve:

- Continued cooling of fuel even after reactor trip,
- Continuous checking of reactivity,
- Limiting radioactive fission products even when decay heat is not completely removed.

The fulfillment of these challenging tasks is ensured by two basic principles; safety barriers and defense-in-depth approach. The three consecutive barriers between the fuel and the environment aim to prevent the release of radioactive products under all conditions.

- Fuel matrix and fuel cladding: During unusual situations and most accidents, the fuel matrix and fuel cladding both keep fission fragments contained and stop the escape of gases produced during fission.
- The primary loop is a closed loop design made of thick steel so if any fuel cladding is damaged the fission products are confined to this secondary barrier.
- The containment building made of thick concrete is the last barrier that aims to prevent the release of fission products into the environment, which exceeds the primary and secondary safety barriers, respectively [Masterson \(2019\)](#).

The defense-in-depth concept NPPs has been adopted to effectively prevent the release of fission products under all circumstances with the 3 safety barriers mentioned above. With the experience gained so far, and feedback from the operators and the designer, this approach is constantly updated to ensure the safe operation of NPPs. This approach encompasses all actions related to safety, including those concerning human behavior, organizational practices, and system design, regardless of whether the system is operating at full capacity or under reduced power conditions. In this context, there are 5 levels in the defense-in-dept approach and they are summarized below (see for details [Internationale Atomenergie-Organisation \(2012\)](#)):

Level	Objective	Main measure
1	Preventing operating malfunctions and system failures	Conservative design and high quality in construction and operation
2	Detecting failures and comprehensive management of operating malfunctions	Systems for control, protection, and review (for maintaining the facility within its normal operating domain) and monitoring (preventing failures)
3	Comprehensive accident management (including design-basis accidents)	Engineered safety features and accident procedures
4	Comprehensive management of severe accidents, prevention of accident progression and mitigation of consequences	Complementary measures and accident management
5	Limiting radiological consequences in the event of a release of radioactive substances	Off-site emergency plan

Table 1.2: Main objectives and measures of defence-in-depth approach.

Accidents can be classified according to their probability [Pro \(1992\)](#).

- Design-Basis Accidents (DBAs): They are postulated accidents that a nuclear site must be built to resist without causing damage to the components, structures, and systems required to guarantee public health and safety [Masterson \(2019\)](#). According to Probabilistic Safety Analyzes (PSA), their incidence is between $10^{-4} - 10^{-2} \text{ year}^{-1} \cdot \text{reactor}^{-1}$.

- Beyond Design-Basis Accidents (BDBAs); They are accident sequences that could happen but were not completely taken into account throughout the design phase since it was thought that they were too unlikely to happen. According to PSA, their incidence is between $10^{-4} - 10^{-6} \text{ year}^{-1} \cdot \text{reactor}^{-1}$.
- Severe Accidents (SAs): They are accidents with an extremely low probability of occurrence but with serious consequences. According to PSA, their incidence is less than $10^{-6} \text{ year}^{-1} \cdot \text{reactor}^{-1}$.

Loss of Coolant Accident (LOCA) can be classified as among the accidental scenarios that could impact a PWRs. Despite the possibility of numerous other accidental scenarios in PWRs, we will focus on LOCA as the main application of this work. LOCAs are design-based/postulated accidents that cause fractures in the reactor coolant pressure boundary and lead to a loss of reactor coolant at a rate greater than the capacity of the reactor make-up system [Masterson \(2019\)](#). As the fracture in the pipes can be small or large, as soon as the leak is detected, the chain reaction in the core is terminated by means of control rods absorbing the neutron. Then, the loss of coolant caused by LOCA is tried to be compensated through safety injection systems and ensure the long-term removal of residual heat. If the safety systems respond and manage to remove the heat in a timely manner, there will be no problems with the reactor core and fuel rods, and almost no radioactivity is released, thus LOCA remains as DBA. However, in the event of a problem in the safety systems or any other malfunction, sudden depressurization happens and the water starts to boil so that the heat increase in the core, and the oxidation of the fuel cladding by the coolant vapor cause the core to deteriorate and the hot fuel rods to melt completely or partially [Masterson \(2019\)](#). In this case, LOCA ceases to be DBA and becomes the SA initiator.

A hypothetical Loss of Coolant Accident can be categorized into two main aspects: the fast-transient aspect and the quasi-stationary aspect. Regardless of whether the transient or stationary phase is considered, it is essential to focus on the breach in the primary coolant loop, as this is where the system transitions into a two-phase flow regime. For the fast-transient aspect, in numerical analysis, it is assumed that the hypothetical coolant loss accident mostly occurs in the cold leg of the primary circuit and involves a double-ended guillotine break. At the breach, a rarefaction wave is generated and propagates through the primary loop. The dynamics of the two-phase flow are crucial in determining the amplitude of the rarefaction wave, which serves as a critical input for fluid-structure interaction (FSI) analysis. Accurate prediction of this amplitude is fundamental for assessing the mechanical forces exerted on various reactor core components. These forces can vary significantly depending on the propagation characteristics of the wave, and any misrepresentation of this input may lead to incorrect estimations of structural loads, potentially compromising the reactor's core integrity.

The quasi-stationary aspect follows once the system stabilizes after the initial transient phase, during which the dynamics become less abrupt. This phase is significantly influenced by the discharge rate of the coolant, a key parameter in the safety analysis of pressurized water reactors during LOCA. Accurate modeling of the discharge rate is essential for the design and improvement of Emergency Core Cooling Systems (ECCS), as it directly impacts the re-flooding and cooling of the reactor core. At the breach, due to the substantial pressure differences between the inside of the primary loop and the surrounding environment, the mass flow rate often becomes choked. In this condition, the coolant flow reaches its critical value, representing the maximum rate at which the coolant exits through the breach. Determining this critical mass flow rate is vital, as it defines the upper limit of the coolant loss and plays an important role in assessing the system's ability to sustain cooling and avoid

core damage.

A metastable state refers to a condition where a substance remains in an intermediate state temporarily before transitioning to a more stable phase. In Pressurized Water Reactors, the coolant, which is water, is typically maintained at high pressure to keep it in a liquid state even at temperatures above its normal boiling point. Under normal operating conditions, this coolant is in a single-phase liquid state and not in a metastable state. During an LOCA, the situation changes dramatically. A LOCA involves a sudden breach in the reactor's primary coolant loop, leading to a rapid pressure drop. As the high-pressure coolant is subjected to a lower-pressure environment, it experiences rapid depressurization. This sudden pressure drop creates conditions where the water can no longer remain in its single-phase liquid state and begins to transition to a two-phase flow domain of liquid and vapor. In this transition period, the coolant may enter a metastable state. This is an intermediate phase where the superheated liquid water exists at a pressure and temperature combination where it should ideally be boiling but hasn't yet fully transitioned to a vapor state. The delay before the complete shift to the two-phase flow domain is when the metastable state occurs. During this short period, the coolant temporarily maintains its liquid form despite the conditions favoring a phase change. Understanding this transient metastable state is crucial because it impacts the behavior of the coolant and the reactor's thermal-hydraulic dynamics. Accurate modeling of this transition, including the metastable state, is essential for predicting the reactor's behavior under accident conditions and ensuring the effectiveness of safety systems designed to mitigate the consequences of a LOCA [Masterson \(2019\)](#).

In summary, based on the aforementioned points, the importance of LOCA analysis and the reason for it being the primary focus of this work can be summarized as follows:

1. **Safety of the Reactor Core:** In the event of a LOCA, the loss of coolant leads to overheating of the reactor core, which can cause core damage or meltdown. Coolant is essential for removing heat from the fuel rods, and without it, core temperatures can increase rapidly, leading to catastrophic failures.
2. **Reactor Integrity and Depressurization Wave Impact:** The rapid depressurization following a LOCA generates a pressure wave that can impose severe mechanical stress on reactor components. LOCA analysis is essential for ensuring that the reactor's structural integrity is maintained under such conditions, preventing material fatigue or failure.
3. **Risk Assessment and Prevention:** By analyzing LOCA scenarios, experts can assess the potential risks associated with coolant loss, identify weak points in the system, and implement preventive measures or enhance safety systems to mitigate these risks.
4. **Development of Safety Systems:** LOCA analysis aids in the design and optimization of emergency core cooling systems, which are critical in providing immediate coolant to the reactor in case of an accident, preventing core damage.
5. **Regulatory Compliance:** LOCA analysis is often mandated by regulatory authorities to ensure reactors meet safety standards. Detailed analysis ensures that reactors can manage coolant loss scenarios and protect the public from radiation exposure.
6. **Operational Planning:** Understanding how pressure, temperature, and coolant levels evolve during a LOCA enables plant operators to develop effective response strategies, stabilizing the reactor and minimizing damage during an accident.

This study focuses on the fast-transient aspect of LOCA involving metastable state. The primary goal is to evaluate the system's behavior under various conditions by testing different computational models across a range of test cases. These tests aim to provide a comprehensive understanding of how different modeling approaches influence the prediction of rarefaction wave propagation, which can serve as a critical input for fluid-structure interaction analysis and potentially aid in assessing core integrity issues during the fast-transient phase.

1.2 Multiphase Flow

Multiphase flow is a complex phenomenon encountered in various natural and industrial processes, where multiple phases coexist and interact within a system. These phases typically include combinations of gases, liquids, and solids, each with distinct physical properties and behaviors. Understanding and modeling multiphase flow is crucial in many fields, such as chemical engineering, petroleum engineering, nuclear safety, and environmental engineering, as described by [Brennen \(2005\)](#) and [Crowe et al. \(2011\)](#). This section delivers a brief review of the fundamental aspects of multiphase flow, including its features, characteristics, and significance. The main focus will be on gas-liquid flows.

Gas-Liquid Flow: Gas-liquid flows are highly complex due to the combined characteristics of an interface that can undergo deformation and the property of compressibility associated with a specific phase in the system. For given flow rates of both phases within a channel, the gas-liquid interfacial distribution can adopt an infinite variety of possible configurations. Despite this variability, these configurations can be classified into distinct types of interfacial distributions, commonly referred to as flow regimes. This classification aids in understanding and predicting the behavior of gas-liquid mixtures in various industrial applications. In-depth examinations of these patterns are provided by [Taitel et al. \(1980\)](#), [Barnea et al. \(1983\)](#), and [Wallis \(2020\)](#).

1. Vertical Gas-Liquid Flow

- **Bubbly Flow:** Small gas bubbles dispersed within a continuous liquid phase. Common in boiling and cavitation processes [Robinson et al. \(2008\)](#).
- **Slug Flow:** Large gas bubbles (slugs) alternate with liquid slugs, often observed in pipelines.
- **Churn Flow:** A chaotic mixture of gas and liquid, where large gas bubbles coalesce and break apart.
- **Annular Flow:** A thin liquid film flows along the pipe wall with a central gas core, typical in high-velocity conditions [Two \(2017\)](#).

2. Horizontal Gas-Liquid Flow

- **Bubbly Flow:** It's similar to the equivalent pattern in vertical flow. Nevertheless, due to the influence of gravity, bubbles tend to gather and concentrate in the upper section of the pipe, as illustrated by [da Silva \(2008\)](#).
- **Plug Flow:** Large gas bubbles (plugs) separated by liquid slugs.
- **Stratified Flow:** Two immiscible liquids flow in separate layers due to density differences, commonly seen in horizontal pipes.

- **Wavy Flow:** A variation of stratified flow where the interface between the gas and liquid phases exhibits waves due to higher gas velocities.
- **Slug Flow:** Similar to plug flow but with more turbulent mixing between the gas and liquid phases.
- **Annular Flow:** A thin layer of liquid moves steadily along the inner surface of the pipe, while a gas core occupies the central region of the flow [Arabi et al. \(2023\)](#).

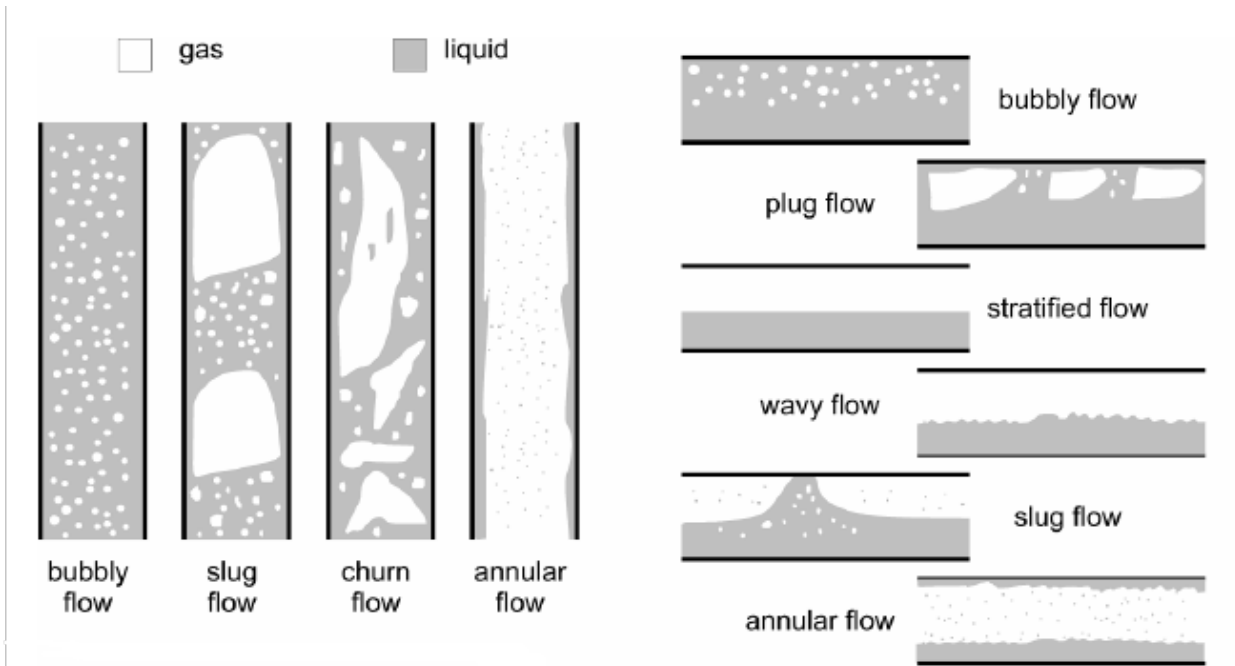


Figure 1.2: Flow patterns in vertical (left) and horizontal (right) pipe by [da Silva \(2008\)](#).

Multiphase flow systems exhibit unique characteristics influenced by the interaction between phases. Key characteristics include :

1. Flow Regimes:

- The spatial distribution and flow pattern of phases, known as flow regimes, vary with flow conditions, geometry, and phase properties. Identifying flow regimes is essential for accurate modeling and control [Ishii and Hibiki \(2011\)](#).

2. Phase Interactions:

- Interactions between phases, such as drag, lift, and interfacial tension, significantly affect the flow dynamics. Such interactions play a crucial role in determining the distribution of phases within the system, the resulting pressure loss along the flow, as well as the rates at which heat and mass are transferred between different regions. [Prosperetti and Tryggvason \(2007\)](#).

3. Non-Linear Behavior:

- Multiphase flow often exhibits non-linear behavior due to complex phase interactions and flow instabilities. Predicting and controlling such behavior requires sophisticated models and simulation techniques [Crowe et al. \(2011\)](#).

4. Transient Nature:

- Multiphase flow can be transient, with flow properties changing over time. Transient phenomena, such as phase separation and coalescence, impact system performance and safety [Brennen \(2005\)](#).

Gas-liquid flows are prevalent in a wide range of fields, including both naturally occurring processes and complex systems designed and developed in various engineering applications. Among natural gas-liquid multiphase flows, rain is likely the most familiar example. However, bubbles and droplets are also crucial in the exchange of heat and mass between the oceans and the atmosphere, as well as in volcanic eruptions. In biological systems, gas-liquid flows are exemplified by the cardiovascular and respiratory systems, where blood flow and air movement are essential processes. Emerging fields such as microfluidics, nanomedicine, and the modeling and simulation of complex flows in living systems, such as blood flow in microvascular networks, depend on an accurate description of these flows [Dias et al. \(2012\)](#).

In engineering, gas-liquid flow systems are useful in many applications in industries. For example, in the power systems such as nuclear power plant or internal combustion engine, the gas-liquid flow is inherently involved. In chemical engineering, equipment such as bubble columns, packed bed reactors, and spray dryers utilize gas-liquid flows to optimize performance. In industrial contexts, the presence of gas-liquid flows can either be advantageous or harmful. Certain flow structures are engineered to enhance system performance. For example, in the chemical industry, the bubbly flow regime is preferred in mixing processes due to its high mass, momentum, and energy transfer rates, facilitated by the fine dispersion of gas bubbles in the liquid, which increases the interfacial area and turbulence [Heijnen and Van't Riet \(1984\)](#). This results in improved mixing and transfer efficiencies. Conversely, some gas-liquid flow regimes can negatively impact system performance or cause damage. In the oil and gas industry, slug flow regimes are undesirable during hydrocarbon production and transportation in pipelines. The high momentum of slug liquids generates substantial forces at elbows, tees, and other process equipment. These fluctuating forces can cause vibrations, leading to cyclic fatigue damage or even pipe rupture [Wang et al. \(2018\)](#), [Mohammed et al. \(2021\)](#). For this reason, they can increase the corrosion rate and maintenance costs of facilities.

Regardless of whether gas-liquid flows are beneficial or harmful, their study is essential due to their inevitability in both natural and engineered systems. A thorough understanding of their behavior enables engineers to either promote or mitigate their occurrence and predict their effects on system performance. This is particularly crucial in the nuclear industry, where safety analyses demand a comprehensive understanding of gas-liquid flows to ensure safe and efficient operation. This study will specifically focus on gas-liquid two-phase flows, examining their dynamics, modeling techniques, and applications. Understanding these flows is critical for advancing safety and efficiency in various industrial applications, especially in the context of nuclear safety.

1.3 Plan of the thesis

Apart from the introductory chapter, which outlines the foundational context and details the primary objectives of this study, the remainder of the thesis is structured in the following manner:

In Chapter 2, a detailed mathematical framework of two-phase flow models is presented. This includes an in-depth discussion on the averaging procedures for two-phase flows, the theory of conservation laws, and the Riemann problem. A variety of two-phase flow models,

ranging from the more complex seven-equation framework to the simpler three-equation approach, are classified and thoroughly examined in detail.

Chapter 3 is devoted to the thermodynamic metastability of the system. Pure substance phase diagrams, liquids and vapors state equation, and the nature and emergence of metastable states are examined in this chapter. The final part of the chapter concerns itself with phase stability and metastable state.

Chapter 4 introduces the numerical solver NSMB. This chapter describes the development and implementation of the three-equation and four-equation models, as well as the numerical methods employed, including the Harten-Lax-van Leer-Contact (HLLC) Riemann solver and high-order extensions. Several validation test cases are also given to demonstrate the accuracy and efficiency of the models.

Chapter 5 compares the four-equation and six-equation models. The numerical solution methods and the relaxation procedures used are studied in this chapter for both models under mechanical, thermal, and chemical relaxations. Validation test cases are presented to compare the performance of the models in various flow scenarios.

Chapter 6 introduces a six-equation model with arbitrary-rate relaxation, which allows for a more flexible treatment of thermal and chemical processes. The chapter explains the numerical solution methods and provides validation against experimental data, highlighting the model's advantages over conventional approaches.

In the final chapter, the main conclusions are outlined, and possible directions for future research and study are explored.

Chapter 2

Mathematical framework of two-phase flow models

Multiphase mixtures are common in nature. Moreover, the nature of compressible multiphase mixtures is important today as they are used in many different industries. For example, conventional power plants, nuclear power plants, internal combustion engines, heat exchangers, and air conditioners. Therefore, the above-mentioned examples and other application areas have an important position in the industrial market. The importance of optimization in engineering applications is clear, so understanding the nature of compressible multiphase flows and obtaining clearer results is an important milestone for progress in these areas. Multiphase flows are more complex than single-phase flows. While single-phase flows can be basically classified into three main categories: laminar, transitional, and turbulent, there are many flow models (bubbly flow, plug flow, etc. see 1.2) for multiphase flows and they are not standardized. Initially, multiphase flow studies were based on empirical and needed correlations, but as they found wider applications, experts focused on mathematical modeling. However, mathematical modeling and numerical calculation has some fundamental challenges. Fundamentally, the main cause of these difficulties is the moving and deformable interface separating the two fluids. The interaction between the fluids involving the transfer of mass, momentum, and energy across these interfaces makes mathematical modeling very challenging [Zein \(2010\)](#). The discontinuity of fluid properties across the interfaces is a challenge for numerical methods. Therefore, interfaces are important for modeling multiphase fluids. Although there are different models for many different situations in the literature, it can be said that there are basically 2 approaches according to the way interfaces are handled [Peluchon et al. \(2017\)](#):

- Sharp interface methods
- Diffuse interface methods

In contrast to the diffuse interface method, where the sharp fluid-fluid interface is switched by a narrow layer where the fluids may mix, sharp interface methods demand additional efforts to find and treat the interfaces specifically.

Sharp interface models have different approaches and these are:

- Lagrangian Methods: In this method, interfaces are positioned and move with local velocity. However, in real fluid flow, severe deformation of the interfaces and distortion of the mesh structure are observed. Due to the deformations, changes in the flow pattern are observed, which requires constant adjustments in the mesh structure, thus making the system complex. Therefore, the numerical solution of this method

is difficult and expensive to implement. For detailed information see [Benson \(1992\)](#), [Saurel and Lemetayer \(2001\)](#).

- Volume of fluid method (Eularian): In this method, when using a fixed mesh, the interfaces are not directly traced, but are reconstructed by calculating the volume ratio of the phases. Initially, this method was used for incompressible flows [Hirt and Nichols \(1981\)](#), but as a result of the work of experts, it has been included in compressible flow applications [Rider et al. \(1995\)](#). For compressible flows, the assessment of the density and internal energy of the fluids is a challenging process and there are many question marks in the mathematical modeling. Although the model results are considered realistic, the lack of open sharing and interpretation of the entire modeling process prevents the evaluation of different experts [Richard Saurel et al. \(2009\)](#).
- Level Set method (Eularian): An implicit method to capture the moving front is the level-set method, which was initially put forth by [Osher and Sethian \(1988\)](#). The fundamental concept is that an auxiliary field specified over the area of interest is presented as the front location's zero-level set. Although this method is not conservative in terms of mass, realistic results can be obtained by combining it with other methods [Ménard et al. \(2007\)](#).
- Ghost Fluid Method (Eularian): The model is initially proposed by [Fedkiw et al. \(1999\)](#), and employed in the simulation of multiphase flows, particularly those involving sharp discontinuities such as shock waves and material interfaces. The method effectively introduces ghost values to maintain the sharpness of the interface while ensuring the correct application of boundary conditions across different phases without introducing numerical diffusion. The method has been particularly powerful in computational fluid dynamics for problems like shock-bubble interactions and the modeling of complex fluid interfaces.
- Arbitrary Lagrangian–Eulerian (ALE) methods: A flexible computational tool that recruits the best in each of the previously described methods of Lagrangian and Eulerian, making it particularly useful for problems involving large deformations, fluid-structure interactions, and moving boundaries. It was originally developed to overcome the limitations of purely Lagrangian or Eulerian methods. The method has seen widespread application in fields ranging from fluid dynamics to structural mechanics, particularly in simulations involving complex interactions between fluids and solid structures. For detailed information see [Hirt et al. \(1997\)](#), [Donea et al. \(2004\)](#), [Lan and Sun \(2021\)](#).
- Front tracking methods: In these methods, different flow solvers are combined with a fixed grid. The method is flexible as a result. At points far from the interface, the Eulerian solver is used, while special schemes are used around the interface [LeVeque and Shyue \(1996\)](#), thus combining them. In general, these methods are conservative in 1D, but lose this property in higher dimensions. Even though these approaches are conceptually straightforward, coding them is quite challenging. For detailed information see [Unverdi and Tryggvason \(1992\)](#), [Tryggvason et al. \(2001\)](#).

In general, the main advantage of sharp interface methods is the absence of artificial diffusive interfaces due to numerical calculations, but they are complex modeling methods and therefore computationally expensive. Finally, they require an initial understanding of the interfaces, hence they are unable to generate emerging interfaces dynamically [Richard Saurel et al. \(2009\)](#).

Let's examine the second approach in more detail, the diffusive interface method. Numerical diffusion is typically viewed as a disadvantage for numerical methods. However, it is a crucial component for capturing discontinuities. It makes it simple to calculate shock or contact discontinuities in gas dynamics applications and predicts the occurrence of these discontinuities [Saurel and Lemetayer \(2001\)](#). These models have a number of benefits over the previous series of models [Richard Saurel et al. \(2009\)](#):

- Globally, the same technique is applied to zones with pure fluids and those with mixtures. Each location of the flow is solved using an extended hyperbolic system.
- These models and techniques can construct interfaces dynamically that do not initially exist.
- These techniques can also handle the interfaces that separate pure fluids from fluid mixtures.

These models can be divided into 2 basic categories;

- Euler equations-based models: The initial effective implementation of this model [Karni \(1996\)](#) relies on the level set technique to find the position of the interface and uses the primitive variable formula of the Euler equations for the pressure at the interface. On the same dates, a similar approach was put forth for perfect gases in one spatial dimension [Abgrall \(1996\)](#). Following these studies, different studies were conducted by experts [Glimm et al. \(1998\)](#) [Abgrall et al. \(2003\)](#). All of these techniques are quite effective and easy to code for physical models that are not too complex. The primary drawback of these methods is the conservation errors that occur with the partial mass of different fluids, giving rise to incorrect calculations of internal energy and temperature at the interface. Additionally, they are challenging to apply to a wide range of equations of state [Saurel and Lemetayer \(2001\)](#).
- Multiphase flow equations-based models: Models based on Euler's equations are not very suitable for industrial applications, as they are not conservative and are applicable for relatively simple physical problems. However, this technique is founded on a multiphase flow model with numerous equations and is very useful due to the fact that it guarantees energy conservation at the interface. Although mathematical modeling and numerical solutions of this model are more difficult the same technique can be used to get resolution for all mesh points. These challenges are compensated by the model's ability to handle even difficult problems with interfaces and mixtures and the broadness of its application [Saurel \(2001\)](#). These models are unconditionally hyperbolic. For this reason, they can use Godunov-type schemes, which have recently been studied in depth by experts. Since novel models allow for the identification of all thermodynamic variables for each phase, they can solve strong shocks in compressible mixtures in addition to detonation waves in condensed materials without the use of a mixture EoS. They can also handle scenarios in which interfaces seem dynamically. For instance, during the rarefaction wave's propagation, gas pockets may occur [Lallemant et al. \(2005\)](#). Following the innovative work of [Saurel and Abgrall \(1999\)](#), other professionals have engaged in in-depth research in this field.

The existence of interfacial surfaces creates significant challenges for the mathematical and physical description of the problem in multiphase flow. A multiphase flow could be conceptualized mathematically as a domain divided into single-phase zones with moving boundaries dividing the component phases [Ishii and Hibiki \(2011\)](#). From the standpoint

of physics, the presence of the interface is what makes it difficult to derive the field and constitutive equations necessary for multiphase flow systems [Ishii and Hibiki \(2011\)](#). The fact that the interface structure of multiphase flows determines both their stationary and dynamic features presents still another difficulty. This discussion leads to the conclusion that it is required to explain the local properties of the flow with the aim of constructing the field and constitutive equations suitable for arranged multiphase flow. By using an appropriate averaging approach, the macroscopic characteristics should be derived from that flow. The interfacial geometry and kinematics of the majority of multiphase flow found in real engineering systems are very complex. Therefore, macroscopic characteristics of the flow are far more crucial than such microscopic details of the fluid motions and other factors in an engineering problem [Ishii and Hibiki \(2011\)](#). The average values of fluid motions and characteristics can be acquired through correct averaging, and they effectively reduce local instant fluctuations. It is crucial to remember that an averaging-based formulation should take into consideration the statistical characteristics of these fluctuations that affect the macroscopic events [Ishii and Hibiki \(2011\)](#). For other standard references, see [Prosperetti and Tryggvason \(2007\)](#), [Bruce Stewart and Wendroff \(1984\)](#).

2.1 Averaging procedure in two-phase flow

Two-phase flow, involving the simultaneous flow of two distinct phases such as liquid and gas, is a complex phenomenon often encountered in various engineering applications. The detailed modeling of two-phase flow presents significant challenges due to the complex interactions between the phases. Averaging techniques are employed to simplify these models, providing a practical means to analyze and predict the behavior of two-phase flows at a macroscopic level. This part summarizes the key averaging methods used in two-phase flow modeling: time averaging, space (volume) averaging, and ensemble averaging.

- **Time Averaging** Time averaging involves averaging properties over a specified time period at a particular spatial location. This method is particularly useful for steady-state or periodic flows, where fluctuations occur around a mean value over time. The time-averaged value of a property ϕ is mathematically expressed as:

$$\langle \phi \rangle_t = \frac{1}{T} \int_0^T \phi(t) dt \quad (2.1)$$

where T represents the time period over which the averaging is performed. Time averaging helps in smoothing out transient fluctuations, providing a stable mean value that is more tractable for analysis and simulation purposes [Ishii and Hibiki \(2011\)](#).

- **Space (Volume) Averaging** Space averaging, also known as volume averaging, involves integrating properties over a defined spatial volume. This technique is crucial for deriving macroscopic conservation equations that describe the behavior of the flow on a larger scale. The space-averaged value of a property ϕ is given by:

$$\langle \phi \rangle_V = \frac{1}{V} \int_V \phi(\mathbf{r}) dV \quad (2.2)$$

where V is the volume of the control region. Volume averaging is particularly effective in applications involving porous media or large-scale industrial processes, where detailed spatial variations are less critical than the overall behavior of the flow [Whitaker \(1999\)](#).

- **Ensemble Averaging** Ensemble averaging is a statistical method involving the aggregation of a huge number of instances or realizations (each being representative for different possible states) of the flow. Such an approach finds application especially in stochastic processes as well as in the studying of turbulent flows. Further, the ensemble averaging can be employed to capture the statistical properties of the flow making possible a probabilistic analysis of two-phase systems [Drew and Passman \(1999\)](#).

Averaged models in two-phase flow are essential for reducing the complexity of modeling and predicting the behavior of these flows in various applications. Different averaging procedures—time averaging, space averaging, ensemble averaging, and the combinations of those techniques—each offer unique advantages and are chosen based on the specific characteristics of the flow and the desired outcomes of the analysis. These models are crucial for designing and optimizing industrial processes involving two-phase flows.

2.1.1 Single phase flow

In this section, we derive multiphase flow models from single-phase flow models using ensemble averaging. This method transforms microscopic equations into macroscopic ones by averaging over a large number of realizations. It provides a comprehensive framework for modeling two-phase flows, addressing the complexities and interfacial dynamics inherent in such systems. Single-phase flow models describe the behavior of a compressible fluid using a set of balance equations for mass, momentum, and energy.

- **Mass Balance (Continuity Equation):**

$$\frac{\partial \rho}{\partial t} + \nabla \cdot (\rho \mathbf{u}) = 0 \quad (2.3)$$

where ρ is the density and \mathbf{u} is the velocity.

- **Momentum Balance (Newton's Second Law):**

$$\frac{\partial(\rho \mathbf{u})}{\partial t} + \nabla \cdot (\rho \mathbf{u} \mathbf{u}) = \nabla \cdot \mathbf{T} + \rho \mathbf{g} \quad (2.4)$$

where \mathbf{T} is the stress tensor ($\mathbf{T} = -p\mathbb{I} + \boldsymbol{\tau}$, where p is the *pressure*, \mathbb{I} a *unit vector tensor* and $\boldsymbol{\tau}$ the *viscous stress*), and \mathbf{g} is the gravitational acceleration.

- **Energy Balance:**

$$\frac{\partial \left(\rho \left(e + \frac{1}{2} \mathbf{u}^2 \right) \right)}{\partial t} + \nabla \cdot \left(\rho \left(e + \frac{1}{2} \mathbf{u}^2 \right) \mathbf{u} \right) = -\nabla \cdot \mathbf{q} + \nabla \cdot (\mathbf{T} \cdot \mathbf{u}) + \rho \mathbf{g} \cdot \mathbf{u} + q_s \quad (2.5)$$

where e is the internal energy, \mathbf{q} is the heat flux, and q_s is the body heating source.

These equations are well-known and provide a foundation for extending the analysis to multiphase flows.

As discussed by [Ishii and Hibiki \(2011\)](#), in order to model multiphase flows, interfacial jump conditions are introduced to account for the discontinuities at the interface between phases. At the interface, a specific form of the balance equation is required to account for the unique characteristics, namely the abrupt changes (or discontinuities) in various variables. By treating the interface as a distinct surface where fluid density, energy, and velocity experience jump discontinuities, the jump conditions can be formulated. These conditions describe the transfer of mass, momentum, and energy across the interface, serving as essential aligning criteria across the two phase [Ishii and Hibiki \(2011\)](#). Therefore, they are crucial for analyses of two-phase flow.

- **Mass Jump Condition:**

$$\llbracket \rho(\mathbf{u} - \mathbf{u}_i) \rrbracket \cdot \mathbf{n} = 0 \quad (2.6)$$

- **Momentum Jump Condition:**

$$\llbracket \rho \mathbf{u}(\mathbf{u} - \mathbf{u}_i) + \mathbf{T} \rrbracket \cdot \mathbf{n} = m_i^s \quad (2.7)$$

- **Energy Jump Condition:**

$$\llbracket \rho \left(e + \frac{1}{2} u^2 \right) (\mathbf{u} - \mathbf{u}_i) + \mathbf{T} \cdot \mathbf{u} - \mathbf{q} \rrbracket \cdot \mathbf{n} = e_i^s \quad (2.8)$$

Here, $\llbracket x \rrbracket = x^+ - x^-$ represents the discontinuity in the variable x across the interface. \mathbf{u}_i denotes the velocity of the interface, \mathbf{n} is the unit normal vector to the interface, m_i^s signifies the resultant interfacial force due to surface tension, and e_i^s represents the surface energy associated with the interface (see for details Müller and Müller (1985), Ishii and Hibiki (2011)).

Generic forms of the balance equations and interfacial conditions can be used to simplify the process, as given by Drew (1992). For balance equations Zein (2010):

$$\frac{\partial \rho \Psi}{\partial t} + \nabla \cdot (\rho \Psi \mathbf{u}) = \nabla \cdot \mathbf{J} + \rho \Phi \quad (2.9)$$

For interfacial conditions:

$$\llbracket \rho \Psi (\mathbf{u} - \mathbf{u}_i) + \mathbf{J} \rrbracket \cdot \mathbf{n} = S_i \quad (2.10)$$

The corresponding values for Ψ , \mathbf{J} , Φ , and S_i are presented in Table 2.1.

	Ψ	\mathbf{J}	Φ	S_i
Mass	1	0	0	0
Momentum	\mathbf{u}	\mathbf{T}	\mathbf{g}	m_i^s
Energy	$e + \frac{1}{2} \mathbf{u}^2$	$\mathbf{T} \cdot \mathbf{u} - \mathbf{q}$	$\mathbf{g} \cdot \mathbf{u} + \frac{q_s}{\rho}$	e_i^s

Table 2.1: The variables in the generic conservation equations and jump equations.

2.1.2 Ensemble averaging procedure

A basic method of averaging involves summing the observed values and then dividing by the number of observations R. A. Berry et al. (2008). The ensemble average extends this idea by summing the values of the variable across different realizations and dividing by the total number of observations Zein (2010). If f is a field (i.e., a function of position \mathbf{x} and time t) for a specific realization μ of the process, the average of f is given by Drew (1992):

$$\bar{f}(\mathbf{x}, t) = \int_{\mathcal{E}} f(\mathbf{x}, t; \mu) dm(\mu) \quad (2.11)$$

where $dm(\mu)$ represents the measure (i.e., the probability) of observing the realization μ , and \mathcal{E} denotes the set of all realizations of the process of interest, referred to as the ensemble. The ensemble average provides a means to interpret the phenomena concerning the repeatability of experiments. While any single experiment or realization may not be exactly repeatable, any repetition will produce a different realization, or member of the ensemble Drew (1992).

Before proceeding with the averaging procedure, it is necessary to establish certain mathematical results. To average the exact equations, we need expressions for $\overline{\partial f / \partial t}$ and $\overline{\nabla f}$. If

f is "well behaved," it follows from the definition of the ensemble average that [Decker et al. \(1989\)](#):

$$\overline{\frac{\partial f}{\partial t}} = \frac{\partial \overline{f}}{\partial t} \quad (2.12)$$

and

$$\overline{\nabla f} = \nabla \overline{f} \quad (2.13)$$

In most multiphase flows, functions are generally discontinuous at the interface. However, they are well-behaved within each phase. Therefore, consider $X_k \nabla f$, where X_k is the phase indicator function for phase k [Decker et al. \(1989\)](#):

$$X_k = \begin{cases} 1, & \text{if } x \in k; \\ 0, & \text{otherwise.} \end{cases} \quad (2.14)$$

Then,

$$\overline{X_k \nabla f} = \overline{\nabla X_k f} - \overline{f \nabla X_k} \quad (2.15)$$

which simplifies to

$$= \nabla \overline{X_k f} - \overline{f \nabla X_k}. \quad (2.16)$$

Additionally,

$$\overline{X_k \frac{\partial f}{\partial t}} = \frac{\partial \overline{X_k f}}{\partial t} - \overline{f \frac{\partial X_k}{\partial t}}. \quad (2.17)$$

which simplifies to

$$\overline{X_k \frac{\partial f}{\partial t}} = \frac{\partial \overline{X_k f}}{\partial t} - \overline{f \frac{\partial X_k}{\partial t}}. \quad (2.18)$$

where Equation 2.16 known as *Gauss rule*, and Equation 2.18 known as *Leibniz rule*. Another important mathematical result also known as *Topological equation* given:

$$\frac{D_i X_k}{Dt} = \frac{\partial X_k}{\partial t} + \mathbf{u}_i \cdot \nabla X_k = 0 \quad (2.19)$$

which emphasizes that the material derivative of X_k is zero (see for details [Drew \(1992\)](#)).

After performing some manipulations using the aforementioned mathematical results, it is now possible to derive the averaged equations. Using ensemble averaging technique, averaged version of generic equation 2.9 can be found:

$$\overline{X_k \frac{\partial \rho \Psi}{\partial t}} + \overline{X_k \nabla \cdot (\rho \Psi \mathbf{u})} = \overline{X_k \nabla \cdot \mathbf{J}} + \overline{X_k \rho \Phi} \quad (2.20)$$

which simplifies to

$$\frac{\partial \overline{X_k \rho \Psi}}{\partial t} + \nabla \cdot \overline{(X_k \rho \Psi \mathbf{u})} - \nabla \cdot \overline{X_k \mathbf{J}} - \overline{X_k \rho \Phi} = \overline{\rho \Psi (\mathbf{u} - \mathbf{u}_i) \cdot \nabla X_k} - \overline{\mathbf{J} \cdot \nabla X_k} \quad (2.21)$$

Using the values in Table 2.1, we can derive the averaged equations for mass, momentum, and energy from this general averaged equation 2.21.

- **Mass balance:** The equation for the averaged mass is given by:

$$\frac{\partial \overline{X_k \rho}}{\partial t} + \nabla \cdot \overline{X_k \rho \mathbf{u}} = \overline{\rho(\mathbf{u} - \mathbf{u}_i) \cdot \nabla X_k} \quad (2.22)$$

with $\tilde{\rho}_k$ and $\hat{\mathbf{u}}_k$ equation will be:

$$\frac{\partial \alpha_k \tilde{\rho}_k}{\partial t} + \nabla \cdot (\alpha_k \tilde{\rho}_k \hat{\mathbf{u}}_k) = \overline{\rho(\mathbf{u} - \mathbf{u}_i) \cdot \nabla X_k} = \Gamma_k \quad (2.23)$$

where

$$\tilde{\rho}_k = \frac{X_k \rho}{\alpha_k}, \quad \text{and} \quad \hat{\mathbf{u}}_k = \frac{X_k \rho \mathbf{u}}{\alpha_k \tilde{\rho}_k} \quad (2.24)$$

$\tilde{\rho}_k$ known as *weighted average density*, $\hat{\mathbf{u}}_k$ known as *mass-weighted average velocity*, and α_k known as *volume fraction*.

- **Mass jump:**

$$\Gamma_1 + \Gamma_2 = 1 \quad (2.25)$$

where Γ_k is an interfacial term that represents mass transfer between the two phases.

- **Momentum balance:** The equation for the averaged momentum is expressed as:

$$\frac{\partial \overline{X_k \rho \mathbf{u}}}{\partial t} + \nabla \cdot \overline{X_k \rho \mathbf{u} \mathbf{u}} = \nabla \cdot \overline{X_k \mathbf{T}} + \overline{X_k \rho \mathbf{g}} + \overline{\rho \mathbf{u}(\mathbf{u} - \mathbf{u}_i) \cdot \nabla X_k} - \overline{\mathbf{T} \cdot \nabla X_k} \quad (2.26)$$

Common method involves presuming that the velocity \mathbf{u} can be represented as

$$\mathbf{u} = \hat{\mathbf{u}} + \check{\mathbf{u}}, \quad (2.27)$$

where $\check{\mathbf{u}}$ represents the velocity fluctuations. Additionally,

$$\overline{X_k \rho \check{\mathbf{u}}} = 0. \quad (2.28)$$

Next, we address the term $\overline{X_k \rho \mathbf{u} \mathbf{u}}$

$$\overline{X_k \rho \mathbf{u} \mathbf{u}} = \chi_k \rho (\hat{\mathbf{u}}_k + \check{\mathbf{u}}_k)(\hat{\mathbf{u}}_k + \check{\mathbf{u}}_k), \quad (2.29)$$

which simplifies to

$$\overline{X_k \rho \mathbf{u} \mathbf{u}} = \alpha_k \tilde{\rho}_k \hat{\mathbf{u}}_k \hat{\mathbf{u}}_k - \alpha_k \mathbf{T}_k^{Re}, \quad (2.30)$$

where

$$\mathbf{T}_k^{Re} = - \frac{\overline{\chi_k \rho \check{\mathbf{u}}_k \check{\mathbf{u}}_k}}{\alpha_k}, \quad (2.31)$$

is known as the *Reynolds stress*. Using *weighted average* and *mass-weighted average*:

$$\tilde{\mathbf{T}}_k = \frac{\overline{X_k \mathbf{T}}}{\alpha_k}, \quad (2.32)$$

$$\hat{\mathbf{g}}_k = \frac{\overline{X_k \rho \mathbf{g}}}{\alpha_k \tilde{\rho}_k}. \quad (2.33)$$

Then, equation (2.26) transforms into

$$\begin{aligned} \frac{\partial(\alpha_k \tilde{\rho}_k \hat{\mathbf{u}}_k)}{\partial t} + \nabla \cdot (\alpha_k \tilde{\rho}_k \hat{\mathbf{u}}_k \hat{\mathbf{u}}_k) &= \nabla \cdot \alpha_k (\tilde{\mathbf{T}}_k + \mathbf{T}_k^{Re}) + \alpha_k \tilde{\rho}_k \hat{\mathbf{g}}_k \\ &+ \overline{\rho \mathbf{u}(\mathbf{u} - \mathbf{u}_i) \cdot \nabla X_k} - \overline{\mathbf{T}_k \cdot \nabla X_k}. \end{aligned} \quad (2.34)$$

If we split the far-right side of the equation into two parts:

$$\overline{\rho \mathbf{u}(\mathbf{u} - \mathbf{u}_i) \cdot \nabla X_k} = u_{ki} \Gamma_k \quad (2.35)$$

$$-\overline{\mathbf{T}_k \cdot \nabla X_k} = M_k \quad (2.36)$$

Then the averaged momentum equation (2.34) can be rewritten as:

$$\frac{\partial(\alpha_k \tilde{\rho}_k \hat{\mathbf{u}}_k)}{\partial t} + \nabla \cdot (\alpha_k \tilde{\rho}_k \hat{\mathbf{u}}_k \hat{\mathbf{u}}_k) = \nabla \cdot \alpha_k (\tilde{\mathbf{T}}_k + \mathbf{T}_k^{Re}) + \alpha_k \tilde{\rho}_k \hat{\mathbf{g}}_k + \mathbf{u}_{ki} \Gamma_k + M_k \quad (2.37)$$

where M_k is interfacial momentum source.

- **Momentum jump:**

$$M_1 + M_2 + u_{1i} \Gamma_1 + u_{2i} \Gamma_2 = \overline{m_i^s} \quad (2.38)$$

where m_i^s consists of interfacial force due to surface tension.

- **Energy balance:** The averaged energy equation can be expressed as:

$$\begin{aligned} \frac{\partial \overline{X_k \rho \left(e + \frac{1}{2} u^2 \right)}}{\partial t} + \nabla \cdot \left(\overline{X_k \rho \left(e + \frac{1}{2} u^2 \right) \mathbf{u}} \right) &= \nabla \cdot \overline{X_k (\mathbf{T} \cdot \mathbf{u} - \mathbf{q})} \\ &+ \overline{X_k (\rho \mathbf{g} \cdot \mathbf{u} + q_s)} + \overline{\rho \left(e + \frac{1}{2} u^2 \right) (\mathbf{u} - \mathbf{u}_i) \cdot \nabla X_k} - \overline{(\mathbf{T} \cdot \mathbf{u} - \mathbf{q}) \cdot \nabla X_k} \end{aligned} \quad (2.39)$$

once more using $\mathbf{u} = \hat{\mathbf{u}} + \check{\mathbf{u}}$, the equation given above will transform:

$$\begin{aligned} \frac{\partial \alpha_k \tilde{\rho}_k \left(\hat{e}_k + \frac{1}{2} \hat{u}_k^2 + u_k^{Re} \right)}{\partial t} + \nabla \cdot \left(\alpha_k \tilde{\rho}_k \hat{u}_k \left(\hat{e}_k + \frac{1}{2} \hat{u}_k^2 + u_k^{Re} \right) \right) &= \\ \nabla \cdot \alpha_k \left((\tilde{\mathbf{T}}_k + \mathbf{T}_k^{Re}) \cdot \hat{\mathbf{u}}_k - \tilde{q}_k - q_k^{Re} \right) + \alpha_k \tilde{\rho}_k \hat{\mathbf{g}}_k \cdot \hat{\mathbf{u}}_k + \alpha_k \tilde{q}_{s,k} & \\ + \overline{\rho \left(e + \frac{1}{2} u^2 \right) (\mathbf{u} - \mathbf{u}_i) \cdot \nabla X_k} - \overline{(\mathbf{T} \cdot \mathbf{u} - \mathbf{q}) \cdot \nabla X_k} & \end{aligned} \quad (2.40)$$

where

$$u_k^{Re} = \frac{\overline{X_k \rho \check{u}_k^2}}{2 \alpha_k \tilde{\rho}_k}, \quad (2.41)$$

is known as *Reynolds kinetic energy fluctuation*. Another new parameter that emerged with the averaging process, q_k^{Re} , which is known as *Reynold energy flux fluctuation*, is given by:

$$q_k^{Re} = \frac{\overline{X_k \rho \check{e}_k \check{u}_k}}{\alpha_k} + \frac{\overline{X_k \rho \check{u}_k^2}}{2\alpha_k} - \frac{\overline{X_k \mathbf{T} \cdot \check{u}_k}}{\alpha_k} \quad (2.42)$$

If we split the far-right side of the equation into two parts just like the momentum term:

$$\rho \left(e + \frac{1}{2} u^2 \right) (\mathbf{u} - \mathbf{u}_i) \cdot \nabla X_k = (e_{ki} + \frac{1}{2} u_{ki}^2) \Gamma_k \quad (2.43)$$

$$W_k = -\overline{\mathbf{T} \cdot \mathbf{u} \cdot \nabla X_k} \quad (2.44)$$

$$E_k = \overline{q \cdot \nabla X_k} \quad (2.45)$$

where W_k is *interfacial work*, and E_k is *interfacial heat source*. Then the averaged energy equation (2.39) can be rewritten as:

$$\begin{aligned} & \frac{\partial \alpha_k \tilde{\rho}_k \left(\hat{e}_k + \frac{1}{2} \hat{u}_k^2 + u_k^{Re} \right)}{\partial t} + \nabla \cdot \alpha_k \tilde{\rho}_k \hat{u}_k \left(\hat{e}_k + \frac{1}{2} \hat{u}_k^2 + u_k^{Re} \right) = \\ & \nabla \cdot \alpha_k \left((\tilde{T}_k + T_k^{Re}) \cdot \hat{u}_k - \tilde{q}_k - q_k^{Re} \right) + \alpha_k \tilde{\rho}_k \hat{g}_k \cdot \hat{u}_k + \alpha_k \tilde{q}_{s,k} \\ & + (e_{ki} + \frac{1}{2} u_{ki}^2) \Gamma_k + E_k + W_k. \end{aligned} \quad (2.46)$$

- **Energy jump:**

$$E_1 + W_1 + E_2 + W_2 + (e_{1i} + \frac{1}{2} u_{1i}^2) \Gamma_1 + (e_{2i} + \frac{1}{2} u_{2i}^2) \Gamma_2 = \bar{e}_i^s \quad (2.47)$$

where e_i^s represents the interfacial energy source.

The resulting averaged model includes six equations: two mass equations (2.23), two momentum equations (2.37), and two energy equations (2.46). Notably, additional terms are present in the model, representing the interfacial transfer processes occurring across the interface. By ignoring all turbulent terms, viscosity, surface tension, and surface energy, a generic model without heat and mass transfer can be formulated in one-dimensional form:

$$\left\{ \begin{array}{l} \frac{\partial \alpha_1 \rho_1}{\partial t} + \frac{\partial \alpha_1 \rho_1 u_1}{\partial x} = 0 \\ \frac{\partial \alpha_1 \rho_1 u_1}{\partial t} + \frac{\partial (\alpha_1 \rho_1 u_1^2 + \alpha_1 p_1)}{\partial x} = +p_I \frac{\partial \alpha_1}{\partial x} + \mathcal{M} \\ \frac{\partial \alpha_1 \rho_1 E_1}{\partial t} + \frac{\partial \alpha_1 u_1 (\rho_1 E_1 + p_1)}{\partial x} = -p_I \frac{\partial \alpha_1}{\partial t} + \mathcal{E} \\ \frac{\partial \alpha_2 \rho_2}{\partial t} + \frac{\partial \alpha_2 \rho_2 u_2}{\partial x} = 0 \\ \frac{\partial \alpha_2 \rho_2 u_2}{\partial t} + \frac{\partial (\alpha_2 \rho_2 u_2^2 + \alpha_2 p_2)}{\partial x} = -p_I \frac{\partial \alpha_1}{\partial x} - \mathcal{M} \\ \frac{\partial \alpha_2 \rho_2 E_2}{\partial t} + \frac{\partial \alpha_2 u_2 (\rho_2 E_2 + p_2)}{\partial x} = +p_I \frac{\partial \alpha_1}{\partial t} - \mathcal{E} \end{array} \right. \quad (2.48)$$

where α_k is volume fraction, ρ_k is the density, u_k is the velocity, p_k is the phasic pressure, and E_k is total specific energy. The terms appear on the right side of the equations p_I , \mathcal{M} , and \mathcal{E} denote interfacial pressure, momentum interchange, and energy interchange between the phases, respectively.

2.1.3 Closure problem

In two-phase flow models, closure relations are essential because the system of conservation equations typically contains more unknowns than equations. This imbalance arises due to the need to describe additional complexities, such as interfacial forces and phase-specific properties. Closure laws provide the necessary additional equations, enabling the determination of all unknown variables and ensuring the model is fully specified and solvable. To close to the generic six-equation model different approaches can be used.

- **Equal pressure:** A widely used method for closing the averaged model involves assuming that both phases have the same pressure. For this assumption, thermodynamic conditions can be written :

$$p_1 = p_2 = p, \quad T_1 \neq T_2, \quad u_1 \neq u_2, \quad g_1 \neq g_2 \quad (2.49)$$

This approach, however, encounters a significant mathematical challenge: it is considered ill-posed, as discussed by [Bruce Stewart and Wendroff \(1984\)](#). This issue has several implications:

- The model fails to accurately represent pressure wave propagation phenomena.
- Numerical methods that rely on the hyperbolic nature of flow equations are unsuitable.
- Numerical solution instabilities may arise.

The issue has been thoroughly examined, and various methods have been suggested to mitigate numerical instabilities. Typically, these methods involve introducing numerical viscosity to dampen the instabilities or incorporating correction terms to eliminate the complex nature of the eigenvalues, see [Lahey et al. \(1980\)](#), [Städtke et al. \(1997\)](#), and [Tiselj and Petelin \(1997\)](#). This approach has been implemented in several industrial two-phase simulation codes, such as NEPTUNE [Mañes et al. \(2014\)](#), WAHA [Tiselj and Martin \(2012\)](#) and RELAP5 [Mangal et al. \(2012\)](#).

- **Evolutionary equation:** A more physical approach to closing the generic six-equation model involves not eliminating certain variables, but instead, adding an additional equation. This can be achieved by introducing an extra equation for the volume fraction, resulting in the complete non-equilibrium seven-equation models. By ignoring all turbulent terms, viscosity, surface tension, and surface energy, a seven-equation model without heat and mass transfer can be formulated in one-dimensional form:

$$\left\{ \begin{array}{l} \frac{\partial \alpha_1}{\partial t} + u_I \frac{\partial \alpha_1}{\partial x} = S_k \\ \frac{\partial \alpha_1 \rho_1}{\partial t} + \frac{\partial \alpha_1 \rho_1 u_1}{\partial x} = 0 \\ \frac{\partial \alpha_1 \rho_1 u_1}{\partial t} + \frac{\partial (\alpha_1 \rho_1 u_1^2 + \alpha_1 p_1)}{\partial x} = +p_I \frac{\partial \alpha_1}{\partial x} + \mathcal{M} \\ \frac{\partial \alpha_1 \rho_1 E_1}{\partial t} + \frac{\partial \alpha_1 u_1 (\rho_1 E_1 + p_1)}{\partial x} = +p_I u_I \frac{\partial \alpha_1}{\partial x} + \mathcal{E} \\ \frac{\partial \alpha_2 \rho_2}{\partial t} + \frac{\partial \alpha_2 \rho_2 u_2}{\partial x} = 0 \\ \frac{\partial \alpha_2 \rho_2 u_2}{\partial t} + \frac{\partial (\alpha_2 \rho_2 u_2^2 + \alpha_2 p_2)}{\partial x} = -p_I \frac{\partial \alpha_1}{\partial x} - \mathcal{M} \\ \frac{\partial \alpha_2 \rho_2 E_2}{\partial t} + \frac{\partial \alpha_2 u_2 (\rho_2 E_2 + p_2)}{\partial x} = -p_I u_I \frac{\partial \alpha_a}{\partial x} - \mathcal{E} \end{array} \right. \quad (2.50)$$

where p_I , u_I , and S_k represent the interfacial pressure, interfacial velocity, and pressure relaxation term, respectively. To complete this system, expressions for the parameters u_I and p_I are required. However, as the exact formulas for u_I and p_I are only known in specific cases, it is common practice to use an approximation or assumption for these parameters. In the literature, one of the most commonly used closure relations was proposed by [Baer and Nunziato \(1986\)](#):

$$p_I = p_1, \quad u_I = u_2 \quad (2.51)$$

where the interfacial velocity is taken to be the same as the velocity of the less compressible phase, and the interfacial pressure is set equal to the pressure of the more compressible phase.

Other closure relations for the interfacial terms have been proposed by [Saurel and Abgrall \(1999\)](#):

$$p_I = \alpha_1 p_1 + \alpha_2 p_2, \quad u_I = \frac{\alpha_1 \rho_1 u_1 + \alpha_2 \rho_2 u_2}{\alpha_1 \rho_1 + \alpha_2 \rho_2} \quad (2.52)$$

The transition from single-phase to two-phase flow models introduces significant mathematical challenges due to the interfacial dynamics and phase interactions. Ensemble averaging provides a systematic approach to bridge this gap transforming microscopic balance equations into macroscopic forms that account for phase discontinuities. This process leads to a set of hyperbolic partial differential equations that govern the evolution of conserved quantities such as mass, momentum, and energy for each phase. Unlike single-phase flow, where conservation laws are relatively straightforward, two-phase flow models introduce non-conservative terms and interfacial source terms, which require special treatment. The resulting system of conservation laws is often solved using hyperbolic methods. The Riemann problem plays a critical role in this context, as it provides a framework for understanding the evolution of discontinuities and the wave structure of the solution. In the following sections, we will look at the theory of conservation laws and the Riemann problem.

2.2 Theory of conservation laws

Hyperbolic balance laws play a fundamental role in the mathematical modeling of various physical phenomena, including fluid dynamics, traffic flow, and wave propagation. These laws are characterized by their ability to describe the evolution of quantities conserved through time, such as mass, momentum, and energy. This part will not seek to examine every detail of the theory of balance laws. Instead, it will provide a concise overview of the fundamental principles and core details relevant to the study presented in this thesis. The primary reference for this work is [Toro \(1997\)](#); however, the reader may also consult sources [LeVeque \(1992\)](#), [Serre \(1999\)](#), and [Alinhac \(2009\)](#) for further information.

Consider a set of conservation laws:

$$\mathbf{U}_t + \mathbf{F}(\mathbf{U})_x = 0, \quad (2.53)$$

Given the initial condition:

$$\mathbf{U}(x, 0) = \mathbf{U}_0(x), \quad (2.54)$$

where $\mathbf{U} \in \mathbb{R}^p$, $x \in \mathbb{R}$, $t > 0$, and $\mathbf{F} : \mathbb{R}^p \rightarrow \mathbb{R}^p$ is a smooth function.

$$\mathbf{U} = \begin{bmatrix} u_1 \\ u_2 \\ \vdots \\ u_m \end{bmatrix}, \quad \mathbf{F}(\mathbf{U}) = \begin{bmatrix} f_1 \\ f_2 \\ \vdots \\ f_m \end{bmatrix}. \quad (2.55)$$

Here, \mathbf{U} is the vector of *conserved variables*, and $\mathbf{F} = \mathbf{F}(\mathbf{U})$ is the *flux vector*, with each component f_i being a function of the components u_j of \mathbf{U} Toro (1997).

The *Jacobian matrix* of the flux function $\mathbf{F}(\mathbf{U})$ in (2.25) is defined as Toro (1997):

$$\mathbf{A}(\mathbf{U}) = \frac{\partial \mathbf{F}}{\partial \mathbf{U}} = \begin{bmatrix} \frac{\partial f_1}{\partial u_1} & \frac{\partial f_1}{\partial u_2} & \cdots & \frac{\partial f_1}{\partial u_m} \\ \frac{\partial f_2}{\partial u_1} & \frac{\partial f_2}{\partial u_2} & \cdots & \frac{\partial f_2}{\partial u_m} \\ \vdots & \vdots & \ddots & \vdots \\ \frac{\partial f_m}{\partial u_1} & \frac{\partial f_m}{\partial u_2} & \cdots & \frac{\partial f_m}{\partial u_m} \end{bmatrix}. \quad (2.56)$$

The entries a_{ij} of $\mathbf{A}(\mathbf{U})$ are the partial derivatives of the components f_i of the vector \mathbf{F} with respect to the components u_j of the vector of conserved variables \mathbf{U} , that is $a_{ij} = \frac{\partial f_i}{\partial u_j}$ Toro (1997).

The *eigenvalues* λ_i of a matrix \mathbf{A} are the roots of the characteristic polynomial given by Toro (1997):

$$|\mathbf{A} - \lambda \mathbf{I}| = \det(\mathbf{A} - \lambda \mathbf{I}) = 0 \quad (2.57)$$

where \mathbf{I} is the *identity matrix*. Physically, eigenvalues represent the speeds at which information propagates. Positive speeds indicate propagation in the direction of increasing x , while negative speeds indicate propagation in the opposite direction.

A *right eigenvector* of a matrix \mathbf{A} associated with an eigenvalue λ_i is a vector $\mathbf{K}^{(i)} = [k_1^{(i)}, k_2^{(i)}, \dots, k_m^{(i)}]^T$ that satisfies $\mathbf{A}\mathbf{K}^{(i)} = \lambda_i \mathbf{K}^{(i)}$. Similarly, a *left eigenvector* of a matrix \mathbf{A} associated with an eigenvalue λ_i is a vector $\mathbf{L}^{(i)} = [l_1^{(i)}, l_2^{(i)}, \dots, l_m^{(i)}]$ such that $\mathbf{L}^{(i)}\mathbf{A} = \lambda_i \mathbf{L}^{(i)}$ Toro (1997).

If the Jacobian matrix $\mathbf{A}(\mathbf{U})$ has m distinct real eigenvalues

$$\lambda_1 < \lambda_2 < \cdots < \lambda_m \quad (2.58)$$

then it has a complete set of eigenvectors and is called *strictly hyperbolic*. If the eigenvalues are not distinct, i.e. Andrianov (2003),

$$\lambda_1 \leq \lambda_2 \leq \cdots \leq \lambda_m, \quad (2.59)$$

but there still exists a complete set of eigenvectors, then the system is termed *non-strictly hyperbolic*.

Consider a hyperbolic system of conservation laws in the form:

$$\mathbf{U}_t + \mathbf{F}(\mathbf{U})_x = 0, \quad (2.60)$$

with real eigenvalues $\lambda_i(U)$ and corresponding right eigenvectors $\mathbf{K}^{(i)}(U)$. The characteristic speed $\lambda_i(U)$ defines what is known as a *characteristic field* Toro (1997).

A λ_i -characteristic field is considered to be *linearly degenerate* if

$$\nabla \lambda_i(U) \cdot \mathbf{K}^{(i)}(U) = 0, \quad \forall U \in \mathbb{R}^m,$$

where \mathbb{R}^m denotes the set of real-valued vectors with m components Toro (1997).

On the other hand, a λ_i -characteristic field is termed *genuinely nonlinear* if

$$\nabla \lambda_i(U) \cdot \mathbf{K}^{(i)}(U) \neq 0, \quad \forall U \in \mathbb{R}^m.$$

The gradient of the eigenvalue $\lambda_i(U)$ is given by:

$$\nabla \lambda_i(U) = \left(\frac{\partial \lambda_i}{\partial u_1}, \frac{\partial \lambda_i}{\partial u_2}, \dots, \frac{\partial \lambda_i}{\partial u_m} \right)^T.$$

The *phase space* refers to the vector space $U = (u_1, \dots, u_m)$; in the case of a 2x2 system, this is referred to as the phase plane $u_1 - u_2$ Toro (1997).

2.3 Riemann Problem

In its simplest form, the Riemann problem is a special initial value problem for hyperbolic partial differential equations. The Riemann problem is a natural setting in which to investigate the propagation of discontinuities in initial data for systems described by hyperbolic conservation laws. Those equations are critical in the ability to predict things like shock waves and other non-linear wave phenomena in fluids, gases, and other physical systems. The configuration of the Riemann problem in the $x-t$ plane is illustrated in Figure 2.1.

Consider a one-dimensional Euler equation:

$$\mathbf{U}_t + \mathbf{F}(\mathbf{U})_x = 0 \tag{2.61}$$

$$\mathbf{U} = \begin{pmatrix} \rho \\ \rho u \\ \rho E \end{pmatrix} \quad \mathbf{F}(\mathbf{U}) = \begin{pmatrix} \rho u \\ \rho u^2 + p \\ \rho u H \end{pmatrix} \tag{2.62}$$

The initial conditions are specified as:

$$U(x, 0) = \begin{cases} U_L & \text{if } x < 0, \\ U_R & \text{if } x > 0. \end{cases} \tag{2.63}$$

It is possible to use primitive variables instead of conserved variables. For the one-dimensional Euler equations, the primitive variables are represented as $\mathbf{W} = (\rho, u, p)^T$. Although we will not provide every detail regarding the mathematical properties of one-dimensional Euler equations here (see for more information Toro (1997)), we can describe the various types of waves that may occur.

The eigenvalues of the system are determined as follows:

$$\lambda_1 = u - a, \quad \lambda_2 = u, \quad \lambda_3 = u + a$$

$$\nabla \lambda_2(U) \cdot \mathbf{K}^{(2)} = 0, \quad \nabla \lambda_1(U) \cdot \mathbf{K}^{(1)} \neq 0, \quad \nabla \lambda_3(U) \cdot \mathbf{K}^{(3)} \neq 0 \tag{2.64}$$

The equations above demonstrate that the characteristic fields associated with $\mathbf{K}^{(1)}$ and $\mathbf{K}^{(3)}$ are genuinely nonlinear, whereas the characteristic field associated with $\mathbf{K}^{(2)}$ is linearly degenerate Toro (1997). The $\mathbf{K}^{(1)}$ and $\mathbf{K}^{(3)}$ characteristic fields correspond to either rarefaction waves or shock waves, while the $\mathbf{K}^{(2)}$ characteristic field corresponds to a contact discontinuity. Let's assume that the left wave corresponds to a rarefaction wave and the right wave corresponds to a shock wave, which is a typical representation in the literature. The wave speeds are denoted by S_1 , S_2 , and S_3 from left to right.

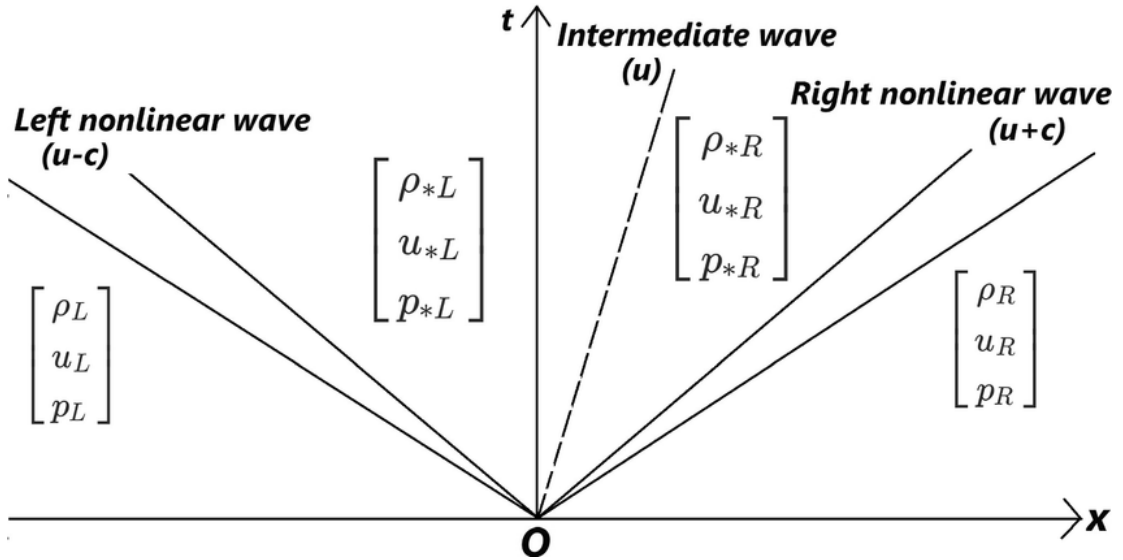


Figure 2.1: The general solution to the Riemann problem for the one-dimensional Euler equations encompasses scenarios where the nonlinear wave can develop as either a rarefaction wave or a shock wave [Toh \(2024\)](#).

- **Contact Discontinuity:** A contact wave is a discontinuity where both pressure and particle velocity remain constant across the wave, but the density changes abruptly. This also affects other density-dependent variables, such as temperature, sound speed, and entropy. For the contact wave [Toro \(1997\)](#):

$$\lambda_2(U_{*L}) = \lambda_2(U_{*R}) = S_2.$$

- **Rarefaction Wave:** A rarefaction wave is an expansion wave in which characteristics fan out, leading to a gradual change in velocity, density, and pressure. For the rarefaction wave [Toro \(1997\)](#):

$$\lambda_1(U_L) \leq \lambda_1(U_{*L})$$

- **Shock Wave:** A shock wave is a discontinuous wave that propagates through a medium, causing an abrupt change in pressure, density, and velocity, often associated with high-speed flow. For the shock wave:

$$\lambda_3(U_{*R}) > S_3 > \lambda_3(U_{*R})$$

2.4 Categorisation of two-phase flow models

Although there are different modeling methods for two-phase flow in the literature, here we will list different models based on the [Baer and Nunziato \(1986\)](#) model. The basis of this method is related to how non-equilibrium is handled. The full non-equilibrium form of the multiphase flow equations-based models, in which each phase has its own velocity, pressure, and temperature, is the most general [R. A. Berry et al. \(2008\)](#). In cases where the flow consists of 2 phases, the most general model is made up of 7 partial differential equations. These 7 equations include the mass, momentum, and energy balance equations for each phase and the volume fraction equation. In the literature, this model is often referred to as the *seven-equation model*. Another important study related to the seven-equation model is the [Saurel and Abgrall \(1999\)](#) model. Saurel and Abgrall's modifications

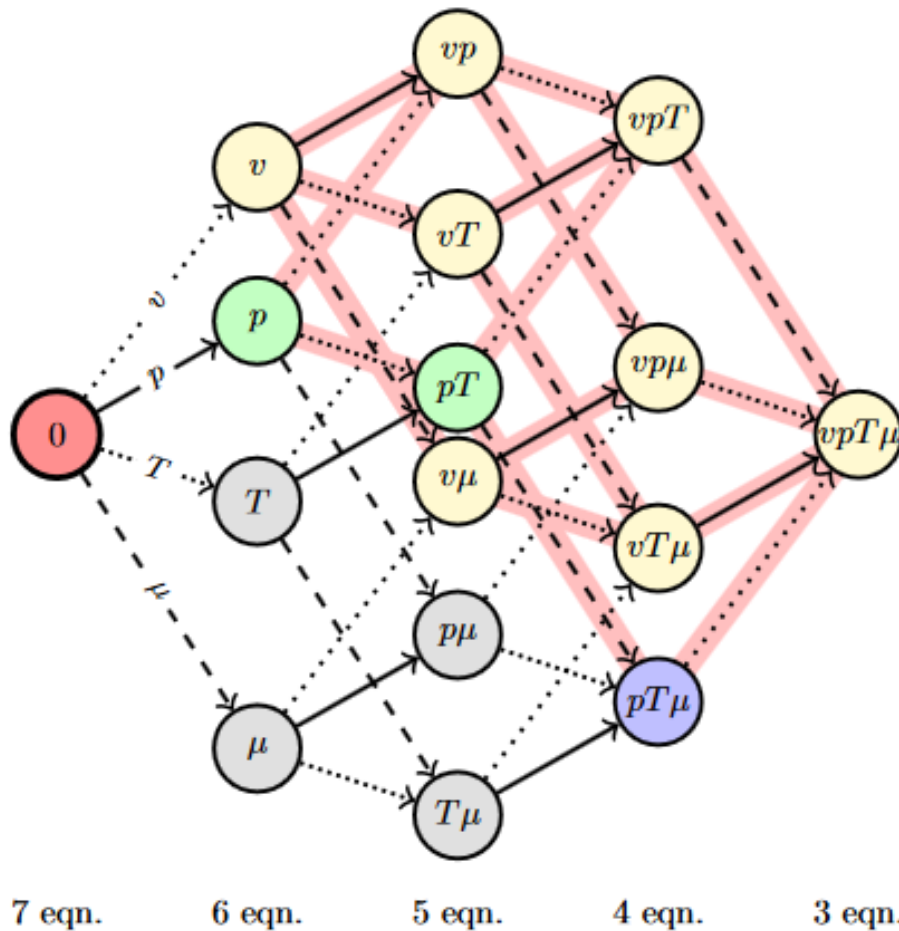


Figure 2.2: Categorization of the two-phase fluid model where considering instantaneous relaxation in zero or more of the variables p (pressure), T (temperature), μ (chemical potential), and v (velocity). Parallel edges signify the same relaxation processes, and each circle denotes a distinct model. Yellow circles represent the *homogeneous models* which assumes that phases move at the same velocity [Linga and Flåtten \(2019\)](#).

address the modeling of relaxation terms for pressure, velocity, and interface variables (see Equation 2.51 and Equation 2.52).

As can be seen in Figure 2.2, the categorization process is done through a 4-dimensional hypercube. While each circle in the figure represents a model, the edges of the hypercube represent the relaxation process, and the parallel edges represent the same relaxation process. As mentioned earlier, the basis of the categorization process begins with the seven-equation model [Baer and Nunziato \(1986\)](#), which is denoted by a "0" in the figure. By moving from left to right and adding equilibria assumptions, homogeneous models, which are the full equilibrium model, can be reached. Numerous models in the figure have previously been developed, presented, and deeply analyzed [Linga and Flåtten \(2019\)](#). The *reduced models* is derived from a simplification of the full seven-equations models. The basic logic is to assign zero relaxation times to different variables. For instance, the *single velocity six-equation model* which was introduced by [Kapila et al.](#) is derived from the seven-equations model, assuming zero velocity relaxation time. This model consists of 2 mass equations, 2 energy equations, a mixing momentum equation, and a volume fraction equation [Richard Saurel et al. \(2009\)](#) [Pelanti and Shyue \(2014\)](#). Another reduced model consists of two each of mass, energy, and momentum. can be obtained by assigning a zero relaxation time for the pressure. This model is called *single pressure six-equation model* and

can be found in literature [Michael Doster and Holmes \(1996\)](#), [Tiselj and Petelin \(1997\)](#), [Zou et al. \(2016\)](#). It is possible to derive *five-equation models*, [Allaire et al. \(2002\)](#), [Murrone and Guillard \(2005\)](#), [Kreeft and Koren \(2010\)](#) by taking one more step to the right. There is a five-equation model introduced by [Kapila et al.](#) with mechanical equilibrium, single velocity, and single pressure in the literature. This model consists of two conservation equations for masses, one conservation equation for the mixture momentum, one conservation equation for the mixture energy, and one non-conservative equation for the void ratio. Starting from the *seven-equation model*, it is also possible to obtain models with *four-equation* and *three-equation*. According to the categorization, different *four-equation models* can be obtained. One of the most applicable *four-equation model* can be described with single velocity, single pressure, and single temperature (yellow circle denoted by vpT in Figure 2.2). The set of Euler equations is represented by the *three-equation model*. It has a single Gibbs free energy as well as a single velocity, pressure, and temperature so there is no slip between the phases. As a result, *Homogeneous Equilibrium Model (HEM)* is created on the assumption of fully thermodynamic equilibrium.

It cannot be claimed that every model within the categorization offers a solution to a problem in the industry. Some types of modeling are based on unrealistic assumptions. This is due to the fact that all relaxation combinations are considered in the categorization, but some of these combinations lack a solid foundation. To comprehend this, one must understand the characteristic times of equilibrium recovery processes. As highlighted in the thesis study by [Labois \(2008\)](#), and [de Lorenzo \(2018\)](#), the pressure relaxation process occurs more rapidly than the velocity, temperature, and chemical relaxation processes, respectively. This distinction is rooted in the fundamental mechanisms governing each relaxation process. Pressure relaxation is primarily driven by the propagation of acoustic waves within the dispersed phase, such as bubbles, and their reflection at the phase interface. This process is relatively fast due to the high speed of sound, and the relaxation time is typically estimated using the time required for a round-trip of an acoustic wave from the bubble interface to its center and back. For velocity relaxation, the process is controlled by the interfacial drag between the dispersed and continuous phases. Drag models, such as those based on particle Reynolds numbers and drag coefficients, are used to evaluate the time required for the velocities of the two phases to be equal. Temperature relaxation, on the other hand, relies on conductive heat transfer between phases, often modeled using Fourier's law. The time required for the dispersed phase to reach thermal equilibrium with the surrounding phase is significantly longer than pressure relaxation. Finally, chemical potential relaxation is more complex, as it is influenced by interphase mass transfer, especially during phase change processes. Since chemical potential relaxation lacks a well-defined analytical method, empirical approaches, such as those used in NEPTUNE [Boucker et al. \(2005\)](#), are often employed. The relaxation times observed in practical scenarios, such as the AMOVI test [Pascal-Ribot and Blanchet \(2007\)](#), confirm this hierarchy, with pressure relaxation being the fastest ($\epsilon_p \approx 5.3 \times 10^{-5}$ s), followed by velocity ($\epsilon_v \approx 0.3$ s) and temperature relaxation ($\epsilon_T \approx 0.57$ s), while chemical potential relaxation can range from 0.1 to 1 second depending on the system's complexity and phase interactions. For the shock tube case (see for details [Labois \(2008\)](#)), the relaxation times are $\epsilon_p \approx 3.0 \times 10^{-8}$ s, $\epsilon_v \approx 5.5 \times 10^{-6}$ s, and $\epsilon_T \approx 2.1 \times 10^{-3}$ s. This ordering emphasize the importance of prioritizing specific relaxation processes when constructing reduced-order models for two-phase flow systems.

As a result, the characteristic times of the equilibrium recovery processes for various quantities can be represented as follows:

$$\epsilon_p \ll \epsilon_v \ll \epsilon_T \ll \epsilon_g$$

where ϵ_p denotes the characteristic time for pressure equilibrium recovery, ϵ_v represents the characteristic time for velocity equilibrium, ϵ_T indicates the characteristic time for temperature equilibrium, and ϵ_g stands for the characteristic time associated with Gibbs free energy equilibrium. Consequently, the $vp\mu$ model in the categorization, which assumes equilibrium in velocity, pressure, and chemical relaxation without thermal equilibrium, is derived for a physical process not encountered in real life. Therefore, the rest of this study will focus on models frequently used in industrial applications.

2.4.1 The seven-equation model

The seven-equation model developed by [Baer and Nunziato \(1986\)](#) is the most comprehensive compressible two-phase flow model. The entire disequilibrium between phases is allowed. In actuality, there is no equilibrium between pressure, temperature, Gibbs free energy, and phase velocity. For the sake of simplicity, only 1D is considered.

In one dimension, the homogeneous portion of the system:

$$\left\{ \begin{array}{l} \frac{\partial \alpha_1}{\partial t} + u_I \frac{\partial \alpha_1}{\partial z} = 0, \\ \frac{\partial(\alpha_1 \rho_1)}{\partial t} + \frac{\partial(\alpha_1 \rho_1 u_1)}{\partial z} = 0, \\ \frac{\partial(\alpha_1 \rho_1 u_1)}{\partial t} + \frac{\partial(\alpha_1 \rho_1 u_1^2 + \alpha_1 p_1)}{\partial z} - p_I \frac{\partial \alpha_1}{\partial z} = 0, \\ \frac{\partial(\alpha_1 \rho_1 E_1)}{\partial t} + \frac{\partial[\alpha_1(\rho_1 E_1 + p_1)u_1]}{\partial z} - p_I u_I \frac{\partial \alpha_1}{\partial z} = 0 \\ \frac{\partial(\alpha_2 \rho_2)}{\partial t} + \frac{\partial(\alpha_2 \rho_2 u_2)}{\partial z} = 0, \\ \frac{\partial(\alpha_2 \rho_2 u_2)}{\partial t} + \frac{\partial(\alpha_2 \rho_2 u_2^2 + \alpha_2 p_2)}{\partial z} - p_I \frac{\partial \alpha_2}{\partial z} = 0, \\ \frac{\partial(\alpha_2 \rho_2 E_2)}{\partial t} + \frac{\partial[\alpha_2(\rho_2 E_2 + p_2)u_2]}{\partial z} - p_I u_I \frac{\partial \alpha_2}{\partial z} = 0 \end{array} \right. \quad (2.65)$$

where u_I and p_I interfacial velocity and pressure. This model is used today, with modifications by [Saurel and Abgrall \(1999\)](#), to describe flame propagation and deflagration-to-detonation transition (DDT) in gas-permeable, reactive granular materials. Also used for supercavitation and expansion tube problems with the work of [Saurel and Lemetayer \(2001\)](#).

As described in [Zein \(2010\)](#), to explore the mathematical characteristics of Saurel and Abgrall model, we reformulate it using primitive variables as follows:

$$\frac{\partial \mathbf{W}}{\partial t} + \mathbf{A} \frac{\partial \mathbf{W}}{\partial x} = 0 \quad (2.66)$$

where

$$\mathbf{W} = (\alpha_1, \rho_1, u_1, p_1, \rho_2, u_2, p_2)^T. \quad (2.67)$$

The matrix A is defined as [Zein \(2010\)](#):

$$A = \begin{pmatrix} u_1 & 0 & 0 & 0 & 0 & 0 & 0 \\ \frac{\rho_1}{\alpha_1}(u_1 - u_I) & u_1 & \rho_1 & 0 & 0 & 0 & 0 \\ \frac{p_1 - p_I}{\alpha_1 \rho_1} & 0 & u_1 & \frac{1}{\rho_1} & 0 & 0 & 0 \\ \frac{\rho_1 c_{I,1}^2}{\alpha_1}(u_1 - u_I) & 0 & \rho_1 c_1^2 & u_1 & 0 & 0 & 0 \\ -\frac{\rho_2}{\alpha_2}(u_2 - u_I) & 0 & 0 & 0 & u_2 & \rho_2 & 0 \\ -\frac{p_2 - p_I}{\alpha_2 \rho_2} & 0 & 0 & 0 & 0 & u_2 & \frac{1}{\rho_2} \\ -\frac{\rho_1 c_{I,2}^2}{\alpha_1}(u_1 - u_I) & 0 & 0 & 0 & 0 & \rho_2 c_2^2 & u_2 \end{pmatrix}. \quad (2.68)$$

The speed of sound c_k is provided, and $c_{I,k}$, the speed of sound at the interface, is determined by [Zein \(2010\)](#):

$$c_k^2 = \frac{p_k}{\rho_k^2} - \frac{\left(\frac{\partial e_k}{\partial \rho_k}\right)_{p_k}}{\left(\frac{\partial e_k}{\partial p_k}\right)_{\rho_k}}, \quad (2.69)$$

$$c_{I,k}^2 = \frac{p_I}{\rho_I} - \left(\frac{\partial e_k}{\partial p_k}\right)_{\rho_k} \left(\frac{\partial e_k}{\partial \rho_k}\right)_{p_k}, \quad k = 1, 2. \quad (2.70)$$

The matrix A has real eigenvalues, given by the following expressions [Zein \(2010\)](#):

$$\begin{cases} \lambda_1 = u_I, \\ \lambda_2 = u_1 - c_1, \\ \lambda_3 = u_1, \\ \lambda_4 = u_1 + c_1, \\ \lambda_5 = u_2 - c_2, \\ \lambda_6 = u_2, \\ \lambda_7 = u_2 + c_2. \end{cases} \quad (2.71)$$

The corresponding right eigenvectors are given as [Zein \(2010\)](#):

$$\mathbf{K}^1 = \begin{pmatrix} \alpha_1 \alpha_2 \eta_1 \eta_2 \\ -\alpha_2 \eta_2 (\rho_1 (\eta_1 - c_{I,1}^2) + p_1 - p_I) \\ \alpha_2 \eta_2 (u_1 - u_I) (p_1 - p_I - \rho_1 c_{I,1}^2) / \rho_1 \\ \alpha_2 \eta_2 (\rho_1 c_{I,1}^2 (u_1 - u_I)^2 - c_1^2 (p_1 - p_I)) \\ -\alpha_1 \eta_1 (\rho_2 (c_{I,2}^2 - \eta_2) - p_2 + p_I) \\ \alpha_1 \eta_1 (u_2 - u_I) (-p_2 + p_I + \rho_2 c_{I,2}^2) / \rho_2 \\ \alpha_1 \eta_1 (-\rho_2 c_{I,2}^2 (u_2 - u_I)^2 + c_2^2 (p_2 - p_I)) \end{pmatrix}, \quad (2.72)$$

$$\mathbf{K}^2 = \begin{pmatrix} 0 \\ \rho_1 \\ -c_1 \\ \rho_1 c_{I,1}^2 \\ 0 \\ 0 \\ 0 \end{pmatrix}, \quad \mathbf{K}^3 = \begin{pmatrix} 0 \\ 1 \\ 0 \\ 0 \\ 0 \\ 0 \\ 0 \end{pmatrix}, \quad \mathbf{K}^4 = \begin{pmatrix} 0 \\ \rho_1 \\ c_1 \\ \rho_1 c_1^2 \\ 0 \\ 0 \\ 0 \end{pmatrix}, \quad (2.73)$$

$$\mathbf{K}^5 = \begin{pmatrix} 0 \\ 0 \\ 0 \\ 0 \\ \rho_2 \\ -c_2 \\ \rho_2 c_2^2 \end{pmatrix}, \quad \mathbf{K}^6 = \begin{pmatrix} 0 \\ 0 \\ 0 \\ 0 \\ 1 \\ 0 \\ 0 \end{pmatrix}, \quad \mathbf{K}^7 = \begin{pmatrix} 0 \\ 0 \\ 0 \\ 0 \\ \rho_2 \\ c_2 \\ \rho_2 c_2^2 \end{pmatrix}, \quad (2.74)$$

where

$$\eta_1 = c_1^2 - (u_1 - u_I)^2, \quad \eta_2 = c_2^2 - (u_2 - u_I)^2.$$

Thus, the system is strictly hyperbolic, except when some eigenvalues coincide. Specifically, the eigenvectors (2.72)–(2.74) become linearly dependent if any of the following conditions are met [Zein \(2010\)](#):

$$\alpha_1 = 0, \quad \alpha_2 = 0, \quad \eta_1 = 0, \quad \eta_2 = 0.$$

It can be demonstrated that the characteristic fields corresponding to the eigenvalues λ_1 , λ_3 , and λ_6 are linearly degenerate. Meanwhile, the fields associated with the eigenvalues λ_2 , λ_4 , λ_5 , and λ_7 are genuinely nonlinear. For a detailed proof and further discussion see: [Gallouët et al. \(2004\)](#), and [Zein \(2010\)](#).

2.4.2 The six-equation model

Single-velocity six-equation model

The seven-equation model is simplified to the six-equation model with a single velocity when zero relaxation time for velocity is assumed, as described by [Kapila et al.](#) Subsequent studies providing numerical solutions include [Richard Saurel et al. \(2009\)](#), [Pelanti and Shyue \(2014\)](#). This model is the yellow circle indicated by v in the categorization in Figure 2.2. Since the phases move at the same speed, it is a homogeneous model as mentioned before. For this reason, wave patterns are relatively simple. However, it should be noted that although homogeneous models have similar wave patterns, the allowable disequilibrium between phases makes their mathematical modeling quite different. For the sake of simplicity, only 1D is considered.

In one dimension, the homogeneous portion of the system:

$$\begin{cases} \frac{\partial \alpha_1}{\partial t} + u \frac{\partial \alpha_1}{\partial z} = 0 \\ \frac{\partial(\alpha_1 \rho_1)}{\partial t} + \frac{\partial(\alpha_1 \rho_1 u)}{\partial z} = 0 \\ \frac{\partial(\alpha_1 \rho_1 E_1)}{\partial t} + \frac{\partial[\alpha_1(\rho_1 E_1 + p_1)u]}{\partial z} + \sum(U, \frac{\partial U}{\partial z}) = 0 \\ \frac{\partial(\rho u)}{\partial t} + \frac{\partial(\rho u^2 + \alpha_1 p_1 + \alpha_2 p_2)}{\partial z} = 0 \\ \frac{\partial(\alpha_2 \rho_2)}{\partial t} + \frac{\partial(\alpha_2 \rho_2 u)}{\partial z} = 0 \\ \frac{\partial(\alpha_2 \rho_2 E_2)}{\partial t} + \frac{\partial[\alpha_2(\rho_2 E_2 + p_2)u]}{\partial z} - \sum(U, \frac{\partial U}{\partial z}) = 0 \end{cases} \quad (2.75)$$

Here, E_k represents the total energy of phase k , defined as $E_k = e_k + \frac{V^2}{2}$, where $Y_k = \frac{\alpha_k \rho_k}{\rho}$, and the mixture density is given by $\rho = \alpha_1 \rho_1 + \alpha_2 \rho_2$, with $k = 1, 2$.

The thermodynamic assumptions in the single-velocity six-equation model allow for the presence of thermodynamic disequilibria:

$$u_1 = u_2 = u, \quad p_1 \neq p_2 \quad T_1 \neq T_2, \quad g_1 \neq g_2.$$

The eigenvalues of the system are given by:

$$\lambda_1 = u - c_{6eqt}, \quad \lambda_{2,3,4,5} = u, \quad \lambda_6 = u + c_{6eqt},$$

where the speed of sound, c_{6eqt} , is defined as:

$$c_{6eqt} = \sqrt{Y_1 c_1^2 + Y_2 c_2^2}.$$

The non-conservative term in the phasic total energy equations is expressed as [Pelanti and Shyue \(2014\)](#):

$$\sum (U, \frac{\partial U}{\partial z}) = -u [Y_2 \frac{\partial \alpha_1 p_1}{\partial z} - Y_1 \frac{\partial \alpha_2 p_2}{\partial z}]$$

This term becomes non-zero when the fluid consists of multiple components traveling at a non-zero velocity.

In numerical implementations, this model exhibits a significant advantage by ensuring the positivity of volume fractions, a notable improvement over the five-equation model. Moreover, this method is less computationally expensive than the seven-equation model, as expected. As mentioned previously, pressure equilibrium is achieved prior to velocity equilibrium. Although this might appear to be an incorrect assumption, the model remains widely utilized in academic literature for scenarios that assume instantaneous pressure relaxation.

Single-pressure six-equation model

The seven-equation model is simplified to the six-equation model with a single pressure when zero relaxation time for pressure is assumed. This model is the circle indicated by p in the categorization in Figure 2.2. For the sake of simplicity, only 1D is considered.

In one dimension, the homogeneous portion of the system:

$$\begin{cases} \frac{\partial(\alpha_1 \rho_1)}{\partial t} + \frac{\partial(\alpha_1 \rho_1 u_1)}{\partial z} = 0 \\ \frac{\partial(\alpha_1 \rho_1 u_1)}{\partial t} + \frac{\partial(\alpha_1 \rho_1 u_1^2 + \alpha_1 p)}{\partial z} - p \frac{\partial \alpha_1}{\partial z} = 0 \\ \frac{\partial(\alpha_1 \rho_1 E_1)}{\partial t} + \frac{\partial[\alpha_1(\rho_1 E_1 + p)u_1]}{\partial z} + p \frac{\partial \alpha_1}{\partial z} = 0 \\ \frac{\partial(\alpha_2 \rho_2)}{\partial t} + \frac{\partial(\alpha_2 \rho_2 u_2)}{\partial z} = 0 \\ \frac{\partial(\alpha_2 \rho_2 u_2)}{\partial t} + \frac{\partial(\alpha_2 \rho_2 u_2^2 + \alpha_2 p)}{\partial z} - p \frac{\partial \alpha_2}{\partial z} = 0 \\ \frac{\partial(\alpha_2 \rho_2 E_2)}{\partial t} + \frac{\partial[\alpha_2(\rho_2 E_2 + p)u_2]}{\partial z} + p \frac{\partial \alpha_2}{\partial z} = 0 \end{cases} \quad (2.76)$$

The system's eigenvalues and their characteristics are influenced by the specific hyperbolization technique employed. Two of the eigenvalues correspond to the phasic velocities,

denoted as $\lambda_1 = u_1$ and $\lambda_2 = u_2$, with the associated fields being linearly degenerate. The remaining four eigenvalues are functions of the phasic densities, velocities, sound speeds, and volume fractions, and the associated fields are genuinely nonlinear. This model is recognized as being ill-posed, which results in numerical instabilities. However, this issue can be mitigated by introducing numerical viscosity, which is frequently employed to stabilize the system. Additionally, this technique is used in mathematical formulations to eliminate complex eigenvalues, as discussed in [Toro \(1989\)](#), [Tiselj and Petelin \(1997\)](#), and [Kumbaro et al. \(2001\)](#).

The thermodynamic assumptions in the single-pressure six-equation model allow for the presence of thermodynamic disequilibria:

$$u_1 \neq u_2 = u, \quad p_1 = p_2 \quad T_1 \neq T_2, \quad g_1 \neq g_2.$$

The WAHA [Tiselj and Martin \(2012\)](#), RELAP5 [Mangal et al. \(2012\)](#), and NEPTUNE [Mañes et al. \(2014\)](#) simulation codes are among the various industrial tools where this model has been successfully implemented.

2.4.3 The five-equation model

The five-equation model can be derived from the seven-equation model by assigning a zero value for the velocity and pressure relaxation time [Kapila et al.](#). Another method can also be obtained by using the single velocity six-equation model and assigning a zero value for the pressure relaxation time. This model is the circle indicated by *vp* in the categorization in Figure 2.2. For the sake of simplicity, only 1D is considered.

In one dimension, the homogeneous portion of the system:

$$\begin{cases} \frac{\partial \alpha_1}{\partial t} + u \frac{\partial \alpha_1}{\partial z} + \alpha_1 \alpha_2 K \frac{\partial u}{\partial z} = 0 \\ \frac{\partial(\alpha_1 \rho_1)}{\partial t} + \frac{\partial(\alpha_1 \rho_1 u)}{\partial z} = 0 \\ \frac{\partial(\alpha_2 \rho_2)}{\partial t} + \frac{\partial(\alpha_2 \rho_2 u)}{\partial z} = 0 \\ \frac{\partial(\rho u)}{\partial t} + \frac{\partial(\rho u^2 + p)}{\partial z} = 0 \\ \frac{\partial(\rho E)}{\partial t} + \frac{\partial[(\rho E + p)u]}{\partial z} = 0 \end{cases} \quad (2.77)$$

where K is:

$$K = \frac{\rho_1 c_1^2 - \rho_2 c_2^2}{\alpha_1 \rho_2 c_2^2 + \alpha_2 \rho_1 c_1^2}$$

The thermodynamic assumptions in the five-equation model allow for the presence of thermodynamic disequilibria:

$$u_1 = u_2 = u, \quad p_1 = p_2 = p \quad T_1 \neq T_2, \quad g_1 \neq g_2.$$

The eigenvalues of the system are given by:

$$\lambda_1 = u - c_{5eqt}, \quad \lambda_{2,3,4} = u, \quad \lambda_5 = u + c_{5eqt},$$

where the speed of sound, c_{5eqt} , is defined as:

$$\frac{1}{\rho c_{5eqt}^2} = \frac{\alpha_1}{\rho_1 c_1^2} + \frac{\alpha_2}{\rho_2 c_2^2}.$$

The model is often referred to as Kapila's model in the literature. The numerical solution of Kapila's five-equation model is problematic. The reason for this, the mixture speed of sound exhibits non-monotonic behavior [Richard Saurel et al. \(2009\)](#), and the void fraction equation contains non-conservative terms. To overcome these problems, [Kreeft and Koren \(2010\)](#) has presented an alternative formulation that is frequently used in numerical calculations. Additionally, [Zhang \(2020\)](#) proposed a straightforward and efficient formulation of the five-equation model.

2.4.4 The four-equation model

In the case of instantaneous thermal relaxation, the five-equation model simplifies to the four-equation model, where pressure and temperature are assumed to be the same. In this scenario, both phases are considered to have equal pressures and temperatures, while a difference in chemical potential is still allowed. This model is the circle indicated by vpT in the categorization in Figure 2.2. For the sake of simplicity, only 1D is considered.

In one dimension, the system without the source term:

$$\begin{cases} \frac{\partial(\alpha_1\rho_1)}{\partial t} + \frac{\partial(\alpha_1\rho_1u)}{\partial z} = 0 \\ \frac{\partial(\alpha_2\rho_2)}{\partial t} + \frac{\partial(\alpha_2\rho_2u)}{\partial z} = 0 \\ \frac{\partial(\rho u)}{\partial t} + \frac{\partial(\rho u^2 + p)}{\partial z} = 0 \\ \frac{\partial(\rho E)}{\partial t} + \frac{\partial[(\rho E + p)u]}{\partial z} = 0 \end{cases} \quad (2.78)$$

The thermodynamic assumptions in the four-equation model allow for the presence of thermodynamic disequilibria:

$$u_1 = u_2 = u, \quad p_1 = p_2 = p, \quad T_1 = T_2 = T, \quad g_1 \neq g_2.$$

The eigenvalues of the system are given by:

$$\lambda_1 = u - c_{4eqt}, \quad \lambda_{2,3} = u, \quad \lambda_4 = u + c_{4eqt},$$

where the mixture speed of sound, c_{4eqt} , assuming no mass transfer between the phases is defined as [Lund \(2012\)](#):

$$c_{4eqt} = \left[\rho \left(\frac{\alpha_1}{\rho_1 c_1^2} + \frac{\alpha_2}{\rho_2 c_2^2} + T \frac{\alpha_1 \rho_1 c_{p,1} \alpha_2 \rho_2 c_{p,2}}{\alpha_1 \rho_1 c_{p,1} + \alpha_2 \rho_2 c_{p,2}} \left(\frac{\gamma_1}{\rho_1 c_1^2} - \frac{\gamma_2}{\rho_2 c_2^2} \right)^2 \right) \right]^{-1/2}.$$

2.4.5 The three-equation model

It is also called the *Homogeneous Equilibrium Model (HEM)* where it is assumed that the two phases are in thermodynamic equilibrium to construct the thermodynamical equation of state for the mixture of the two phases in the literature [Bruce Stewart and Wendroff \(1984\)](#) [Menikoff and Plohr \(1989\)](#) [Clerc \(2000\)](#). This model is the yellow circle indicated by $vpT\mu$ in the categorization in Figure 2.2. HEM can be written in the following form in 1D :

$$\begin{cases} \frac{\partial\rho}{\partial t} + \frac{\partial(\rho u)}{\partial z} = 0 \\ \frac{\partial(\rho u)}{\partial t} + \frac{\partial(\rho u^2 + p)}{\partial z} = 0 \\ \frac{\partial(\rho E)}{\partial t} + \frac{\partial[(\rho E + p)u]}{\partial z} = 0 \end{cases} \quad (2.79)$$

where u, ρ, p , and E indicate mixture velocity, mixture density, pressure, and specific total energy, respectively.

The thermodynamic assumptions in the three-equation model:

$$u_1 = u_2 = u, \quad p_1 = p_2 = p \quad T_1 = T_2 = T, \quad g_1 = g_2.$$

The eigenvalues of the system are given by:

$$\lambda_1 = u - c_{HEM}, \quad \lambda_2 = u, \quad \lambda_3 = u + c_{HEM},$$

where the speed of sound, c_{HEM} , is defined as:

$$c_{HEM} = \sqrt{\left(\frac{\partial p}{\partial \rho}\right)_s}.$$

Despite its simplicity, this model has been applied frequently for the analysis of critical two-phase flows in variable section ducts and for the modeling of heat exchangers [Porsching \(1977\)](#) [Toumi \(1992\)](#) [Zhang and Brooks \(2021\)](#). This model has well-known weaknesses, such as its inability to recreate strong kinetic or thermodynamic non-equilibrium effects, such as fast depressurization. Correction terms can be used to account for non-equilibrium effects when they are minor; but, if they are significant, additional equations are required for accurate flow physics prediction.

2.4.6 Additional significant models

This part references two additional suitable models. These models consider the temperature difference between the vapor phase and the metastable liquid phase.

Homogeneous Relaxation Model

The Homogeneous Relaxation Model (HRM) by [Bilicki&Kestin Phy \(1990\)](#) is the most straightforward conservative two-phase flow model that takes into account thermal and chemical non-equilibrium. A mass equation for one phase with a relaxation source term for the flow quality is added to the mixed Euler equations to create the HRM system [de Lorenzo \(2018\)](#). It is therefore important at this stage to evaluate the assumptions used for building different models made from the specified 4-equation formulation in the literature. In the 4-equation model discussed previously, this corresponded to assumptions of thermal and mechanical equilibrium, which are not applicable in the case of the homogeneous relaxation model. In the HRM, the following assumptions apply [Log \(2023\)](#):

$$p_g = p_\ell = p, \tag{2.80}$$

$$T_g = T_{\text{sat}}(p) \neq T_\ell. \tag{2.81}$$

Hence, the diverse 4-equation models available in the literature are inherently built upon distinct assumptions and are employed to address to different needs. The homogeneous relaxation model can be written in the following form in 1D:

$$\begin{cases} \frac{\partial \rho}{\partial t} + \frac{\partial(\rho u)}{\partial x} = 0 \\ \frac{\partial(\rho u)}{\partial t} + \frac{\partial(\rho u^2 + p)}{\partial x} = 0 \\ \frac{\partial(\rho E)}{\partial t} + \frac{\partial[(\rho E + p)u]}{\partial x} = 0 \\ \frac{\partial(\alpha_\nu \rho_\nu)}{\partial t} + \frac{\partial(\alpha_\nu \rho_\nu u)}{\partial x} = \Gamma_{l \rightarrow v} \end{cases} \tag{2.82}$$

The mass transfer is represented through a source term Γ , which aims to gradually adjust the existing vapor mass fraction to the equilibrium mass fraction, incorporating a specific delay for liquid vaporization [de Lorenzo \(2018\)](#).

$$\frac{\partial(\alpha_v \rho_v)}{\partial t} + \frac{\partial(\alpha_v \rho_v u)}{\partial x} = -\rho \frac{x - x_{eq}}{\Theta} \quad (2.83)$$

The left-hand side of the last equation represents the time and spatial derivatives of the vapor mass fraction, while the right-hand side of the equation represents the mass transfer rate, which depends on the difference between the actual vapor quality and the equilibrium quality and is scaled by the relaxation time constant Θ . The mass transfer rate is negative when $x > x_{eq}$, indicating that mass is transferred from the vapor to the liquid phase, and positive when $x < x_{eq}$, indicating that mass is transferred from the liquid to the vapor phase. A key aspect of HRM is the presumption that the vapor phase consistently exists in saturation conditions. This assumption is logical, as in the fast transient flow conditions being examined, the problems related to the metastable states of the liquid are of paramount importance [de Lorenzo \(2018\)](#). As thermal equilibrium is not maintained, the flow quality, x , does not match the thermodynamic quality and is defined as:

$$x = \frac{\alpha_v \rho_v}{\rho} \quad (2.84)$$

Equilibrium quality $x_{eq}(h, P)$ defined as:

$$x_{eq} = \frac{h - h_{SL}(P)}{h_{SG}(P) - h_{SL}(P)} \quad (2.85)$$

where $h_{SL}(P)$ represents the specific enthalpy of the saturated liquid, and $h_{SG}(P)$ represents the specific enthalpy of the saturated vapor.

The concept of the homogeneous relaxation model involves incorporating an extra differential equation into the homogeneous equilibrium model framework. This new equation is used to portray the swift and localized pace at which the flow quality variable x moves towards its respective unconstrained equilibrium value x_{eq} . In simpler terms, the previous presumption of x instantaneously aligning with x_{eq} is no longer upheld, so the relaxation time constant (Θ) was introduced. It's obvious that for the implementation of HRM, one needs local relaxation time Θ which has a paramount importance on the results. Downar-Zapolski et al. [Downar-Zapolski et al. \(1996\)](#) introduced two correlations derived from the empirical data obtained in the Moby Dick experiments. The study involving Moby Dick experiments [Reocreux \(1974\)](#) has provided valuable insights into comprehending critical two-phase, single-component flows. These experiments were conducted within a channel configuration comprising a linear segment followed by a conical expansion section featuring a divergence inclined at an angle of 7 degrees. The geometric design of the channel was meticulously devised to enable a one-dimensional mathematical representation of the resulting flows. The findings encompassed information regarding mass-flow rates, pressure variations, and void fraction distributions as they relate to longitudinal distance. The first correlation:

$$\Theta = \Theta_0 \alpha_v^{-0.257} \left[\frac{P_S(T_{in}) - P}{P_S(T_{in})} \right]^{-2.24} \quad (2.86)$$

where $\Theta_0 = 6.51 \times 10^{-4}$ has the dimension of time in seconds. The first correlation provides relatively accurate outcomes at low pressures (up to 10 bar). However, an alternative correlation is provided for higher pressures :

$$\Theta = \Theta_0 \alpha_v^{-0.54} \left[\frac{P_S(T_{in}) - P}{P_{crit} - P_S(T_{in})} \right]^{-1.76} \quad (2.87)$$

where $\Theta_0 = 3.84 \times 10^{-7}$ s, and P_{crit} is the pressure of the critical point.

Delayed Equilibrium Model

The Delayed Equilibrium Model (DEM) was developed to account for the non-equilibrium thermal condition that occur in critical flow situations. Traditional models often assume immediate thermal equilibrium between phases, which does not always accurately reflect real-world scenarios. The DEM, on the other hand, considers the presence of three distinct phases: saturated liquid, saturated vapor, and metastable liquid [Log \(2023\)](#). This approach is based on experimental observations where local temperature measurements oscillate between the stagnation temperature and local saturation temperature, indicating the presence of metastable liquid phases [Bartosiewicz and Seynhaeve \(2013\)](#). The basic assumptions of the DEM are as follows [de Lorenzo \(2018\)](#):

1. The mixture consists of three phases: saturated liquid, saturated vapor, and metastable liquid.
2. Two phases (saturated liquid and vapor) are at thermal equilibrium, while the metastable liquid is at various temperatures.
3. The mixture is at pressure and mechanical equilibrium.
4. The metastable phase undergoes an isentropic transformation [De Lorenzo et al. \(2017b\)](#).

The governing equations of the model can be written in 1D in a pipe with a uniform cross-sectional area [Log \(2023\)](#):

$$\begin{cases} \frac{\partial \rho}{\partial t} + \frac{\partial(\rho u)}{\partial x} = 0, \\ \frac{\partial(\rho u)}{\partial t} + \frac{\partial(\rho u^2 + p)}{\partial x} = 0, \\ \frac{\partial \rho E}{\partial t} + \frac{\partial[(\rho E + p)u]}{\partial x} = 0, \\ \frac{\partial(\alpha_{l,m}\rho_{l,m})}{\partial t} + \frac{\partial(\alpha_{l,m}\rho_{l,m}u)}{\partial x} = \Gamma_{l,m}. \end{cases} \quad (2.88)$$

where the subscript ℓ, m represents the metastable liquid phase, and $\Gamma_{\ell, m}$ indicates the mass transfer rate from the metastable liquid phase to the stable liquid-vapor mixture.

For the prediction of critical, steady flow in a nozzle, the last equation modified:

$$\frac{\partial(\alpha_{l,M}\rho_{l,M}A_z)}{\partial t} + \frac{\partial(\alpha_{l,M}\rho_{l,M}u_m A_z)}{\partial z} = \Gamma_{l,M}A_z. \quad (2.89)$$

The mass transfer is described by the source term, $\Gamma_{l,M}$, which represents the rate at which the metastable phase converts to the saturated mixture during the flow. Suggested by [Bartosiewicz and Seynhaeve \(2014\)](#) for modeling the change in the saturated mass fraction, y , as:

$$\frac{dy}{dx} = \left(C_1 \frac{P_w}{A} + C_2 \right) (1 - y) \left(\frac{p_{sat}(T_{l,m}) - p}{p_{crit} - p_{sat}(T_{l,m})} \right)^{0.25} \quad (2.90)$$

with $C_1 = 0.008$ and $C_2 = 0.56$, where p_{crit} represents the critical pressure of the fluid.

The DEM is particularly useful in modeling critical flows in various engineering applications, including:

1. Nuclear Reactor Safety:

The DEM is extensively used in the safety analysis of nuclear reactors, especially for evaluating the discharge rates during LOCAs. Accurate prediction of the coolant discharge rate is essential for understanding the depressurization rate and the timing of core uncovering, which are critical for initiating and managing emergency cooling systems [Bartosiewicz and Seynhaeve \(2014\)](#).

2. Critical Flow Modeling:

The DEM provides a robust framework for predicting critical mass flow rates and pressure distributions in systems where traditional equilibrium models fall short. This includes applications in both short and long tubes, nozzles, and other configurations where metastable liquid phases play a significant role [De Lorenzo et al. \(2017b\)](#).

3. Carbon Dioxide Transonic Flows:

Recent developments have extended the application of the DEM to the study of CO₂ transonic flows in nozzles. This has significant implications for the design and analysis of refrigeration and air conditioning systems using CO₂ as a refrigerant [Angielczyk et al. \(2020\)](#).

4. Steam Generator Tubes:

DEM is used to model choked flow in steam generator tubes, which is critical in evaluating the safety margins in nuclear reactors. This application helps in understanding the onset of flashing and the subsequent development of two-phase flow, which is essential for the design of steam generators and related components [Bartosiewicz and Seynhaeve \(2013\)](#).

5. Supercritical Water Reactors:

The DEM is also applicable to the analysis of supercritical water reactors, where it aids in predicting the behavior of coolant flow under varying pressure and temperature conditions. This application is vital for the development of next-generation nuclear reactors [De Lorenzo et al. \(2017b\)](#).

The DEM's relevance to LOCA scenarios in nuclear reactors cannot be overstated. During a LOCA, the sudden breach of the reactor's primary circuit leads to the rapid release of coolant, resulting in complex two-phase flow conditions. The DEM helps in accurately predicting the critical flow rates and understanding the thermal non-equilibrium effects that occur during such events. This predictive capability is crucial for designing effective emergency response systems and ensuring reactor safety. Moreover, the DEM has been validated against experimental data, such as the Super Moby-Dick experiments and the Marviken tests, which simulate real-scale reactor conditions. These validations have shown that the DEM provides a more accurate prediction of critical flow rates compared to traditional models. This improved accuracy is essential for the development and verification of safety protocols and emergency cooling systems in nuclear reactors as explained by [Bartosiewicz and Seynhaeve \(2013\)](#).

2.5 Godunov's method

Godunov's method is an important numerical technique used to solve hyperbolic systems of conservation laws, which are crucial in simulating phenomena like shock waves and rarefaction waves. This method was introduced by [Godunov \(1959\)](#) and has become a foundational tool in computational fluid dynamics.

A conservative scheme in a numerical method could be expressed:

$$U_i^{n+1} = U_i^n + \frac{\Delta t}{\Delta x} (F_{i+\frac{1}{2}} - F_{i-\frac{1}{2}}) \quad (2.91)$$

Here, $F_{i+\frac{1}{2}}$ and $F_{i-\frac{1}{2}}$ are the numerical fluxes at the cell boundaries, determined by the chosen Riemann solver. The terms Δt and Δx represent the time step and the spatial step, respectively. The discretization of the domain is given by:

$$\Delta x = x_{i+\frac{1}{2}} - x_{i-\frac{1}{2}} = \frac{L}{M} \quad (2.92)$$

where L is the length of the domain and M is the number of cells.

Godunov's method involves discretizing the computational domain into finite volumes or cells. The solution's integral average from the Riemann problems, denoted as $RP(U_i^n, U_{i-1}^n)$ and $RP(U_i^n, U_{i+1}^n)$, can be written as:

$$U_i^{n+1} = \frac{1}{\Delta x} \int_{x_{i-\frac{1}{2}}}^{x_{i+\frac{1}{2}}} \tilde{U}(x, \Delta t) dx. \quad (2.93)$$

Here, $\tilde{U}(x, t)$ represents the composite solution from the Riemann problem. Since $\tilde{U}(x, t)$ is the exact solution of the conservation law, it can be expressed in integral form as:

$$\int_{x_{i-\frac{1}{2}}}^{x_{i+\frac{1}{2}}} \tilde{U}(x, \Delta t) dx = \int_{x_{i-\frac{1}{2}}}^{x_{i+\frac{1}{2}}} \tilde{U}(x, 0) dx + \int_0^{\Delta t} F(\tilde{U}(x_{i-\frac{1}{2}}, t)) dt - \int_0^{\Delta t} F(\tilde{U}(x_{i+\frac{1}{2}}, t)) dt. \quad (2.94)$$

The inter-cell fluxes are defined as follows:

$$F_{i-\frac{1}{2}} = \frac{1}{\Delta t} \int_0^{\Delta t} F(\tilde{U}(x_{i-\frac{1}{2}}, t)) dt \quad (2.95)$$

$$F_{i+\frac{1}{2}} = \frac{1}{\Delta t} \int_0^{\Delta t} F(\tilde{U}(x_{i+\frac{1}{2}}, t)) dt \quad (2.96)$$

The fluxes depend on the solution $\tilde{U}(x, t)$, which represents the exact solution of the Riemann problem at specific local coordinates. Specifically, the conditions are given by [Toro \(1997\)](#):

$$\tilde{U}_{i-\frac{1}{2}}(t) = U_{i-\frac{1}{2}}(0) \quad \text{and} \quad \tilde{U}_{i+\frac{1}{2}}(t) = U_{i+\frac{1}{2}}(0) \quad (2.97)$$

The inter-cell fluxes are then computed as [Toro \(1997\)](#):

$$F_{i-\frac{1}{2}} = F(U_{i-\frac{1}{2}}(0)) \quad (2.98)$$

$$F_{i+\frac{1}{2}} = F(U_{i+\frac{1}{2}}(0)) \quad (2.99)$$

From these equations, the inter-cell flux in Godunov's method is generalized as:

$$F_{i+\frac{1}{2}}^{\text{God}} = F(U_{i+\frac{1}{2}}(0)) \quad (2.100)$$

The key innovation of Godunov's method is the use of Riemann solvers at the cell interfaces to compute the fluxes. These Riemann problems are set up using piecewise constant data, as can be seen in [Figure 2.3](#), from adjacent cells, which simplifies the problem of determining the evolution of an initial discontinuity. For the Euler equations, solving the

Riemann problem involves determining the interaction of waves that result from the discontinuity: shock waves, rarefaction waves, and contact discontinuities Toro (1997). The exact Godunov method involves solving these Riemann problems exactly, but this can be computationally expensive. Hence, approximate Riemann solvers, such as the Roe solver Roe (1981) or the HLLC (Harten-Lax-van Leer-Contact) solver Toro et al. (1994), are often used to reduce computational cost.

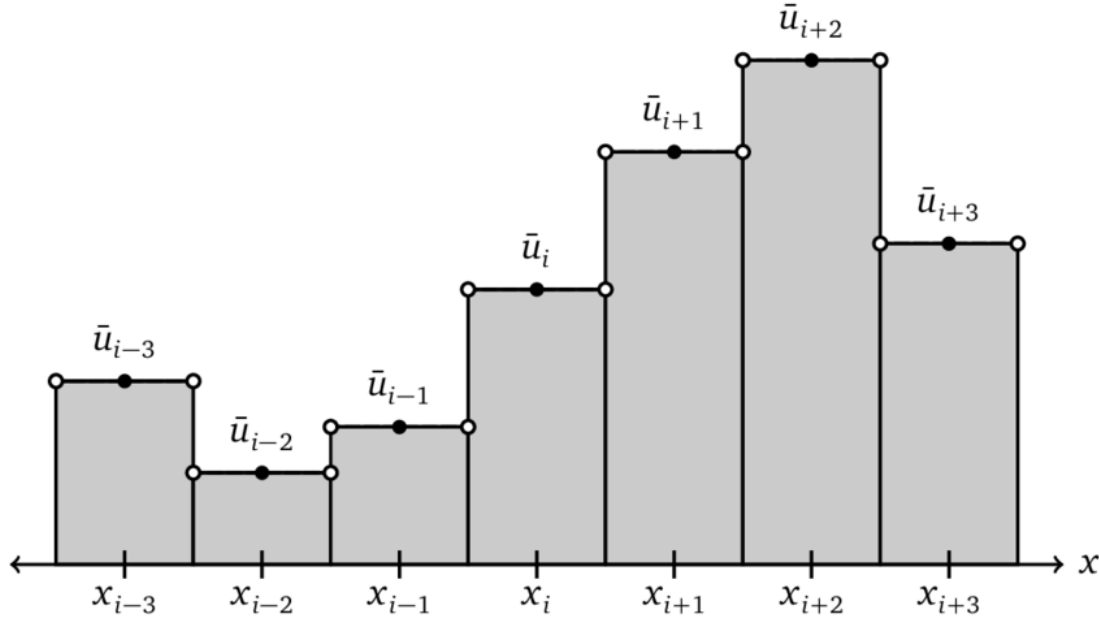


Figure 2.3: Representation of data as piecewise constants in the finite volume Godunov scheme by Núñez-De La Rosa (2015).

However Godunov method guarantee that the numerical scheme is conservative, this only means that in the absence of sources or sink each total quantity of conserved variable stay constant throughout time. This conservation property is essential for precisely capturing the physical way of acting of systems, especially in simulations where the flow may contain shocks or other discontinuities, increasing the importance of ensuring that properties of the flow remain physical. A characteristic feature of Godunov's method is its ability to take discontinuities without generating unphysical oscillations, which often distinguishes it from more primitive numerical methods. In contrast, calculating the solutions to the Riemann problem at each cell interface is computationally expensive for typical three-dimensional (3D) simulations or when high accuracy is sought.

In conclusion, Godunov's method serves as a cornerstone in computational fluid dynamics, providing a dependable approach for solving hyperbolic PDEs. Its capability to manage complex wave interactions is invaluable for analyzing flows with discontinuities. The method remains a focus of active research, with continuous efforts aimed at developing more efficient and accurate Riemann solvers and extending its application to more complex systems of equations.

2.6 Summary

This chapter presents a detailed mathematical framework for two-phase flow models. It begins by categorizing the models into sharp and diffuse interface methods. This is followed by an in-depth discussion of averaging techniques, particularly the ensemble averaging procedure, which is used to obtain two-phase flow models from single-phase flow models. The

chapter then introduces key concepts of the theory of conservation laws, and the Riemann problem. Various two-phase flow models are categorized and analyzed, starting with the comprehensive seven-equation model, which accounts for complete non-equilibrium between phases, and progressing to the simplified three-equation models that assume full equilibrium. These models are classified based on how they handle differences in pressure, velocity, and temperature between phases, providing insight into their computational advantages and limitations in practical applications.

Chapter 3

Thermodynamic metastability

The third chapter presents a bibliographic overview of thermodynamics and the behavior of metastable fluids. It begins by covering fundamental concepts related to the phase diagram of pure substances. Basic thermodynamic principles such as the Gibbs phase rule and thermodynamic potentials are also introduced to provide the necessary context for further discussions. Subsequently, various equations of state are discussed. The focus then moves to the metastable state, where the conditions required for metastability are described. A brief discussion is presented on different nucleation processes, emphasizing both homogeneous and heterogeneous nucleation. Finally, the chapter concludes with an exploration of the significance of metastability in both natural and industrial applications.

3.1 Pure substance phase diagram

A pure substance does not necessarily have to be composed of a single chemical element or compound. As long as the mixture is homogeneous, a combination of different chemical elements or compounds can also qualify as a pure substance—at least in the context of thermodynamics. For example, water and air can be considered pure substances. In essence, a pure substance is one that maintains a consistent chemical composition throughout. As is well known, substances can exist in different phases. For example, water can exist in solid, liquid, or gas phases at constant pressure but at different temperatures. In many industrial applications, two different phases of a pure substance coexist in equilibrium, such as in the boiler and condenser of conventional power plants or the evaporator and condenser of air conditioners Çengel et al. (2019). Understanding these phase transitions is therefore crucial for industrial efficiency. Property diagrams are used to observe changes in a pure substance during the phase change process. Figure 3.1 shows the $T - v$ diagram for pure water.

If water is at a pressure and temperature where it is completely in the liquid phase, and its temperature is lower than the boiling point at that specific pressure, it is referred to as *subcooled liquid*. If water is at a certain pressure and the temperature corresponds to the boiling point at that pressure, the water remains in liquid form. But if it gets anymore heat, then the liquid will vaporize. Water in this state is called a *saturated liquid*. If sufficient heat transfer occurs, all liquid in the system will be boiled & converted into vapor. From this point on, any temperature loss of the system causes the vapor to return back into the liquid phase. The state of the substance in this condition is called *saturated vapor*. If heat transfer to the system continues after all the liquid has evaporated, the resulting phase is called *superheated vapor*. As can be seen in Figure 3.1, during the phase change process at constant pressure, the line between saturated liquid and saturated vapor remains constant despite heat transfer (for the regions below the critical point). The energy gained or lost

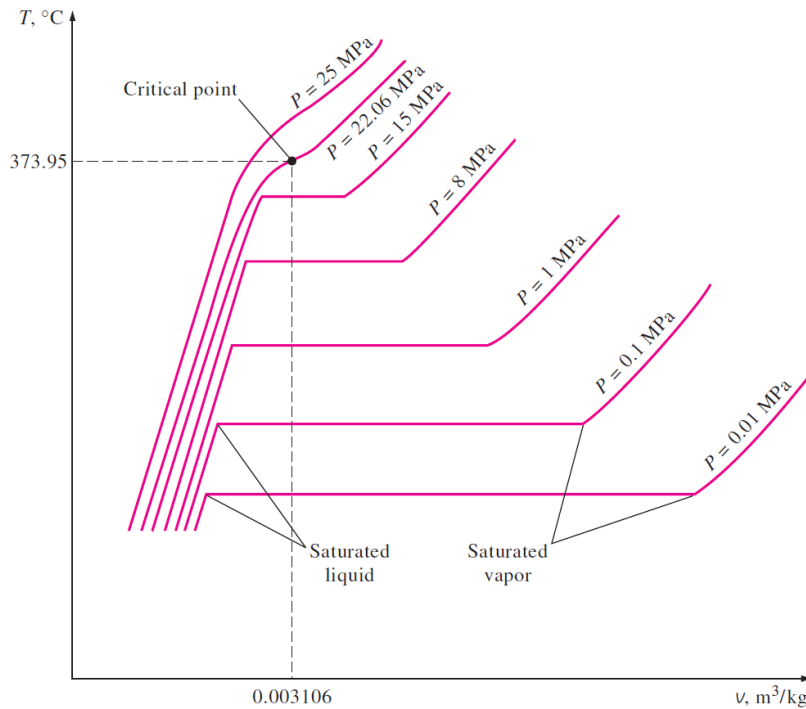


Figure 3.1: $T - v$ diagram of pure water by Çengel et al. (2019).

during this process is called *latent heat*. As the pressure increases, the straight line between saturated liquid and saturated vapor continues to decrease progressively, and at the so-called *critical point*, the line is replaced by a point. Beyond the critical point, saturated liquid and vapor are indistinguishable. The temperature, pressure, and specific volume at this point are important and have specific values for water Çengel et al. (2019):

$$T_{cr} = 373.95 \text{ } ^\circ\text{C}, P_{cr} = 22.06 \text{ MPa}, v_{cr} = 0.003106 \text{ m}^3/\text{kg}$$

The *dome* can be obtained by combining the saturated liquid points and saturated vapor points for different pressures given in Figure 3.1. As it can be seen in Figure 3.2 obtained for pure substances after the merging process, the graph is basically divided into 3 sections: subcooled (compressed) liquid region on the left, saturated liquid-vapor mixture in the middle and superheated vapor section on the right.

Although the figures provided so far have focused on the liquid and vapor phases, it is also possible to examine solid-liquid and solid-vapor phase changes by including the solid phase, as shown in Figure 3.3. At this point, a distinction should be noted. The majority of substances *contract* when they solidify. However, water, for example, *expands* when it freezes. Water is an extremely unique substance with several distinctive properties. For example, the downward slope of the melting curve suggests that solid ice has a lower density compared to liquid water. Another anomaly is that water reaches its maximum density at 277.13 K, as noted by Stillinger (1980). All three states of a pure substance can occasionally coexist in equilibrium at a specific condition known as the *triple point* Çengel et al. (2019). The triple point of water occurs at a pressure of 0.6117 kPa and a temperature of 273.16 K. At this precise temperature and pressure, all three phases of water—solid, liquid, and vapor—can coexist in equilibrium.

According to the Gibbs phase rule Gibbs (1878), when there is only one phase, the system has 2 degrees of freedom. This means that two variables must be fixed to fully describe the properties of the matter, such as pressure and temperature Achuthan (2009). If two phases exist and are in equilibrium, as shown along the vaporization line in Figure 3.3,

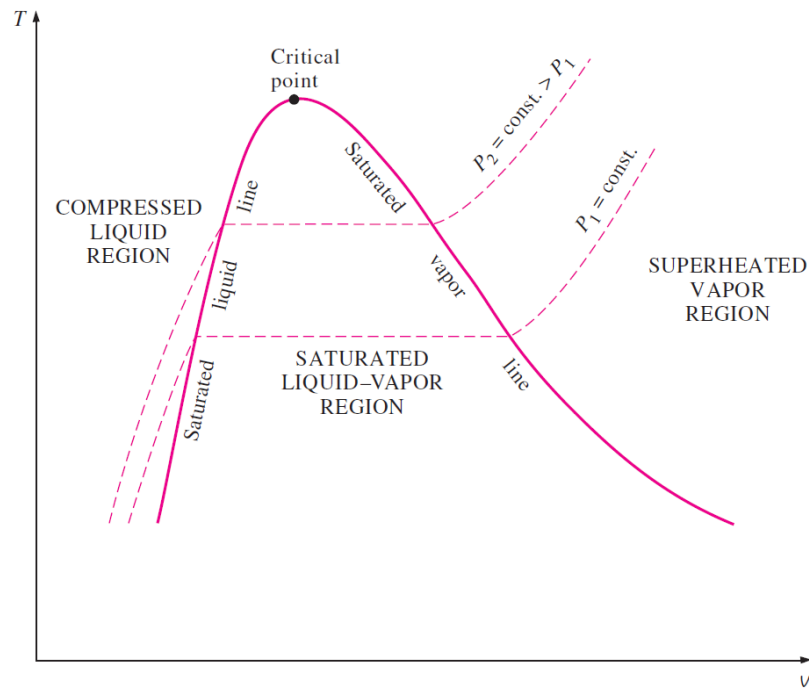


Figure 3.2: $T - v$ diagram of pure substance by Çengel et al. (2019).

the system has only a single degree of freedom. This implies that pressure and temperature are not independent variables; a change in one will result in a corresponding change in the other, establishing a direct relationship between them. At the critical and triple points, the system has zero degrees of freedom, meaning these points are fixed and cannot be altered by changing other variables.

The Gibbs phase rule is expressed as Muhlbauer and Raal (2023):

$$F = C - P + 2$$

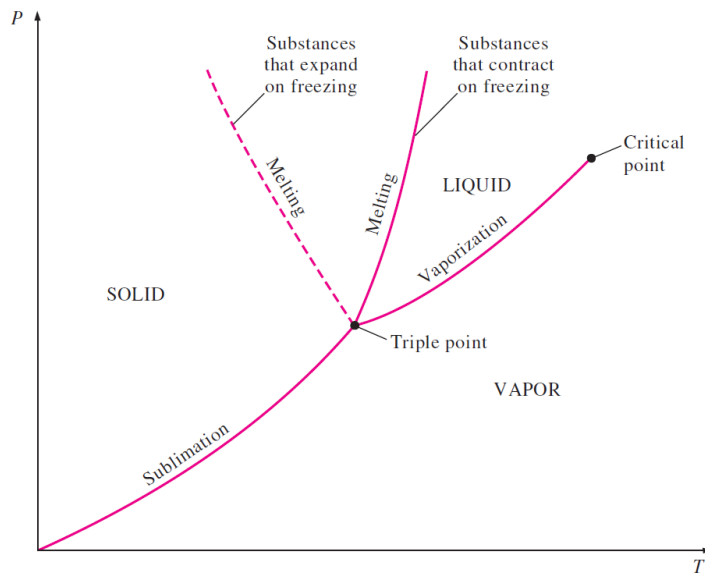
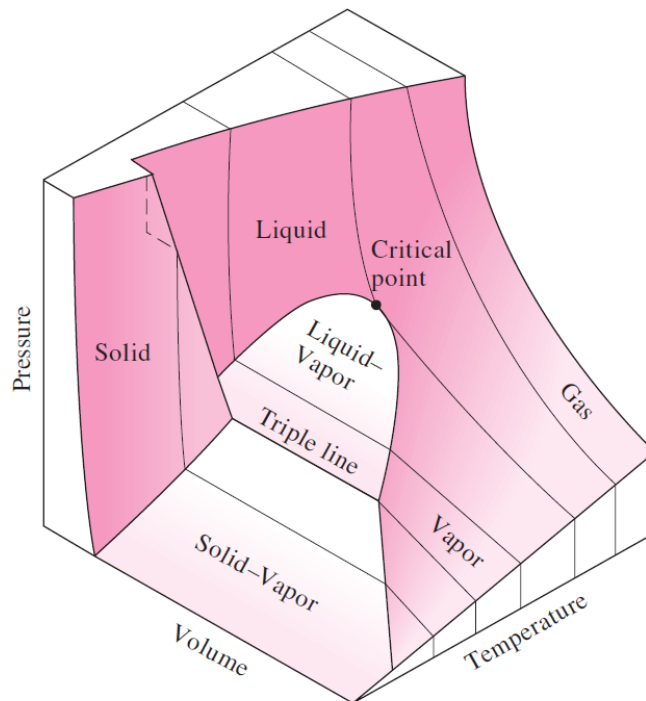
For a single-component (pure phases) system: $F = 1 - P + 2 = 3 - P$

where:

- F is the number of degrees of freedom,
- C is the number of components,
- P is the number of phases present Muhlbauer and Raal (2023).

An equation of state is any relation between a substance's pressure, temperature, and specific volume. Equations of state are another name for property relationships that involve additional attributes of material at equilibrium states. Typically, thermodynamic potentials representing a system's equilibrium behavior are used to build this thermodynamic relation. The four basic thermodynamic potentials are:

- Internal Energy $de = Tds - Pdv$
- Enthalpy $dh = Tds + vdP$
- Gibbs Free Energy $dg = -sdT + vdP$
- Helmholtz Free Energy $df = -sdT - Pdv$

(a) $p - T$ diagram for pure substances.(b) $p - v - T$ diagram for pure water.Figure 3.3: (a) $p - T$ and (b) $p - v - T$ diagrams for pure water by Çengel et al. (2019).

where s is the specific entropy, v is the specific volume, T is temperature and P is pressure. According to thermodynamic potentials, the *complete EoS* can be expressed as:

$$e(s, v) \quad h(s, P) \quad g(T, P) \quad f(T, v)$$

Here, the thermodynamic potentials are represented using their natural variables, which allow for the computation of other thermodynamic quantities through partial differentiation. Therefore, no additional connections are required to characterize the thermodynamic behavior of the substance. However, within the framework of compressible flow, to complete

the Euler equations, a specific form of the EoS is required:

$$P(v, e) = T(v, e)$$

Such a connection for P is referred to as an *incomplete EoS* in relation to a complete EoS. An incomplete EoS can determine a complete one, but not always the other way around. The most important thing is to arrive at the correct entropy equation [Menikoff and Plohr \(1989\)](#). Legendre transformations (for further information, see [Alberty \(2001\)](#)) can be used in this context to transition from one potential to another. When combined with the symmetry of second derivatives, these transformations lead to the derivation of *Maxwell's relations*:

$$\left\{ \begin{array}{l} \left(\frac{\partial T}{\partial v} \right)_s = - \left(\frac{\partial P}{\partial s} \right)_v \\ \left(\frac{\partial T}{\partial P} \right)_s = \left(\frac{\partial v}{\partial s} \right)_P \\ \left(\frac{\partial s}{\partial v} \right)_T = \left(\frac{\partial P}{\partial T} \right)_v \\ \left(\frac{\partial s}{\partial P} \right)_T = - \left(\frac{\partial v}{\partial T} \right)_P \end{array} \right.$$

It is also useful to define some commonly used thermodynamic properties. The specific heat of a substance is the amount of energy required to raise the temperature of a unit mass by one degree. When this process occurs at constant volume, it is referred to as the *specific heat at constant volume* (c_v). Conversely, when the process occurs at constant pressure, it is called the *specific heat at constant pressure* (c_p) [Çengel et al. \(2019\)](#). These properties are defined as follows [Achuthan \(2009\)](#):

$$c_v = \left(\frac{\partial e}{\partial T} \right)_v = T \left(\frac{\partial s}{\partial T} \right)_v ,$$

$$c_p = \left(\frac{\partial h}{\partial T} \right)_P = T \left(\frac{\partial s}{\partial T} \right)_P .$$

In addition, the following general relation can be written for specific heats:

$$c_p - c_v = -T \left(\frac{\partial v}{\partial T} \right)_P^2 \left(\frac{\partial P}{\partial v} \right)_T ,$$

$$c_p - c_v = \frac{vT\beta^2}{\alpha} .$$

where α is the isothermal compressibility and β is the coefficient of volume expansion:

$$\alpha = -\frac{1}{v} \left(\frac{\partial v}{\partial P} \right)_T , \quad \beta = \frac{1}{v} \left(\frac{\partial v}{\partial T} \right)_P$$

3.2 Equation of state

Ideal Gas Equation of State

The ideal-gas equation of state is the fundamental and famous equation of state for substances in the gas phase. Within a correctly chosen region, this EoS accurately estimates the

$P - v - T$ behavior of a gas Çengel et al. (2019). Robert Boyle discovered in 1662 that the pressure of gases is inversely related to their volume during his studies in a vacuum chamber. According to an experimental finding by J. Charles and J. Gay-Lussac, the volume of a gas is correlated to its temperature at low pressures. The EoS of ideal gases emerged as a result of combining Boyle's work with those of Charles and Gay-Lussac:

$$PV = NR_uT$$

where P denotes pressure, V represents the volume occupied by the gas, N denotes the mole number, R_u denotes the universal gas constant and T denotes the temperature. It should be noted that while the ideal gas EoS approach has satisfactory inaccuracy at low-pressure and high-temperature values, different approaches need to be applied in different situations. At high pressure and low temperatures, an important role is played by molecular interactions.

Van der Waals Equation of State

Van der Waals initially proposed this real gas EoS van der Waals (1873), and it has two constants that are based on how a substance behaves when it reaches a critical point. It is provided by:

$$\left(P + \frac{a}{v^2}\right)(v - b) = RT$$

The two constants in the equation, a and b , are determined from the critical point data only. Basically, Van der Waals aimed to extend the application of the ideal gas equation of state by adding 2 more effects to the equation that were not taken into account in the ideal gas model. These are repulsion forces and the space taken up by the molecules themselves Çengel et al. (2019).

Peng-Robinson Equation of State

The Peng-Robinson equation Peng and Robinson (1976) is a cubic equation of state developed to improve the accuracy of phase behavior predictions, particularly near the critical region. It refines the attractive term and introduces a temperature-dependent parameter:

$$P = \frac{RT}{v - b} - \frac{a\alpha(T)}{v(v + b) + b(v - b)},$$

where a and b are fluid-specific constants, and $\alpha(T)$ is a temperature-dependent function that adjusts the attraction term. This EoS is widely used in engineering applications due to its improved accuracy for vapor-liquid equilibrium calculations and real-fluid behavior under high pressures.

Virial Equation of State

The equation of state of a substance can alternatively be written as a series, such as:

$$P = \frac{RT}{v} + \frac{a_{vir}(T)}{v^2} + \frac{b_{vir}(T)}{v^3} + \frac{c_{vir}(T)}{v^4} + \dots$$

This equation is a polynomial series of a simple law and is constructed using a specific volume. Here $a_{vir}(T)$, $b_{vir}(T)$ are called virial coefficients and they depend on the fluid under consideration and its temperature. It is possible to obtain the coefficients as a result of experiment as well as theoretically. The concept of the virial expansion was further

advanced by various scientists, notably [Kamerlingh Onnes \(1902\)](#), who enhanced the theory and determined the virial coefficients. Over time, many researchers in thermodynamics and statistical mechanics have studied and elaborated on the virial equation and its coefficients.

Mie-Grüneisen Equation of State

The pressure and volume of a solid at a specific temperature are related by the Mie-Grüneisen equation of state. It was first named after Mie's work [Mie \(1903\)](#) and then Grüneisen's work [Grüneisen \(1912\)](#). In fluid mechanics and shock wave physics, where the conservation equations encompass pressure, volume, and internal energy rather than just temperature, the $P(V, E)$ form is very helpful [Heuzé \(2012\)](#).

$$P(V, E) = P_\infty(V) + \frac{\Gamma(V)}{V}(E - E_{ref}(V))$$

$$\Gamma(V) = V \left(\frac{\partial P}{\partial E} \right)_V = - \left(\frac{\partial \log(T)}{\partial \log(V)} \right)_S$$

where Γ is the Grüneisen coefficient and $P_\infty(V)$ is given as a function of the fluid. The stiffened gas EoS can be obtained from the Mie-Grüneisen EoS if low-density variations are assumed.

Stiffened Gas Equation of State

The stiffened equation of state is frequently employed when thinking about water under extremely high pressures in instances like underwater nuclear explosions, sonic shock lithotripsy, and sonoluminescence [Le Métayer et al. \(2004\)](#). This approach is well-suited for stiff fluids like water, as it represents the linearized version of the Mie-Grüneisen equation of state, a formulation that was initially developed to describe the properties of solid materials:

$$P(\rho, e) = (\gamma - 1)\rho(e - q) - \gamma P_\infty$$

where $\gamma = C_p/C_v$ is the heat capacity ratio, C_p and C_v are thermal capacities, q the energy of formation and P_∞ is a constant reference pressure [Goncalves et al. \(2019\)](#). The speed of sound c is given;

$$c^2 = \gamma \frac{P + P_\infty}{\rho} = (\gamma - 1)C_p T$$

Noble-Abel Equation of State

In computations for rocket propulsion as well as the interior ballistics of guns, the Noble-Abel equation of state is frequently utilized [Johnston \(2005\)](#).

$$P(v, e) = \frac{R(e - q)}{C_v(v - b)}$$

where R is the specific gas constant, b is the covolume and C_v is specific heat at constant volume. The speed of sound is essential knowledge for compressible flow models. It's described as;

$$c^2 = \frac{c_{IG}^2}{1 - \rho b}$$

where $c_{IG}^2 = \gamma P/\rho$. An alternative version, the first-order virial (VO1) EoS proposed by [Neron and Saurel \(2022\)](#), is explored for its accuracy, showing better performance than NA, especially at higher gas densities, although it requires solving a non-linear equation.

Noble-Abel Stiffened-Gas Equation of State

Noble-Abel EoS and the Stiffened Gas EoS are combined to create this equation of state. It was developed by [Le Métayer and Saurel \(2016\)](#):

$$P(v, e) = (\gamma - 1) \frac{(e - q)}{(v - b)} - \gamma P_\infty$$

where γ , P_∞ , q and b are constant coefficients. The term $(\gamma - 1)(e - q)$ refers thermal agitation while $(v - b)$ represents repulsive effects, and γP_∞ corresponds to attractive effects. The speed of sound can be found:

$$c^2 = -v^2 \left(\frac{\partial P}{\partial v} \right)_s = \frac{\gamma v^2 (P + P_\infty)}{v - b}$$

Extended version of this EoS proposed by [Chiapolino and Saurel \(2018\)](#). This version incorporates variable attractive and repulsive effects to enhance accuracy for the liquid phase under wide temperature and pressure variations [Chiapolino](#). This extension improves the modeling of the transition from pure phase to supercritical states and includes variable specific heat for the gas phase, making it suitable for high temperatures. The formulation shows good agreement with experimental phase diagrams for different fluids.

3.3 Phase Stability and Metastable States

Phase transitions are often idealized as quasi-equilibrium processes under equilibrium saturation conditions in classical thermodynamics. However, real phase changes usually occur under non-equilibrium conditions. For instance, during actual vaporization processes, a portion of the liquid is frequently superheated above the equilibrium saturation temperature. Similarly, in real systems, condensation processes often begin only after some of the vapor phase has been subcooled below the equilibrium saturation temperature [Carey \(2020\)](#). To define stability, we begin by considering a closed system. After performing the necessary mathematical derivations, the criteria for stability and equilibrium can be summarized as follows (see Chapter 5 for detailed information [Carey \(2020\)](#)):

$$\begin{aligned} \delta U &= 0 && \text{criterion of equilibrium} \\ \delta^m U &> 0 \text{ for the smallest } m \text{ at which } \delta U^m \neq 0 && \text{criterion of stability} \\ \delta^m S &< 0 \text{ for the smallest } m \text{ at which } \delta S^m \neq 0 && \text{criterion of stability} \end{aligned}$$

It is known from thermodynamics that an isolated system achieves a highest level of entropy at equilibrium. Moreover, δS and $\delta^n S$ serve as abbreviations for the terms in sequential order:

$$\delta S = \left(\frac{\partial S}{\partial e} \right)_v de + \left(\frac{\partial S}{\partial v} \right)_e dv$$

As a result the detailed examination of the stability criterion, it provides 2 conditions that provide stability. These are [Carey \(2020\)](#):

$$\begin{aligned} c_v &> 0 \text{ criterion for thermal stability} \\ \left(\frac{\partial P}{\partial v} \right)_T &< 0 \text{ criterion for mechanical stability} \end{aligned}$$

If these two criteria are met in a thermodynamic system, the system is said to be *intrinsically stable*. The term *metastable state* refers to a non-equilibrium state in which a liquid is superheated above its equilibrium saturation temperature and a vapor is subcooled below its equilibrium saturation temperature Carey (2020). For a better understanding of the phenomenon, Figure 3.4 can be used. To relate it to thermodynamics, the abscissa can be positioned as a specific volume and the ordinate as Gibbs free energy. It is the process by which the A-sphere reaches the position of the C-sphere, which corresponds to the absolute minimum, in order to reach system equilibrium. If the process is thought of as a liquid-vapor phase transition, sphere A corresponds to metastable liquid, while sphere C is stable vapor. In order for the system to reach equilibrium, the activation energy must be overcome.

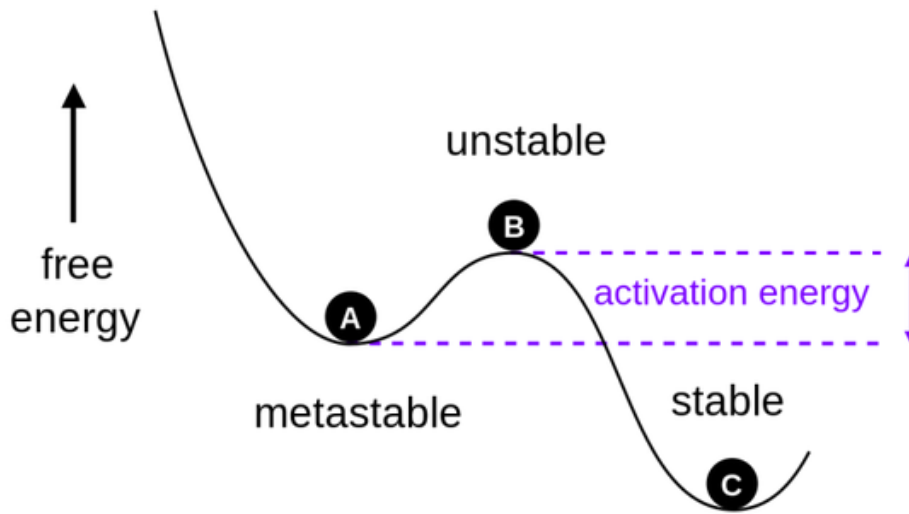


Figure 3.4: Stability, metastability, and instability concepts.

In summary, the metastable state must undergo perturbation in order to reach a steady state, but this perturbation is not random and does not occur if it is below the activation value, but only above the activation value. On the other hand, a stable state remains in its state regardless of perturbation. Last but not least, if susceptible to arbitrarily small perturbations, the unstable state transitions to another state.

Mechanical stability demands that $\left(\frac{\partial P}{\partial v}\right)_T < 0$, as was previously demonstrated. Although it is not in thermodynamic equilibrium, liquid or vapor in a metastable area is not mechanically unstable Carey (2020). The term *spinodal limit* refers to the point at which $\left(\frac{\partial P}{\partial v}\right)_T$ flips from negative to positive. The location of the spinodal limit points in the saturation dome is called the *spinodal curve* Carey (2020). Spinodal lines and metastable regions can be seen in the Figure 3.5. Point B in the figure stands for a saturated liquid state, and section BC for a metastable superheated liquid. Section EFG is a physically feasible zone after the liquid spinodal point C because section CDE is an unstable region that does not meet the required conditions for the stability of a phase Carey (2020). The EF region represents metastable vapor, while stable vapor is observed from point F. In theory, using $\left(\frac{\partial P}{\partial v}\right)_T = 0$ and an equation of state can be used to accurately find the spinodal limit. However, there are no good enough equations of state that apply to the superheated liquid region Pinhasi et al. (2005). Moreover, because the liquid always starts to flash before it reaches this limit ($\left(\frac{\partial P}{\partial v}\right)_T = 0$), simply specifies a hypothetical limit that could never be tested empirically. As a result, it is frequently replaced by an experimentally verifiable em-

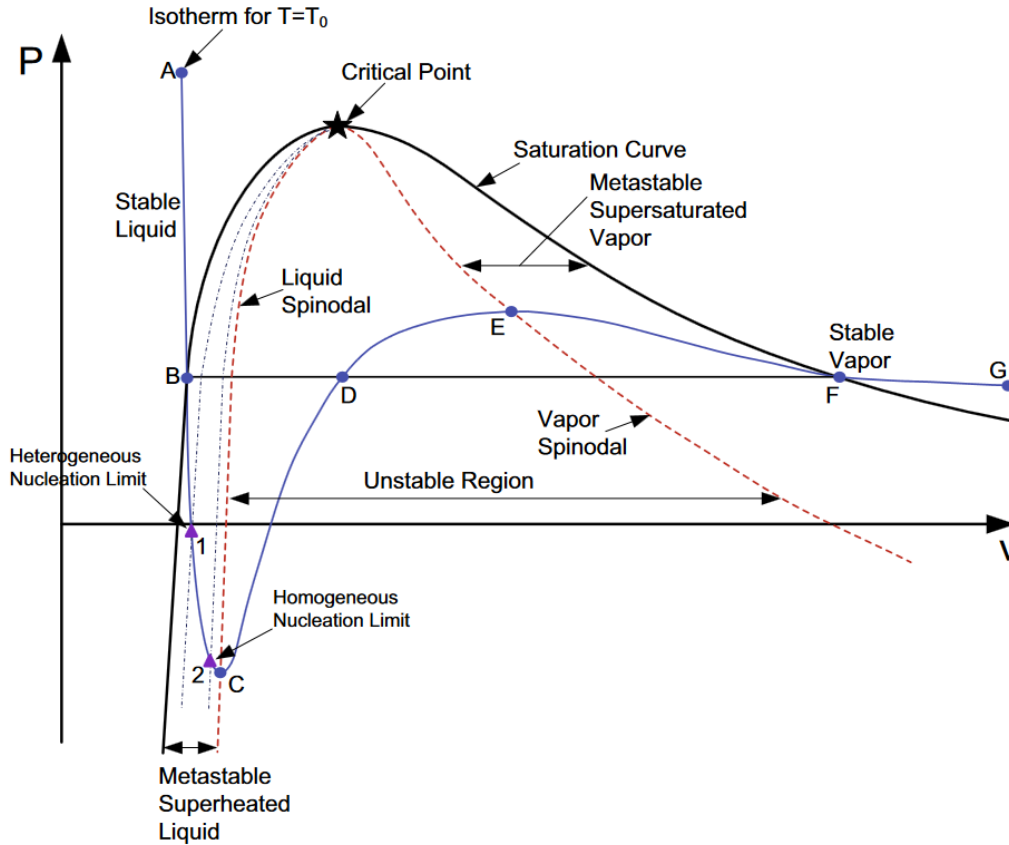


Figure 3.5: Spinodal lines and metastable regions on a P-v diagram by Kim et al. (2021). A-B represents the stable liquid phase, B-C represents the metastable superheated liquid phase, C-D-E indicates the unstable region, D-E shows the metastable supersaturated vapor phase, F-G depicts the stable vapor phase.

pirical kinetic *homogeneous* nucleation limit Lienhard and Karimi (1981). It is only possible to attain the homogeneous nucleation limit under tightly controlled lab conditions. In most real-life situations, it is impossible to achieve these ideal conditions, and the metastable liquid will change phases before it reaches the homogenous nucleation limit. In this scenario, nucleation takes place around pre-existing nuclei or gaseous seeds that are dispersed in an uneven and random manner. *Heterogeneous nucleation* is the name given to this flashing inception mechanism Liao and Lucas (2017).

The homogeneous nucleation limit has been widely explored in the literature for various fluids. Studies focusing on water flashing experiments under different initial conditions and depressurization rates, such as those conducted by Lienhard et al. (1978), have demonstrated that high-pressure drops lead to greater levels of superheating. Building on this, Alamgir and Lienhard (1981) introduced an empirical correlation to estimate the pressure undershoot observed during rapid depressurization of hot water, from Classical Nucleation Theory (CNT) Volmer and Weber (1926), Becker and Döring (1935):

$$\Delta P = \left[\frac{16\pi\sigma^3}{3k_B T_c (1 - v_l/v_g)^2 \frac{G_b}{\phi}} \right]^{0.5},$$

where k_B is the Boltzmann constant, T_c refers to the critical temperature, and v_l and v_g represent the specific volumes of the liquid and vapor phases, respectively. Here, G_b denotes the Gibbs number, while ϕ accounts for the reduction factor ($0 < \phi < 1$) Liao and Lucas (2017). The empirical relationship for the ratio G_b/ϕ at the point where flashing begins is

given as:

$$\frac{G_b}{\phi} = \frac{28.2 \pm 5.8}{0.10587T_r^{28.46} \cdot (1 + 14\Sigma^{0.8})},$$

where $T_r = T_i/T_c$ corresponds to the relative temperature, and Σ is the static depressurization rate [Liao and Lucas \(2017\)](#).

[Barták \(1990\)](#) revised the correlation initially proposed by [Alamgir and Lienhard \(1981\)](#), incorporating new experimental results gathered under various starting conditions. Their findings revealed that the original correlation [Alamgir and Lienhard \(1981\)](#) could not accurately predict the achieved superheat when compared to their updated version. For cases involving low depressurization rates, further analysis demonstrated that the estimates of superheat provided by [Alamgir and Lienhard \(1981\)](#) was unreliable. To address this issue, [Elias and Chambre' \(1993\)](#) introduced a comparable correlation for determining the maximum achievable superheat during flashing flows, which performed effectively across both low and high depressurization conditions.

The fluids used in industrial systems are difficult to find in pure form. Impurities, irregularities and similar structures present in the system prevent the fluids from reaching the deep metastable state, reducing the amount of activation energy mentioned earlier. However, if desired, the structures that trigger the nucleation mechanism can be eliminated and the liquid form can be observed in a range from $-41\text{ }^\circ\text{C}$ to $280\text{ }^\circ\text{C}$ [Mossop \(1955\)](#), [Apfel \(1972\)](#) at atmospheric pressure. However, as will be observed in these experiments, it is not possible to delay boiling or freezing after a certain point and the new phase appears suddenly. In industry and in nature, it is possible to encounter situations where pure water is in a metastable phase. In industry, systems containing high-pressure pipes in an atmospheric pressure environment, for example, in nuclear power plants, rapid pressure losses as a result of accidents trigger the formation of superheated metastable liquid which we will see in detail in Chapter 6. In addition, metastable liquid is observed in the cryogenic, metals processing, and paper industries. In nature, supercooled water can be found in clouds, and trees rely on metastable liquids in the process of transporting structures such as water and minerals from their roots to their leaves. Groundwaters exposed to high thermal flux (magmas, volcanic regions) may have metastable states [Debenedetti \(1996\)](#).

3.4 Summary

This chapter explores the concept of thermodynamic metastability, focusing on phase transitions and the behavior of pure substances under varying thermodynamic conditions. It begins by explaining the phase diagrams of pure substances, including the key regions of subcooled liquid, saturated liquid-vapor mixture, and superheated vapor. Critical points, as well as the triple point of water, are discussed to highlight the unique properties of phase transitions.

The chapter also covers various equations of state, from the Ideal Gas Law to more complex models like the Van der Waals and Mie-Grüneisen equations. These EoS provide essential relationships between pressure, volume, and temperature, especially when modeling real gases and fluids in industrial applications.

A large part is devoted to phase stability and metastable states, specifically differentiating stable, unstable, and metastable behaviors. The metastable state, where a liquid or vapor exists in non-equilibrium conditions, is particularly analyzed for its industrial relevance and natural occurrences. The chapter concludes by discussing the spinodal curve, which marks the boundary between metastable and unstable phases, and the role of nucleation in phase transitions.

Chapter 4

Numerical solver

In this fourth chapter, an introduction to the Navier-Stokes Multi-Block (NSMB) solver is first provided. Following this, detailed information is presented on the two different two-phase flow models that are already implemented in the solver, including the numerical solution methods utilized and the high-order extensions applied. The chapter then proceeds to the validation work conducted using the four-equation model in NSMB, where several well-known test cases from the literature are employed. Through this validation process, both the strengths and limitations of the model are thoroughly analyzed, providing valuable insights into its performance under various conditions.

4.1 Navier-Stokes Multi-Block solver

The Navier-Stokes Multi-blocks (NSMB) approach originated from the development of a structured multi-block Euler code (EULMB) at the Swiss Federal Institute of Technology in Lausanne (EPFL) in 1989. This code was created with support from the European Centre for Research and Advanced Training in Scientific Computation (CERFACS) and the Royal Institute of Technology (KTH). The original solver was written in Fortran 77, with dynamic memory allocation implemented using the MemCom library. Since 2001, Fortran 90 modules have been integrated, enhancing code modularity and extensibility. The NSMB solver is a program that uses the finite volume method to solve the compressible or incompressible Navier-Stokes equations on multi-block structured grids. It has been optimized for high-performance computing (HPC) through the Single Program Multiple Data (SPMD) paradigm, with Message Passing Interface (MPI) enabling efficient parallel computations. The solver can handle both steady and unsteady problems. It offers various numerical schemes for both spatial and temporal discretization, including central schemes. The solver also provides different methods for handling turbulence. Between 1992 and 2003, the NSMB consortium consisting of different universities and industrial partners completed the first phase of the solver. Since 2004, further developments have been carried out by the following institutions (see for further information [Vos et al. \(2014\)](#), [Hoarau et al. \(2016\)](#) [NSM \(2018\)](#)):

- École Polytechnique Fédérale de Lausanne (EPFL)
- Eidgenössische Technische Hochschule Zürich (ETH Zürich)
- Institut de Mécanique des Fluides de Toulouse (IMFT)
- Universität der Bundeswehr München

- CFS Engineering
- RUAG Aerospace
- ICUBE-Université de Strasbourg

The following sections will present the cavitation models and numerical methods already implemented in the solver.

4.2 Three equation model

It is also called the Homogeneous Equilibrium Model (HEM). The motion of fluids is controlled by three fundamental physical equations of conservation: the equations for conservation of mass, momentum, and energy. It is presumed that the phases in the system are thoroughly mixed and that the size of the dispersed particles is small enough to eliminate any considerable relative motion between them. The phases are closely connected and move with equal velocity, while also being in kinematic and thermodynamic equilibrium - meaning that they maintain the same pressure, temperature, and velocity. HEM can be written in the following form in 1D:

$$\begin{cases} \frac{\partial \rho}{\partial t} + \frac{\partial(\rho u)}{\partial z} = 0 \\ \frac{\partial(\rho u)}{\partial t} + \frac{\partial(\rho u^2 + p)}{\partial z} = 0 \\ \frac{\partial(\rho E)}{\partial t} + \frac{\partial[(\rho E + p)u]}{\partial z} = 0 \end{cases} \quad (4.1)$$

where u, ρ, p , and E indicate mixture velocity, mixture density, pressure, and specific total energy, respectively. In order to fully describe and close a physical system, it is essential to establish an equation of state that establishes a relationship between temperature, pressure, internal energy, and density. For the case of pure-phase substances, the convex stiffened gas EoS can be used [Le Métayer et al. \(2004\)](#), [Goncalvès \(2013\)](#):

$$P(\rho, e) = (\gamma - 1)\rho(e - q) - \gamma P_\infty \quad (4.2)$$

$$P(\rho, T) = \rho(\gamma - 1)C_v T - P_\infty \quad (4.3)$$

$$T(\rho, h) = \frac{h - q}{C_p} \quad (4.4)$$

where $\gamma = C_p/C_v$ is the heat capacity ratio, C_p and C_v are thermal capacities, q the energy of formation and P_∞ is a constant reference pressure. The speed of sound c is given by:

$$c^2 = \gamma \frac{P + P_\infty}{\rho} = (\gamma - 1)C_p T \quad (4.5)$$

For the two-phase mixture area, a sinusoidal barotropic law can be utilized [Delannoy and Kueny \(1990\)](#), [Goncalvès \(2014\)](#):

$$P(\rho, \alpha) = P_{vap} + \left(\frac{\rho_l^{sat} - \rho_v^{sat}}{2} \right) c_{min}^2 \text{Arcsin}(A(1 - 2\alpha)) \quad (4.6)$$

$$T(\rho, h) = \frac{h_l - q_l}{C_{pl}} = \frac{h_v - q_v}{C_{pv}} \quad (4.7)$$

The sinusoidal barotropic law is distinguished by its maximum slope of $1/c_{min}^2$. The model includes an adjustable parameter, c_{min} , which represents the lowest possible speed of sound within the mixture. The original method treated pure phases as incompressible and with infinite speed of sound in each phase. In the modified approach [Goncalves and Patella \(2009\)](#), a constant A with a value close to 1 is included to connect the compressible pure phases and prevent the speed of sound from reaching an infinite value. The speed of sound c is given by:

$$c^2 = \left(\frac{\partial P}{\partial \rho} \right)_s = \left(\frac{\partial P}{\partial \rho} \right)_T = \frac{Ac_{min}^2}{\sqrt{1 - A^2(1 - 2\alpha)^2}} \quad (4.8)$$

4.3 Four equation model

The 4-equation model [Goncalves and Zeidan \(2018\)](#) is a reduced version of the 5-equation Kapila model [Kapila et al.](#), assuming that the liquid is in the saturation state. The model is made up of three conservation laws for mixture properties and an extra equation for the volume fraction. The phases are assumed to be tightly linked and moving at equal velocity. In addition, the phases are presumed to be in both thermal and mechanical equilibrium [Goncalves and Zeidan \(2018\)](#). Below can be found inviscid two-dimensional equations represented by variables $w=(\rho, \rho \vec{V}, \rho E, \alpha)$ [Goncalves et al. \(2019\)](#):

$$\begin{cases} \frac{\partial \rho}{\partial t} + \text{div}(\rho \vec{V}) = 0 \\ \frac{\partial(\rho \vec{V})}{\partial t} + \text{div}(\rho \vec{V} \otimes \vec{V} + PId) = 0 \\ \frac{\partial(\rho E)}{\partial t} + \text{div}(\rho \vec{V} H) = 0 \\ \frac{\partial \alpha}{\partial t} + \vec{V} \cdot \text{grad}(\alpha) = K \text{div}(\vec{V}) \end{cases} \quad (4.9)$$

Here K is:

$$K = \frac{\rho_l c_l^2 - \rho_v c_v^2}{\frac{\rho_l c_l^2}{1-\alpha} + \frac{\rho_v c_v^2}{\alpha}} \quad (4.10)$$

where $\vec{V} = (u, v)$ denotes the center of mass velocity, $E = e + \frac{V^2}{2}$ is the total energy of the mixture, and $H = h + \frac{V^2}{2}$ is the enthalpy of the mixture. The term K refers to the sound speed of pure phases c_k and it reflects the impacts of volume changes in each phase [Goncalves and Zeidan \(2018\)](#). An equation of state (EoS), which connects the pressure and temperature to the internal energy and density, is required to complete the system. For pure phases, the above-mentioned convex stiffened gas EoS can be used.

On the basis of the stiffened gas EoS, it is possible to derive a formula for the pressure and temperature for the two-phase mixture area using the thermal and mechanical equilibrium assumption [Saurel et al. \(2008\)](#). These formulas, along with functions for the void fraction α and the mass fraction of gas $Y = \alpha \rho_v / \rho$, are available in all possible fluid states [Goncalves et al. \(2019\)](#):

$$P(\rho, e, \alpha, Y) = (\gamma(\alpha) - 1)\rho(e - q(Y)) - \gamma(\alpha)P_\infty(\alpha) \quad (4.11)$$

$$\frac{1}{\gamma(\alpha) - 1} = \frac{\alpha}{\gamma_v - 1} + \frac{1 - \alpha}{\gamma_l - 1} \quad (4.12)$$

$$q(Y) = Yq_v + (1 - Y)q_l \quad (4.13)$$

$$P_\infty(\alpha) = \frac{\gamma(\alpha) - 1}{\gamma(\alpha)} \left[\alpha \frac{\gamma_v}{\gamma_v - 1} P_\infty^v + (1 - \alpha) \frac{\gamma_l}{\gamma_l - 1} P_\infty^l \right] \quad (4.14)$$

$$T(\rho, h, Y) = \frac{h - q(Y)}{C_p(Y)} \quad (4.15)$$

$$C_p(Y) = Y C_{p_v} + (1 - Y) C_{p_l} \quad (4.16)$$

Acoustic waves propagate at the Wallis speed of sound in the absence of mass transfer. This speed is denoted by:

$$\frac{1}{\rho c_{wallis}^2} = \frac{\alpha}{\rho_v c_v^2} + \frac{1 - \alpha}{\rho_l c_l^2} \quad (4.17)$$

The set of four equations constitutes a system of conservation laws that exhibit a hyperbolic character [Goncalves and Zeidan \(2018\)](#). The eigenvalues of this model are as follows [Goncalvès \(2013\)](#):

$$\lambda_1 = u - c_{wallis}, \quad \lambda_{2,3,4} = u, \quad \lambda_5 = u + c_{wallis},$$

The mass transfer term becomes active when the local pressure P drops below the vapor pressure $P_{vap}(T)$ which is calculated as [Goncalves and Zeidan \(2018\)](#), [d'Agostino and Salvetti \(2017\)](#):

$$P_{vap}(T) = P_{vap}(T_{ref}) + \frac{dP}{dT}(T - T_{ref}) \quad (4.18)$$

The void ratio equation expression changes when mass transfer between phases takes place and becomes:

$$\frac{\partial \alpha}{\partial t} + \text{div}(\alpha \vec{V}) = (K + \alpha) \text{div}(\vec{V}) + \left(\frac{\frac{c_v^2}{\alpha} + \frac{c_l^2}{1-\alpha}}{\frac{\rho_l c_l^2}{1-\alpha} + \frac{\rho_v c_v^2}{\alpha}} \right) \dot{m} \quad (4.19)$$

One can develop a series of models where \dot{m} is expressed by assuming that the mass transfer is proportional to the divergence of the velocity [Goncalves and Zeidan \(2018\)](#):

$$\dot{m} = \frac{\rho_l \rho_v}{\rho_l - \rho_v} \left(1 - \frac{c^2}{c_{wallis}^2} \right) \text{div}(\vec{V}) \quad (4.20)$$

The enthalpy of each phase can be used to describe the speed of sound in the mixture [Goncalvès and Charrière \(2014\)](#):

$$\rho c^2 = (\gamma(\alpha) - 1) \left[\frac{\rho_v \rho_l}{(\rho_l - \rho_v)} (h_v - h_l) \right] \quad (4.21)$$

4.3.1 Numerics

In this section, the fundamental methods of discretization in both space and time are introduced. The four-equations model can be expressed as a matrix in one-dimensional space as [Goncalves and Zeidan \(2018\)](#):

$$\frac{\partial U}{\partial t} + \frac{\partial G(U)}{\partial x} + B(U) \frac{\partial u}{\partial x} = 0 \quad (4.22)$$

Here U , $G(U)$, and $B(U)$ is given:

$$U = \begin{pmatrix} w \\ \alpha \end{pmatrix}, \quad G(U) = \begin{pmatrix} F(w) \\ au \end{pmatrix}, \quad B(U) = \begin{pmatrix} 0 \\ -K - \alpha \end{pmatrix} \quad (4.23)$$

where F denotes the convective flux. Using the finite volume technique, the computational domain can be divided into regular meshes, if this is done for the spatial domain and the temporal domain, the above equation can be reformulated as follows:

$$\Delta x \frac{U_i^{n+1} - U_i^n}{\Delta t} + G_{i+1/2}^n - G_{i-1/2}^n + \int_{x_{i-1/2}}^{x_{i+1/2}} B(U) \frac{\partial u}{\partial x} = 0 \quad (4.24)$$

where i and n stand for discretization in space and time, respectively. With the exception of the non-conservative part, it is possible to determine the numerical flux through the use of numerical methods. Numerous formulations for approximating the numerical flux can be found in existing literature, including Rusanov scheme [Rusanov \(1962\)](#), AUSM-type scheme [Liou and Steffen \(1993\)](#), Jameson-Schmidt-Turkel scheme [Jameson et al. \(1981\)](#), and HLLC scheme [Toro et al. \(1994\)](#). The HLLC scheme has been widely used in literature, this study will focus on this scheme.

4.3.2 Harten-Lax-van Leer-Contact Riemann solver

The HLLC approximate Riemann solver takes into account two averaged intermediate states, w_L^* and w_R^* , separated by the contact wave speed S_M . At a cell interface, the numerical flux $F_{i+1/2}$ can be represented as [Goncalves and Zeidan \(2018\)](#):

$$F_{i+1/2} = \begin{cases} F(w_L), & \text{if } S_L > 0 \\ F(w_L^*), & \text{if } S_L \leq 0 < S_M \\ F(w_R^*), & \text{if } S_M \leq 0 \leq S_R \\ F(w_R), & \text{if } S_R < 0 \end{cases} \quad (4.25)$$

As described by [Goncalves and Zeidan \(2018\)](#), the speeds of the smallest and largest waves at the cell interface are referred to as S_L and S_R , respectively. $F(w_k^*)$, P^* , S_M are defined as follows:

$$w_K^* = \begin{pmatrix} \rho_K^* \\ (\rho u)_K^* \\ (\rho E)_K^* \\ \alpha_K^* \end{pmatrix} = \frac{1}{S_K - S_M} \begin{pmatrix} \rho_K(S_K - u_K) \\ (\rho u)_K(S_K - u_K) + P^* - P_K \\ (\rho E)_K(S_K - u_K) + P^* S_M - P_K u_K \\ \alpha_K(S_K - u_K) \end{pmatrix} \quad (4.26)$$

$$F(w_K^*) = \begin{pmatrix} \rho_K^* S_M \\ (\rho u)_K^* S_M + P^* \\ (\rho E)_K^* S_M + P^* S_M \\ \alpha_K^* S_M \end{pmatrix} \quad (4.27)$$

The value of pressure P^* is determined by the following expression [Goncalves and Zeidan \(2018\)](#):

$$P^* = P_L + \rho_L(u_L - S_L)(u_L - S_M) = P_R + \rho_R(u_R - S_R)(u_R - S_M) \quad (4.28)$$

The speed of the contact wave, denoted as S_M , is defined by the following expression:

$$S_M = \frac{P_R - P_L + \rho_L u_L (S_L - u_L) - \rho_R u_R (S_R - u_R)}{\rho_L (S_L - u_L) - \rho_R (S_R - u_R)} \quad (4.29)$$

with the wave speeds S_L and S_R :

$$S_L = \text{Min}(u_L - c_L, u_R - c_R) \quad S_R = \text{Max}(u_L + c_L, u_R + c_R)$$

On the other hand, the discretization of the non-conservative part is based on the technique presented in [Daude et al. \(2014\)](#). The expression for the $B(U)$ term is given by:

$$\int_{x_{i-1/2}}^{x_{i+1/2}} B(U) \frac{\partial u}{\partial x} \simeq B(U_i)(u_{i+1/2} - u_{i-1/2}) \quad (4.30)$$

where the interface cell values:

$$u_{i+1/2} = \begin{cases} u_L & \text{if } S_L > 0 \\ \frac{S_L - u_L}{S_L - S_M} S_M & \text{if } S_L \leq 0 < S_M \\ \frac{S_R - u_R}{S_R - S_M} S_M & \text{if } S_M \leq 0 \leq S_R \\ u_R & \text{if } S_R < 0 \end{cases} \quad (4.31)$$

4.3.3 High order extensions

The MUSCL (Monotonic Upstream-centered Scheme for Conservation Law) reconstruction is a straightforward numerical technique for spatial resolution. Originally proposed by [Van Leer \(1977\)](#), this method presumes linear variation within a cell, as depicted in Figure 4.1. The primary concept involves using discrete average values at the cell boundaries to reconstruct the average interface values. To achieve this, a second-order expansion is applied to determine the slope of the reconstructed variables. Typically, two types of approximations are employed:

- **One-sided approximation:**

$$w_{j+\frac{1}{2}}^L = w_j + \frac{w_j - w_{j-1}}{2}, \quad w_{j+\frac{1}{2}}^R = w_j - \frac{w_{j+2} - w_{j+1}}{2} \quad (4.32)$$

- **Centered approximation:**

$$w_{j+\frac{1}{2}}^L = w_j + \frac{w_{j+1} - w_j}{2}, \quad w_{j+\frac{1}{2}}^R = w_{j+1} - \frac{w_{j+1} - w_j}{2} \quad (4.33)$$

These formulations can be generalized by incorporating a parameter ϕ , yielding:

$$w_{j+\frac{1}{2}}^L = w_j + \frac{1 - \phi}{4}(w_j - w_{j-1}) + \frac{1 + \phi}{4}(w_{j+1} - w_j) \quad (4.34)$$

Setting $\phi = -1, 1, \frac{1}{3}$ corresponds to one-sided, centered, and third-order approximations, respectively.

However, the MUSCL method alone can lead to oscillations around strong shocks and discontinuities. To mitigate this, TVD (Total Variation Diminishing) methods, introduced by [Harten \(1983\)](#), are used. A numerical scheme's solution is considered TVD if it meets the following conditions:

$$TV[w^{n+1}] \leq TV[w^n] \quad (4.35)$$

This approach can be integrated into the general MUSCL framework by introducing another parameter Ψ , as follows:

$$w_{j+\frac{1}{2}}^L = w_j + \frac{1 - \phi}{4}\Psi(r_L)(w_j - w_{j-1}) + \frac{1 + \phi}{4}\Psi\left(\frac{1}{r_L}\right)(w_{j+1} - w_j) \quad (4.36)$$

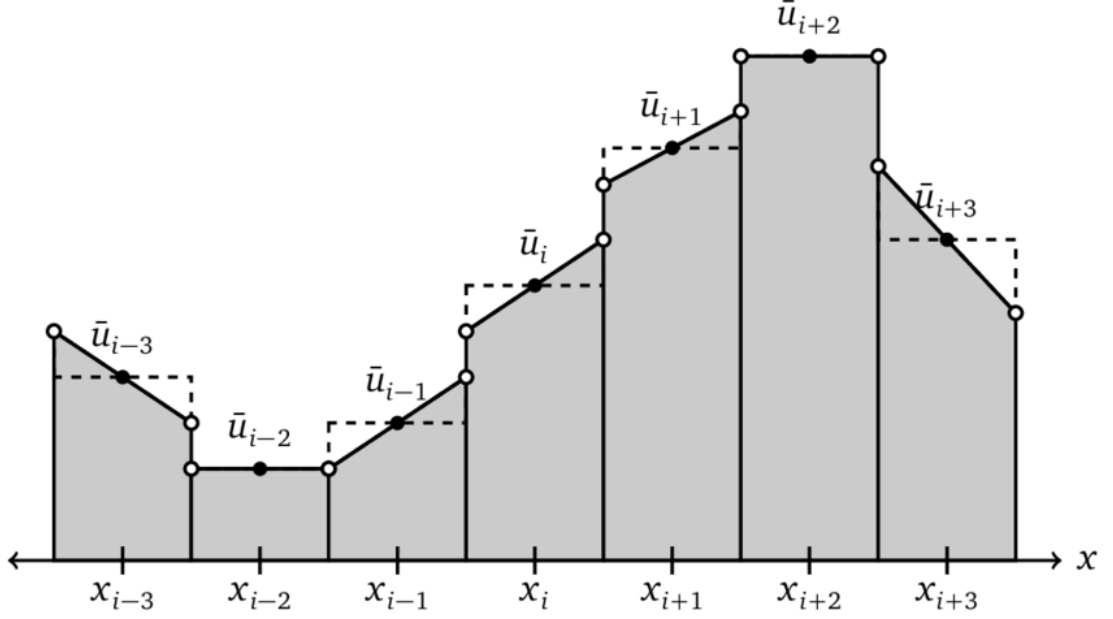


Figure 4.1: Representation of data as piecewise linear in the finite volume MUSCL scheme by Núñez-De La Rosa (2015).

$$r_L = \frac{w_{i+1} - w_i}{w_i - w_{i-1}} \quad (4.37)$$

$$w_{j+\frac{1}{2}}^R = w_j - \frac{1+\phi}{4}\Psi(r_R)(w_{j+1} - w_j) + \frac{1-\phi}{4}\Psi\left(\frac{1}{r_R}\right)(w_{j+1} - w_j) \quad (4.38)$$

$$r_R = \frac{w_{j+1} - w_j}{w_{j+2} - w_{j+1}} \quad (4.39)$$

Commonly used TVD slope limiters include:

- superbee: $\Psi(r) = \max(0, \min(1, 2r), \min(2, r))$
- minmod: $\Psi(r) = \max(0, \min(1, r))$
- van Albada: $\Psi(r) = \max(0, \frac{r+r^2}{1+r^2})$

4.4 Validation test cases

Case 1:

This test case is proposed by Richard Saurel et al. (2009). A one-meter-long shock tube with two chambers and chambers separated at $x = 0.6$ m Gonçalves and Zeidan (2018). The starting void fraction of spinel is 0.4046 everywhere. The pressure in the left part is 10^{10} Pa while the right part is at atmospheric pressure. The fluids are initially at rest and are controlled by the stiffened gas EoS. The variables are:

$$\begin{pmatrix} \gamma \\ P_\infty \\ \rho \end{pmatrix}_{\text{Epoxy}} = \begin{pmatrix} 2.43 \\ 5.3 \times 10^9 \text{ Pa} \\ 1185 \text{ kg/m}^3 \end{pmatrix}, \quad \begin{pmatrix} \gamma \\ P_\infty \\ \rho \end{pmatrix}_{\text{Spinel}} = \begin{pmatrix} 1.62 \\ 141 \times 10^9 \text{ Pa} \\ 3622 \text{ kg/m}^3 \end{pmatrix} \quad (4.40)$$

Results are displayed in 80 μs , calculations are made with a mesh of 6000 cells, and the results are compared to the exact solution [Petitpas et al. \(2007\)](#). While void ratio and mixture density profiles are shown in Figure 4.2, mixture pressure and velocity are presented in Figure 4.3. HLLC 2 and HLLC 3 refer to the second and third-order extensions. The wave structure of this test case is relatively simple: on the left side of the initial discontinuity, a rarefaction wave is observed, while on the right side, a shock wave is clearly formed. As can be seen, the results are quite similar except for some deviations in the HLLC third-order scheme. The deviations observed in the third-order HLLC scheme can be mitigated using the Hancock predictor-corrector strategy, which introduces an additional correction step to enhance solution accuracy.

Case 2:

Beginning with an initial velocity discontinuity positioned in the center of the tube, a problem involving a double rarefaction tube is taken into consideration, and proposed in [Zein et al. \(2010\)](#), [Goncalves and Zeidan \(2018\)](#). A one-meter-long tube occupied by liquid water at atmospheric pressure and with density 1150 kg/m^3 will be used for this test. A weak volume fraction of vapor is 0.01 initially added to the liquid. The left velocity is -2 m/s while the right velocity is 2 m/s , and the fluid is controlled by the stiffened gas EoS [Zein et al. \(2010\)](#):

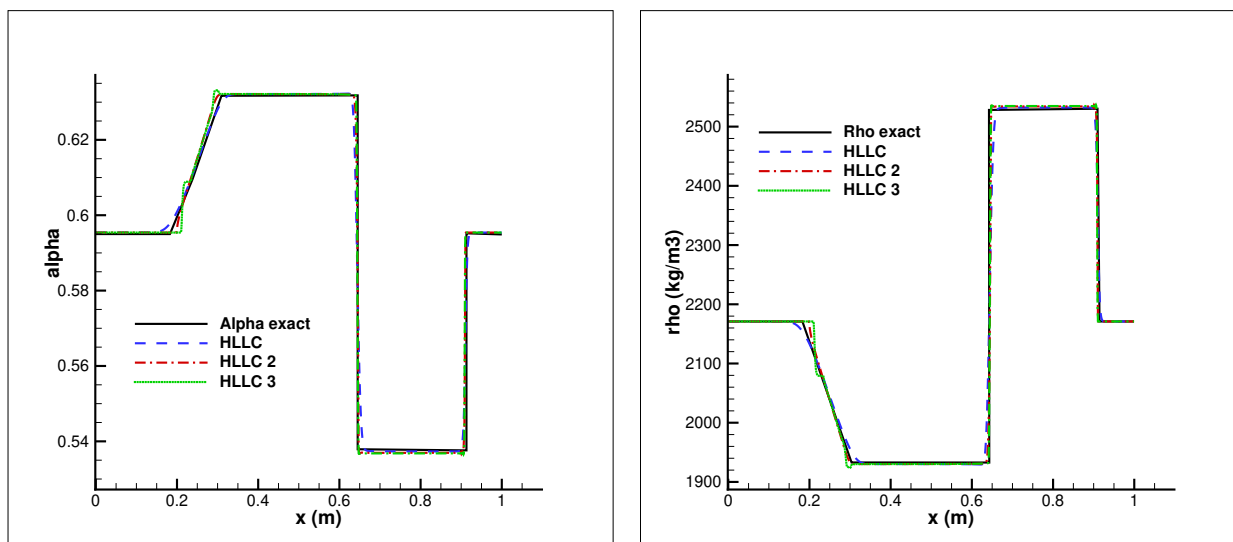
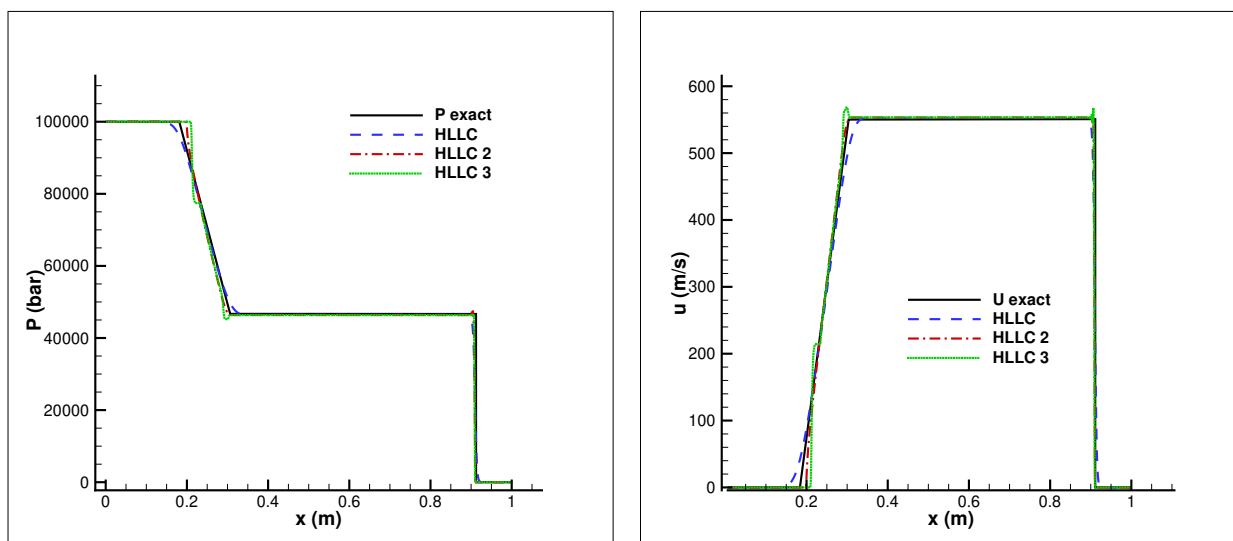
$$\begin{pmatrix} \gamma \\ P_\infty \\ q \\ C_p \end{pmatrix}_{\text{Liq}} = \begin{pmatrix} 2.35 \\ 10^9 \text{ Pa} \\ -0.1167 \times 10^7 \text{ J kg}^{-1} \\ 4267 \text{ J kg}^{-1} \text{ K}^{-1} \end{pmatrix}, \quad \begin{pmatrix} \gamma \\ P_\infty \\ q \\ C_p \end{pmatrix}_{\text{Gas}} = \begin{pmatrix} 1.43 \\ 0 \text{ Pa} \\ 0.2030 \times 10^7 \text{ J kg}^{-1} \\ 1487 \text{ J kg}^{-1} \text{ K}^{-1} \end{pmatrix} \quad (4.41)$$

Results are displayed in 3.2 ms, calculations are made with a mesh of 6000 cells, and the results are compared to the two-fluid solution. While volume fraction and mixture density profiles are shown in Figure 4.4, mixture pressure and velocity are presented in Figure 4.5. The solution involves two expansion waves. The void ratio rises in the middle of the tube as a result of mechanical expansion, leading to the formation of a pocket [Saurel et al. \(2008\)](#). Minor deviations are observed in the maximum void fraction value and minimum density at the middle of the tube; except this, the result profiles show good agreement with the two-fluid reference results.

Case 3:

This test case, proposed by [Lund and Aursand \(2012\)](#), includes the depressurization of a pipe filled with CO_2 . The pipe's total length is 80 meters, with the initial discontinuity located at 50 meters. The initial conditions are: on the left side, the pressure P_L is 60 bar, the temperature T_L is 273 K, and the volume fraction α_L is 1×10^{-5} ; on the right side, the pressure P_R is 10 bar, the temperature T_R is 273 K, and the volume fraction α_R is $1 - \alpha_L$. The parameters for the equation of state are presented [Bacigaluppi et al. \(2021\)](#):

$$\begin{pmatrix} \gamma \\ P_\infty \\ q \\ C_v \\ q' \end{pmatrix}_{\text{Liq}} = \begin{pmatrix} 1.23 \\ 1.32 \times 10^8 \text{ Pa} \\ -6.23 \times 10^5 \text{ J kg}^{-1} \\ 2.44 \times 10^3 \text{ J kg}^{-1} \text{ K}^{-1} \\ -5.34 \times 10^3 \text{ J kg}^{-1} \text{ K}^{-1} \end{pmatrix}, \quad \begin{pmatrix} \gamma \\ P_\infty \\ q \\ C_v \\ q' \end{pmatrix}_{\text{Gas}} = \begin{pmatrix} 1.06 \\ 8.86 \times 10^5 \text{ Pa} \\ -3.01 \times 10^5 \text{ J kg}^{-1} \\ 2.41 \times 10^3 \text{ J kg}^{-1} \text{ K}^{-1} \\ -1.03 \times 10^4 \text{ J kg}^{-1} \text{ K}^{-1} \end{pmatrix} \quad (4.42)$$

Figure 4.2: Void ratio and mixture density profiles along the tube, case 1, $t=80 \mu\text{s}$.Figure 4.3: Mixture pressure and velocity profiles along the tube, case 1, $t=80 \mu\text{s}$.

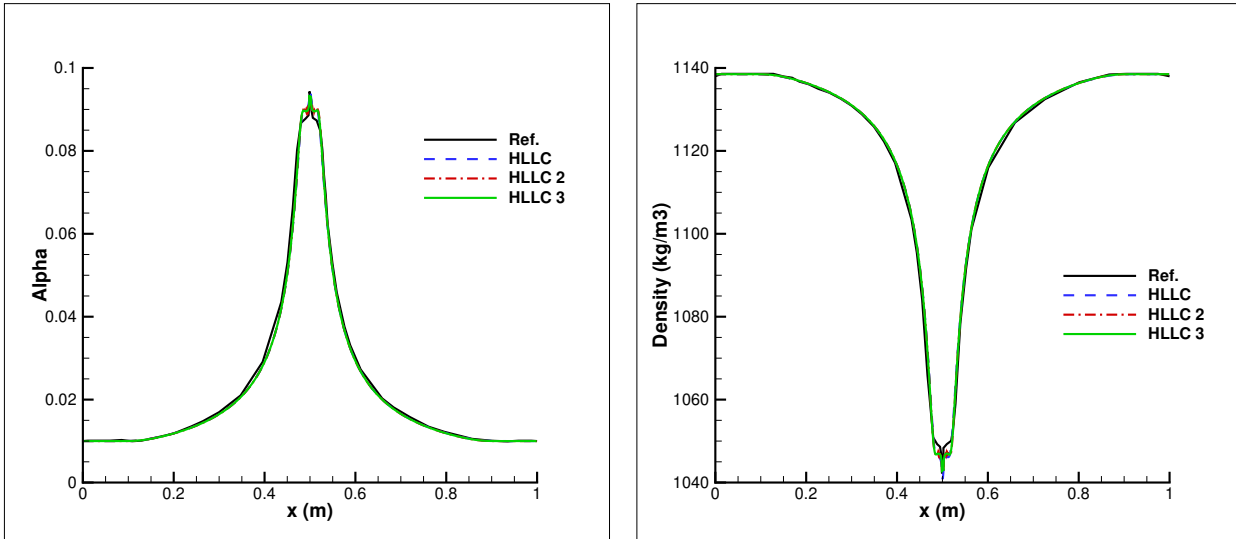


Figure 4.4: Void ratio and mixture density profiles along the tube, case 2, $t=3.2$ ms.

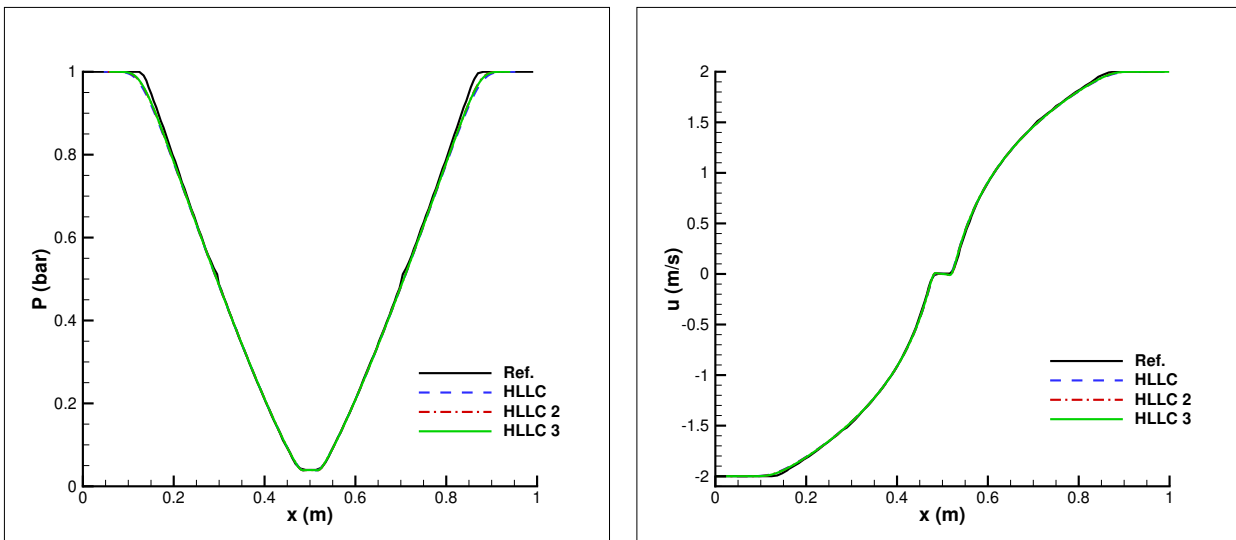


Figure 4.5: Mixture pressure and velocity profiles along the tube, case 2, $t=3.2$ ms.

In this test case, a series of simulations were conducted to analyze the depressurization of a shock tube filled with CO_2 . All simulations were performed using the HLLC scheme. The simulations were conducted with varying mesh resolutions of 1000, 2000, and 4000 computational nodes. Figures 4.6 and 4.7 illustrate the results, where 'HLLC-1000 nodes', 'HLLC-2000 nodes', and 'HLLC-4000 nodes' represent the solutions obtained with 1000, 2000, and 4000 nodes, respectively. The results indicate that the solution obtained with 4000 nodes provided the best match to the wave structure and was closest to the exact solution. Therefore, this resolution was selected for subsequent simulations, as it balanced computational efficiency with sufficient accuracy.

In Figure 4.8, the results for the first, second, and third-order HLLC schemes are presented. The comparison demonstrates that these simulations align closely with the reference solution, indicating a strong agreement and validating the accuracy of the higher-order numerical methods employed.

In the revised version of the depressurization scenario for a pipe filled with CO_2 , mass transfer processes are included. The resulting temperature variations from the liquid-to-vapor phase transition generate a new wave that forms between the initial discontinuity and the right section of the pipe.

As illustrated in Figure 4.9, the 4-equation model performs effectively without mass transfer. However, when the mass transfer is triggered, the results significantly deviate from the reference solutions, indicating discrepancies in the model's capacity to accurately reflect the physical processes under these conditions.

Case 4:

This experiment, also known as the Canon experiment, involves creating a 100% break in the system to rapidly depressurize a horizontal pipe, and it was designed by [Riegel \(1978\)](#). As shown in Figure 4.10, the pipe used in these experiments is 4.389 meters long with an internal diameter of 102.3 millimeters. One end of the pipe is sealed with a membrane, while the other end is closed.

At the initial time (time zero), the pipe is filled with under-saturated water. Upon rupture of the membrane, a rarefaction wave is initiated, propagating through the length of the pipe. In the Canon experiments, the void fraction is measured at a specific location, while pressure readings are taken at multiple points along the pipe.

For the Canon test case ($p_0, T_0 = 32 \text{ bar}, 220^\circ\text{C}$), the stiffened gas EoS parameters are given in Table 4.1. The computational domain is 10 meters, with a tank at atmospheric pressure on the right. The initial conditions are provided in Table 4.2.

Table 4.1: EoS parameters for liquid and vapor phases in the Canon experiment.

	Liquid	Vapor
γ	1.66	1.34
P_∞ (Pa)	769317123.86	0.00
q (J.kg ⁻¹)	-1359570.00	2032350.00
C_v (J.kg ⁻¹ .K ⁻¹)	2807.61	1162.00
q' (J.kg ⁻¹ .K ⁻¹)	11671.61	2351.11

The results, displayed after 0.08 s, are presented in Figures 4.11 through 4.13. Specifically, Figure 4.11 shows the evolution of the void ratio over time at the P_T location, while Figure 4.12, and Figure 4.13 show the pressure evolution over time at the P1 and P5 locations, respectively. For the simulation, different constant dP/dT values were evaluated,

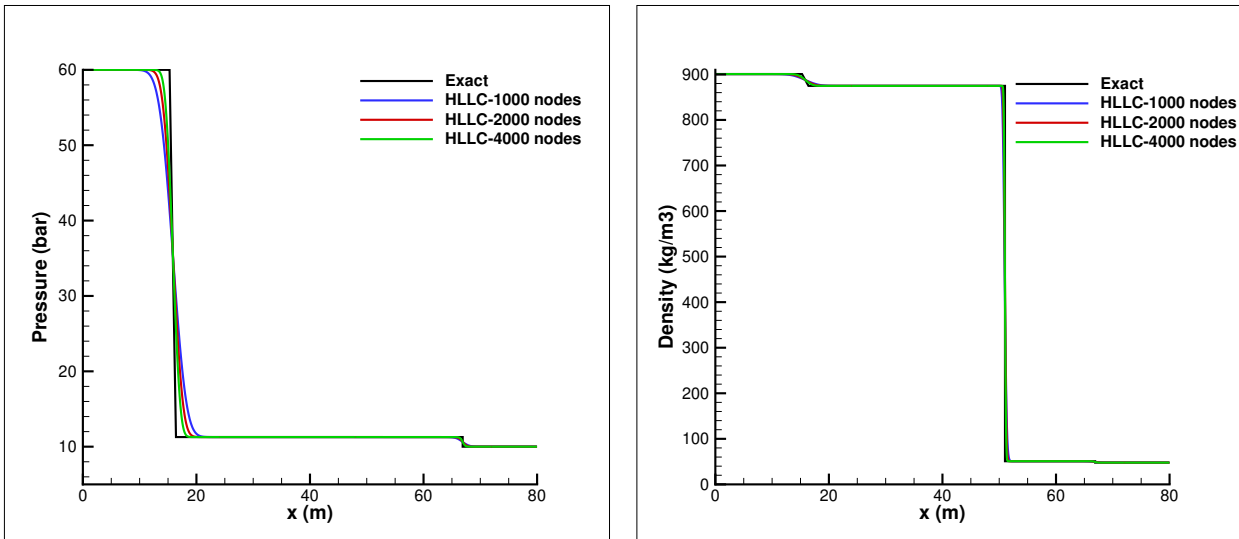


Figure 4.6: Results of CO_2 pipe depressurization for pressure, and density, case 3, at $t=0.08$ s, without mass transfer.

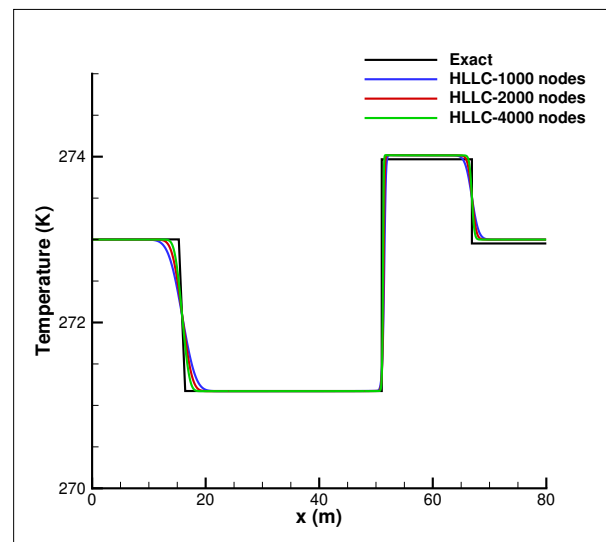


Figure 4.7: Results of CO_2 pipe depressurization for temperature, case 3, at $t=0.08$ s, without mass transfer.

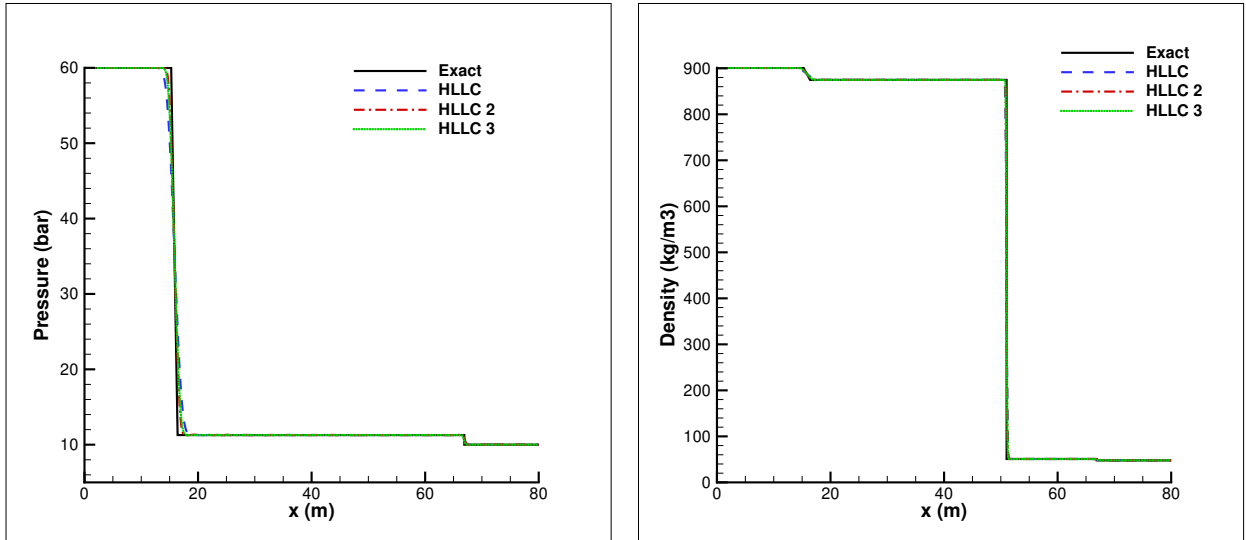


Figure 4.8: Results of CO_2 pipe depressurization for pressure, and density with high order scheme, case 3, at $t= 0.08$ s, without mass transfer.

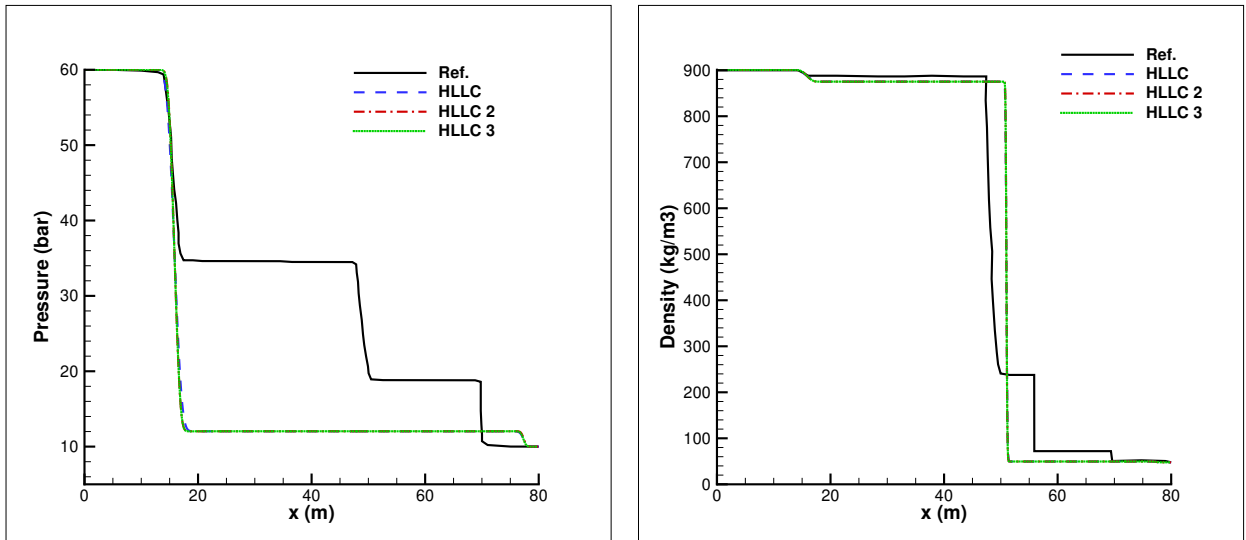


Figure 4.9: Results of CO_2 pipe depressurization for pressure, and density, case 3, at $t= 0.08$ s, with mass transfer.

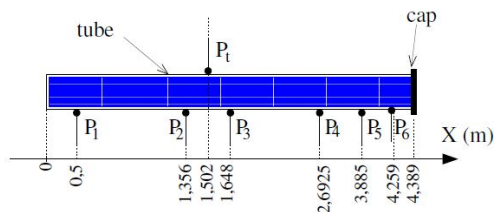


Figure 4.10: Schematic of experiment facility by Hurisse and Quibel (2022).

Table 4.2: Initial conditions for the Canon experiment.

	Pipe	Tank
α_l	$1 - 10^{-3}$	10^{-3}
α_v	10^{-3}	$1 - 10^{-3}$
ρ_l (kg.m ⁻³)	841.12	837.74
ρ_v (kg.m ⁻³)	16.72	0.52
P_l (bar)	32	1
P_v (bar)	32	1

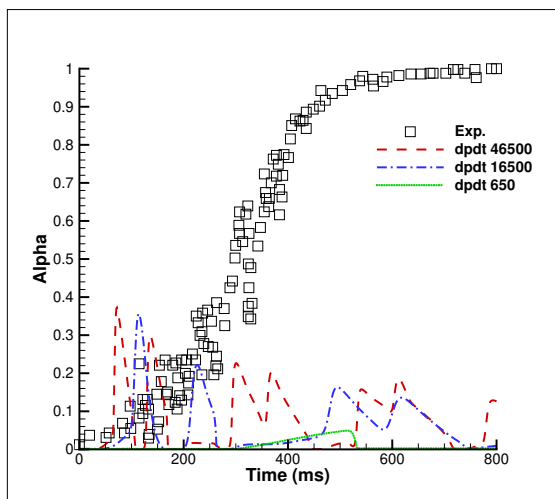
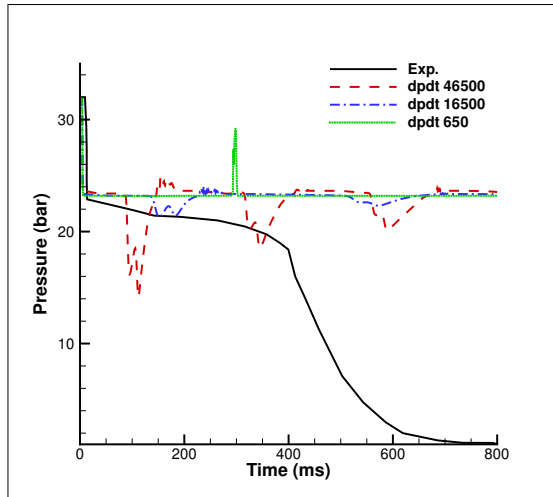
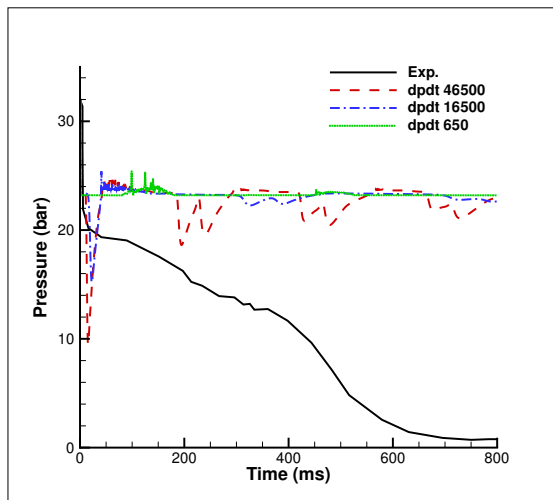


Figure 4.11: Void ratio vs time at P_T location, case 4, at $t=800$ ms.

specifically 46,500, 16,500, and 650 Pa/K, respectively. As illustrated in the figures below, the results obtained from the 4-equation model accurately predicted the initial pressure drop within the first few milliseconds for the Canon experiment. However, as the process continued, the simulation results diverged significantly from the experimental data (denoted as Exp.). To achieve more accurate results for CO_2 and this test case, a more complex model is required. For this reason, new models will be discussed in the next chapter.

4.5 Summary

This chapter introduced the NSMB solver, a tool for solving compressible and incompressible Navier-Stokes equations using structured multi-block grids. The solver utilizes various numerical schemes. The three-equation and four-equation models for two-phase flow modeling were discussed in detail. Numerical methods, including the HLLC Riemann solver and

Figure 4.12: Pressure vs time at P1 location, case 4, at $t=800$ ms.Figure 4.13: Pressure vs time at P5 location, case 4, at $t=800$ ms.

high-order extensions such as MUSCL and TVD limiters, were explored to enhance accuracy and stability in simulations involving shock waves and discontinuities. The chapter concluded with validation test cases, demonstrating the performance of the four-equation model. While the results showed good agreement with the reference solutions, particularly for the last two test cases, more complex methodologies are required. The findings from these simulations set the stage for exploring new models in the following chapter.

Chapter 5

Comparative Study: 4-Equation vs. 6-Equation Models

In this fifth chapter, a comparative study of the four-equation and six-equation models for simulating compressible two-phase flow is presented. These models were selected for comparison due to their balance between computational efficiency and physical accuracy. As simplified versions of the more comprehensive seven-equation model, they allow for faster numerical simulations while still capturing the essential features of two-phase flows. The chapter begins by presenting the mathematical formulation of both models. The six-equation model, a relaxed velocity equilibrium model, accounts for mechanical, thermal, and chemical non-equilibrium effects, while the four-equation model only considers chemical non-equilibrium between the phases. Although these models typically operate based on the principle of instantaneous relaxation, the final section demonstrates how non-instantaneous chemical relaxation is applied. In the last part of the chapter, both models are validated using a series of test cases to assess their strengths and weaknesses. In contrast to the previous chapter, the results in this chapter are obtained from the custom-built solver rather than the NSMB solver. The complexity and scale of NSMB would require extensive modifications to multiple subroutines, or the development of certain components from scratch to implement these models. Therefore, a custom-built solver was specifically developed for this study.

5.1 Governing Equations

Numerical modeling of compressible two-phase flow plays a crucial role across various engineering disciplines, including the design of submarine and naval vehicles, as well as in the aerospace and nuclear power sectors. Cavitation involves the study of fluids that exist in multiple phases and exhibit complex hydrodynamic and thermodynamic behaviors, such as the transition between liquid and vapor states, the dynamic generation of interfaces, the implosion of vapor formations, and the resultant shock waves and their interactions [Ishii and Hibiki \(2011\)](#). The literature presents a range of methods for simulating two-phase flow, ranging from complete models with seven-equations [Baer and Nunziato \(1986\)](#) to one-fluid homogeneous mixture model [Clerc \(2000\)](#). In this study, focus is placed on two distinct modeling approaches: the four-equation model [Saurel et al. \(2016\)](#), [Goncalves and Hoarau \(2022\)](#), and the single-velocity six-equation model [Pelanti and Shyue \(2014\)](#).

The six-equation model discussed in this study is a relaxed velocity equilibrium model derived from the seven-equation Baer–Nunziato model under the condition of instantaneous kinetic equilibrium [Pelanti \(2022\)](#). This model is comprised of an advection equation for the volume fraction of one phase, separate mass and total energy equations for each phase, and

a mixture momentum equation while mechanical, thermal, and chemical non-equilibrium effects are preserved in the six-equation model [Pelanti and Shyue \(2014\)](#). When instantaneous pressure relaxation is assumed, this model simplifies to the widely recognized compressible two-phase flow model developed by [Kapila et al.](#). The six-equation single-velocity compressible two-phase flow model with stiff mechanical relaxation, proposed by [Pelanti and Shyue \(2014\)](#) is formulated as follows:

$$\left\{ \begin{array}{l} \frac{\partial \alpha_1}{\partial t} + \vec{u} \cdot \nabla \alpha_1 = \mu(p_1 - p_2), \\ \frac{\partial(\alpha_1 \rho_1)}{\partial t} + \nabla \cdot (\alpha_1 \rho_1 \vec{u}) = 0, \\ \frac{\partial(\alpha_2 \rho_2)}{\partial t} + \nabla \cdot (\alpha_2 \rho_2 \vec{u}) = 0, \\ \frac{\partial(\rho \vec{u})}{\partial t} + \nabla \cdot (\rho \vec{u} \otimes \vec{u}) + \nabla(\alpha_1 p_1 + \alpha_2 p_2) = 0, \\ \frac{\partial(\alpha_1 E_1)}{\partial t} + \nabla \cdot (\alpha_1 (E_1 + p_1) \vec{u}) + \Sigma = -\mu p_{int}(p_1 - p_2), \\ \frac{\partial(\alpha_2 E_2)}{\partial t} + \nabla \cdot (\alpha_2 (E_2 + p_2) \vec{u}) - \Sigma = \mu p_{int}(p_1 - p_2). \end{array} \right. \quad (5.1)$$

The variable α_k represents the volume fraction of phase, and it is assumed that the saturation condition holds, i.e., $\alpha_1 + \alpha_2 = 1$. The term p_k denotes the phasic pressure, while ρ_k represents the phasic density, moreover, the phasic total energy, E_k , is defined as $E_k = \mathcal{E}_k + \frac{1}{2} \rho_k u^2$, where $\mathcal{E}_k = \rho_k \epsilon_k$ is the phasic internal energy, and ϵ_k is the phasic specific internal energy [Pelanti and Shyue \(2014\)](#). The μ defines the mechanical relaxation parameter.

The right-hand side represents the pressure relaxation process, where the interface pressure p_{int} and the acoustic impedance Z_k are defined as:

$$p_{int} = \frac{Z_2 p_1 + Z_1 p_2}{Z_1 + Z_2}, \quad \text{and} \quad Z_k = \rho_k c_k, \quad (5.2)$$

where c_k is the speed of sound in phase k . It is assumed that mechanical relaxation occurs instantaneously, implying that $\mu \rightarrow +\infty$.

The speed of sound associated with Equation 5.1, is given by:

$$c = \sqrt{Y_1 c_1^2 + Y_2 c_2^2}, \quad (5.3)$$

where c_k phasic speed of sound.

It should be emphasized that the single-velocity six-equation model proposed by [Pelanti and Shyue \(2014\)](#) is specifically designed to efficiently handle interfaces, cavitation, and evaporation waves while maintaining clarity and computational efficiency. The central concept of this method is the use of a different mathematical framework for the conventional six-equation model system by [Richard Saurel et al. \(2009\)](#), applied during the numerical discretization process. Unlike the traditional model, which employs two equations for phasic internal energy, this approach utilizes two equations for phasic total energy. Despite the fact that these models align mathematically, the proposed model provides significant numerical advantages. It facilitates the development of a straightforward numerical method that ensures essential consistency properties, particularly in terms of conserving total energy within the mixture and maintaining the mixture's thermodynamic state. Specifically, the model inherently recovers a conservative discrete form of the mixture total energy equation, thereby eliminating the need for an additional conservation law to correct the thermodynamic state, as outlined in the classical six-equation model [Pelanti and Shyue \(2014\)](#).

It is essential to emphasize that the single-velocity six-equation two-phase flow model, as introduced in Equation 5.1, includes a non-conservative advection equation for the phasic volume fraction α_1 and non-conservative terms within the phasic total energy equations, so the non-conservative terms in the phasic total energy equations are as follows [De Lorenzo et al. \(2021\)](#):

$$\Sigma = -\vec{u} \cdot [Y_2 \nabla(\alpha_1 p_1) - Y_1 \nabla(\alpha_2 p_2)] \quad (5.4)$$

where $Y_k = \alpha_k \rho_k / \rho$. It is crucial to highlight that combining the two non-conservative phasic total energy equations yields the equation that expresses the conservation of the mixture's total energy $E = \mathcal{E} + \frac{1}{2}u^2 = \alpha_1 E_1 + \alpha_2 E_2$ [Pelanti and Shyue \(2014\)](#). Unlike other models such as [Zein et al. \(2010\)](#), a conservative discrete form of the mixture total energy equation can be automatically recovered. The terms within Σ primarily represent energy exchange due to forces exerted between the phases [De Lorenzo et al. \(2018\)](#).

The model with heat and mass transfer can be written as follow:

$$\left\{ \begin{array}{l} \frac{\partial \alpha_1}{\partial t} + \vec{u} \cdot \nabla \alpha_1 = \mu(p_1 - p_2), \\ \frac{\partial(\alpha_1 \rho_1)}{\partial t} + \nabla \cdot (\alpha_1 \rho_1 \vec{u}) = \nu(g_2 - g_1), \\ \frac{\partial(\alpha_2 \rho_2)}{\partial t} + \nabla \cdot (\alpha_2 \rho_2 \vec{u}) = -\nu(g_2 - g_1), \\ \frac{\partial(\rho \vec{u})}{\partial t} + \nabla \cdot (\rho \vec{u} \otimes \vec{u}) + \nabla(\alpha_1 p_1 + \alpha_2 p_2) = 0, \\ \frac{\partial(\alpha_1 E_1)}{\partial t} + \nabla \cdot (\alpha_1 (E_1 + p_1) \vec{u}) + \Sigma = -\mu p_{int}(p_1 - p_2) + \theta(T_2 - T_1) + e_{int} \nu(g_2 - g_1), \\ \frac{\partial(\alpha_2 E_2)}{\partial t} + \nabla \cdot (\alpha_2 (E_2 + p_2) \vec{u}) - \Sigma = \mu p_{int}(p_1 - p_2) - \theta(T_2 - T_1) - e_{int} \nu(g_2 - g_1). \end{array} \right. \quad (5.5)$$

where T_k denotes the phasic temperature and g_k the phasic chemical potential, with θ and ν defining the thermal and chemical relaxation parameters, respectively. It is unnecessary to define e_{int} due to the way chemical relaxation is managed. To simplify the numerical procedure, it is possible to rewrite the Equation 5.5 in compact form:

$$\partial_t U + \nabla \cdot f(U) + \sigma(U, \nabla U) = S_\mu(U) + S_\theta(U) + S_\nu(U), \quad (5.6)$$

$$U = \begin{pmatrix} \alpha_1 \\ \alpha_1 \rho_1 \\ \alpha_2 \rho_2 \\ \rho \vec{u} \\ \alpha_1 E_1 \\ \alpha_2 E_2 \end{pmatrix}, \quad f(U) = \begin{pmatrix} 0 \\ \alpha_1 \rho_1 \vec{u} \\ \alpha_2 \rho_2 \vec{u} \\ \rho \vec{u} \otimes \vec{u} + (\alpha_1 p_1 + \alpha_2 p_2) \mathbf{I} \\ \alpha_1 (E_1 + p_1) \vec{u} \\ \alpha_2 (E_2 + p_2) \vec{u} \end{pmatrix}, \quad \sigma(U, \nabla U) = \begin{pmatrix} \vec{u} \cdot \nabla \alpha_1 \\ 0 \\ 0 \\ 0 \\ \Sigma \\ -\Sigma \end{pmatrix}, \quad (5.7)$$

$$S_\mu(U) = \begin{pmatrix} \mu(p_1 - p_2) \\ 0 \\ 0 \\ 0 \\ -\mu p_{int}(p_1 - p_2) \\ \mu p_{int}(p_1 - p_2) \end{pmatrix}, \quad S_\theta(U) = \begin{pmatrix} 0 \\ 0 \\ 0 \\ 0 \\ \theta(T_2 - T_1) \\ -\theta(T_2 - T_1) \end{pmatrix}, \quad S_\nu(U) = \begin{pmatrix} 0 \\ \nu(g_2 - g_1) \\ -\nu(g_2 - g_1) \\ 0 \\ \nu e_{int}(g_2 - g_1) \\ -\nu e_{int}(g_2 - g_1) \end{pmatrix}, \quad (5.8)$$

As a final remark, in the original paper by [Pelanti and Shyue \(2014\)](#), the phasic volume fraction equation includes an additional term, $\frac{\nu(g_2 - g_1)}{\rho_1}$, following the $\mu(p_1 - p_2)$ term. This

term was initially introduced to capture the effect of the mass transfer process on the progression of the volume fraction. However, further analysis by the author in [Pelanti \(2022\)](#) reveals that this term does not significantly affect the results under the conditions studied, as mass transfer effects are still accounted for through the pressure relaxation process. Consequently, the term is not included in the current model, as it is considered unnecessary for ensuring the model's accuracy (see [Pelanti \(2022\)](#) for details).

A four-equation model is employed to depict a two-phase flow in kinetic, mechanical, and thermal equilibrium. This model is derived from the seven-equation Baer-Nunziato two-phase model [Baer and Nunziato \(1986\)](#), under the conditions of velocity, pressure, and temperature equilibrium. It includes one mass equation for each phase, along with momentum and energy equations for the mixture. The four-equation model can be written in the following form:

$$\begin{cases} \frac{\partial(\alpha_1\rho_1)}{\partial t} + \nabla \cdot (\alpha_1\rho_1\vec{u}) = v(g_2 - g_1), \\ \frac{\partial(\alpha_2\rho_2)}{\partial t} + \nabla \cdot (\alpha_2\rho_2\vec{u}) = -v(g_2 - g_1), \\ \frac{\partial(\rho\vec{u})}{\partial t} + \nabla \cdot (\rho\vec{u} \otimes \vec{u}) + \nabla(p) = 0, \\ \frac{\partial E}{\partial t} + \nabla \cdot ((E + p)\vec{u}) = 0. \end{cases} \quad (5.9)$$

In this context, ρ_k represents the phasic density, while α_k ($\alpha_1 + \alpha_2 = 1$) denotes the volume fraction, for each respective phase. Additionally, ρ , u , P , and E ($E = \mathcal{E} + \frac{1}{2}\rho u^2$) denotes mixture velocity, density, pressure, and total energy respectively. The right-hand side depicts mass transfer, with g_l and g_v representing the chemical potentials of the gaseous and liquid phases.

A fundamental requirement for fully describing and closing a physical system is an equation of state that correlates temperature, pressure, internal energy, and density. A stiffened gas equation of state is selected for this purpose [Chiapolino et al. \(2017\)](#):

$$p_k(\mathcal{E}_k, \rho_k) = (\gamma_k - 1)(\mathcal{E}_k - \rho_k q_k) - \gamma_k p_{\infty, k}, \quad (5.10)$$

$$T_k(p_k, \rho_k) = \frac{p_k + p_{\infty, k}}{\rho_k c_{v, k} (\gamma_k - 1)}, \quad (5.11)$$

According to the aforementioned relationships, the specific enthalpy (h_k), the specific entropy (s_k), and Gibbs free energy (g_k), for each phase are determined [Chiapolino et al. \(2017\)](#):

$$h_k(p_k, T_k) = c_{p, k} T + q_k. \quad (5.12)$$

$$s_k(p_k, T_k) = c_{v, k} \ln \left(\frac{T_k^{\gamma_k}}{(p_k + p_{\infty, k})^{\gamma_k - 1}} \right) + q'_k, \quad (5.13)$$

$$g_k(p_k, T_k) = (\gamma_k c_{v, k} - q'_k) T_k - c_{v, k} T_k \ln \frac{T_k^{\gamma_k}}{(p_k + p_{\infty, k})^{\gamma_k - 1}} + q_k. \quad (5.14)$$

where $\gamma = \frac{c_p}{c_v}$ is the heat capacity ratio, with c_p and c_v representing the specific heat capacities at constant pressure and constant volume, respectively. P_∞ , q , and q' are defining parameters of the thermodynamic nature of the fluid. The speed of sound c_k is given by the following equation:

$$c_k = \sqrt{\frac{\gamma_k (P_k + P_{\infty, k})}{\rho_k}}. \quad (5.15)$$

Considering the four-equation model, the mixture pressure and temperature can be defined as (see for details [Saurel et al. \(2016\)](#)):

$$p = \frac{-a_1 + \sqrt{a_1^2 - 4a_0a_2}}{2a_2}, \quad (5.16)$$

$$T = (\epsilon - q^*) \left(\sum \frac{Y_k c_{vk} (p_k + \gamma_i p_{\infty,k})}{p_k + p_{\infty,k}} \right)^{-1}. \quad (5.17)$$

with

$$\epsilon_k(p_k, T_k) = \frac{(p_k + \gamma_k p_{\infty,k}) C_{v,k} T_k}{p_k + p_{\infty,k}} + q_k, \quad (5.18)$$

$$\epsilon = Y_1 \epsilon_1(T, p) + Y_2 \epsilon_2(T, p), \quad (5.19)$$

$$\begin{cases} a_2 = Y_1 c_{v,1} + Y_2 c_{v,2}, \\ a_1 = Y_1 c_{v,1} (p_{\infty,2} + \gamma_1 p_{\infty,1} - (\gamma_1 - 1)Q) + Y_2 c_{v,2} (p_{\infty,1} + \gamma_2 p_{\infty,2} - (\gamma_2 - 1)Q), \\ a_0 = -Q((\gamma_1 - 1)Y_1 c_{v,1} p_{\infty,2} + (\gamma_2 - 1)Y_2 c_{v,2} p_{\infty,1}) + p_{\infty,1} p_{\infty,2} (\gamma_1 Y_1 c_{v,1} + \gamma_2 Y_2 c_{v,2}). \end{cases} \quad (5.20)$$

where $q^* = Y_1 q_1 + Y_2 q_2$, and $Q = \rho(\epsilon - q^*)$.

5.2 Numerical solution method

Fractional step method is utilized to obtain the numerical solution of the aforementioned system as discussed by [Pelanti and Shyue \(2014\)](#). This method involves a cycle of solving the homogeneous hyperbolic system and addressing a system of ordinary differential equations incorporating pressure relaxation source terms [Strang \(1968\)](#). This can be summarized as:

$$U_i^{n+1} = L_{hyp}^{\Delta t} L_p^{\Delta t} U_i^n \quad (5.21)$$

where $L_{hyp}^{\Delta t}$ represents the hyperbolic operator, and $L_p^{\Delta t}$ represents the pressure relaxation part. The utilization of the hyperbolic operator to U_i^n yields an middle state, denoted as $\tilde{U}_i = L_{hyp}^{\Delta t} U_i^n$, which serves as the starting point for the pressure relaxation in the subsequent step. Consequently, the numerical scheme for the hyperbolic part can be written as:

$$\tilde{U}_i^{n+1} = U_i^n - \frac{\Delta t}{\Delta x} (\mathcal{A}^+ \Delta U_{i-1/2} + \mathcal{A}^- \Delta U_{i+1/2}) \quad (5.22)$$

where $\mathcal{A}^\pm \Delta U_{i\pm 1/2}$ are the so-called fluctuations at interfaces [Pelanti and Shyue \(2014\)](#). The fluctuations can be determined as:

$$\mathcal{A}^+ \Delta U_{i-1/2} = \sum_{m=1}^M s_{i-1/2}^{m+} \mathcal{W}_{i-1/2}^m \mathcal{A}^- \Delta U_{i+1/2} = \sum_{m=1}^M s_{i-1/2}^{m-} \mathcal{W}_{i-1/2}^m \quad (5.23)$$

where \mathcal{W}^m and s^m denoted the m th wave and associated speed respectively, of the approximate Riemann solution wave structure while $s^+ = \max(s, 0)$ and $s^- = \min(s, 0)$ [de Lorenzo \(2018\)](#).

Different methods for calculating the numerical flux are found in the current literature. In this study, the HLLC [Toro et al. \(1994\)](#) method has been chosen for evaluation. A challenge in developing an HLLC-type solver for the current model is associated with the non-conservative nature of the phasic energy equations, as there is a lack of a concept of a weak solution in the distributional framework for these equations [Abgrall and Karni \(2010\)](#),

Pelanti and Shyue (2014). However, it is important to highlight that to accurately establish the initial thermodynamic state for solving the homogeneous system, it is only necessary for the sum of the phasic total energies computed at the previous time level to satisfy the mixture energy consistency Pelanti and Shyue (2014). Disregarding the non-conservative terms in the phasic total energy equations, except for the first equation governing the advection of α_1 , leads to a conservative system Pelanti and Shyue (2019). In this context, the interfacial fluctuations can be defined as follows:

$$\mathcal{A}^+ \Delta U_{i-1/2} = F_i - F_{i-1/2}^{HLLC}, \mathcal{A}^- \Delta U_{i+1/2} = F_{i+1/2}^{HLLC} - F_i \quad (5.24)$$

As a result solver consist of three waves \mathcal{W}^i , moving at speeds de Lorenzo (2018):

$$s^1 = S_L, s^2 = S^*, s^3 = S_R \quad (5.25)$$

that separates four constant states U_L, U_L^*, U_R^*, U_R , where U_L^* and U_R^* represent the left and right states, respectively, to the middle wave. The middle wave speed can be defined as Toro (1997) :

$$S^* = \frac{P_R - P_L + \rho_L u_L (S_L - u_L) - \rho_R u_R (S_R - u_R)}{\rho_L (S_L - u_L) - \rho_R (S_R - u_R)} \quad (5.26)$$

with the wave speeds S_L and S_R Davis (1988):

$$S_L = \text{Min}(u_L - c_L, u_R - c_R) \quad S_R = \text{Max}(u_L + c_L, u_R + c_R)$$

At the interface of a cell, the numerical flux can be expressed as:

$$F_{i+1/2}^{HLLC} = \begin{cases} F_L, & \text{if } S_L > 0 \\ F_L^* = F_L + S_L(U_L^* - U_L), & \text{if } S_L \leq 0 < S_M \\ F_R^* = F_R + S_R(U_R^* - U_R), & \text{if } S_M \leq 0 \leq S_R \\ F_R, & \text{if } S_R < 0 \end{cases} \quad (5.27)$$

where,

$$U = \begin{bmatrix} \alpha_1 \\ \alpha_1 \rho_1 \\ \alpha_2 \rho_2 \\ \rho u \\ \alpha_1 \rho_1 E_1 \\ \alpha_2 \rho_2 E_2 \end{bmatrix} \quad U_k^* = \begin{bmatrix} \alpha_{1,k} \\ (\alpha_1 \rho_1)_k \frac{S_k - u_k}{S_k - S^*} \\ (\alpha_2 \rho_2)_k \frac{S_k - u_k}{S_k - S^*} \\ \rho_k \frac{S_k - u_k}{S_k - S^*} S^* \\ (\alpha_1 \rho_1)_k \frac{S_k - u_k}{S_k - S^*} \left(\frac{E_{1,k}}{\rho_{1,k}} + (S^* - u_k) \left(S^* + \frac{p_{1,k}}{\rho_{1,k} (S_k - u_k)} \right) \right) \\ (\alpha_2 \rho_2)_k \frac{S_k - u_k}{S_k - S^*} \left(\frac{E_{2,k}}{\rho_{2,k}} + (S^* - u_k) \left(S^* + \frac{p_{2,k}}{\rho_{2,k} (S_k - u_k)} \right) \right) \end{bmatrix}$$

with $k = l, r$.

In the context of the four-equation model, as detailed by Saurel et al. (2016), it is assumed that the central wave is a contact wave, with the velocity and pressure remaining constant across it:

$$\begin{cases} P_L^* = P_R^* = P^*, \\ u_L^* = u_R^* = u^* = S^*. \end{cases} \quad (5.28)$$

The Rankine-Hugoniot conditions for the partial density transport and momentum equations are expressed as follows:

$$\begin{aligned} S_K (\alpha_1 \rho_1)_k^* - (\alpha_1 \rho_1)_k S^* &= S_K (\alpha_1 \rho_1)_k - (\alpha_1 \rho_1)_k u_k, \\ S_K (\alpha_2 \rho_2)_k^* - (\alpha_2 \rho_2)_k S^* &= S_K (\alpha_2 \rho_2)_k - (\alpha_2 \rho_2)_k u_k, \\ S_K \rho_k^* S^* - \rho_k^* (S^*)^2 - P^* &= S_K \rho_k u_k - \rho_k u_k^2 - P_k, \end{aligned} \quad (5.29)$$

where k corresponds to L or R .

When summing these relations for partial densities, the following results are obtained:

$$\begin{aligned} S_K \rho_k^* - \rho_k^* S^* &= S_K \rho_k - \rho_k u_k, \\ S_K \rho_k^* S^* - \rho_k^* (S^*)^2 - P^* &= S_K \rho_k u_k - \rho_k u_k^2 - P_k, \end{aligned} \quad (5.30)$$

By combining these expressions, the relationship between the pressures is found:

$$P^* = P_k + \rho_k (u_k - S_K)(u_k - S^*), \quad (5.31)$$

By substituting the expression for P^* into the above equations, the central wave speed is obtained, as already provided in Equation 5.26:

$$S^* = u^* = \frac{P_R - P_L + \rho_L u_L (S_L - u_L) - \rho_R u_R (S_R - u_R)}{\rho_L (S_L - u_L) - \rho_R (S_R - u_R)}. \quad (5.32)$$

Finally, using the Rankine-Hugoniot jump conditions, the states on either side of the central wave can be fully determined based on the initial conditions on both sides.

$$\begin{cases} \rho_k^* = \rho_k \frac{u_k - S_k}{S^* - S_k}, \\ u_k^* = u^* = S^*, \\ \frac{E_k^*}{\rho_k^*} = \frac{E_k}{\rho_k} + \frac{P_k (u_k - S^*)}{\rho_k (u_k - S_k)} - S^* (u_k - S^*), \\ Y_k^* = Y_k, \end{cases} \quad (5.33)$$

These relations fully define the intercell set of variables U_K^* , thereby determining the flux $F(U_K^*)$ as follows:

$$F(U_K^*) = F_K + S_K (U_K^* - U_K). \quad (5.34)$$

5.3 Relaxation procedure

As highlighted in [Pelanti and Shyue \(2014\)](#), it is crucial to recognize that during any relaxation process, the following conditions are maintained:

$$\begin{cases} \partial_t \rho = 0, \\ \partial_t (\rho \vec{u}) = 0, \\ \partial_t E = 0. \end{cases} \quad (5.35)$$

As a result, the mixture's velocity, density, internal energy, and total energy remain invariant throughout the transfer:

$$\vec{u} = \text{unchanged}, \quad \rho = \text{unchanged}, \quad \mathcal{E} = \text{unchanged}, \quad E = \text{unchanged}.$$

Moreover, in the absence of chemical relaxation, the partial densities remain unchanged, as described by:

$$\partial_t (\alpha_k \rho_k) = 0, \quad k = 1, 2 : \quad (5.36)$$

$$\alpha_k \rho_k = \text{unchanged}$$

Throughout the relaxation process, it is considered that the characteristic time for mechanical relaxation is shorter than that for thermal and chemical relaxation [Pelanti and Shyue \(2019\)](#). Consequently, thermal and chemical relaxation are activated only after mechanical relaxation has been completed. It should be noted that quantities denoted by '0' are derived from the homogeneous system, those with a superscript '*' correspond to mechanical equilibrium, those with a superscript '**' indicate thermal equilibrium, and those with a superscript '***' represent chemical equilibrium.

5.3.1 Mechanical relaxation

After addressing the hyperbolic components of the system, the subsequent interactions between the fluids, represented by various source terms, are considered. The six-equation model, being a simplified computational approach derived from the five-equation system, necessitates that, for reasons of physical consistency, the process is instantaneous, such that $\mu \rightarrow \infty$. The governing system of equations is given by:

$$\begin{cases} \partial_t(\alpha_1) = \mu(p_1 - p_2), \\ \partial_t(\alpha_1\rho_1) = 0, \\ \partial_t(\alpha_2\rho_2) = 0, \\ \partial_t(\rho\vec{u}) = 0, \\ \partial_t(\alpha_1 E_1) = -\mu p_{int}(p_1 - p_2), \\ \partial_t(\alpha_2 E_2) = \mu p_{int}(p_1 - p_2). \end{cases} \quad (5.37)$$

By maintaining constant partial densities and mixture momentum during the mechanical relaxation process, it is possible to derive the following results:

$$\begin{aligned} \partial_t(\alpha_1 E_1) &= \partial_t(\alpha_1 \mathcal{E}_1) = -p_1 \partial_t \alpha_1, \\ \partial_t(\alpha_2 E_2) &= \partial_t(\alpha_2 \mathcal{E}_2) = p_1 \partial_t \alpha_1. \end{aligned}$$

By summing these equations, it can be observed that $\partial_t E = \partial_t \mathcal{E} = 0$, indicating that $E^0 = E^*$ and $\mathcal{E}^0 = \mathcal{E}^*$. This result implies that both the total energy and the total internal energy of the two-phase mixture remain unchanged as the phasic pressures relax towards the equilibrium value p^* [Pelanti and Shyue \(2014\)](#).

An estimation is introduced by presuming a linear variation of the interface pressure p_{int} with α_1 , as discussed by [Pelanti and Shyue \(2014\)](#):

$$p_{int} = p_1^0 + \frac{p_1^* - p_1^0}{\alpha_1^* - \alpha_1^0}(\alpha_1 - \alpha_1^0). \quad (5.38)$$

Under this assumption, the system can be readily integrated, yielding the following results:

$$(\alpha_1 E_1)^* - (\alpha_1 E_1)^0 = (\alpha_1 \mathcal{E}_1)^* - (\alpha_1 \mathcal{E}_1)^0 = -\frac{p_1^0 + p_1^*}{2}(\alpha_1^* - \alpha_1^0), \quad (5.39)$$

$$(\alpha_2 E_2)^* - (\alpha_2 E_2)^0 = (\alpha_2 \mathcal{E}_2)^* - (\alpha_2 \mathcal{E}_2)^0 = \frac{p_1^0 + p_1^*}{2}(\alpha_1^* - \alpha_1^0). \quad (5.40)$$

Applying the same methodology outlined in [Pelanti and Shyue \(2014\)](#), by imposing the condition $p_1^* = p_2^* = p_{int}^* = p^*$, and utilizing the stiffened gas EoS, the following quadratic equation can be derived:

$$a_2(p^*)^2 + a_1 p^* + a_0 = 0, \quad (5.41)$$

where the coefficients a_2 , a_1 , and a_0 are defined as:

$$\begin{cases} a_2 = 1 + \gamma_2 \alpha_1^0 + \gamma_1 \alpha_2^0, \\ a_1 = M_1 \alpha_2^0 + M_2 \alpha_1^0 - (1 + \gamma_2) \alpha_1^0 p_1^0 - (1 + \gamma_1) \alpha_2^0 p_2^0, \\ a_0 = -(M_2 \alpha_1^0 p_1^0 + M_1 \alpha_2^0 p_2^0), \\ M_1 = 2\gamma_1 P_{\infty,1} + (\gamma_1 - 1) p_{int}^0 \quad (\text{definition of } M_1), \\ M_2 = 2\gamma_2 P_{\infty,2} + (\gamma_2 - 1) p_{int}^0 \quad (\text{definition of } M_2). \end{cases} \quad (5.42)$$

The solution for p^* is:

$$p^* = \frac{-a_1 + \sqrt{(a_1)^2 - 4a_2 a_0}}{2a_2}, \quad (5.43)$$

The volume fraction α_1^* at equilibrium can then be determined as [Pelanti and Shyue \(2014\)](#):

$$\alpha_1^* = \frac{(\gamma_1 - 1)p^* + 2p_1^0 + M_1}{(\gamma_1 + 1)p^* + M_1} \alpha_1^0. \quad (5.44)$$

5.3.2 Thermal relaxation

Given that pressure relaxation proceeds more rapidly than temperature relaxation, it is assumed that temperature relaxation proceeds under the equilibrium pressure established during the pressure relaxation phase. The system to be solved is represented by the following equations in the limit as $\mu \rightarrow \infty$ and $\theta \rightarrow \infty$:

$$\begin{cases} \partial_t(\alpha_1) = \mu(p_1 - p_2), \\ \partial_t(\alpha_1 \rho_1) = 0, \\ \partial_t(\alpha_2 \rho_2) = 0, \\ \partial_t(\rho \vec{u}) = 0, \\ \partial_t(\alpha_1 E_1) = -\mu p_{int}(p_1 - p_2) + \theta(T_2 - T_1), \\ \partial_t(\alpha_2 E_2) = \mu p_{int}(p_1 - p_2) - \theta(T_2 - T_1). \end{cases} \quad (5.45)$$

As mentioned before the partial densities, mixture momentum, and both the mixture internal and total energy remain constant during the thermal relaxation [Pelanti and Shyue \(2014\)](#):

$$(\alpha_k \rho_k)^0 = (\alpha_k \rho_k)^{**}, \quad (\rho \vec{u})^0 = (\rho \vec{u})^{**}, \quad \mathcal{E}^0 = \mathcal{E}^{**}, \quad E^0 = E^{**}.$$

The mechanical and thermal equilibrium conditions imposed are:

$$p_1^{**} = p_2^{**} \equiv p^{**}, \quad T_1^{**} = T_2^{**} \equiv T^{**}.$$

Applying the same methodology outlined in [Pelanti and Shyue \(2014\)](#), and by considering the process as instantaneous, thus assuming equal pressures and temperatures, the stiffened gas law can be utilized to derive the following analytical solutions for pressure:

$$a'_2 (p^{**})^2 + a'_1 p^{**} + a'_0 = 0, \quad (5.46)$$

where the coefficients a'_2 , a'_1 , and a'_0 are defined as follows:

$$\left\{ \begin{array}{l} a'_2 = c_{v,1}(\alpha_1\rho_1)^0 + c_{v,2}(\alpha_2\rho_2)^0, \\ a'_1 = q_1c_{v,1}(\gamma_1 - 1) \left((\alpha_1\rho_1)^0 \right)^2 + q_2c_{v,2}(\gamma_2 - 1) \left((\alpha_2\rho_2)^0 \right)^2 \\ \quad + (\alpha_1\rho_1)^0 c_{v,1}(\gamma_1 p_{\infty,1} + p_{\infty,2}) + (\alpha_2\rho_2)^0 c_{v,2}(\gamma_2 p_{\infty,2} + p_{\infty,1}) \\ \quad + (\alpha_1\rho_1)^0 (\alpha_2\rho_2)^0 (q_1c_{v,2}(\gamma_2 - 1) + q_2c_{v,1}(\gamma_1 - 1)) \\ \quad - \mathcal{E}^0 \left(c_{v,1}(\gamma_1 - 1)(\alpha_1\rho_1)^0 + c_{v,2}(\gamma_2 - 1)(\alpha_2\rho_2)^0 \right), \\ a'_0 = q_1c_{v,1}(\gamma_1 - 1)p_{\infty,2} \left((\alpha_1\rho_1)^0 \right)^2 + q_2c_{v,2}(\gamma_2 - 1)p_{\infty,1} \left((\alpha_2\rho_2)^0 \right)^2 \\ \quad + p_{\infty,1}p_{\infty,2} \left((\alpha_1\rho_1)^0 c_{v,1}\gamma_1 + (\alpha_2\rho_2)^0 c_{v,2}\gamma_2 \right) \\ \quad + (\alpha_1\rho_1)^0 (\alpha_2\rho_2)^0 (q_1c_{v,2}(\gamma_2 - 1)p_{\infty,1} + q_2c_{v,1}(\gamma_1 - 1)p_{\infty,2}) \\ \quad - \mathcal{E}^0 \left(c_{v,1}(\gamma_1 - 1)p_{\infty,2}(\alpha_1\rho_1)^0 + c_{v,2}(\gamma_2 - 1)p_{\infty,1}(\alpha_2\rho_2)^0 \right), \\ p^{**} = \frac{-a'_1 + \sqrt{(a'_1)^2 - 4a'_2a'_0}}{2a'_2} \end{array} \right. \quad (5.47)$$

Upon determining p^{**} from the above equation, the equilibrium volume fraction α_1^{**} can be expressed as:

$$\alpha_1^{**} = \frac{c_{v,1}(\gamma_1 - 1)(p^{**} + p_{\infty,2})(\alpha_1\rho_1)^0}{c_{v,1}(\gamma_1 - 1)(p^{**} + p_{\infty,2})(\alpha_1\rho_1)^0 + c_{v,2}(\gamma_2 - 1)(p^{**} + p_{\infty,1})(\alpha_2\rho_2)^0}, \quad (5.48)$$

and the equilibrium temperature T^{**} is given by:

$$T^{**} = \frac{(p^{**} + p_{\infty,1})\alpha_1^{**}}{(\gamma_1 - 1)c_{v,1}(\alpha_1\rho_1)^0}. \quad (5.49)$$

Finally, thermal relaxation is only activated at specific locations, primarily at liquid-vapor interfaces, and is set to zero in all other regions:

$$\theta = \begin{cases} \infty & \text{if } \delta_I \leq \alpha_1 \leq 1 - \delta_I, \\ 0 & \text{otherwise,} \end{cases} \quad (5.50)$$

where the variable δ_I determines the positions of the liquid-vapor interface (such as $\delta_I = 10^{-5}$).

5.3.3 Chemical relaxation

Finally, the chemical transfers between the phases must be considered. Although the chemical relaxation procedure is explained here for the six-equation model, this technique is equally applicable to the four-equation model. The system to be solved is represented by the following equations in the limit as $\mu \rightarrow \infty$, $\theta \rightarrow \infty$, and $\nu \rightarrow \infty$:

$$\left\{ \begin{array}{l} \partial_t(\alpha_1) = \mu(p_1 - p_2), \\ \partial_t(\alpha_1\rho_1) = \nu(g_2 - g_1), \\ \partial_t(\alpha_2\rho_2) = -\nu(g_2 - g_1), \\ \partial_t(\rho\bar{u}) = 0, \\ \partial_t(\alpha_1 E_1) = -\mu p_{int}(p_1 - p_2) + \theta(T_2 - T_1) + \nu e_{int}(g_2 - g_1), \\ \partial_t(\alpha_2 E_2) = \mu p_{int}(p_1 - p_2) - \theta(T_2 - T_1) - \nu e_{int}(g_2 - g_1). \end{array} \right. \quad (5.51)$$

As mentioned before the mixture density, momentum, and both the mixture's internal and total energy remain constant during the chemical relaxation [Pelanti and Shyue \(2014\)](#):

$$(\rho)^0 = (\rho)^{***}, \quad (\rho\bar{u})^0 = (\rho\bar{u})^{***}, \quad \mathcal{E}^0 = \mathcal{E}^{***}, \quad E^0 = E^{***}.$$

The mechanical, thermal, and chemical equilibrium conditions imposed are:

$$p_1^{***} = p_2^{***} \equiv p^{***}, \quad T_1^{***} = T_2^{***} \equiv T^{***}, \quad g_1^{***} = g_2^{***} \equiv g^{***}.$$

Then, using the following relations:

$$\rho^0 = \alpha_1^{***} \rho_1^{***} + \alpha_2^{***} \rho_2^{***}, \quad (5.52)$$

$$\mathcal{E}^0 = \alpha_1^{***} \mathcal{E}_1^{***} + \alpha_2^{***} \mathcal{E}_2^{***}. \quad (5.53)$$

Applying the same methodology outlined in [Pelanti and Shyue \(2014\)](#), it is possible to obtain a quadratic equation:

$$a_2(p^{***})(T^{***})^2 + a_1(p^{***})T^{***} + a_0(p^{***}) = 0, \quad (5.54)$$

where the coefficients $a_2(p^{***})$, $a_1(p^{***})$, and $a_0(p^{***})$ are defined as follows:

$$\left\{ \begin{array}{l} a_2(p^{***}) = \rho^0 c_{v,1} c_{v,2} [(\gamma_2 - 1)(p^{***} + \gamma_1 p_{\infty,1}) - (\gamma_1 - 1)(p^{***} + \gamma_2 p_{\infty,2})], \\ a_1(p^{***}) = \mathcal{E}^0 [(\gamma_1 - 1)c_{v,1}(p^{***} + p_{\infty,2}) - (\gamma_2 - 1)c_{v,2}(p^{***} + p_{\infty,1})] \\ \quad + \rho^0 [(\gamma_2 - 1)c_{v,2} q_1 (p^{***} + p_{\infty,1}) - (\gamma_1 - 1)c_{v,1} q_2 (p^{***} + p_{\infty,2})] \\ \quad + c_{v,2}(p^{***} + p_{\infty,1})(p^{***} + \gamma_2 p_{\infty,2}) - c_{v,1}(p^{***} + p_{\infty,2})(p^{***} + \gamma_1 p_{\infty,1}), \\ a_0(p^{***}) = (q_2 - q_1)(p^{***} + p_{\infty,1})(p^{***} + p_{\infty,2}). \end{array} \right. \quad (5.55)$$

Given that the equilibrium temperature as a function of pressure is represented by a quadratic equation, there are two unknowns in the problem. To solve this, the equilibrium condition for Gibbs free energy must be defined. The theoretical pressure-temperature saturation curve for liquid and vapor phases is established by satisfying the Gibbs free energy equilibrium condition, where the Gibbs free energies of the two phases, g_1 and g_2 , are set equal. Using the stiffened gas equation of state, the pressure-temperature saturation curve is characterized by the following equation [Le Métayer et al. \(2004\)](#):

$$A_s + \frac{B_s}{T} + C_s \ln T + D_s \ln(p + p_{\infty,1}) - \ln(p + p_{\infty,2}) = 0 \quad (5.56)$$

with

$$\left\{ \begin{array}{l} A_s = \frac{c_{p,1} - c_{p,2} + q_2' - q_1'}{c_{p,2} - c_{v,2}} \\ B_s = \frac{q_2 - q_1}{c_{p,2} - c_{v,2}} \\ C_s = \frac{c_{p,2} - c_{p,1}}{c_{p,2} - c_{v,2}}, \\ D_s = \frac{c_{p,1} - c_{v,1}}{c_{p,2} - c_{v,2}}. \end{array} \right. \quad (5.57)$$

This non-linear equation (Equation 5.56) can be effectively addressed using the Newton-Raphson method, particularly applied to pressure. Once the pressure is determined, the equilibrium temperature, volume fraction, and equilibrium densities are then calculated as follows:

$$T^{***}(p^{***}) = \frac{-a_1(p^{***}) + \sqrt{a_1(p^{***})^2 - 4a_0(p^{***})a_2(p^{***})}}{2a_2(p^{***})} \quad (5.58)$$

$$\alpha_1^{***} = \frac{\rho^0 - \rho_2^{***}}{\rho_1^{***} - \rho_2^{***}} \quad (5.59)$$

$$\rho_k^{***} = \frac{p^{***} + p_{\infty,k}}{(\gamma_k - 1)c_{v,k}T^{***}} \quad (5.60)$$

It is important to highlight that the equilibrium solution derived from Equation 5.52 and Equation 5.53 with equilibrium conditions might not always meet the criteria for being physically admissible. In such cases, the mixture is assumed to be primarily composed of the species with the largest entropy, denoted by m the value $\alpha_m^{***} = 1 - \beta$ is fixed, where β can be assigned a small value, such as 10^{-8} . Using this assumption, the system of equations for the unknowns p^{***} , T^{***} , and ρ_k^{***} is constructed based on conservation laws (Equation 5.52 & Equation 5.53) and equilibrium conditions for pressure and temperature. For the stiffened gas equation of state, this reduces to a single quadratic equation for p^{***} again. The physically admissible root is selected for the new quadratic equation as the one that maximizes the total entropy (see for details [Pelanti and Shyue \(2014\)](#), [Faccanoni et al. \(2012\)](#)).

Similar to the thermal relaxation process, thermo-chemical transfer processes are activated at liquid-vapor interfaces under metastable thermodynamic conditions, specifically when the liquid temperature T_{liq} exceeds the saturation temperature T_{sat} at the given pressure [Pelanti and Shyue \(2014\)](#).

$$\nu = \begin{cases} \infty & \text{if } \delta_I \leq \alpha_1 \leq 1 - \delta_I \text{ and } T_{\text{liq}} > T_{\text{sat}}, \\ 0 & \text{otherwise.} \end{cases} \quad (5.61)$$

As described in [De Lorenzo et al. \(2017a\)](#), chemical relaxation, which is characterized by an infinite rate, can be modeled by the evolution of the vapor mass fraction using the following differential equation:

$$\frac{DY_{\text{vap}}}{Dt} = -\frac{Y_{\text{vap}} - Y_{\text{vap}}^{***}}{\Theta}, \quad (5.62)$$

$$Y_{\text{vap}}^{n+1} = Y_{\text{vap}}^{***} - (Y_{\text{vap}}^{***} - Y_{\text{vap}}^n) \exp^{-\Delta t / \Theta}. \quad (5.63)$$

where Y_{vap}^{***} represents the equilibrium vapor mass fraction obtained through chemical relaxation, Y_{vap}^n denotes the vapor mass fraction obtained from the homogeneous system, while Θ_t refers to the relaxation time provided by established literature relations. During transient events such as rapid depressurization, the formation of metastable states, caused by the delayed onset of vaporization, can only be accurately described by models incorporating non-instantaneous mass transfer. As we will observe later in this chapter, particularly in Case 3 with the second experimental result, this approach provides a more accurate representation of the physical process.

In the following sections, numerous test cases are carried out. The solution was performed using a custom-built solver, with a minmod limiter applied for the high-order scheme.

5.4 Validation test cases

In this section, we validate the custom-built solver using a series of distinct test cases. The validation begins with the CO_2 depressurization test case, previously analyzed in Chapter 4 as an academic benchmark. Following this, two test cases directly related to PWR LOCA applications—the Canon experiment, also analyzed in Chapter 4, and the Super-Canon experiment—are simulated to further evaluate the solver's capability to accurately simulate various physical scenarios and ensure its reliability for the comparative study conducted in this work.

Case 1:

This test scenario, previously analyzed in Chapter 4 as Case 3 and introduced by [Lund and Aursand \(2012\)](#), examines the depressurization process within a pipe containing CO₂. The pipe has a total length of 80 meters, with an initial discontinuity positioned at 50 meters. The initial conditions are as follows: on the left side, the pressure P_L is 60 bar, the temperature T_L is 273 K, and the volume fraction α_L is 1×10^{-5} ; on the right side, the pressure P_R is 10 bar, the temperature T_R is 273 K, and the volume fraction α_R is $1 - \alpha_L$. The fluids are modeled using a stiffened gas equation of state, with parameters provided in Table 5.1 [Bacigaluppi et al. \(2021\)](#).

Table 5.1: EoS parameters for liquid and vapor phases in the shock CO₂ test.

	Liquid	Vapor
γ	1.23	1.06
P_∞ (Pa)	1.32×10^8	8.86×10^5
q (J.kg ⁻¹)	-6.23×10^5	-3.01×10^5
q' (J.kg ⁻¹ .K ⁻¹)	-5.34×10^3	-1.03×10^4
C_v (J.kg ⁻¹ .K ⁻¹)	2.44×10^3	2.41×10^3

The results, displayed after 0.08 s, are presented in Figures 5.1 through 5.8. Figure 5.1 presents a comparative study of pressure (left) and temperature (right) profiles using the 6-equation, both solved with the HLLC scheme across varying grid resolutions of 1000, 2000, 4000, and 5000 nodes. Similarly, Figure 5.2 illustrates the comparative analysis for density (left) and velocity (right) profiles using the 4-equation under the same conditions. Figures 5.3 and 5.4 show the final results for pressure, temperature, density, and velocity profiles, obtained using the finest grid resolution of 5000 nodes, comparing the 4-equation and 6-equation models against the exact solution. As demonstrated in Figure 5.3 and Figure 5.4, the results obtained from the solver show good agreement with the reference data. Thus far, all results have been calculated under a scenario without mass transfer. In this first scenario, the density profile consists of three distinct waves: an expansion wave on the left, a shock wave on the right, and an initial contact discontinuity at $x = 50$. As expected, the results of the four-equation and six-equation two-phase models converge to the same solution. Notably, the four-equation model reduces the computational cost by approximately 46% compared to the six-equation model. Specifically, the computation time for the six-equation model is 235 seconds, whereas it is 127 seconds for the four-equation model. Subsequently, all simulations were conducted according to the mass transfer scenario. Figure 5.5 presents a comparative study of pressure (left) and temperature (right) profiles using the 6-equation, both solved with the HLLC scheme across varying grid resolutions of 1000, 2000, 4000, and 5000 nodes. Similarly, Figure 5.6 illustrates the comparative analysis for density (left) and velocity (right) profiles using the 4-equation under the same conditions. Figures 5.7 and 5.8 show the final results for pressure, temperature, density, and velocity profiles, obtained using the finest grid resolution of 5000 nodes, comparing the 6-equation and 4-equation models with second and third-order HLLC (via minmod limiter) against the reference solution [Lund and Aursand \(2012\)](#). In the second scenario with mass transfer, we observe that thermochemical transfer is activated at liquid-vapor interfaces within metastable thermodynamic conditions ($T_{liq} > T_{sat}$). The temperature variation caused by the liquid-to-vapor transition generates a new wave between the initial discontinuity and the right section of the pipe. As demonstrated in Figure 5.7 and Figure 5.8, the results obtained from the solver show good agreement with the reference data, contrasting with the

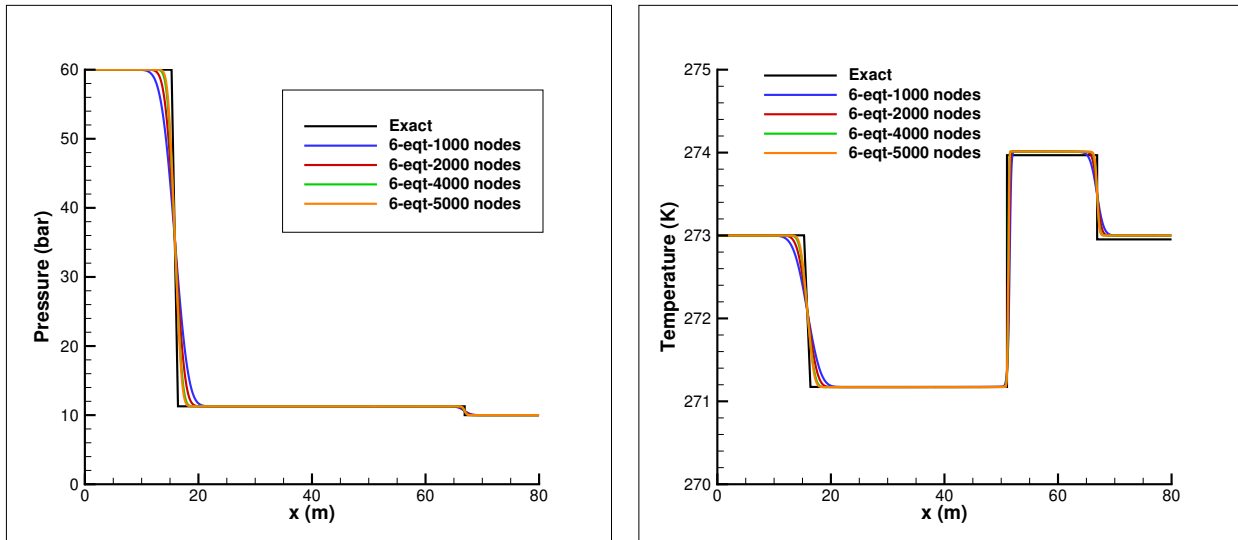


Figure 5.1: Comparison of convergence studies for CO_2 pipe depressurization using 6-equation model: pressure (left) and temperature (right) profiles, using the HLLC scheme with 1000, 2000, 4000, and 5000 nodes, case 1, at $t = 0.08$ s, without mass transfer.

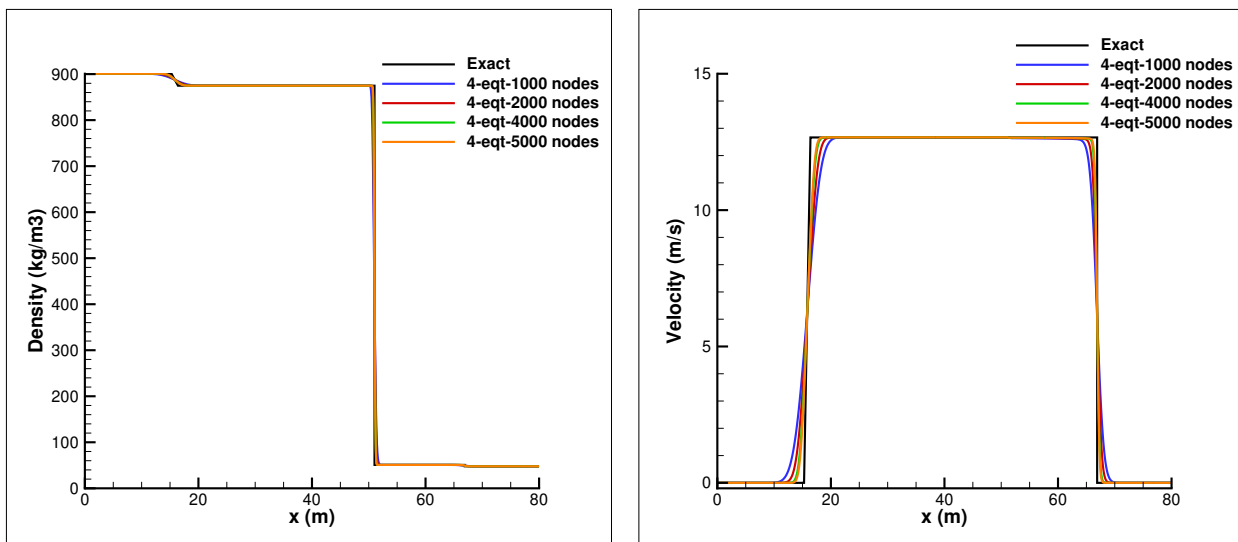


Figure 5.2: Comparison of convergence studies for CO_2 pipe depressurization using 4-equation model: density (left) and velocity (right) profiles, using the HLLC scheme with 1000, 2000, 4000, and 5000 nodes, case 1, at $t = 0.08$ s, without mass transfer.

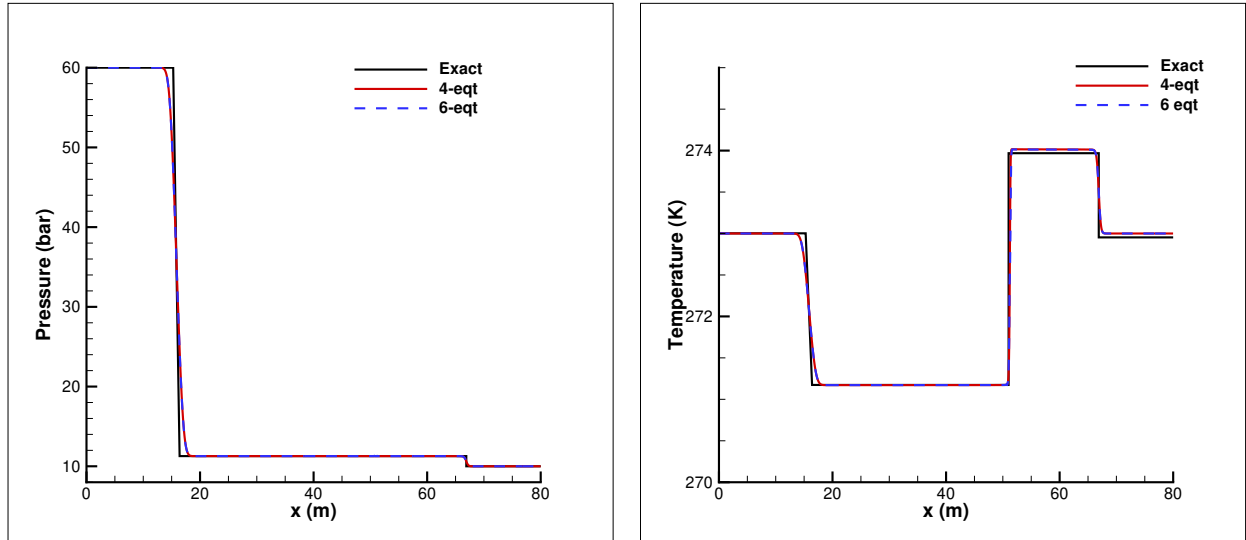


Figure 5.3: Results of CO₂ pipe depressurization using the 6-equation model (blue dashed) and 4-equation model (red solid): pressure (left) and temperature (right) profiles, case 1, at $t = 0.08$ s, without mass transfer. CPU time: 235 s (6-equation) vs 127 s (4-equation)

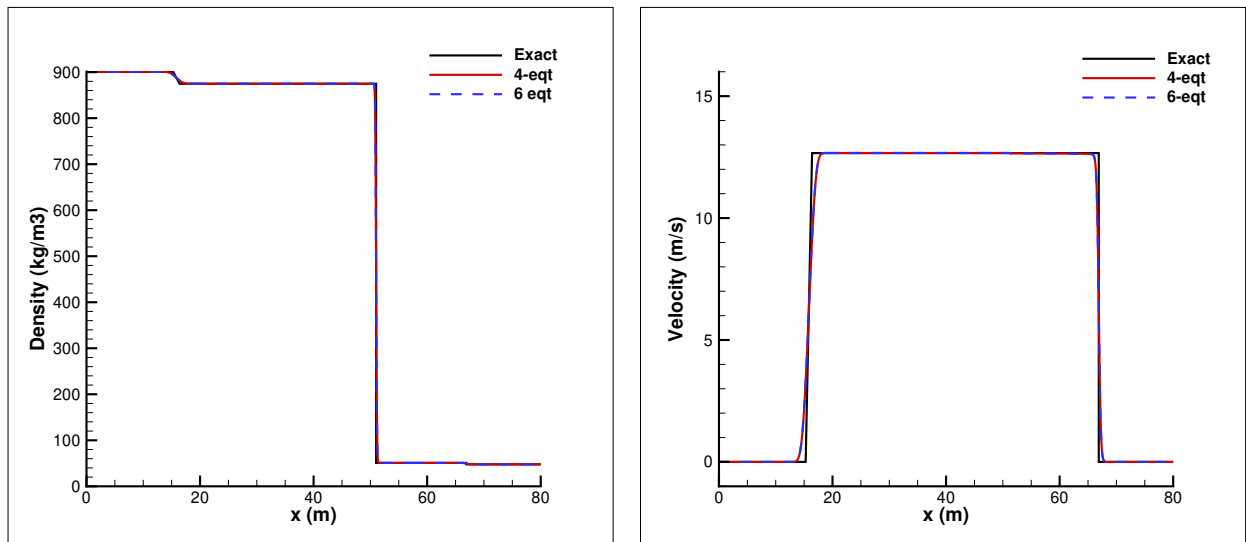


Figure 5.4: Results of CO₂ pipe depressurization using the 6-equation model (blue dashed) and 4-equation model (red solid): density (left) and velocity (right) profiles, case 1, at $t = 0.08$ s, without mass transfer.

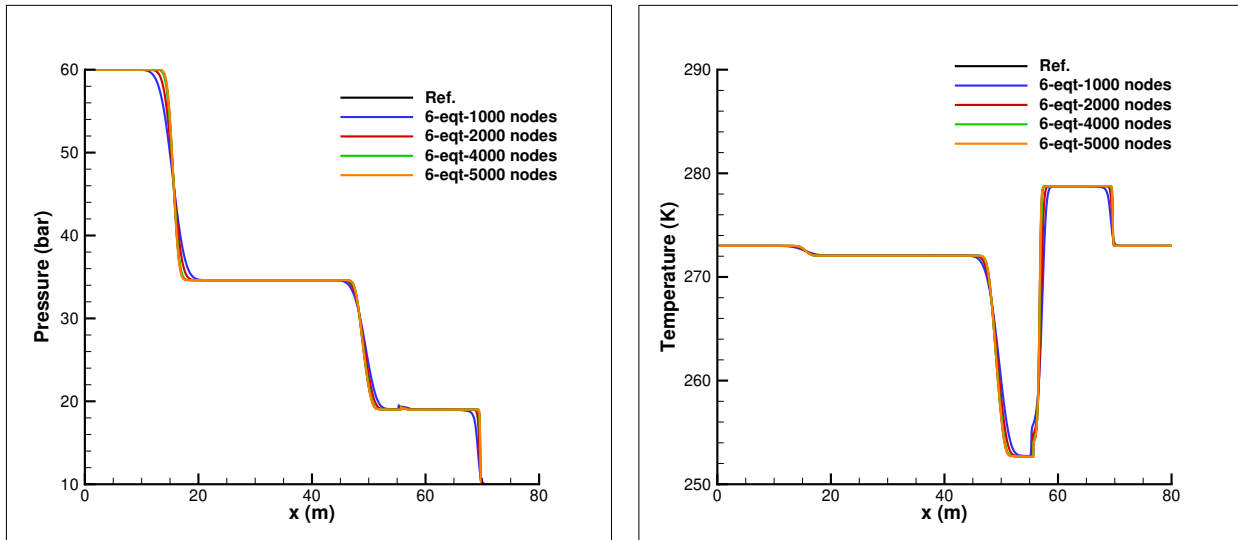


Figure 5.5: Comparison of convergence studies for CO_2 pipe depressurization using 6-equation model: pressure (left) and temperature (right) profiles, using the HLLC scheme with 1000, 2000, 4000, and 5000 nodes, case 1, at $t = 0.08$ s, with mass transfer.

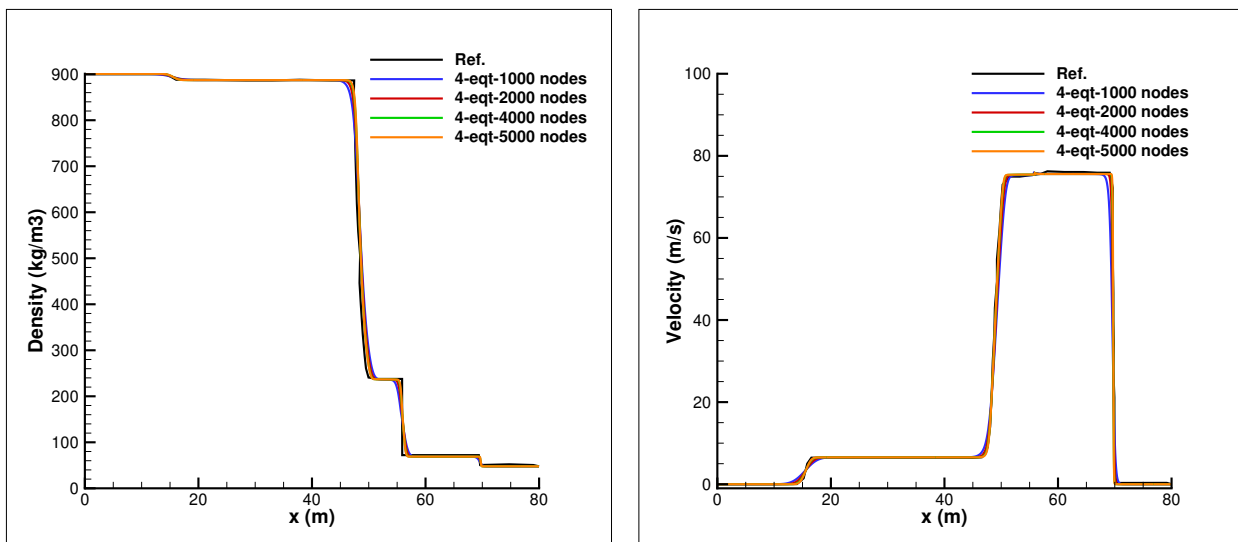


Figure 5.6: Comparison of convergence studies for CO_2 pipe depressurization using 4-equation model: density (left) and velocity (right) profiles, using the HLLC scheme with 1000, 2000, 4000, and 5000 nodes, case 1, at $t = 0.08$ s, with mass transfer.

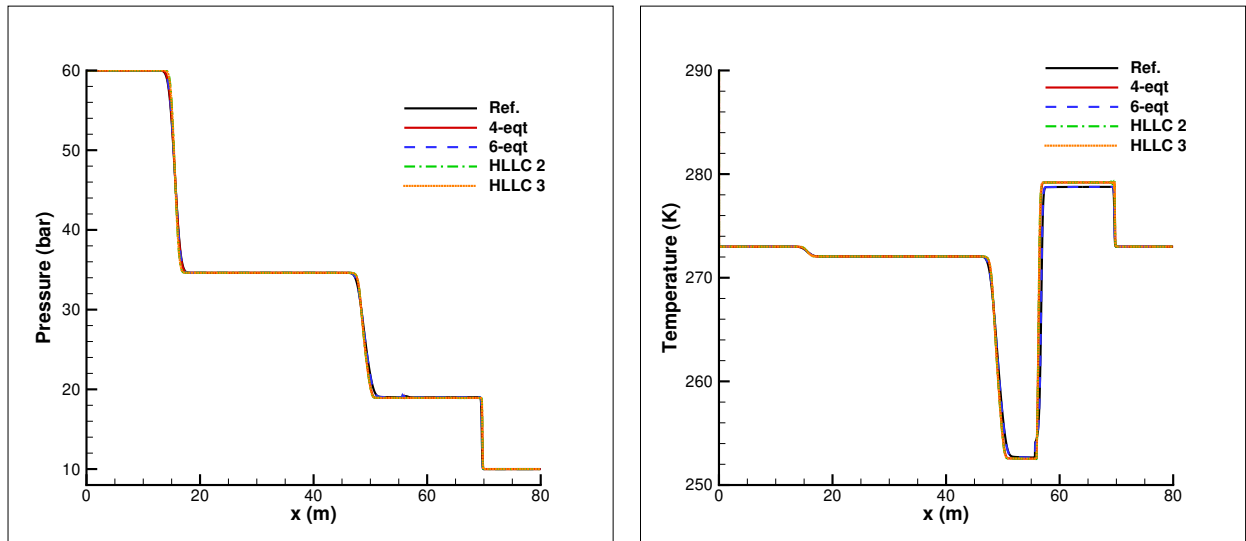


Figure 5.7: Results of CO₂ pipe depressurization using the 6-equation model (blue dashed) and 4-equation model (red solid), along with HLLC second-order (green dash-dot) and third-order (orange dotted) results: pressure (left) and temperature (right) profiles, case 1, at $t = 0.08$ s, with mass transfer. CPU times: 265 s (6-equation), 141 s (4-equation), 149 s (HLLC 2), and 168 s (HLLC 3).

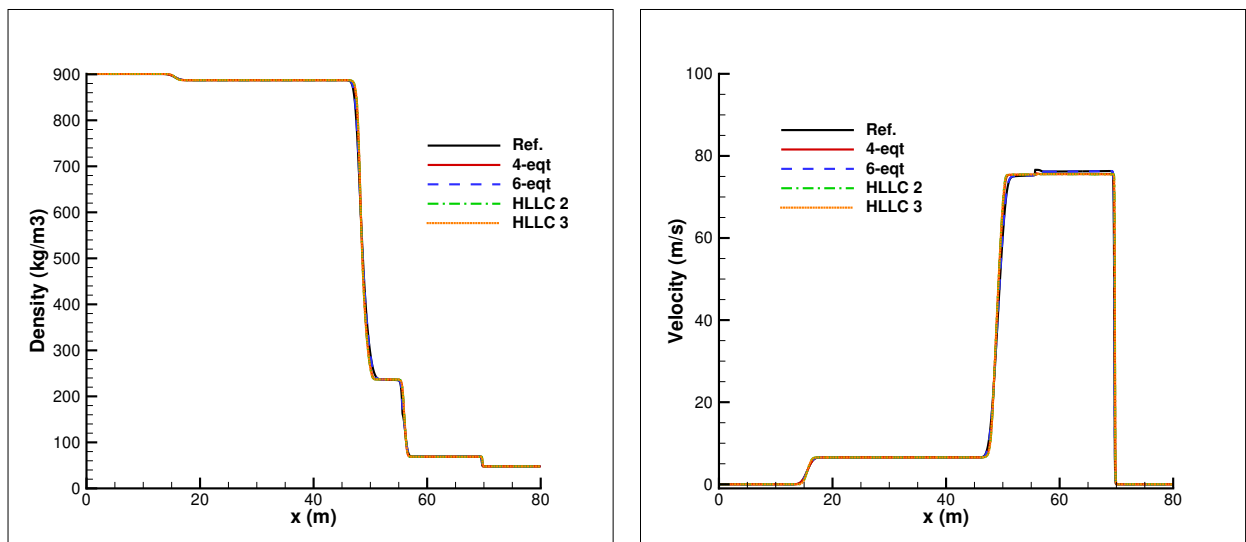


Figure 5.8: Results of CO₂ pipe depressurization using the 6-equation model (blue dashed) and 4-equation model (red solid), along with HLLC second-order (green dash-dot) and third-order (orange dotted) results: density (left) and velocity (right) profiles, case 1, at $t = 0.08$ s, with mass transfer.

results from Chapter 4 (see Figure 4.9).

Case 2:

The test case, previously analyzed in Chapter 4 as Case 4, is known as the Canon experiment and was originally proposed by Riegel (1978). This experimental setup involves initiating a complete system breach to quickly depressurize a horizontal pipe. As illustrated in Figure 4.10, the pipe utilized in this study measures 4.389 meters in length with an internal diameter of 102.3 millimeters. One end of the pipe is sealed with a membrane, while the opposite end is closed. At the beginning of the experiment, the pipe is filled with subcooled water. Upon the rupture of the membrane, a rarefaction wave travels through the entire length of the pipe.

In the Canon experiment, the void fraction is measured at a single point P_T while the pressure is measured at various locations within the pipe from P_1 to P_6 .

For the experiment, the initial pressure and temperature of the pipe were set to 32 bar and 220°C, while the pressure and temperature of the experimental environment were 1 bar and ambient temperature. However, in the numerical simulation, since we are performing two-phase flow calculations, the environment was filled with steam at 1 bar and 220°C instead of air. The numerical simulations were conducted using a 1D simplified geometry, with one side closed and the other connected to an atmospheric pressure tank. The stiffened gas equation of state and initial conditions are detailed in Table 4.1 and Table 4.2.

The results, displayed after 800 ms, are presented in Figures 5.9 through 5.20. Figures 5.9 to 5.14 present a convergence study conducted for both the 6-equation and 4-equation models. Specifically, Figure 5.9 illustrates the convergence analysis for the void fraction using 500, 1000, and 1500 nodes, with the left side showing results for the 6-equation model and the right side for the 4-equation model. Similarly, Figure 5.10 provides the convergence results for pressure at location P1, while Figures 5.11, 5.12, 5.13, and 5.14 present the results for locations P2, P3, P4, and P5, respectively. Figure 5.15 presents the results for the void ratio at the P_T location, obtained from different models. These models include the six-equation model and the four-equation model. Additionally, non-instantaneous chemical relaxation is implemented in two different formulations, as described by Equations 5.62 and 5.63, and are denoted as 4-eqt-D1 (Equations 5.64) and 4-eqt-D2 (Equations 5.65) in the legend. The relaxation times for these formulations are derived using the following approach Downar-Zapolski et al. (1996), Lochon (2016):

$$\begin{cases} \Theta = \Theta_0 \alpha_v^{-0.257} \left[\frac{P_s(T_{in}) - P}{P_s(T_{in})} \right]^{-2.24} \\ \Theta_0 = 6.51 \times 10^{-7} \end{cases} \quad (5.64)$$

$$\begin{cases} \Theta = \Theta_0 \alpha_v^{-0.54} \left[\frac{P_s(T_{in}) - P}{P_{crit} - P_s(T_{in})} \right]^{-1.76} \\ \Theta_0 = 3.84 \times 10^{-7} \end{cases} \quad (5.65)$$

where $P_s(T_{in})$ saturation pressure corresponding to the initial temperature, and P_{crit} is the critical pressure (22.064 MPa). Finally, the results obtained from the numerical solver were compared with the results in the literature Lepareux (1994). Due to the significant differences between the initial numerical results and the experimental data, results from the literature were included to provide a more meaningful comparison and enhance the assessment of the solver's performance. The mentioned comparisons were conducted also for both the P1 and P5 locations, as presented in Figures 5.16 and Figures 5.20, respectively.

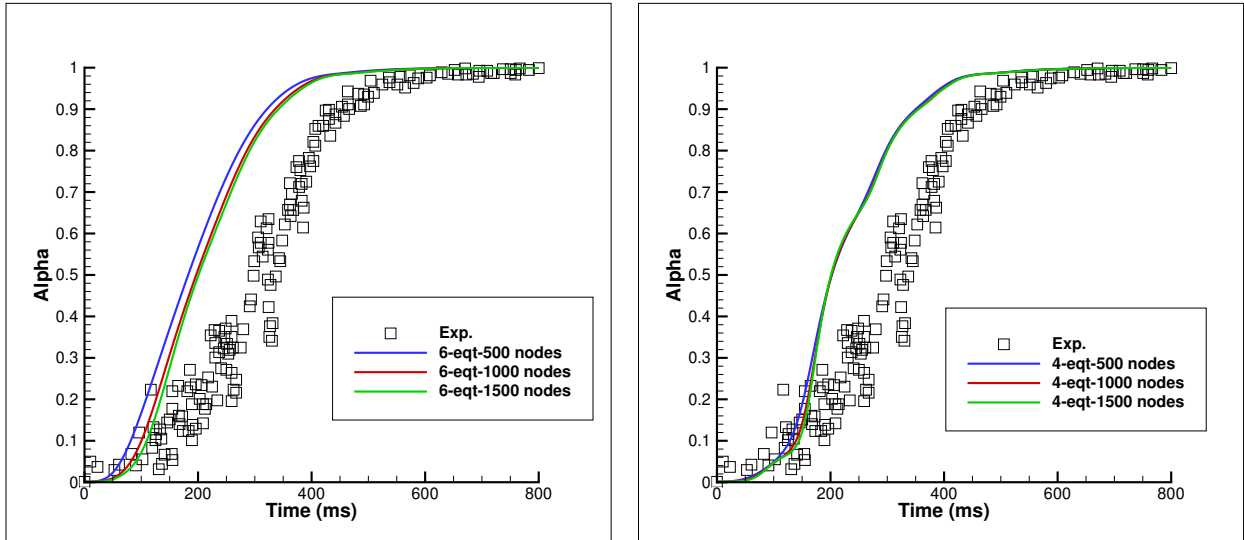


Figure 5.9: Comparison of convergence studies for void ratio at PT location (2.887 m upstream from the breach): 6-equation model (left) and 4-equation model (right), using the HLLC scheme with 500, 1000, and 1500 nodes, case 2.

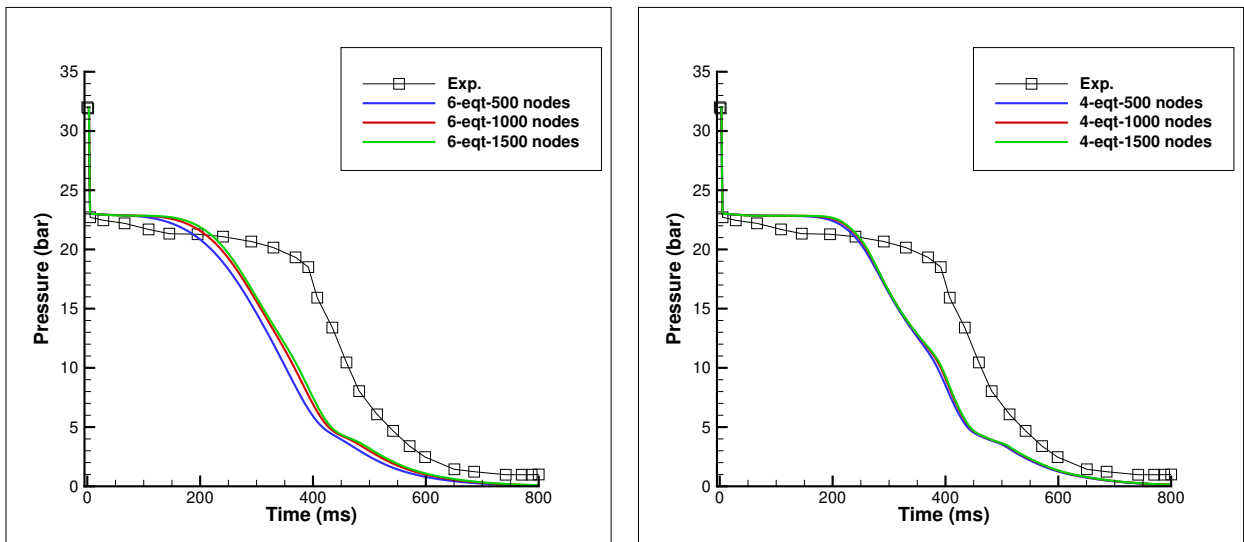


Figure 5.10: Comparison of convergence studies for pressure at P1 location (3.899 m upstream from the breach): 6-equation model (left) and 4-equation model (right), using the HLLC scheme with 500, 1000, and 1500 nodes, case 2.

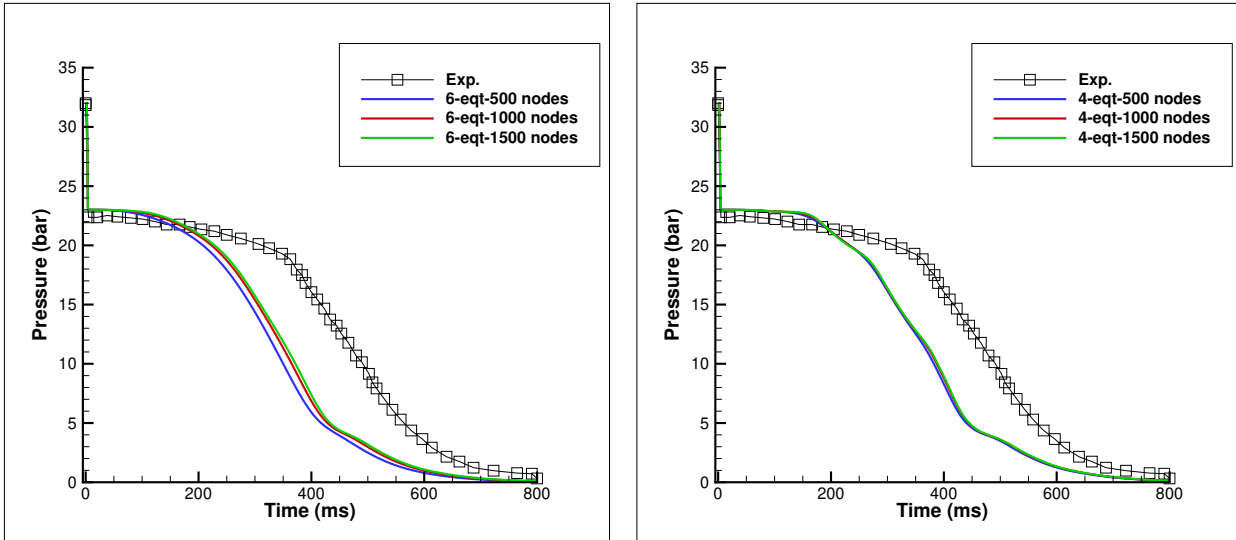


Figure 5.11: Comparison of convergence studies for pressure at P2 location (3.033 m upstream from the breach): 6-equation model (left) and 4-equation model (right), using the HLLC scheme with 500, 1000, and 1500 nodes, case 2.

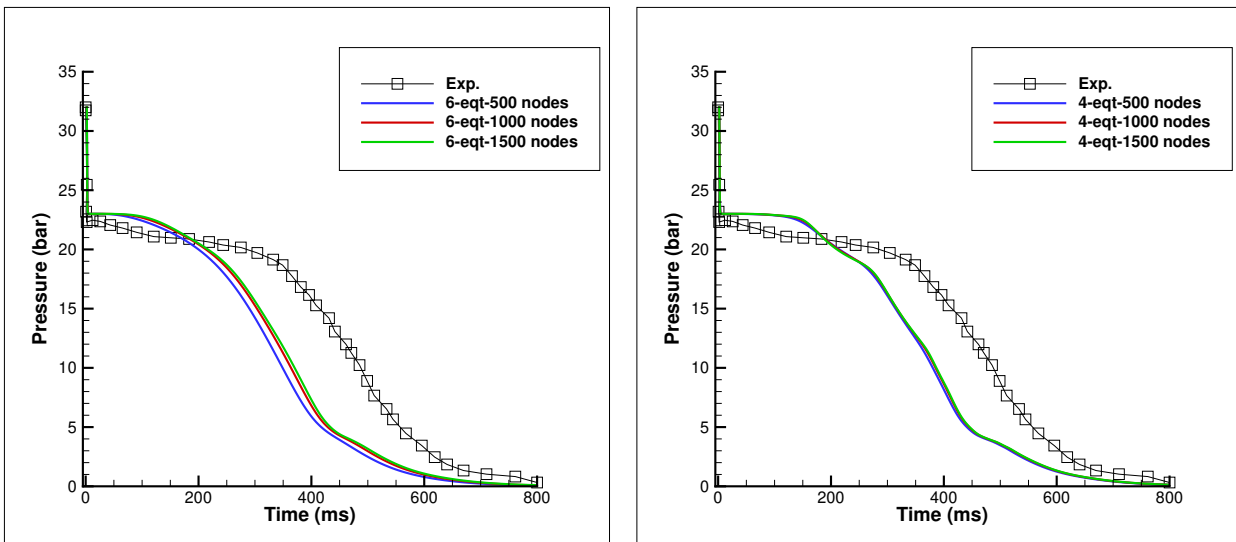


Figure 5.12: Comparison of convergence studies for pressure at P3 location (2.471 m upstream from the breach): 6-equation model (left) and 4-equation model (right), using the HLLC scheme with 500, 1000, and 1500 nodes, case 2.

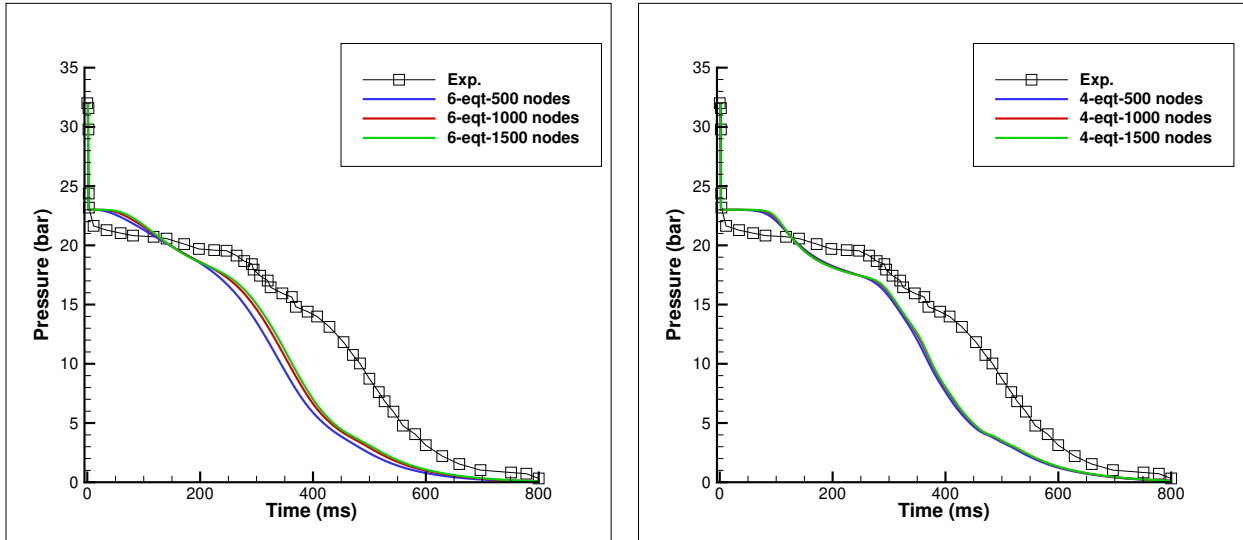


Figure 5.13: Comparison of convergence studies for pressure at P4 location (3.033 m upstream from the breach): 6-equation model (left) and 4-equation model (right), using the HLLC scheme with 500, 1000, and 1500 nodes, case 2.

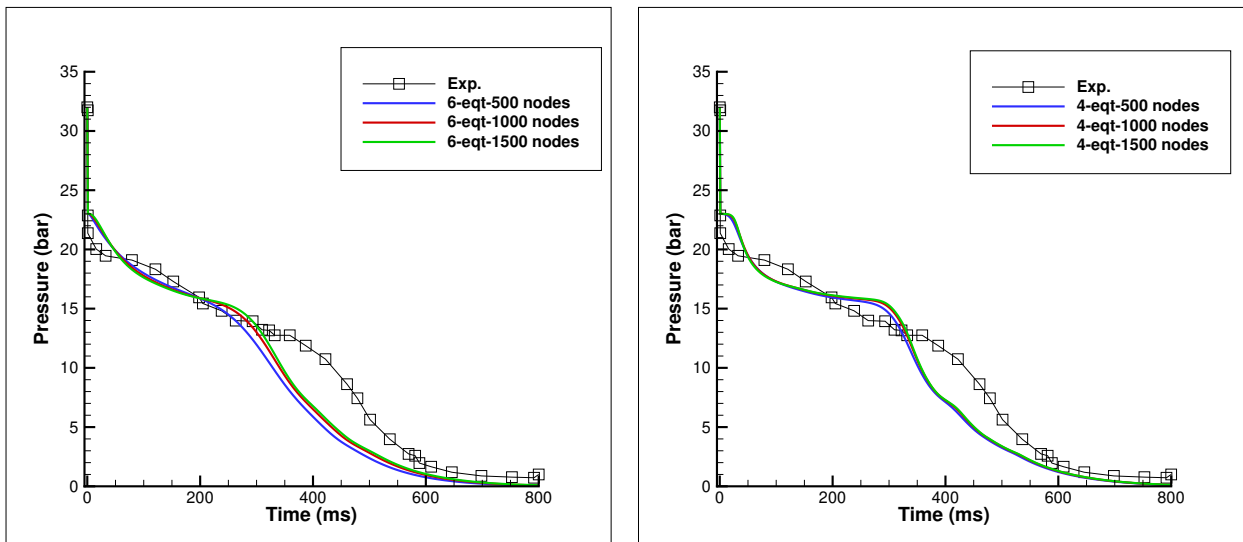


Figure 5.14: Comparison of convergence studies for pressure at P5 location (2.471 m upstream from the breach): 6-equation model (left) and 4-equation model (right), using the HLLC scheme with 500, 1000, and 1500 nodes, case 2.

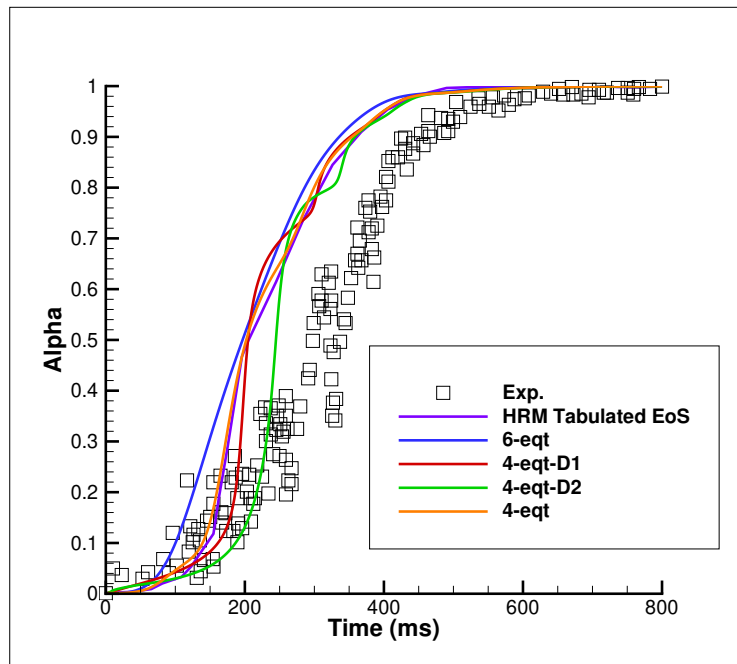


Figure 5.15: Comparison of void ratio profiles at location PT (2.887 m upstream from the breach) in the Canon experiment: experimental results (Exp., black square markers), 6-equation model (6-eqt, blue solid line), 4-equation model (4-eqt, orange solid line), 4-equation model with non-instantaneous mass transfer (4-eqt-D1/D2, red/green solid line) from the solver, and HRM Tabulated EoS results (HRM Tabulated EoS, purple solid line) obtained from the literature by [Lepareux \(1994\)](#), case 2.

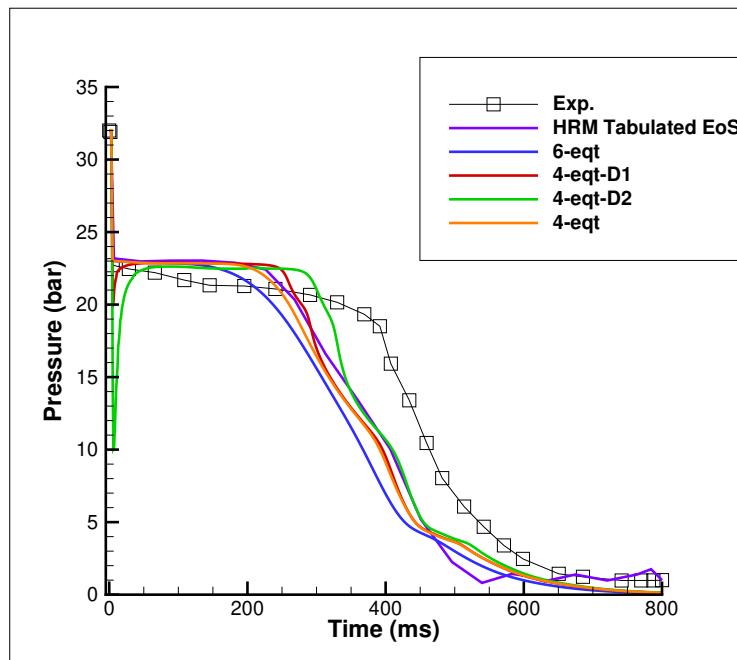


Figure 5.16: Comparison of pressure profiles at location P1 (3.899 m upstream from the breach) from the Canon experiment: experimental results (Exp., black square markers), 6-equation model (6-eqt, blue solid line), 4-equation model (4-eqt, orange solid line), 4-equation model with non-instantaneous mass transfer (4-eqt-D1/D2, red/green solid line) from the solver, and HRM Tabulated EoS results (HRM Tabulated EoS, purple solid line) obtained from the literature by [Lepareux \(1994\)](#), case 2.

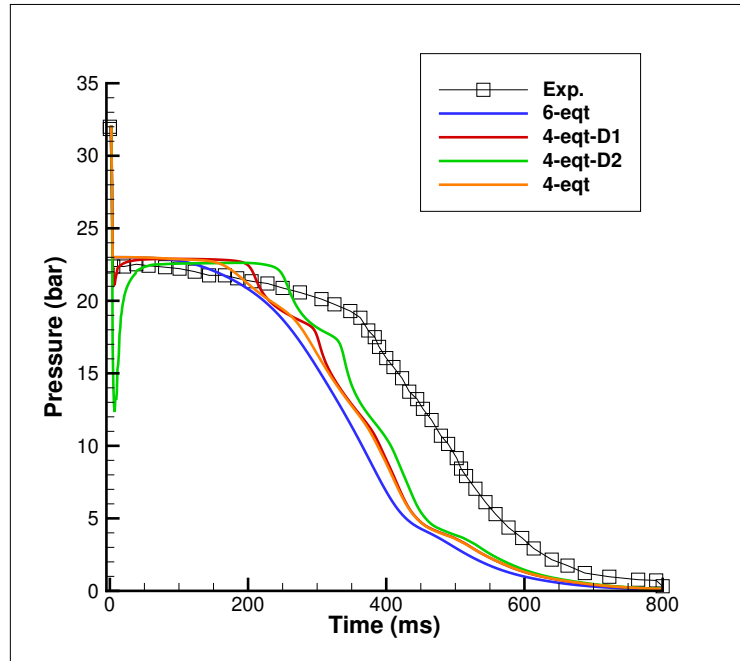


Figure 5.17: Comparison of pressure profiles at location P2 (3.033 m upstream from the breach) from the Canon experiment: experimental results (Exp., black square markers), 6-equation model (6-eqt, blue solid line), 4-equation model (4-eqt, orange solid line), 4-equation model with non-instantaneous mass transfer (4-eqt-D1/D2, red/green solid line), case 2.

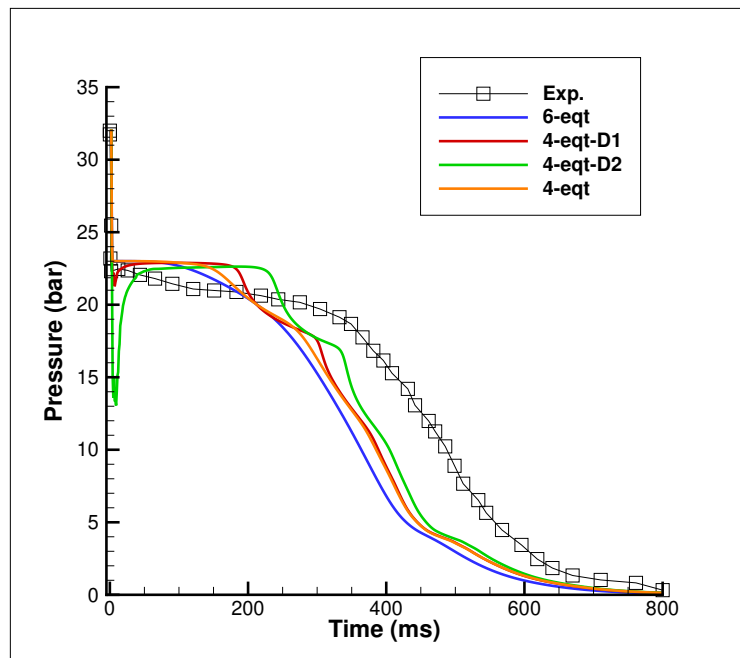


Figure 5.18: Comparison of pressure profiles at location P3 (2.471 m upstream from the breach) from the Canon experiment: experimental results (Exp., black square markers), 6-equation model (6-eqt, blue solid line), 4-equation model (4-eqt, orange solid line), 4-equation model with non-instantaneous mass transfer (4-eqt-D1/D2, red/green solid line), case 2.

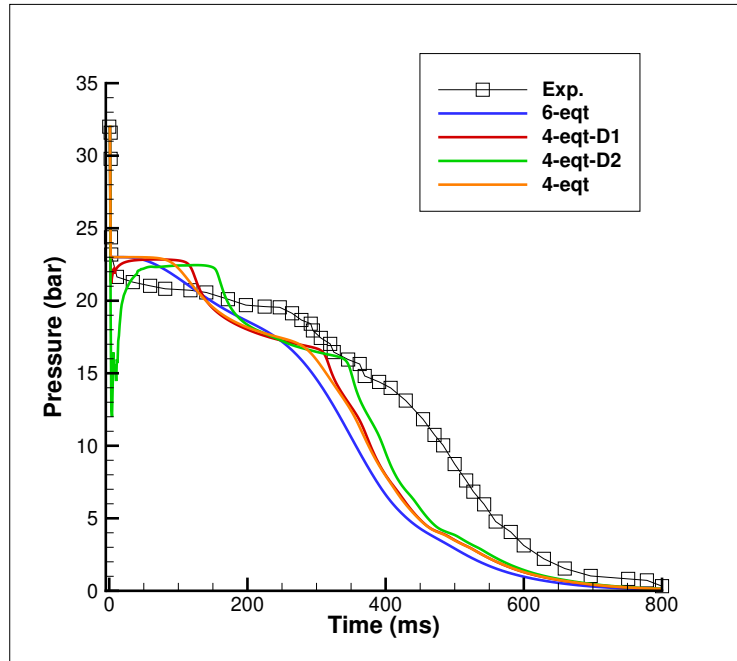


Figure 5.19: Comparison of pressure profiles at location P4 (1.6965 m upstream from the breach) from the Canon experiment: experimental results (Exp., black square markers), 6-equation model (6-eqt, blue solid line), 4-equation model (4-eqt, orange solid line), 4-equation model with non-instantaneous mass transfer (4-eqt-D1/D2, red/green solid line), case 2.

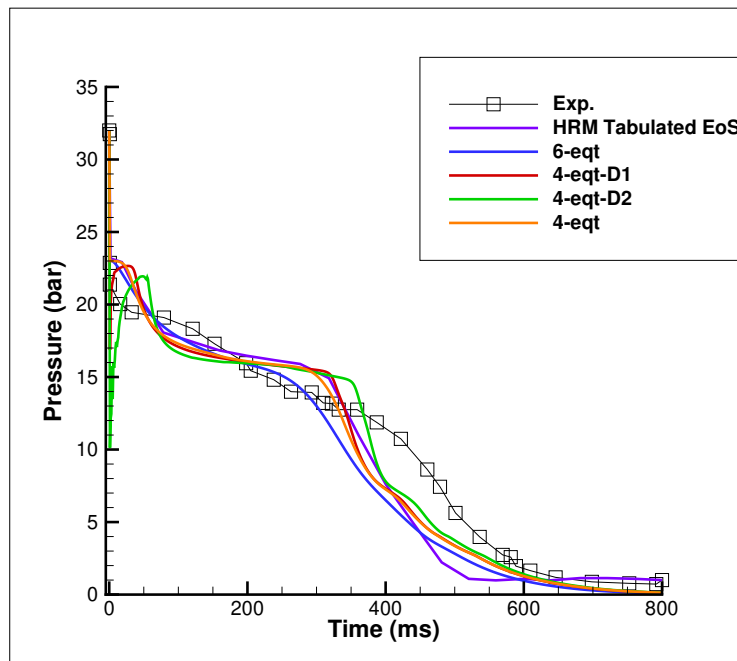


Figure 5.20: Comparison of pressure profiles at location P5 (0.504 m upstream from the breach) from the Canon experiment: experimental results (Exp., black square markers), 6-equation model (6-eqt, blue solid line), 4-equation model (4-eqt, orange solid line), 4-equation model with non-instantaneous mass transfer (4-eqt-D1/D2, red/green solid line) from the solver, and HRM Tabulated EoS results (HRM Tabulated EoS, purple solid line) obtained from the literature by [Lepareux \(1994\)](#), case 2.

Additionally, the comparison results for the P2, P3, and P4 locations are shown sequentially in Figures 5.17, Figures 5.18, and Figures 5.19.

At the onset of the transient, a rarefaction wave is generated at the open end of the pipe and propagates along its length. As this wave rapidly travels through the tube, the pressure of the liquid water decreases, triggering vaporization. Subsequently, the pressure continues to drop until it reaches the asymptotic value corresponding to the external atmospheric pressure. Both the six-equation and four-equation models predicted the vaporization process to occur earlier than observed in the experiments, with a discrepancy of approximately 0.2 seconds. Both the six-equation and four-equation models show good agreement with the HRM tabulated Equation of State (EoS) results, which have been selected as a reference for comparison in the literature [Lepareux \(1994\)](#). The four-equation model performs slightly better than the six-equation model. Although the non-instantaneous mass transfer results in the 4-eqt-D1 and 4-eqt-D2 models cause a significant pressure drop during the initial milliseconds of the simulation (for instances see Figures 5.16, and Figures 5.20), their subsequent prediction of the vaporization process is more accurate. Specifically, these models reduce the gap between the actual and numerically predicted vaporization times to 0.1 seconds, compared to the 0.2-second discrepancy observed with both the six-equation and standard four-equation models. Absolute and mean absolute error analyses were conducted for both the P1 and P5 locations, comparing the models and the HRM results. For both locations, the 4-eqt-D2 model produced the lowest mean absolute error (see Appendix A).

Case 3:

This test setup was also designed by [Riegel \(1978\)](#). Unlike the Canon experiment, the temperature and pressure values are higher. The primary reason for the changes in pressure and temperature was to represent the pressure and temperature values of the primary loop of a PWR. In this experiment, three different temperature values were tested: 280°C, 300°C, and 320°C, corresponding to the core inlet temperature, the average temperature in the core, and the core outlet temperature, respectively. A pressure value of 150 bar was chosen to represent a LOCA scenario in the primary circuit of a PWR. For the numerical simulation study, the average core temperature of 300°C was considered. Additionally, experiments have utilized varying breach diameters at the outlet of the pipe; however, this study is limited to the scenario involving a fully opened pipe. The test setup remains unchanged, as depicted in Figure 4.10. The numerical simulations were conducted using a 1D simplified geometry, with one side closed and the other connected to an atmospheric pressure tank. The stiffened gas equation of state and initial conditions are detailed in Table 5.2 and Table 5.3.

Table 5.2: EoS parameters for liquid and vapor for the Super-Canon experiment.

	Liquid	Vapor
γ	1.38	1.49
P_∞ (Pa)	570798395.20	0.00
q (J.kg ⁻¹)	-1530700.00	2288300.00
C_v (J.kg ⁻¹ .K ⁻¹)	3612.17	603.37
q' (J.kg ⁻¹ .K ⁻¹)	-515.21	4829.37

In this experiment, during the initial phase, two different kinds of pressure profiles were identified. In one case, the pressure reduced to about 75 bar while in the other to as low as 55 bar. This variety can be attributed to the process where the generation of vapor takes

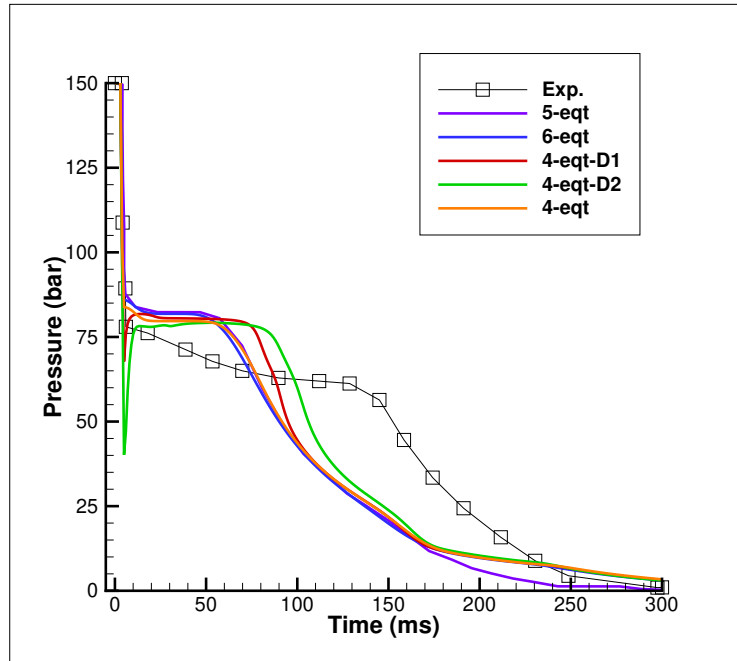


Figure 5.21: Comparison of pressure profiles at location P1 (3.899 m upstream from the breach) from the Super-Canon experiment: experimental results (Exp., black square markers), 6-equation model (6-eqt, blue solid line), 4-equation model (4-eqt, orange solid line), 4-equation model with non-instantaneous mass transfer (4-eqt-D1/D2, red/green solid line) from the solver, and 5-equation model results (5-eqt, purple solid line) obtained from the literature by [Daude et al. \(2014\)](#), case 3.

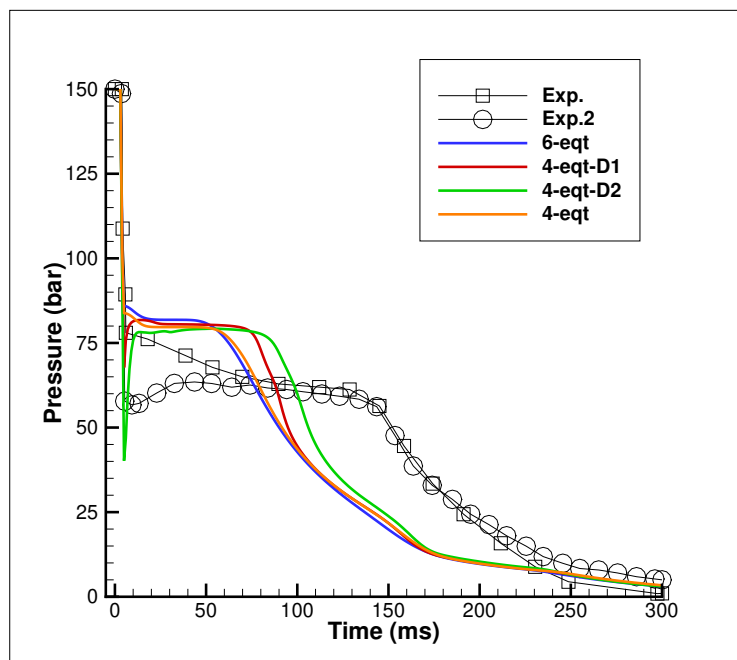


Figure 5.22: Comparison of pressure profiles at location P1 (3.899 m upstream from the breach) from the Super-Canon experiment: experimental results (Exp., black square markers), second experimental result (Exp.2, black circle marker), 6-equation model (6-eqt, blue solid line), 4-equation model (4-eqt, orange solid line), 4-equation model with non-instantaneous mass transfer (4-eqt-D1/D2, red/green solid line), case 3.

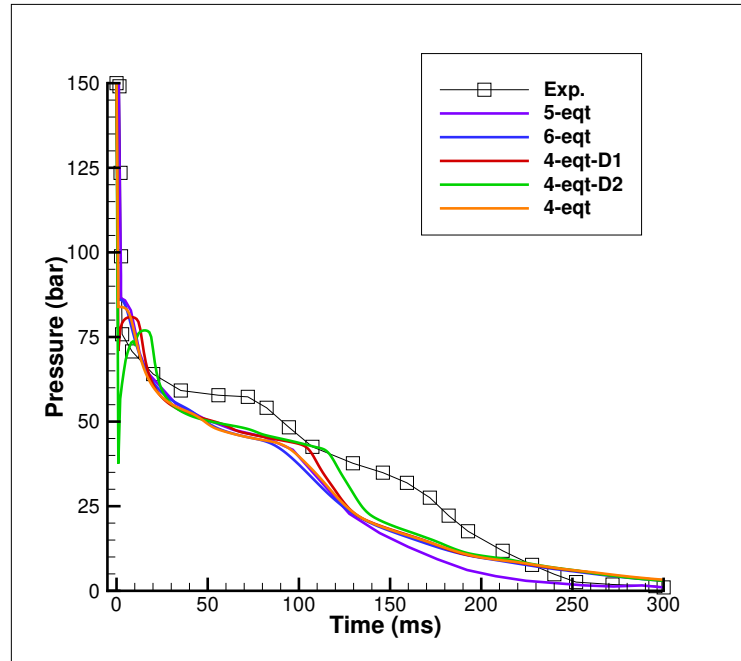


Figure 5.23: Comparison of pressure profiles at location P5 (0.504 m) from the Super-Canon experiment: experimental results (Exp., black square markers), 6-equation model (6-eqt, blue solid line), 4-equation model (4-eqt, orange solid line), 4-equation model with non-instantaneous mass transfer (4-eqt-D1/D2, red/green solid line) from the solver, and 5-equation model results (5-eqt, purple solid line) obtained from the literature by [Daude et al. \(2014\)](#), case 3.

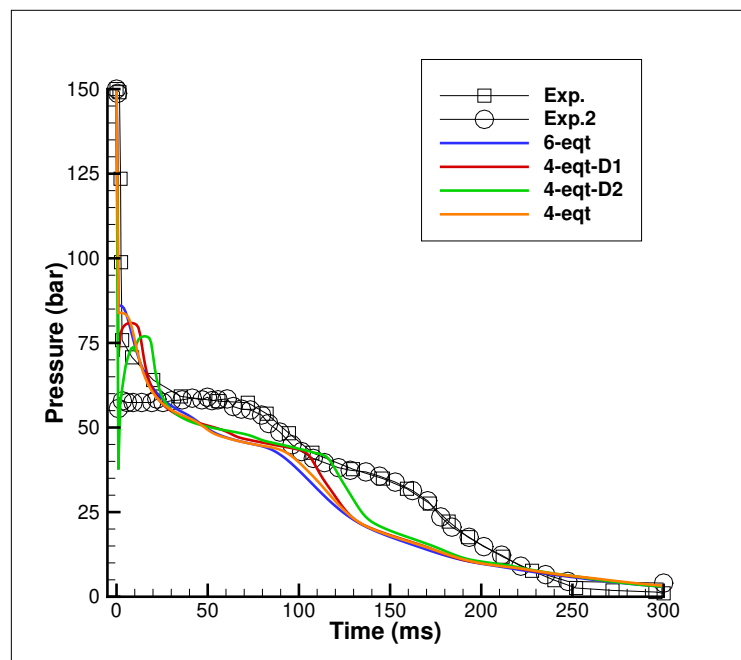


Figure 5.24: Comparison of pressure profiles at location P5 (0.504 m upstream from the breach) from the Super-Canon experiment: experimental results (Exp., black square markers), second experimental result (Exp.2, black circle marker), 6-equation model (6-eqt, blue solid line), 4-equation model (4-eqt, orange solid line), 4-equation model with non-instantaneous mass transfer (4-eqt-D1/D2, red/green solid line), case 3.

Table 5.3: Initial conditions for the Super-Canon experiment.

	Pipe	Tank
α_l	$1 - 10^{-3}$	10^{-3}
α_v	10^{-3}	$1 - 10^{-3}$
ρ_l (kg.m ⁻³)	736.45	717.72
ρ_v (kg.m ⁻³)	88.23	0.59
P_l (bar)	150	1
P_v (bar)	150	1

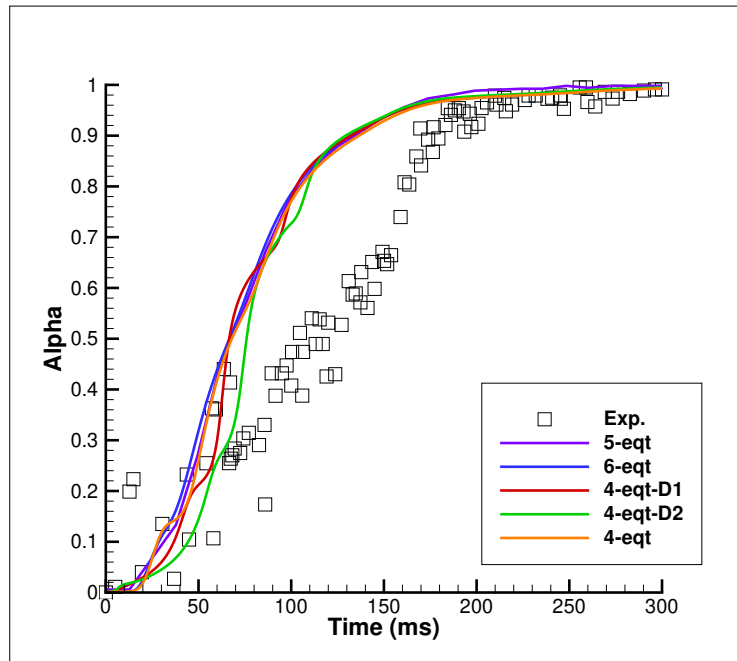


Figure 5.25: Comparison of void ratio profiles at location P1 (2.887 m upstream from the breach) in the Super-Canon experiment: experimental results (Exp., black square markers), 6-equation model (6-eqt, blue solid line), 4-equation model (4-eqt, orange solid line), 4-equation model with non-instantaneous mass transfer (4-eqt-D1/D2, red/green solid line) from the solver, and 5-equation model results (5-eqt, purple solid line) obtained from the literature by [Daude et al. \(2014\)](#), case 3.

place after a certain pressure drop. The vapor forms by homogeneous or heterogeneous nucleation based on the characteristics of the water being utilized. In the presence of dissolved particles – heterogeneous nucleation takes place and the process of vapor formation is promoted as well as the system remains closer to equilibrium. On the other hand, when there is less of the impurity present in the water, the process of vapor generation will take place through homogeneous nucleation which is a slow process and this results in a much larger pressure drop. Thus, the difference in the type of nucleation caused by the presence or lack of impurities provides the explanation for the differences detected between the two experimental pressure profiles [Hurisse \(2017\)](#).

The results, displayed after 0.03 s, are presented in Figures 5.21 through 5.25. Specifically, Figure 5.21 presents the pressure evolution at the P1 location using the 6-equation model, the 4-equation model, and the 4-equation model with non-instantaneous mass transfer, similar to the Canon case. The latter is described by Equations 5.62 and 5.63, and is denoted as 4-eqt-D1 (Equation 5.64) and 4-eqt-D2 (Equation 5.65) in the legend. As with the Canon case, the results are also compared to the 5-equation model, which can be found in the literature [Daude et al. \(2014\)](#). In Figure 5.22, the second experimental result, men-

tioned earlier, is also introduced and represented as Exp.2 with black circle markers. Similar to the P1 location, two figures are provided for the P5 location. In Figure 5.23, the pressure evolution at the P5 location is examined using different models, and in Figure 5.24, the second experimental result is introduced, as was done for the P1 location. Finally, Figure 5.25 presents the void fraction at the P_T location, where the results from both experiments are combined and displayed as Exp. in the legend.

This experiment functions as a benchmark test case for evaluating nuclear safety codes, especially in the context of LOCA scenarios. At the beginning of the experiment, the pipe is filled with subcooled water. Upon the rupture of the membrane, a rarefaction wave travels through the entire length of the pipe. The overall pressure behavior in the Super-Canon experiment follows a similar pattern to the Canon experiment, with a sudden drop from the initial pressure to a plateau, followed by a gradual decrease toward the external pressure. However, it is important to note that the plateau pressure in the Super-Canon experiment is around 75 bar in experiment 1 and around 55 bar in experiment 2, both of which differ significantly from the saturation pressure of 86 bar at the initial temperature, unlike what is observed in the Canon experiment. As a result, the liquid water tends to penetrate deeper into the metastable region. Similarly to the Canon experiment, the simulations indicate that vaporization occurs earlier than expected in both the six-equation and four-equation models. Both the six-equation and four-equation models show good agreement with the five-equation model, which has been chosen as a reference for comparison in the literature [Daude et al. \(2014\)](#). The four-equation model demonstrates slightly better performance compared to the six-equation model. The non-instantaneous mass transfer results in the 4-eqt-D1 and 4-eqt-D2 models exhibit a significant pressure drop at the start of the simulation. Notably, the 4-eqt-D2 model accurately captures the initial pressure drop, particularly in the case of the second experimental result. While the computational cost of the 6-equation model is nearly three times higher than that of the 4-equation model, it is important to note that the computational cost also increases for the 4-eqt-D1 and 4-eqt-D2 variants relative to the baseline 4-equation model. Specifically, the 4-eqt-D1 variant increase a 34% increase in computation time, while the 4-eqt-D2 variant results in a 43% increase. Within the current wide range of pressure and temperature conditions, the stiffened gas EoS simplistic to accurately capture the thermodynamic behavior of water. To better align with the experimental results, more complex equations of state, for instance the IAPWS Industrial Formulation, as well as finite-rate mass transfer, are believed to be necessary. Nevertheless, the six-equation and four-equation models show reasonably good agreement with the five-equation model, demonstrating their capability to simulate the flashing phenomenon, even in complex and challenging numerical scenarios. Absolute and mean absolute error analyses were conducted for both the P1 and P5 locations, comparing the models and the five-equation model results. For both locations, the 4-eqt-D2 model produced the lowest mean absolute error (see Appendix B).

5.5 Summary

In this chapter, a comparative study between the four-equation and six-equation models for compressible two-phase flow is conducted, focusing on numerical methods and validation test cases. The six-equation model, derived from the seven-equation Baer-Nunziato model, includes relaxation to velocity equilibrium while retaining mechanical, thermal, and chemical non-equilibrium effects. In contrast, the four-equation model assumes equilibrium for velocity, pressure, and temperature between both phases, simplifying the system.

The numerical solution of both the four-equation and six-equation models is achieved

using a fractional step method, where the system is split into a hyperbolic part and a relaxation part. The hyperbolic system is solved using an HLLC Riemann solver, and relaxation procedures are then applied to account for mechanical, thermal, and chemical equilibrium. While mechanical and thermal relaxations are implemented as instantaneous processes, for chemical relaxation, both instantaneous and non-instantaneous options are provided.

Validation of various test cases with four-equation and six-equation models has been carried out. In the case of the depressurization test for the CO_2 , one can see that both models highly well correlate with the reference solution. The models proved to be capable of illustrating the pressure and temperature trends in the depressurization process and thus their ability to simulate the phase transition behaviors under these conditions. For the Canon experiment, both the four-equation and six-equation models showed good agreement with the HRM tabulated Equation of State (EoS) reference solution. However, both models predicted the vaporization process to occur earlier than observed experimentally, with a discrepancy of approximately 0.2 seconds. The four-equation model with non-instantaneous mass transfer (4-eqt-D1 and 4-eqt-D2) further improved the accuracy of the vaporization time, reducing the discrepancy to 0.1 seconds. The Super-Canon experiment serves as a benchmark for evaluating nuclear safety codes, particularly in LOCA scenarios. It revealed two distinct pressure plateaus, with the second experimental result indicating deeper metastable states for water. Both the four-equation and six-equation models predicted early vaporization, though they showed good agreement with the reference five-equation model. The four-equation model, especially the 4-eqt-D2 variant with non-instantaneous mass transfer, more accurately captured the initial pressure drop in the second experimental result. As demonstrated by the last test case, the use of a non-instantaneous chemical relaxation procedure is essential for a more accurate description of the metastable state. For this reason, the next chapter is dedicated to the arbitrary relaxation procedure.

Chapter 6

Six-equation model with arbitrary-rate relaxation

This chapter focuses on the implementation and analysis of the six-equation model with arbitrary-rate relaxation, concentrating on the dynamics of two-phase flow systems. It begins by discussing the mathematical formulation of the single-velocity six-equation model, where both phases are assumed to be in kinetic equilibrium, while accounting for mechanical, thermal, and chemical non-equilibrium. The mechanical, thermal, and chemical relaxation mechanisms are explored in detail, highlighting their roles in driving the system toward equilibrium under different conditions. Notably, the model is capable of handling non-instantaneous mass transfer processes, which are critical for accurately modeling metastable states during rapid phase transitions. The numerical methods employed to solve the governing equations are also elaborated. In the final part of the chapter, the model is validated through a series of test cases, demonstrating its effectiveness in handling metastable states. As in the previous chapter, the results are derived from the custom-built solver specifically developed for this study.

6.1 Single velocity six-equation model

Let us examine a compressible flow of two phases, under the assumption that both phases are in kinetic equilibrium and move with velocity \vec{u} . For each phase, the volume fraction, density, pressure, and specific internal energy are symbolized as $\alpha_k, \rho_k, p_k, \epsilon_k$, with $k = 1$ and $k = 2$ corresponding to the respective phases. Based on the work of [Pelanti and Shyue \(2014\)](#), the system governing two-phase flow contains $5 + d$ equations, with d indicates the spatial dimension:

$$\left\{ \begin{array}{l} \partial_t \alpha_1 + \vec{u} \cdot \nabla \alpha_1 = \mathcal{V}, \\ \partial_t (\alpha_1 \rho_1) + \nabla \cdot (\alpha_1 \rho_1 \vec{u}) = \mathcal{N}, \\ \partial_t (\alpha_2 \rho_2) + \nabla \cdot (\alpha_2 \rho_2 \vec{u}) = -\mathcal{N}, \\ \partial_t (\rho \vec{u}) + \nabla \cdot (\rho \vec{u} \otimes \vec{u} + (\alpha_1 p_1 + \alpha_2 p_2) \mathbf{I}) = 0, \\ \partial_t (\alpha_1 E_1) + \nabla \cdot (\alpha_1 (E_1 + p_1) \vec{u}) + \Sigma = -p_{int} \mathcal{V} + \mathcal{H} + \left(g_{int} + \frac{|\vec{u}|^2}{2} \right) \mathcal{N}, \\ \partial_t (\alpha_2 E_2) + \nabla \cdot (\alpha_2 (E_2 + p_2) \vec{u}) - \Sigma = p_{int} \mathcal{V} - \mathcal{H} - \left(g_{int} + \frac{|\vec{u}|^2}{2} \right) \mathcal{N}, \end{array} \right. \quad (6.1)$$

where the phasic internal energy per unit volume with $\mathcal{E}_k = \rho_k \epsilon_k$, and the phasic total energy per unit volume with $E_k = \mathcal{E}_k + \rho_k \frac{|\vec{u}|^2}{2}$. The mixture density is $\rho = \sum_{k=1}^2 \alpha_k \rho_k$, the

mixture internal energy per unit volume is $\mathcal{E} = \sum_{k=1}^2 \alpha_k \mathcal{E}_k$, and the mixture total energy is $E = \sum_{k=1}^2 \alpha_k \mathcal{E}_k$ Pelanti (2022).

The system of two-phase equations represented by Equation 6.1 is hyperbolic, and its corresponding eigenvalues along the direction \vec{n} are as follows Pelanti (2022):

$$\lambda_{1,5+d} = \vec{u} \cdot \vec{n} \pm c_f, \quad (6.2)$$

$$\lambda_k = \vec{u} \cdot \vec{n}, \quad \text{where } k = 2, \dots, 4 + d. \quad (6.3)$$

By summing the total energy equations of each phase, a conservation law for the total energy of the mixture is obtained. The non-conservative component Σ , found in the phasic total energy equations, is described by Pelanti (2022):

$$\partial_t(E) + \nabla \cdot (E\vec{u} + (\alpha_1 p_1 + \alpha_2 p_2)\vec{u}) = 0 \quad (6.4)$$

$$\Sigma = -\vec{u} \cdot \vec{\Xi}, \quad \vec{\Xi} = Y_2 \nabla(\alpha_1 p_1) - Y_1 \nabla(\alpha_2 p_2). \quad (6.5)$$

In this expression, $Y_k = \frac{\alpha_k \rho_k}{\rho}$ represents the mass fraction of one of the phases. The volume transfer between the phases is represented by \mathcal{V} , while heat transfer is denoted by \mathcal{H} and mass transfer is described by \mathcal{N} . These transfer quantities are formulated as relaxation terms:

$$\mathcal{V} = \mu(p_1 - p_2), \quad \mathcal{H} = \theta(T_2 - T_1), \quad \mathcal{N} = \nu(g_2 - g_1), \quad (6.6)$$

In this case, p_k stands for the phasic pressure, T_k for the phasic temperature and g_k for the phasic chemical potential. The parameter μ represents the rate of mechanical relaxation, while θ denotes thermal and ν chemical relaxation. As described by Pelanti (2022), the mechanical relaxation is always considered as instantaneous, so $\mu \rightarrow +\infty$. There is no particular assumption made about the rates of heat&mass transfer.

As can be seen in Equation 6.1, both interfacial pressure p_{int} and interfacial chemical potential g_{int} are present in the system. While it is necessary to define the interfacial pressure, the definition of the interfacial chemical potential is not required due to the manner in which the relaxation process is addressed.

$$p_{int} = \frac{Z_2 p_1 + Z_1 p_2}{Z_1 + Z_2}, \quad Z_k = \rho_k c_k \quad (6.7)$$

here Z_k is the acoustic impedance. Ensuring the alignment of relaxation parameters and interface quantities with the second law of thermodynamics is crucial, particularly in guaranteeing that the entropy production for the mixture is positive (see for details Flåtten and Lund (2011)).

The speed of sound associated with Equation 6.2, referred to as the frozen speed of sound, is provided by Pelanti (2022):

$$c_f = \sqrt{Y_1 c_1^2 + Y_2 c_2^2}, \quad (6.8)$$

here c_k phasic speed of sound.

To fully describe and close a physical system, an equation of state is required to relate temperature, pressure, internal energy, and density. For this purpose, the stiffened gas equation of state is utilized Pelanti and Shyue (2014):

$$p_k(\mathcal{E}_k, \rho_k) = (\gamma_k - 1)(\mathcal{E}_k - \rho_k q_k) - \gamma_k p_{\infty, k}, \quad (6.9)$$

$$T_k(p_k, \rho_k) = \frac{p_k + p_{\infty,k}}{\rho_k c_{v,k}(\gamma_k - 1)}. \quad (6.10)$$

Using these relationships, the specific enthalpy (h_k), specific entropy (s_k), and Gibbs free energy (g_k) for phases can be determined:

$$h_k(p_k, T_k) = c_{p,k}T_k + q_k, \quad (6.11)$$

$$s_k(p_k, T_k) = c_{v,k} \ln \left(\frac{T_k^{\gamma_k}}{(p_k + p_{\infty,k})^{\gamma_k - 1}} \right) + q'_k, \quad (6.12)$$

$$g_k(p_k, T_k) = (\gamma_k c_{v,k} - q'_k)T_k - c_{v,k}T_k \ln \left(\frac{T_k^{\gamma_k}}{(p_k + p_{\infty,k})^{\gamma_k - 1}} \right) + q_k. \quad (6.13)$$

Here, $\gamma = \frac{c_p}{c_v}$ is the heat capacity ratio, where c_p and c_v represent the specific heat capacities at constant pressure and constant volume, respectively. The constants $p_{\infty,k}$, q , and q' characterize the thermodynamic behavior of the fluid. The speed of sound c_k is given by:

$$c_k = \sqrt{\frac{\gamma_k(p_k + p_{\infty,k})}{\rho_k}}. \quad (6.14)$$

The theoretical pressure-temperature saturation curve for liquid and vapor phases is derived by enforcing the equilibrium condition for Gibbs free energy, ensuring that the Gibbs free energies of the two phase, g_1 and g_2 , are identical. Utilizing the stiffened gas equation of state, this saturation curve is described by the following equation [Le Métayer et al. \(2004\)](#):

$$A_s + \frac{B_s}{T} + C_s \ln T + D_s \ln(p + p_{\infty,1}) - \ln(p + p_{\infty,2}) = 0, \quad (6.15)$$

where the coefficients A_s , B_s , C_s , and D_s are defined as:

$$\begin{cases} A_s = \frac{c_{p,1} - c_{p,2} + q'_2 - q'_1}{c_{p,2} - c_{v,2}}, \\ B_s = \frac{q_2 - q_1}{c_{p,2} - c_{v,2}}, \\ C_s = \frac{c_{p,2} - c_{p,1}}{c_{p,2} - c_{v,2}}, \\ D_s = \frac{c_{p,1} - c_{v,1}}{c_{p,2} - c_{v,2}}. \end{cases} \quad (6.16)$$

6.2 Numerical solution method

To simplify the numerical procedure, it is possible to rewrite the Equation 6.1 in compact form:

$$\partial_t U + \nabla \cdot f(U) + \sigma(U, \nabla U) = S_\mu(U) + S_\theta(U) + S_\nu(U), \quad (6.17)$$

$$U = \begin{pmatrix} \alpha_1 \\ \alpha_1 \rho_1 \\ \alpha_2 \rho_2 \\ \rho \vec{u} \\ \alpha_1 E_1 \\ \alpha_2 E_2 \end{pmatrix}, \quad f(U) = \begin{pmatrix} 0 \\ \alpha_1 \rho_1 \vec{u} \\ \alpha_2 \rho_2 \vec{u} \\ \rho \vec{u} \otimes \vec{u} + (\alpha_1 p_1 + \alpha_2 p_2) \mathbf{I} \\ \alpha_1 (E_1 + p_1) \vec{u} \\ \alpha_2 (E_2 + p_2) \vec{u} \end{pmatrix}, \quad \sigma(U, \nabla U) = \begin{pmatrix} \vec{u} \cdot \nabla \alpha_1 \\ 0 \\ 0 \\ 0 \\ \Sigma \\ -\Sigma \end{pmatrix}, \quad (6.18)$$

$$S_\mu(U) = \begin{pmatrix} \mathcal{V} \\ 0 \\ 0 \\ 0 \\ -p_{int}\mathcal{V} \\ p_{int}\mathcal{V} \end{pmatrix}, \quad S_\theta(U) = \begin{pmatrix} 0 \\ 0 \\ 0 \\ 0 \\ Q \\ -Q \end{pmatrix}, \quad S_\nu(U) = \begin{pmatrix} 0 \\ \mathcal{N} \\ -\mathcal{N} \\ 0 \\ (g_{int} + \frac{|\bar{u}|^2}{2})\mathcal{N} \\ -(g_{int} + \frac{|\bar{u}|^2}{2})\mathcal{N} \end{pmatrix}, \quad (6.19)$$

A classical fractional step method, which is proposed by [Strang \(1968\)](#), is employed to numerically solve this system. This method alternates between solving the homogeneous hyperbolic portion of the system using a numerical scheme and solving a sequence of ODEs that account for the relaxation source terms. To solution procedure can be summarized:

1. Solution of the Homogeneous Hyperbolic System:

$$\partial_t U + \nabla \cdot f(U) + \sigma(U, \nabla U) = 0. \quad (6.20)$$

During subsequent steps, the quantities computed will be denoted with the superscript 0.

2. Relaxation Steps

2.1 Mechanical Relaxation:

$$\partial_t U = S_\mu(U). \quad (6.21)$$

This process instantaneously brings the flow to pressure equilibrium. The quantities calculated at this stage will be denoted with the superscript *.

2.2 Thermal Relaxation:

$$\partial_t U = S_\mu(U) + S_\theta(U), \quad (6.22)$$

At this stage, the phases are driven into thermal equilibrium, with pressure equilibrium being maintained. The quantities calculated at this stage will be denoted with the superscript **.

2.3 Chemical Relaxation

$$\partial_t U = S_\mu(U) + S_\theta(U) + S_\nu(U), \quad (6.23)$$

At this stage, the phases are driven into full thermodynamic equilibrium, with pressure equilibrium sustained. The quantities calculated at this stage will be denoted with the superscript ***.

Given that the solution to the homogeneous hyperbolic system of the six-equation model has already been discussed in the previous chapter, this section will focus exclusively on presenting the HLLC structure.

At the interface of a cell, the numerical flux can be expressed as:

$$F_{i+1/2}^{HLLC} = \begin{cases} F_L, & \text{if } S_L > 0 \\ F_L^* = F_L + S_L(U_L^* - U_L), & \text{if } S_L \leq 0 < S_M \\ F_R^* = F_R + S_R(U_R^* - U_R), & \text{if } S_M \leq 0 \leq S_R \\ F_R, & \text{if } S_R < 0 \end{cases} \quad (6.24)$$

where,

$$U = \begin{bmatrix} \alpha_1 \\ \alpha_1 \rho_1 \\ \alpha_2 \rho_2 \\ \rho u \\ \alpha_1 \rho_1 E_1 \\ \alpha_2 \rho_2 E_2 \end{bmatrix} \quad U_k^* = \begin{bmatrix} \alpha_{1,k} \\ (\alpha_1 \rho_1)_k \frac{S_k - u_k}{S_k - S^*} \\ (\alpha_2 \rho_2)_k \frac{S_k - u_k}{S_k - S^*} \\ \rho_k \frac{S_k - u_k}{S_k - S^*} S^* \\ (\alpha_1 \rho_1)_k \frac{S_k - u_k}{S_k - S^*} \left(\frac{E_{1,k}}{\rho_{1,k}} + (S^* - u_k) \left(S^* + \frac{p_{1,k}}{\rho_{1,k} (S_k - u_k)} \right) \right) \\ (\alpha_2 \rho_2)_k \frac{S_k - u_k}{S_k - S^*} \left(\frac{E_{2,k}}{\rho_{2,k}} + (S^* - u_k) \left(S^* + \frac{p_{2,k}}{\rho_{2,k} (S_k - u_k)} \right) \right) \end{bmatrix}$$

with $k = l, r$.

6.3 Relaxation procedure

As discussed in [Pelanti \(2022\)](#), it is important to note that for any relaxation process, the following conditions hold:

$$\partial_t \rho = 0, \quad (6.25)$$

$$\partial_t (\rho \vec{u}) = 0, \quad (6.26)$$

$$\partial_t E = 0. \quad (6.27)$$

As a result, the mixture's velocity, density, internal energy, and total energy stay constant throughout the transfer:

$$\vec{u} = \text{unchanged}, \quad \rho = \text{unchanged}, \quad \mathcal{E} = \text{unchanged}, \quad E = \text{unchanged}.$$

Furthermore, if chemical relaxation is not initiated, the partial densities will stay constant, as demonstrated by:

$$\partial_t (\alpha_k \rho_k) = 0, \quad (6.28)$$

$$\alpha_k \rho_k = \text{unchanged}.$$

For a complete determination of the relaxed states during mechanical&thermal relaxation, two independent variables need to be specified. In contrast, the chemical relaxation step requires determining three variables due to variations in the partial densities.

6.3.1 Mechanical relaxation procedure

Instantaneous mechanical relaxation processes will always be assumed, implying $\mu \rightarrow +\infty$. Before initiating the mechanical relaxation process, it is crucial to write the equation for the phasic pressure, which can be expressed as:

$$\partial_t p_k + \vec{u} \cdot \nabla p_k + \rho_k c_k^2 \nabla \cdot \vec{u} = \frac{(-1)^{k-1}}{\alpha_k} \{ -[\Gamma_k (\mathcal{E}_k + p_{int}) + \chi_k \rho_k] \mathcal{V} + \Gamma_k \mathcal{H} + (\Gamma_k g_{int} + \chi_k) \mathcal{N} \}. \quad (6.29)$$

The relaxation process begins by formulating the ordinary differential equations with respect to the volume fraction α_1 and the phasic pressures p_1 and p_2 [Pelanti \(2022\)](#).

$$\partial_t \alpha_1 = \mu (p_1 - p_2), \quad (6.30)$$

$$\partial_t p_1 = \frac{\mu}{\alpha_1} [\Gamma_1(\mathcal{E}_1 + p_{int}) + \chi_1 \rho_1] (p_2 - p_1), \quad (6.31)$$

$$\partial_t p_2 = -\frac{\mu}{\alpha_2} [\Gamma_2(\mathcal{E}_2 + p_{int}) + \chi_2 \rho_2] (p_2 - p_1). \quad (6.32)$$

Where $\Gamma_k = \left(\frac{\partial p_k}{\partial \mathcal{E}_k} \right)_{\rho_k}$ corresponds to the Grüneisen coefficient of phase k , and $\chi_k = \left(\frac{\partial p_k}{\partial \rho_k} \right)_{\mathcal{E}_k}$. The initial condition for this system is derived from the solution of the homogeneous system, represented by a superscript 0, and $\mu > 0$ is treated as a constant.

As discussed in Pelanti (2022), to prepare for subsequent discussions, it is essential to write the equations for the phasic pressures. Let us introduce the quantities η_k , for which the inverse values align with the coefficients of $(p_2 - p_1)$:

$$\frac{1}{\eta_k^p} = \frac{1}{\alpha_k} [\Gamma_k(\mathcal{E}_k + p_{int}) + \chi_k \rho_k] = \frac{1}{\alpha_k} [\Gamma_k(p_1 - p_k) + \rho_k c_k^2]. \quad (6.33)$$

An approximation is introduced by assuming η_k^p remains constant over time, $\eta_k^p = \eta_k^{p0}$. Consequently, the Equation 6.31, and 6.32 can be rewritten:

$$\partial_t p_1 = \mu \frac{1}{\eta_1^{p0}} (p_2 - p_1), \quad (6.34)$$

$$\partial_t p_2 = -\mu \frac{1}{\eta_2^{p0}} (p_2 - p_1). \quad (6.35)$$

An ordinary differential equation for the pressure difference $\Delta p = p_2 - p_1$ is obtained:

$$\partial_t \Delta p = -\mu \left(\frac{1}{\eta_1^{p0}} + \frac{1}{\eta_2^{p0}} \right) \Delta p, \quad (6.36)$$

which yields the exact solution after a time interval Δt :

$$\Delta p^* = \Delta p^0 e^{-\omega_p \Delta t}, \quad (6.37)$$

where

$$\omega_p = \mu \left(\frac{1}{\eta_1^{p0}} + \frac{1}{\eta_2^{p0}} \right). \quad (6.38)$$

The process towards mechanical equilibrium, characterized by $\omega_p > 0$, implies that during pressure relaxation, volume transfer causes the phase with the lower pressure to be compressed while the phase with the higher pressure expands, provided that $\mu > 0$ Pelanti (2022). This behavior aligns with the relaxation terms in the parent six-equation model.

The partial differential equation 6.30 for the α_1 can be solved by applying the expression for Δp^* . By performing the integration:

$$\alpha_1^* = \alpha_1^0 - \frac{\Delta p^0}{\left(\frac{1}{\eta_1^{p0}} + \frac{1}{\eta_2^{p0}} \right)} \left(1 - e^{-\omega_p \Delta t} \right). \quad (6.39)$$

where α_1^* represents the volume fraction after the mechanical relaxation.

As $\mu \rightarrow +\infty$ indicating instantaneous pressure relaxation, the previously mentioned equation for the volume fraction approaches the equilibrium value:

$$\alpha_{1,\mu \rightarrow \infty}^* = \alpha_1^0 - \frac{\Delta p^0}{\left(\frac{1}{\eta_1^{p0}} + \frac{1}{\eta_2^{p0}} \right)}. \quad (6.40)$$

One of the primary advantages of this model is its ability to achieve mixture-energy consistency at the discrete level. The quantities computed during any relaxation step are denoted with the symbol \dagger , where \dagger represents $*$, $**$, or $***$. Let $E^{0,C}$ indicate discrete quantities of the mixture's total energy, based on a conservative approximation of the conservation law for E in equation 6.4. To ensure mixture-energy consistency, it is essential to satisfy two key conditions (see for details [Pelanti and Shyue \(2014\)](#), [Pelanti \(2022\)](#)):

1. Mixture total energy conservation consistency:

$$E^0 = E^{0,C}$$

2. Relaxed pressure consistency:

$$\mathcal{E}^0 = \alpha_1^\dagger \mathcal{E}_1(p^\dagger, \rho_1^\dagger) + \alpha_2^\dagger \mathcal{E}_2(p^\dagger, \rho_2^\dagger),$$

The formula mentioned above for calculating equilibrium pressure may require an iterative procedure. However, for the stiffened gas EoS, or more generally for equations of state that can be expressed in the form of the Mie–Grüneisen EoS, an explicit expression for pressure can be derived [Richard Saurel et al. \(2009\)](#):

$$p(\mathcal{E}, \rho_1, \rho_2, \alpha_1) = \frac{\mathcal{E} - (\alpha_1 \rho_1 q_1 + \alpha_2 \rho_2 q_2) - \left(\frac{\alpha_1 \gamma_1 p_{\infty,1}}{\gamma_1 - 1} + \frac{\alpha_2 \gamma_2 p_{\infty,2}}{\gamma_2 - 1} \right)}{\frac{\alpha_1}{\gamma_1 - 1} + \frac{\alpha_2}{\gamma_2 - 1}}.$$

Equilibrium pressure following mechanical relaxation, ensuring mixture-energy consistency, can be determined as follows:

$$\mathcal{E}^0 = \alpha_1^* \mathcal{E}_1 \left(p^*, \frac{(\alpha_1 \rho_1)^0}{\alpha_1^*} \right) + \alpha_2^* \mathcal{E}_2 \left(p^*, \frac{(\alpha_2 \rho_2)^0}{\alpha_2^*} \right). \quad (6.41)$$

6.3.2 Thermal relaxation procedure

In order to describe the process of thermal relaxation, the reduced five-equation pressure equilibrium model will be introduced first. The p-relaxed model comprises a set of $4 + d$ equations (see [Kapila et al.](#), and [Pelanti \(2022\)](#)):

$$\begin{aligned} \partial_t \alpha_1 + \vec{u} \cdot \nabla \alpha_1 - \frac{\alpha_1 \alpha_2}{A} (\rho_2 c_2^2 - \rho_1 c_1^2) \nabla \cdot \vec{u} &= \frac{1}{A} (\alpha_2 \Gamma_1 + \alpha_1 \Gamma_2) \mathcal{H} \\ &\quad + \frac{1}{A} (\alpha_2 \tau_{I1} + \alpha_1 \tau_{I2}) \mathcal{N}, \\ \partial_t (\alpha_1 \rho_1) + \nabla \cdot (\alpha_1 \rho_1 \vec{u}) &= \mathcal{N}, \\ \partial_t (\alpha_2 \rho_2) + \nabla \cdot (\alpha_2 \rho_2 \vec{u}) &= -\mathcal{N}, \\ \partial_t (\rho \vec{u}) + \nabla \cdot (\rho \vec{u} \otimes \vec{u} + p \mathbf{I}) &= 0, \\ \partial_t E + \nabla \cdot ((E + p) \vec{u}) &= 0, \end{aligned} \quad (6.42)$$

where

$$A = \alpha_1 \rho_2 c_2^2 + \alpha_2 \rho_1 c_1^2, \quad (6.43)$$

and

$$\tau_{Ik} = \Gamma_k (g_{int} - h_k) + c_k^2 = \Gamma_k g_{int} + \chi_k. \quad (6.44)$$

The speed of sound for this model is defined by the well-established Wood's speed of sound Pelanti (2022):

$$\frac{1}{\rho c_{wallis}^2} = \frac{\alpha}{\rho_v c_v^2} + \frac{1 - \alpha}{\rho_l c_l^2} \quad (6.45)$$

The equations for the mixture pressure and the phasic temperatures can be formulated as follows:

$$\partial_t p + \vec{u} \cdot \nabla p + \rho c_p^2 \nabla \cdot \vec{u} = \frac{1}{A} \left[(\Gamma_1 \rho_2 c_2^2 - \Gamma_2 \rho_1 c_1^2) \mathcal{H} + (\rho_2 c_2^2 \tau_{I1} - \rho_1 c_1^2 \tau_{I2}) \mathcal{N} \right]. \quad (6.46)$$

$$\begin{aligned} \partial_t T_k + \vec{u} \cdot \nabla T_k + \frac{\rho c_p^2}{\phi_k} \left(-\zeta_k + \frac{1}{c_k^2} \right) \nabla \cdot \vec{u} = \\ \frac{1}{\phi_k A} \left[(-1)^k \frac{\rho_k}{\alpha_k} (\alpha_2 \Gamma_1 + \alpha_1 \Gamma_2) - \zeta_k (\Gamma_1 \rho_2 c_2^2 - \Gamma_2 \rho_1 c_1^2) \right] \mathcal{H} \\ + \frac{1}{\phi_k} \left\{ (-1)^{k-1} \frac{1}{\alpha_k} + \frac{1}{A} \left[(-1)^k \frac{\rho_k}{\alpha_k} (\alpha_2 \tau_{I1} + \alpha_1 \tau_{I2}) - \zeta_k (\rho_2 c_2^2 \tau_{I1} - \rho_1 c_1^2 \tau_{I2}) \right] \right\} \mathcal{N}. \end{aligned} \quad (6.47)$$

where ϕ_k , and ζ_k defined as:

$$\phi_k = \left(\frac{\partial p_k}{\partial T_k} \right)_{p_k} = -\rho_k \beta_k \quad \text{and} \quad \zeta_k = \left(\frac{\partial \rho_k}{\partial p_k} \right)_{T_k} = \rho_k \kappa_{Tk}, \quad (6.48)$$

$$\beta_k = \frac{\Gamma_k C_{pk}}{c_k^2 \alpha_k \rho_k} \quad \text{and} \quad \kappa_{Tk} = \frac{1}{\rho_k c_k^2} + \frac{\beta_k^2 T_k \alpha_k}{C_{pk}} \quad (6.49)$$

where β_k represents the thermal expansion coefficient, κ_{Tk} denotes the isothermal compressibility, and $C_{pk} = \alpha_k \rho_k c_{pk}$ is the phasic extensive heat capacity at constant pressure.

To initiate the thermal relaxation process, the focus shifts to the ordinary differential equations that include the heat transfer source term relevant to the reduced five-equation pressure equilibrium model Pelanti (2022). These ODEs describe the thermal relaxation dynamics of the model, specifically in terms of the volume fraction α_1 (Equation 6.42) and the phasic temperatures T_1 and T_2 (Equation 6.47):

$$\partial_t \alpha_1 = \theta \frac{B}{A} (T_2 - T_1), \quad (6.50)$$

$$\partial_t T_1 = \theta \frac{1}{\phi_1 A} \left[-\frac{\rho_1}{\alpha_1} B - \zeta_1 (\Gamma_1 \rho_2 c_2^2 - \Gamma_2 \rho_1 c_1^2) \right] (T_2 - T_1), \quad (6.51)$$

$$\partial_t T_2 = \theta \frac{1}{\phi_2 A} \left[\frac{\rho_2}{\alpha_2} B - \zeta_2 (\Gamma_1 \rho_2 c_2^2 - \Gamma_2 \rho_1 c_1^2) \right] (T_2 - T_1). \quad (6.52)$$

where A defined in Equation 6.43, and B defined as:

$$B = \alpha_2 \Gamma_1 + \alpha_1 \Gamma_2 \quad (6.53)$$

The initial condition for the thermal relaxation step correlates with pressure equilibrium result obtained from the mechanical relaxation process, indicated by the superscript *. Similar to the mechanical relaxation procedure, establish the values η_k , for which the inverse values are associated with the coefficients of $(T_2 - T_1)$:

$$\frac{1}{\eta_k^T} = \frac{\frac{\rho_k}{\alpha_k} B + (-1)^{k-1} \zeta_k (\Gamma_1 \rho_2 c_2^2 - \Gamma_2 \rho_1 c_1^2)}{\phi_k A}. \quad (6.54)$$

In a manner similar to the pressure relaxation step, it is assumed that the quantities η_k^T remain unchanged over the period, $\eta_k^T = \eta_k^{T^*}$. Consequently, the solution is expressed as follows:

$$\partial_t T_1 = \theta \frac{1}{\eta_1^{T^*}} (T_2 - T_1), \quad (6.55)$$

$$\partial_t T_2 = -\theta \frac{1}{\eta_2^{T^*}} (T_2 - T_1). \quad (6.56)$$

An ordinary differential equation for the temperature difference $\Delta T = T_2 - T_1$ is obtained:

$$\partial_t \Delta T = -\theta \left(\frac{1}{\eta_1^{T^*}} + \frac{1}{\eta_2^{T^*}} \right) \Delta T, \quad (6.57)$$

leading to the exact solution after a certain time period Δt :

$$\Delta T^{**} = \Delta T^* e^{-\omega_T \Delta t}, \quad (6.58)$$

here

$$\omega_T = \theta \left(\frac{1}{\eta_1^{T^*}} + \frac{1}{\eta_2^{T^*}} \right). \quad (6.59)$$

In the context of the relaxation terms within the parent six-equation model, a process aimed at thermal equilibrium is considered. This is characterized by $\omega_T > 0$, indicating that heat transfer occurs from the higher-temperature phase to the lower-temperature phase when $\theta > 0$ [Pelanti \(2022\)](#).

The partial differential Equation 6.50 governing the α_1 can be solved by employing the result for ΔT^{**} , under the assumption that $\frac{B}{A}$ remains constant:

$$\alpha_1^{**} = \alpha_1^* + \left(\frac{B}{A} \right)^* \frac{\Delta T^*}{\left(\frac{1}{\eta_1^{T^*}} + \frac{1}{\eta_2^{T^*}} \right)} \left(1 - e^{-\omega_T \Delta t} \right). \quad (6.60)$$

where α_1^{**} represents the volume fraction after the thermal relaxation.

As $\theta \rightarrow +\infty$ indicating instantaneous thermal relaxation, the previously mentioned equation for the volume fraction approaches the equilibrium value:

$$\alpha_{1, \theta \rightarrow \infty}^{**} = \alpha_1^* + \left(\frac{B}{A} \right)^* \frac{\Delta T^*}{\left(\frac{1}{\eta_1^{T^*}} + \frac{1}{\eta_2^{T^*}} \right)}. \quad (6.61)$$

The equilibrium temperature is given by:

$$T_{\theta \rightarrow \infty} = \frac{\eta_1^{T^*} T_1^* + \eta_2^{T^*} T_2^*}{\eta_1^{T^*} + \eta_2^{T^*}}. \quad (6.62)$$

The equilibrium pressure after thermal relaxation (p^{**}), ensuring mixture-energy consistency, can be determined as follows:

$$\mathcal{E}^0 = \alpha_1^{**} \mathcal{E}_1 \left(p^{**}, \frac{(\alpha_1 \rho_1)^0}{\alpha_1^{**}} \right) + \alpha_2^{**} \mathcal{E}_2 \left(p^{**}, \frac{(\alpha_2 \rho_2)^0}{\alpha_2^{**}} \right). \quad (6.63)$$

6.3.3 Chemical relaxation procedure

The chemical relaxation process can be described by first introducing the reduced four-equation model, as discussed in [Pelanti \(2022\)](#). It is assumed that both phases have equal pressure, $p_1 = p_2 = p$, and equal temperature, $T_1 = T_2 = T$. The reduced model consists of $3 + d$ equations:

$$\begin{aligned}\partial_t(\alpha_1\rho_1) + \nabla \cdot (\alpha_1\rho_1\vec{u}) &= \mathcal{N}, \\ \partial_t(\alpha_2\rho_2) + \nabla \cdot (\alpha_2\rho_2\vec{u}) &= -\mathcal{N}, \\ \partial_t(\rho\vec{u}) + \nabla \cdot (\rho\vec{u} \otimes \vec{u} + p\mathbf{I}) &= 0, \\ \partial_t E + \nabla \cdot ((E + p)\vec{u}) &= 0,\end{aligned}\tag{6.64}$$

The speed of sound for the model is determined by:

$$\frac{1}{c_{4-eqt}^2} = \frac{1}{c_{5-eqt}^2} + \frac{\rho T C_{p1} C_{p2}}{C_{p1} + C_{p2}} \left(\frac{\Gamma_2}{\rho_2 c_2^2} - \frac{\Gamma_1}{\rho_1 c_1^2} \right)^2,\tag{6.65}$$

where c_{5-eqt} is given by in Equation 6.45.

The equations governing the volume fraction α_1 , pressure p , and temperature T are now presented (see [Demou et al. \(2022\)](#)):

$$\begin{aligned}\partial_t\alpha_1 + \vec{u} \cdot \nabla\alpha_1 + \rho c_{4-eqt}^2 \left[\alpha_1\alpha_2 \left(\frac{1}{\rho_2 c_2^2} - \frac{1}{\rho_1 c_1^2} \right) + \frac{T C_{p1} C_{p2}}{C_{p1} + C_{p2}} \left(\frac{\Gamma_2}{\rho_2 c_2^2} - \frac{\Gamma_1}{\rho_1 c_1^2} \right) \right. \\ \left. \left(\frac{\alpha_1\Gamma_2}{\rho_2 c_2^2} + \frac{\alpha_2\Gamma_1}{\rho_1 c_1^2} \right) \right] \nabla \cdot \vec{u} \\ = \mathcal{N}K_\alpha,\end{aligned}\tag{6.66}$$

$$\partial_t p + \vec{u} \cdot \nabla p + \rho c_{4-eqt}^2 \nabla \cdot \vec{u} = \mathcal{N}K_p,\tag{6.67}$$

$$\partial_t T + \vec{u} \cdot \nabla T + \frac{\rho c_{4-eqt}^2 T}{C_{p1} + C_{p2}} \left(\frac{C_{p1}\Gamma_1}{\rho_1 c_1^2} + \frac{C_{p2}\Gamma_2}{\rho_2 c_2^2} \right) \nabla \cdot \vec{u} = \mathcal{N}K_T,\tag{6.68}$$

where

$$K_\alpha = \frac{1}{H_T} \left[\left(\frac{\alpha_1}{\Gamma_1} + \frac{\alpha_2}{\Gamma_2} \right) (\alpha_1\phi_1 + \alpha_2\phi_2) + \alpha_1\alpha_2 \left(\frac{\chi_1}{\Gamma_1} - \frac{\chi_2}{\Gamma_2} \right) (\phi_1\zeta_2 - \phi_2\zeta_1) \right],\tag{6.69}$$

$$K_p = \frac{1}{H_T} \left[\left(\frac{\chi_1}{\Gamma_1} - \frac{\chi_2}{\Gamma_2} \right) (\alpha_1\phi_1\rho_2 + \alpha_2\phi_2\rho_1) + \left(\frac{\rho_2 c_2^2}{\Gamma_2} - \frac{\rho_1 c_1^2}{\Gamma_1} \right) (\alpha_1\phi_1 + \alpha_2\phi_2) \right].\tag{6.70}$$

$$\begin{aligned}K_T = \frac{1}{H_T} \left[\left(\frac{\chi_2}{\Gamma_2} - \frac{\chi_1}{\Gamma_1} \right) (\alpha_1\zeta_1\rho_2 + \alpha_2\zeta_2\rho_1) + \left(\frac{\rho_1 c_1^2}{\Gamma_1} - \frac{\rho_2 c_2^2}{\Gamma_2} \right) (\alpha_1\zeta_1 + \alpha_2\zeta_2) \right. \\ \left. + \left(\frac{\alpha_1}{\Gamma_1} + \frac{\alpha_2}{\Gamma_2} \right) (\rho_2 - \rho_1) \right],\end{aligned}\tag{6.71}$$

with

$$H_T = \alpha_1\alpha_2 \left(\frac{\rho_1 c_1^2}{\Gamma_1} - \frac{\rho_2 c_2^2}{\Gamma_2} \right) (\phi_1\zeta_2 - \phi_2\zeta_1) + \left(\frac{\alpha_1}{\Gamma_1} + \frac{\alpha_2}{\Gamma_2} \right) (\alpha_1\phi_1\rho_2 + \alpha_2\phi_2\rho_1).\tag{6.72}$$

where ϕ_k , and ζ_k given in Equation 6.48.

In many cases, it is practical to assume that the chemical relaxation process occurs while maintaining mechanical and thermal equilibrium, which is the scenario considered here. To initiate the chemical relaxation process, the focus shifts to the ordinary differential equations that include the mass transfer source term relevant to the reduced four-equation model Pelanti (2022). These ODEs describe the chemical relaxation dynamics of the model, specifically with respect to volume fraction α_1 , the partial density ($\alpha_1\rho_1$), and chemical potentials g_k . Using Equation 6.66, $\partial_t\alpha_1 = \mathcal{N}K_\alpha$, Equation 6.64, $\partial_t(\alpha_1\rho_1) = \mathcal{N}$, and Equation 6.67, $\partial_tp = \mathcal{N}K_p$, along with Equation 6.68, $\partial_tT = \mathcal{N}K_T$, the relationship $\partial_tg_k = \frac{1}{g_k}\partial_tp_k - s_k\partial_tT_k$ is utilized:

$$\partial_t\alpha_1 = \nu K_\alpha(g_2 - g_1), \quad (6.73)$$

$$\partial_tg_1 = \nu \left(\frac{K_p}{\rho_1} - s_1K_T \right) (g_2 - g_1), \quad (6.74)$$

$$\partial_tg_2 = \nu \left(\frac{K_p}{\rho_2} - s_2K_T \right) (g_2 - g_1), \quad (6.75)$$

$$\partial_t(\alpha_1\rho_1) = \nu(g_2 - g_1). \quad (6.76)$$

where s_k is the phasic entropy.

The initial condition for the chemical relaxation step aligns with the temperature equilibrium result obtained from the thermal relaxation step, indicated by the superscript **. Similar to the thermal relaxation procedure, establish the values η_k , for which the inverse values are associated with the coefficients of $(g_2 - g_1)$:

$$\frac{1}{\eta_k^g} = \frac{(-1)^{k-1}}{\rho_k} K_p - s_k K_T. \quad (6.77)$$

In a manner similar to the thermal relaxation step, it is assumed that the quantities η_k^g remain constant over time, $\eta_k^g = \eta_k^{g^{**}}$. Consequently, the solution is expressed as follows:

$$\partial_tg_1 = \nu \frac{1}{\eta_1^{g^{**}}} (g_2 - g_1), \quad (6.78)$$

$$\partial_tg_2 = -\nu \frac{1}{\eta_2^{g^{**}}} (g_2 - g_1). \quad (6.79)$$

An ordinary differential equation for the chemical potential $\Delta g = g_2 - g_1$ is obtained:

$$\partial_t\Delta g = -\nu \left(\frac{1}{\eta_1^{g^{**}}} + \frac{1}{\eta_2^{g^{**}}} \right) \Delta g. \quad (6.80)$$

leading to the exact solution after a certain time period Δt :

$$\Delta g^{***} = \Delta g^{**} e^{-\omega_g \Delta t}, \quad (6.81)$$

where

$$\omega_g = \nu \left(\frac{1}{\eta_1^{g^{**}}} + \frac{1}{\eta_2^{g^{**}}} \right). \quad (6.82)$$

A process toward chemical equilibrium, $\omega_g > 0$, is anticipated as the mass transfer takes place from the phase with the highest chemical potential to the phase with the lowest,

according to the chemical potential relaxation terms in the parent six-equation model, if $\nu > 0$ Pelanti (2022).

The partial differential equations Equation 6.73, and Equation 6.76 governing the α_1 and the $\alpha_1\rho_1$ can be solved using the solution for Δg^{***} , under the assumption that K_α remains constant:

$$\alpha_1^{***} = \alpha_1^{**} + K_\alpha^{**} \frac{\Delta g^{**}}{\left(\frac{1}{\eta_1^{g^{**}}} + \frac{1}{\eta_2^{g^{**}}}\right)} \left(1 - e^{-\omega_g \Delta t}\right), \quad (6.83)$$

$$(\alpha_1\rho_1)^{***} = (\alpha_1\rho_1)^{**} + \frac{\Delta g^{**}}{\left(\frac{1}{\eta_1^{g^{**}}} + \frac{1}{\eta_2^{g^{**}}}\right)} \left(1 - e^{-\omega_g \Delta t}\right), \quad (6.84)$$

where α_1^{***} represents the volume fraction, and $(\alpha_1\rho_1)^{***}$ denotes the partial density after chemical relaxation.

As $\nu \rightarrow +\infty$ indicating instantaneous chemical relaxation, the previously mentioned equation for the α_1 , and $(\alpha_1\rho_1)^{***}$ approaches the equilibrium value:

$$\alpha_1^{***} = \alpha_1^{**} + K_\alpha^{**} \frac{\Delta g^{**}}{\left(\frac{1}{\eta_1^{g^{**}}} + \frac{1}{\eta_2^{g^{**}}}\right)}, \quad (6.85)$$

$$(\alpha_1\rho_1)^{***} = (\alpha_1\rho_1)^{**} + \frac{\Delta g^{**}}{\left(\frac{1}{\eta_1^{g^{**}}} + \frac{1}{\eta_2^{g^{**}}}\right)}, \quad (6.86)$$

The equilibrium chemical potential is given by:

$$g_{\nu \rightarrow \infty} = \frac{\eta_1^{g^{**}} g_1^{**} + \eta_2^{g^{**}} g_2^{**}}{\eta_1^{g^{**}} + \eta_2^{g^{**}}}. \quad (6.87)$$

The equilibrium pressure after chemical relaxation (p^{***}), ensuring mixture-energy consistency, can be determined as follows:

$$\mathcal{E}^0 = \alpha_1^{***} \mathcal{E}_1 \left(p^{***}, \frac{(\alpha_1\rho_1)^{***}}{\alpha_1^{***}} \right) + \alpha_2^{***} \mathcal{E}_2 \left(p^{***}, \frac{(\alpha_2\rho_2)^{***}}{\alpha_2^{***}} \right). \quad (6.88)$$

As a final remark, it should be highlighted that the mass transfer process might result in full evaporation or condensation, which could potentially eliminate one of the phases. In the numerical model, it is crucial to maintain the presence of both phases. Therefore, a pure phase is represented as a mixture with a volume fraction $\alpha_k = 1 - \epsilon_R$, where $0 < \epsilon_R \ll 1$, such as $\epsilon_R = 10^{-8}$ (see for details Faccanoni et al. (2012), Pelanti and Shyue (2014)).

6.4 Validation test cases

This section presents the validation of the custom-developed solver through a variety of test cases. The validation begins with the shock tube and double rarefactions test cases, as an academic benchmark. Following this, three test cases directly related to PWR LOCA applications—the Edwards and O'Brien, the Canon experiment, also analyzed in Chapters 4&5, and the Bartak experiment—are simulated to further evaluate the solver's capability to simulate various physical scenarios.

Case 1:

The first test case is derived from [Chiapolino et al. \(2017\)](#), focusing on the behavior within a shock tube containing a liquid-vapor mixture. Initially, two mixtures with different pressures and temperatures are separated by a diaphragm. A one-meter-long shock tube with two chambers is separated at $x = 0.5$ m. The initial conditions are: on the left side, the pressure P_L is 2 bar, the temperature T_L is 394.2489 K; on the right side, the pressure P_R is 1 bar, the temperature T_R is 372.8827 K, and the mass fraction of the liquid phase y_L is 0.2 for both sides. The experiment begins when the diaphragm breaks, allowing observation of the changes in the mixtures on both sides. This test case is especially useful for checking the accuracy of mass transfer calculations. The fluids are modeled using a stiffened gas EoS, using parameters provided in Table 6.1.

Table 6.1: EoS parameters for liquid and vapor phases in the shock tube test by [Chiapolino et al. \(2017\)](#).

	Liquid	Vapor
γ	2.35	1.43
P_∞ (Pa)	1×10^9	0
q (J.kg ⁻¹)	-1167×10^3	2030×10^3
q' (J.kg ⁻¹ .K ⁻¹)	0	-23.4×10^3
C_v (J.kg ⁻¹ .K ⁻¹)	1816	1040

The results are displayed after 0.8 ms in Figures 6.1 to 6.9, covering various scenarios. Figure 6.1 shows the comparison of convergence studies for density, while Figure 6.2 presents the comparison of convergence studies for pressure. Additionally, Figure 6.3 illustrates the comparison of convergence studies for temperature. Figure 6.4 shows a comparison of pressure profiles using 1000 nodes with HLLC first, second, and third order schemes, where HLLC represents the first order, HLLC 2 represents the second order, and HLLC 3 represents the third order solutions. Figure 6.5 presents a comparison of temperature profiles using 1000 nodes with HLLC first, second, and third-order schemes. Figures 6.6 to 6.9 compare the results obtained from the solver (1000 nodes, second order) with the solutions available in the literature [Carlier \(2019\)](#) which is depicted as Ref. in the Legendre. Figure 6.6 compares the results for density, Figure 6.7 compares the results for pressure, Figure 6.8 compares the results for temperature, and Figure 6.9 compares the results for the mass fraction of the liquid. The results obtained from the solver show good agreement with the reference solutions. In each figure, the left panel represents results without mass transfer, and the right panel represents results with mass transfer. Without mass transfer, the density profile reveals a clear initial contact discontinuity, which moves due to the initial temperature gradient (shifting from $x = 0.5$ m to around $x = 0.6$ m at $t = t_{\max}$), and exhibits two nonlinear waves: a rarefaction and a shock. In contrast, with mass transfer activated, the density profile still shows the initial contact discontinuity but is influenced by liquefaction and evaporation. The temperature profile without mass transfer shows a structure with four distinct regions, defined by nonlinear waves and a contact discontinuity. With mass transfer, the temperature evolves due to the initial temperature gradient and subsequent liquefaction and evaporation, resulting in an equilibrium temperature between the shock and the rarefaction.

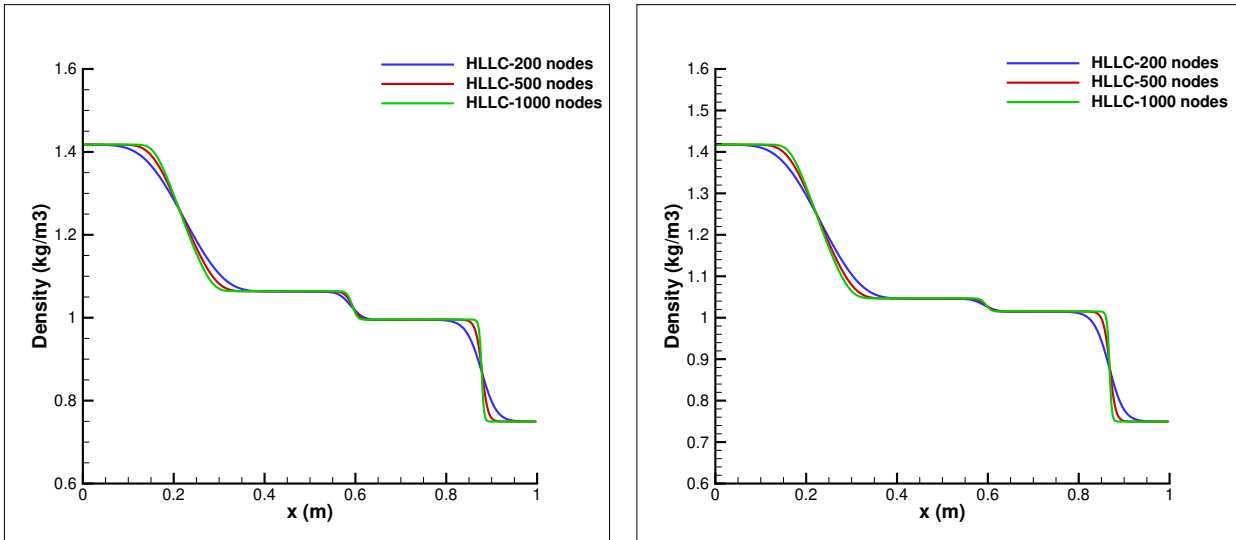


Figure 6.1: Comparison of convergence studies for density: (left) without mass transfer and (right) with mass transfer, using the HLLC scheme with 200, 500, and 1000 nodes, case 1, $t = 0.8ms$.

Case 2:

A double rarefaction tube problem, as proposed in [Zein et al. \(2010\)](#), and [Goncalves and Zeidan \(2018\)](#), is considered with an initial velocity discontinuity located at the midpoint of the tube. For this test, a one-meter-long tube filled with liquid water at atmospheric pressure and a density of 1150 kg/m^3 is utilized. Initially, a weak volume fraction of vapor (0.01) is added to the liquid. The left side velocity is set to -2 m/s , while the right side velocity is set to 2 m/s . The fluid behavior is governed by the stiffened gas EoS, using parameters provided in Table 6.2.

The results are displayed after 0.8 ms in Figures 6.10 to 6.15, covering various scenarios. Figure 6.10 shows the comparison of convergence studies for pressure, while Figure 6.11 presents the comparison of convergence studies for velocity. Based on these comparisons, it was decided to utilize the HLLC second-order scheme with 5000 nodes for subsequent simulations. Therefore, all further simulations were conducted using the HLLC second-order scheme with 5000 nodes to ensure consistency and accuracy in the results. Figures 6.12 through 6.15 present profiles for different relaxation methods: pressure profiles in Figure 6.12, velocity profiles in Figure 6.13, void ratio profiles in Figure 6.14, and mass fraction of vapor profiles in Figure 6.15. Five distinct relaxation procedures are analyzed:

- Instantaneous mechanical relaxation (p-relax)
- Instantaneous mechanical relaxation with finite-rate thermal relaxation (pT-finite)
- Instantaneous mechanical and thermal relaxation (pT)
- Instantaneous mechanical and thermal relaxation with finite-rate chemical relaxation (pTg-finite)
- Instantaneous mechanical, thermal, and chemical relaxation (pTg)

These figures illustrate the effects of each relaxation method on the respective physical quantities. Phase transition therefore only initiated in the last two scenarios. For this test case, the chemical relaxation procedure is initiated only at the point where the equilibrium temperature exceeds the saturation temperature. For the case of instantaneous

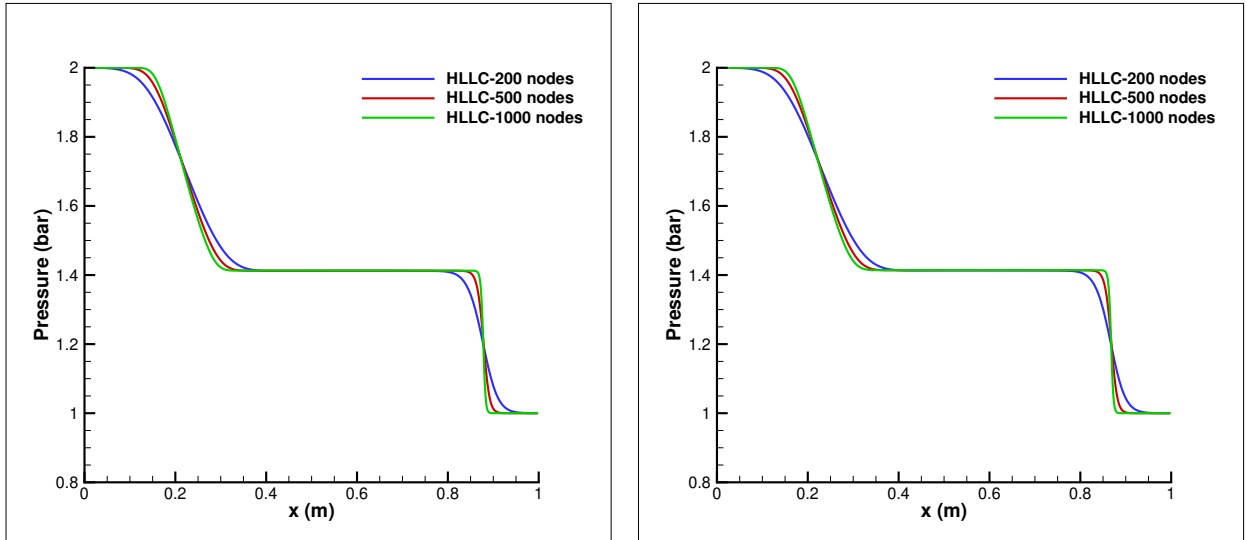


Figure 6.2: Comparison of convergence studies for pressure: (left) without mass transfer and (right) with mass transfer, using the HLLC scheme with 200, 500, and 1000 nodes, case 1, $t = 0.8ms$.

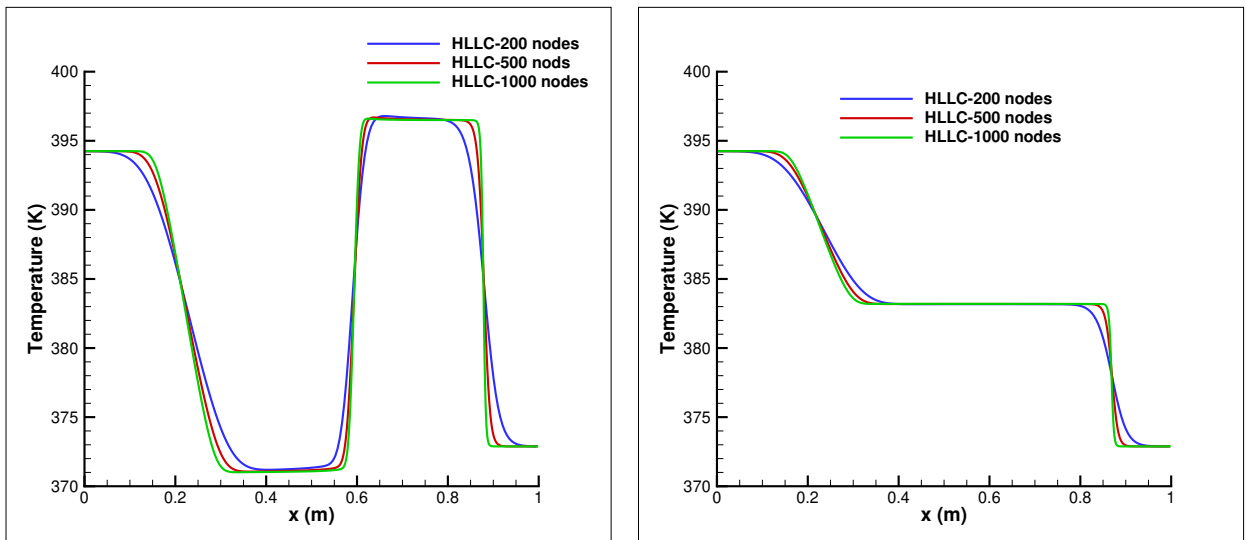


Figure 6.3: Comparison of convergence studies for temperature: (left) without mass transfer and (right) with mass transfer, using the HLLC scheme with 200, 500, and 1000 nodes, case 1, $t = 0.8ms$.

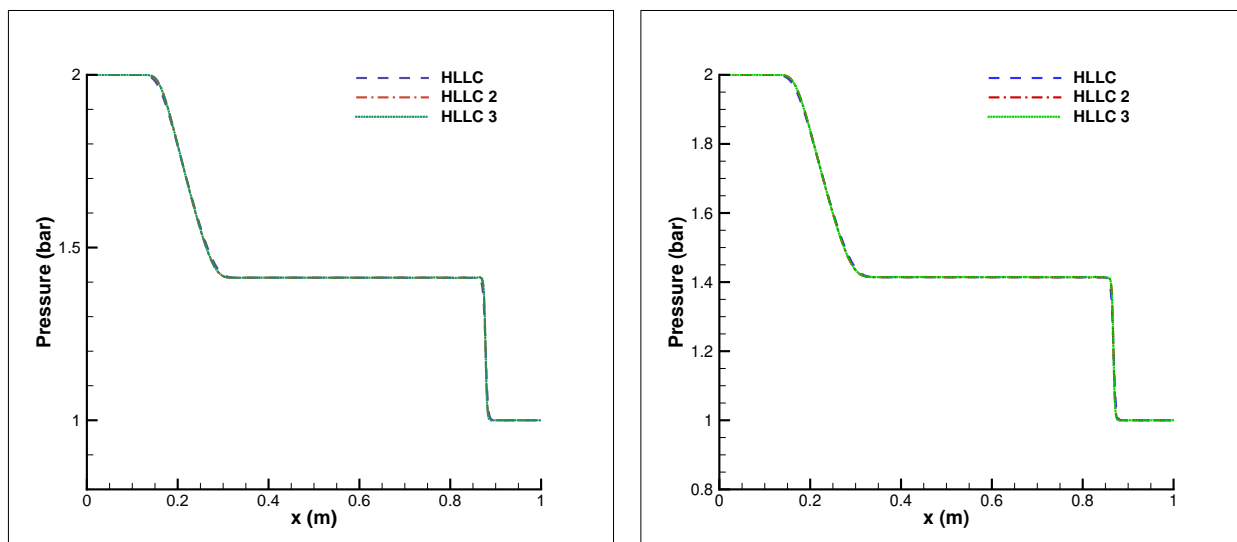


Figure 6.4: Comparison of pressure profiles using 1000 nodes with HLLC first, second, and third order: (left) without mass transfer and (right) with mass transfer, case 1, $t = 0.8$ ms.

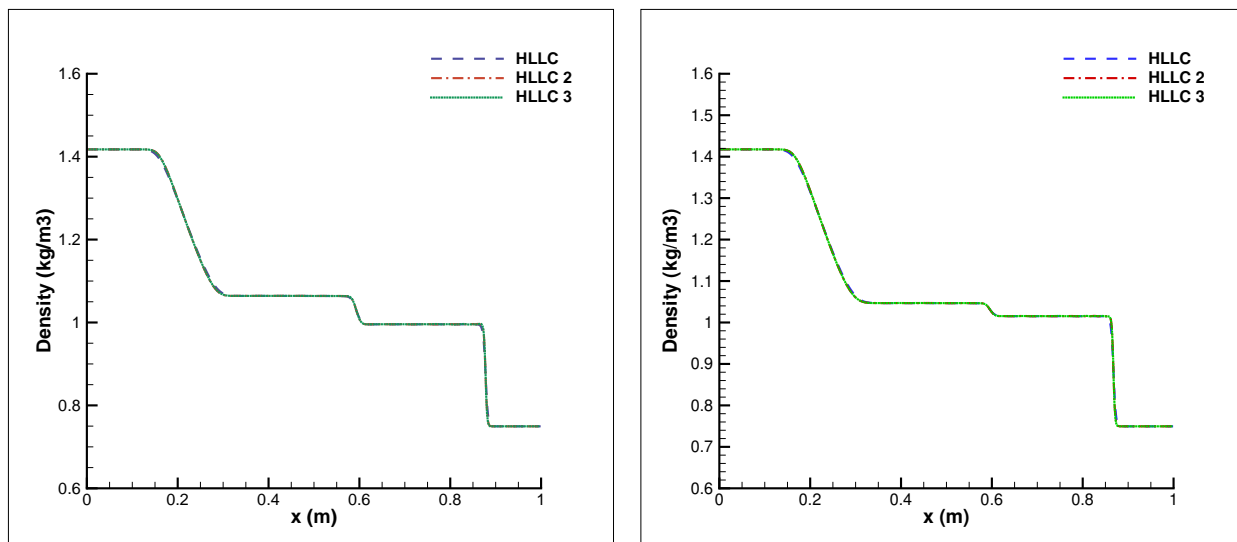


Figure 6.5: Comparison of density profiles using 1000 nodes with HLLC first, second, and third order: (left) without mass transfer and (right) with mass transfer, case 1, $t = 0.8$ ms.

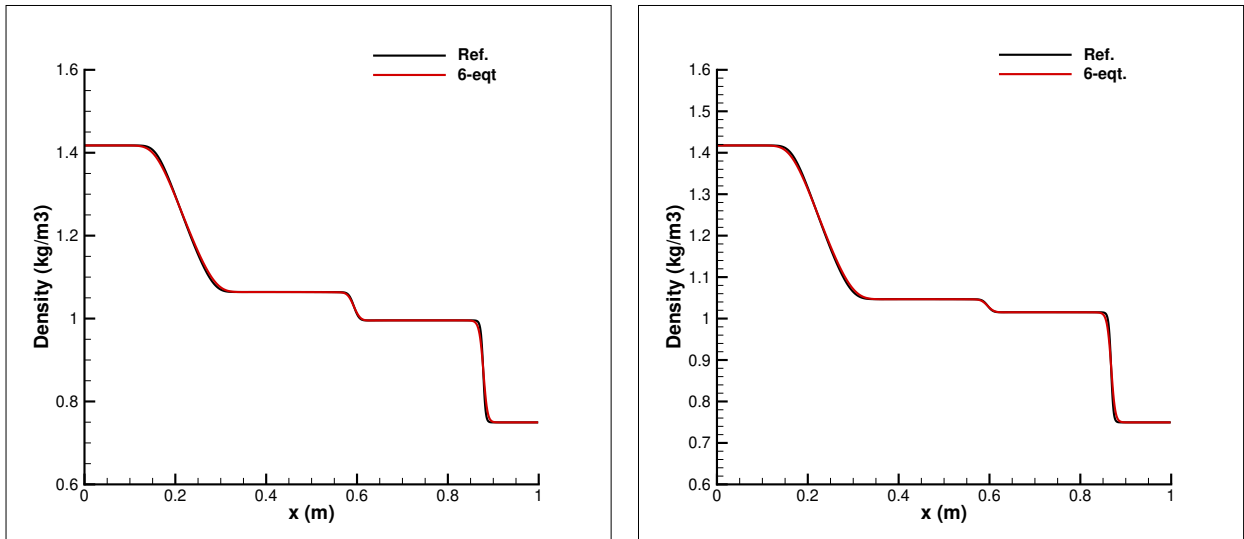


Figure 6.6: Comparison of the density profiles from the solver results with the reference solution: (left) without mass transfer and (right) with mass transfer, case 1, $t = 0.8ms$.

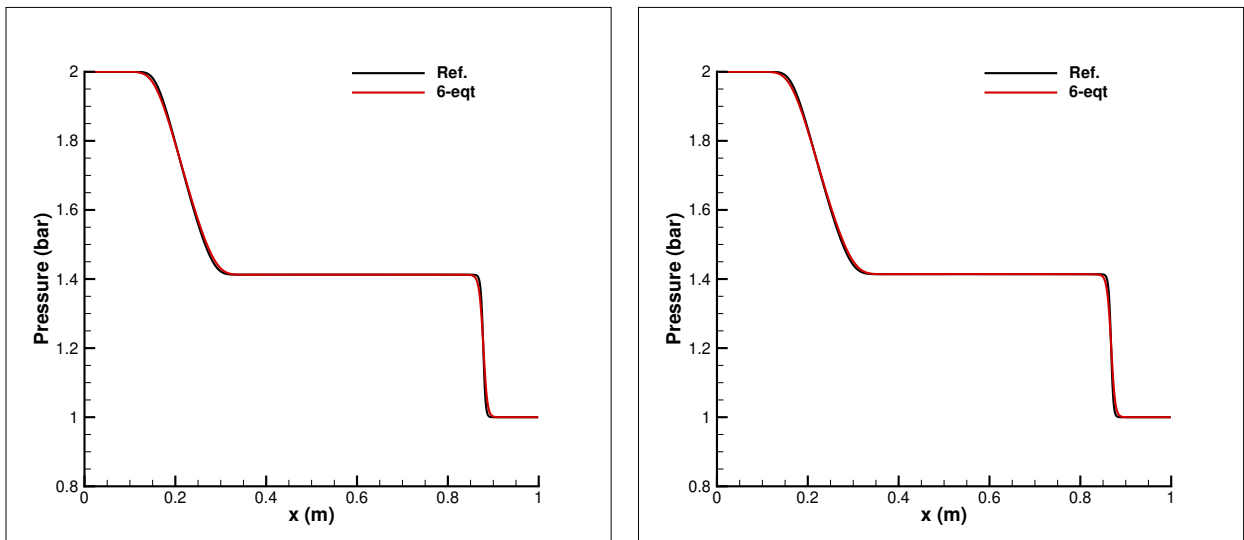


Figure 6.7: Comparison of the pressure profiles from the solver results with the reference solution: (left) without mass transfer and (right) with mass transfer, case 1, $t = 0.8ms$.

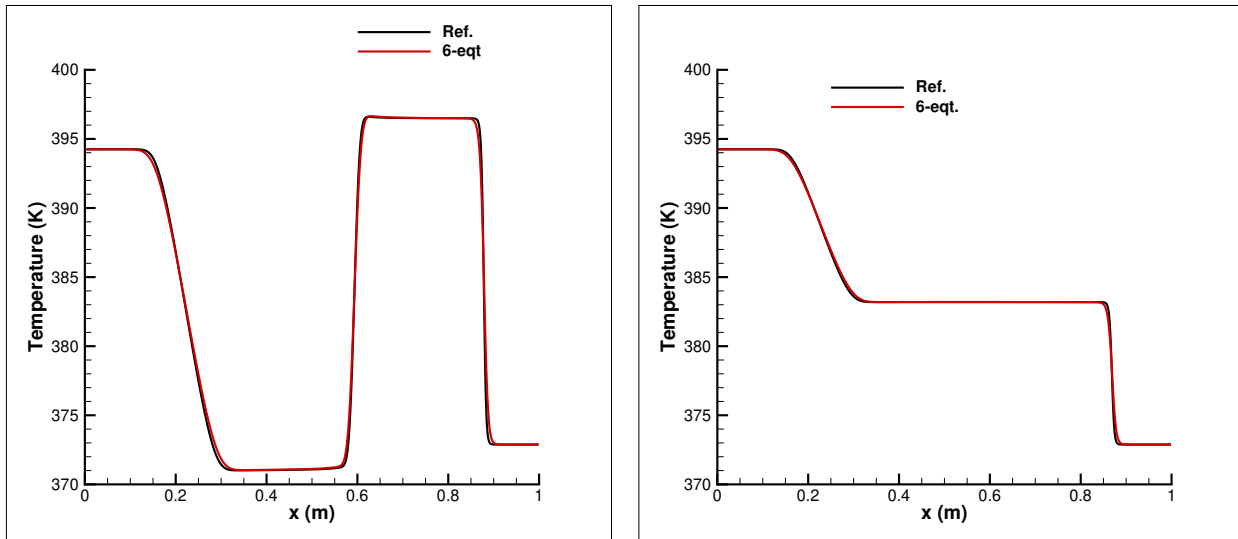


Figure 6.8: Comparison of the temperature profiles from the solver results with the reference solution: (left) without mass transfer and (right) with mass transfer, case 1, $t = 0.8ms$.

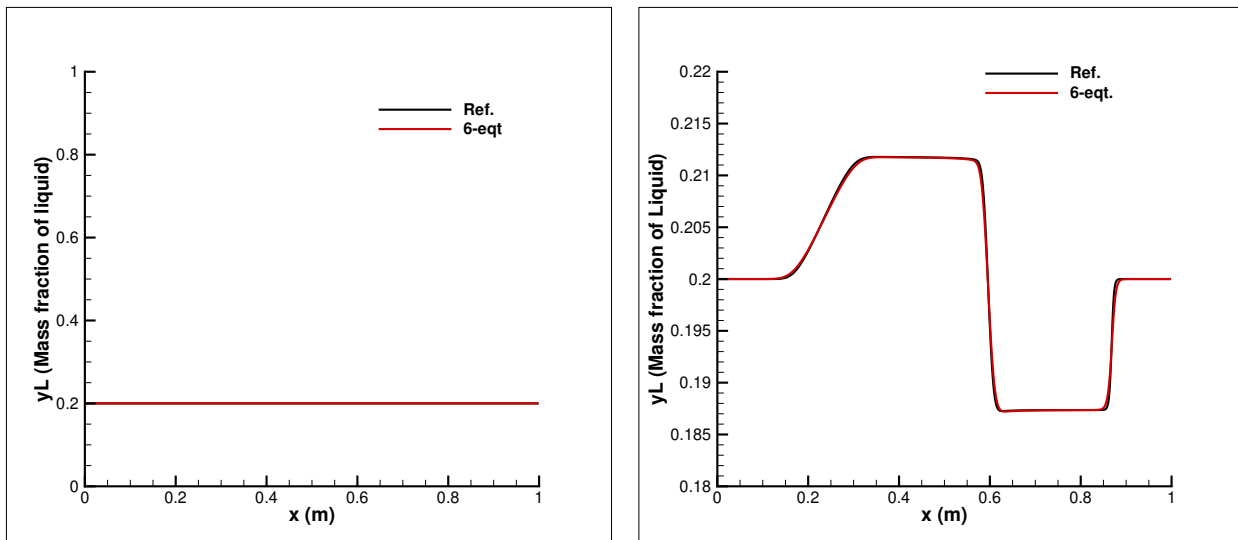


Figure 6.9: Comparison of the liquid mass fraction profiles from the solver results with the reference solution: (left) without mass transfer and (right) with mass transfer, case 1, $t = 0.8ms$.

mechanical relaxation with finite-rate thermal relaxation, the volume fraction α is updated using Equation 6.60, where $\theta = 2000 \text{ Pa/s.K}$. For the case of instantaneous mechanical and thermal relaxation with finite-rate chemical relaxation, the volume fraction α is updated using Equation 6.83, and the partial density $\alpha_1 \rho_1$ is updated using Equation 6.84, where $\nu = 10^{-4} \text{ Pa.kg}^2/\text{s.J}^2$ Pelanti (2022). In all scenarios, the solution exhibits two rarefactions traveling in opposite directions, leading to a drop in pressure at the center of the tube and a corresponding increase in the vapor volume fraction. Notably, if the mass transfer is not initiated, the vapor mass fraction stays unchanged, indicating that the cavitation process is purely mechanical. Conversely, if mass transfer is initiated, the result includes two evaporation waves. Under these circumstances, the vapor mass fraction rises in the central part of the tube, and the pressure reaches its saturation point. In contrast, in the absence of mass transfer, the pressure keeps dropping in the middle of the tube. As expected, the computational cost increases with the complexity of the relaxation procedure. For the *p-relax* case, the total computational time is 840 seconds. When the *pT-relax* strategy is applied, the computational time increases by approximately 8%, while the *pTg-relax* strategy results in an increase of approximately 21%. It is important to note that, for cases involving substantial phase transitions, where evaporation and condensation influence the flow, the *pTg* strategy, is crucial to capture the dynamics accurately. Additionally, for scenarios involving metastable states during depressurization, finite-rate mass transfer models provide a more accurate representation of the slow evolution toward equilibrium compared to abrupt instantaneous relaxation.

Table 6.2: EoS parameters for liquid and vapor phases in Case 2.

	Liquid	Vapor
γ	2.35	1.43
P_∞ (Pa)	1×10^9	0
q (J.kg ⁻¹)	-1167×10^3	2030×10^3
q' (J.kg ⁻¹ .K ⁻¹)	0	-23.4×10^3
C_p (J.kg ⁻¹ .K ⁻¹)	4267	1487

Case 3:

The experiment, originally proposed by Edwards and O'Brien (1970), represents a benchmark challenge for assessing and validating computational solvers, as noted in the comparative analysis by Garner (1973). The primary objective of this experiment was to replicate the phase transition phenomena, which are critical in safety assessments of water-cooled nuclear reactors. Specifically, the experiment closely simulates scenarios of loss-of-coolant accidents in Pressurized Water Reactors, where rapid depressurization leads to significant phase changes.

The experimental setup comprised a horizontal water-filled heating pipe, designed to maintain the internal pressure above the saturation threshold. This configuration aimed to reproduce the conditions prevalent during a loss-of-coolant accident. The pipe itself measured 4.096 meters in length with an inner diameter of 7.315 cm, as illustrated in Figure 6.16. A key aspect of the experiment involved the use of a glass disk, positioned at the pipe's extremity. This disk was engineered to fracture upon the impact of a pellet fired from a gun, thereby initiating the rapid depressurization process. The complete opening of the disk was estimated to occur within 1 ms.

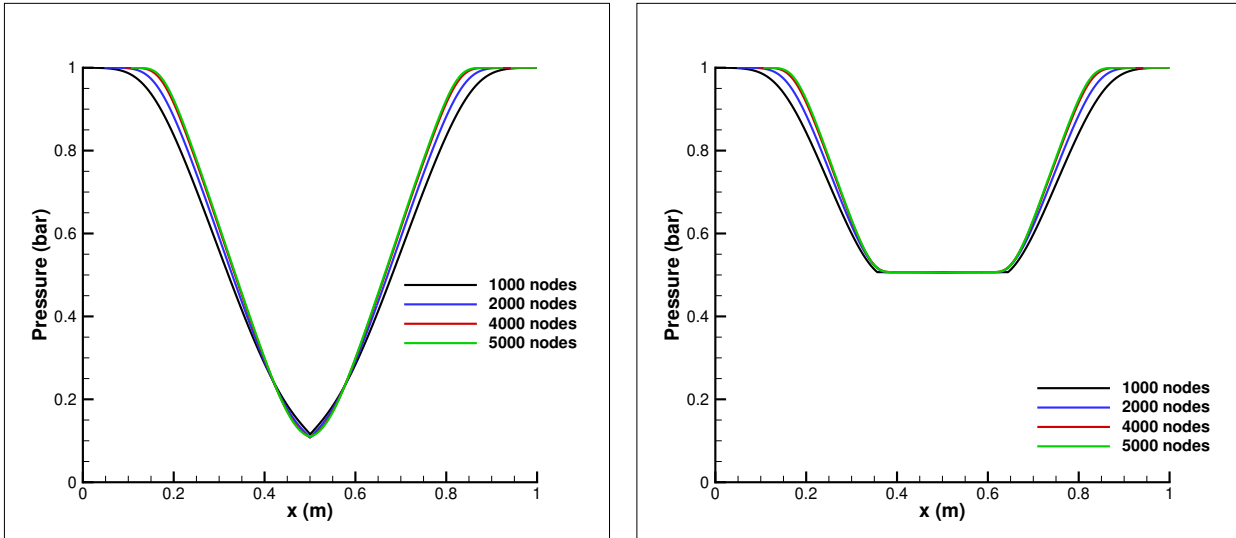


Figure 6.10: Comparison of convergence studies for pressure: (left) without mass transfer and (right) with mass transfer, using the HLLC scheme with 1000, 2000, 4000, and 5000 nodes, case 2, $t = 3.2ms$.

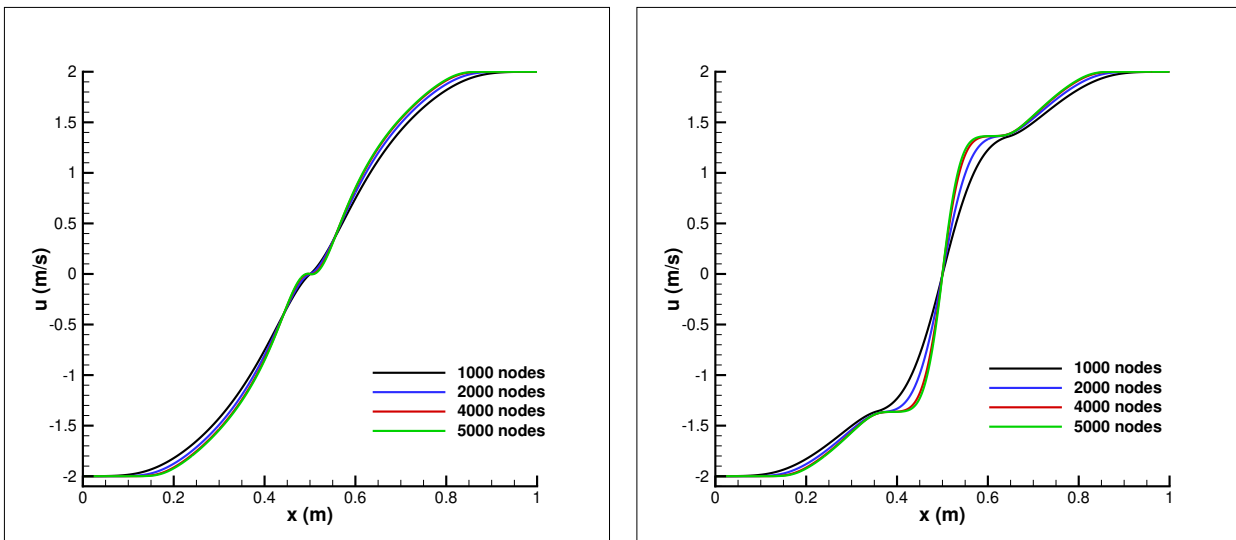


Figure 6.11: Comparison of convergence studies for velocity: (left) without mass transfer and (right) with mass transfer, using the HLLC scheme with 1000, 2000, 4000, and 5000 nodes, case 2, $t = 3.2ms$.

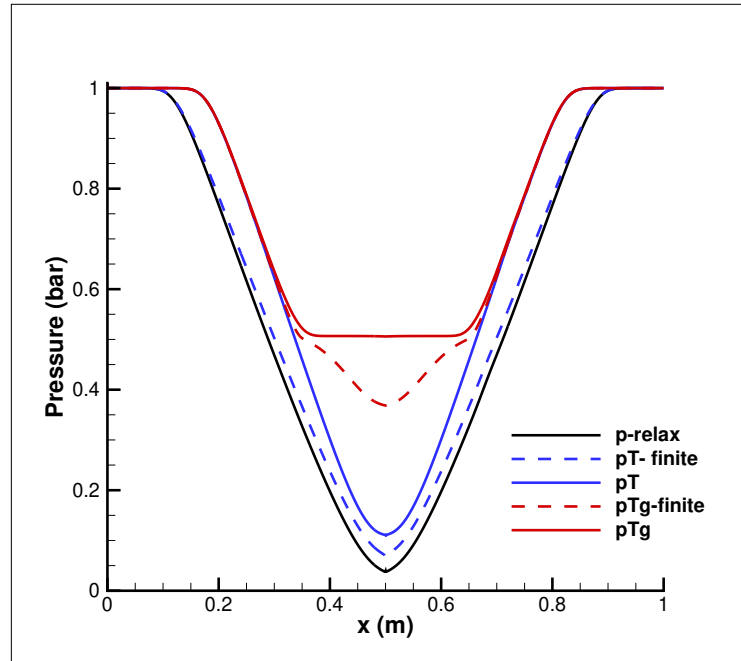


Figure 6.12: Pressure profiles for different relaxation methods: instantaneous mechanical relaxation (p-relax, black solid line), instantaneous mechanical relaxation and finite-rate thermal relaxation (pT-finite, blue dashed line), instantaneous mechanical and thermal relaxation (pT, blue solid line), instantaneous mechanical and thermal relaxation with finite-rate chemical relaxation (pTg-finite, red dashed line), and instantaneous mechanical, thermal, and chemical relaxation (pTg, red solid line), case 2, $t = 3.2$ ms.

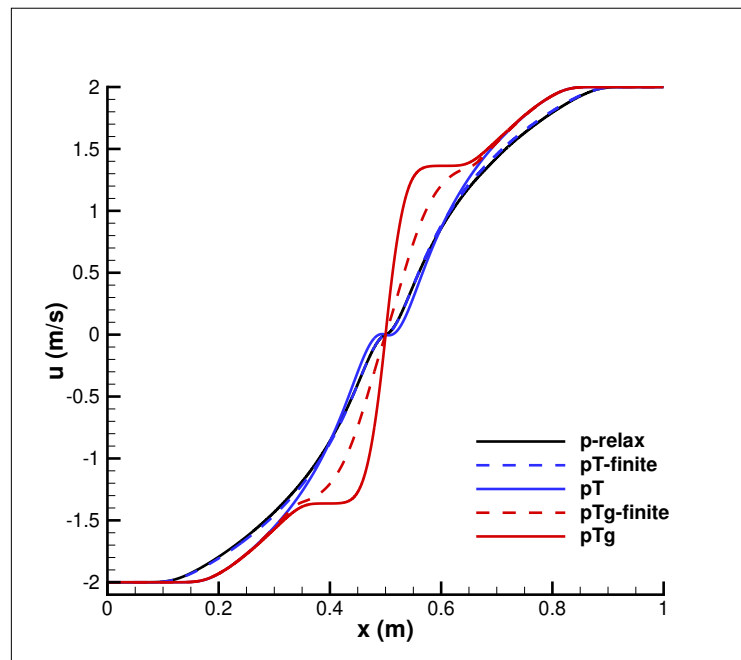


Figure 6.13: Velocity profiles for different relaxation methods: instantaneous mechanical relaxation (p-relax, black solid line), instantaneous mechanical relaxation and finite-rate thermal relaxation (pT-finite, blue dashed line), instantaneous mechanical and thermal relaxation (pT, blue solid line), instantaneous mechanical and thermal relaxation with finite-rate chemical relaxation (pTg-finite, red dashed line), and instantaneous mechanical, thermal, and chemical relaxation (pTg, red solid line), case 2, $t = 3.2$ ms.

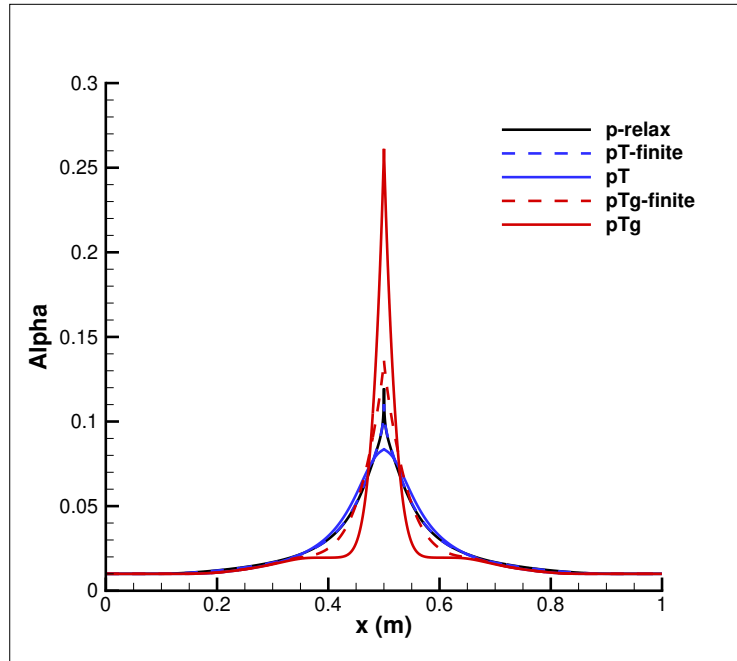


Figure 6.14: Void ratio profiles for different relaxation methods: instantaneous mechanical relaxation (p-relax, black solid line), instantaneous mechanical relaxation and finite-rate thermal relaxation (pT-finite, blue dashed line), instantaneous mechanical and thermal relaxation (pT, blue solid line), instantaneous mechanical and thermal relaxation with finite-rate chemical relaxation (pTg-finite, red dashed line), and instantaneous mechanical, thermal, and chemical relaxation (pTg, red solid line), case 2, $t = 3.2$ ms.

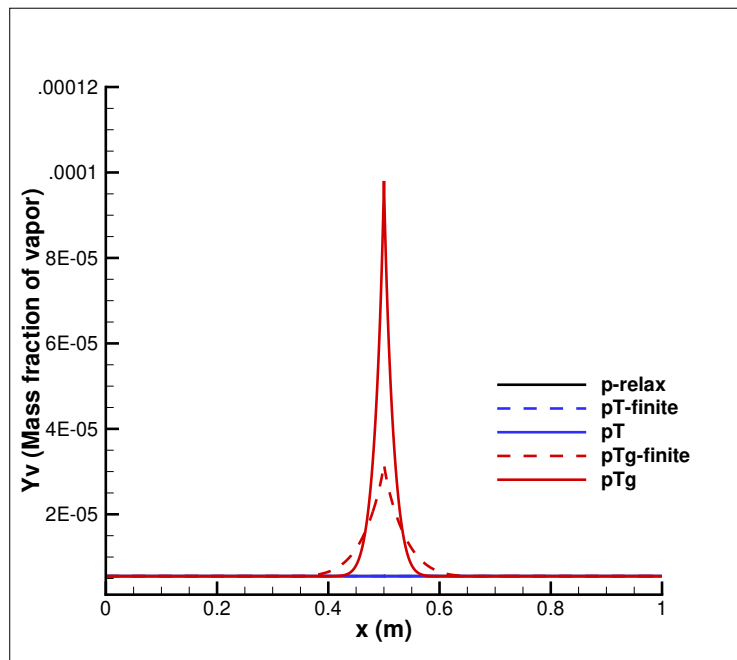


Figure 6.15: Vapor mass fraction profiles for different relaxation methods: instantaneous mechanical relaxation (p-relax, black solid line), instantaneous mechanical relaxation and finite-rate thermal relaxation (pT-finite, blue dashed line), instantaneous mechanical and thermal relaxation (pT, blue solid line), instantaneous mechanical and thermal relaxation with finite-rate chemical relaxation (pTg-finite, red dashed line), and instantaneous mechanical, thermal, and chemical relaxation (pTg, red solid line), case 2, $t = 3.2$ ms.

During the experiment, several monitoring stations were used on the longitudinal section of the pipeline, which recorded pressure, temperature, and density fluctuations in real-time. These measurements were essential for the investigation of phase transition processes and modelling checks.

It is noteworthy that post-experiment observations revealed a small amount of shattered glass surrounding the pipe's opening, suggesting a reduction of approximately 12.5% in the effective flow area compared to the pipe's cross-sectional area. The initial experimental conditions were characterized by pressures ranging from 3.55 to 17.34 MPa and temperatures between 514.8 to 616.5 K. The present study focuses on an experimental scenario initiated with initial conditions of 70 bar and 502 K. Pressure measurements were systematically monitored at both ends of the pipe, specifically at the GS1 and GS7 positions, while temperature readings were obtained at the GS5 location. In addition to these measurements, a densitometer utilizing advanced X-ray technology was positioned at GS5 to accurately determine the void fraction.

To approximate this experiment numerically, a one-dimensional geometry design was used. The computational domain was discretized using a mesh consisting of 1000 cells. The boundary conditions are defined similar to the experimental configuration: the closed-end condition of the pipe, and the other end connected to the atmospheric pressure tank. For simplicity, a full break scenario was considered.

The initial conditions for the Edwards and O'Brien test are provided in Table 6.3. Since the initial temperature is similar to that of the Canon experiment, the equation of state parameters used are the same and are provided in Table 6.4.

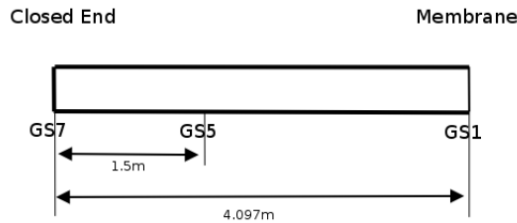


Figure 6.16: Schematic of experiment facility for the Edwards and O'Brien.

Table 6.3: Initial conditions for the Edwards and O'Brien experiment.

Parameter	Pipe	Tank
α_l	$1 - 10^{-3}$	10^{-3}
α_v	10^{-3}	$1 - 10^{-3}$
ρ_l (kg.m ⁻³)	809.40	802.2
ρ_v (kg.m ⁻³)	35.03	0.50
P_l (bar)	70	1
P_v (bar)	70	1

The results, displayed after 600 ms, are presented in Figures 6.17 through 6.22. Specifically, Figure 6.17 illustrates the void ratio profiles obtained using different relaxation models. Figure 6.18 offers a comparison between the experimental results, the pTg-finite results from the current study, and the RELAP5 results from the literature. Figure 6.19 presents the pressure profile at the G5 location for various relaxation models, while Figure 6.20 provides a similar comparison with experimental data and RELAP5 outcomes. Additionally,

Table 6.4: EoS parameters for liquid and vapor phases for the Edwards and O'Brien experiment.

	Liquid	Vapor
γ	1.66	1.33
P_∞ (Pa)	7693×10^5	0
q (J.kg ⁻¹)	-13.5×10^5	20.3×10^5
q' (J.kg ⁻¹ .K ⁻¹)	11.6×10^3	2.3×10^3
C_p (J.kg ⁻¹ .K ⁻¹)	4670	1550

Figure 6.21 displays the pressure profile at the G7 location under different relaxation conditions, and Figure 6.22 concludes with a comparison of these results against experimental observations and RELAP5 data from the literature, specifically as cited in [Sun et al. \(2021\)](#).

Finite-rate mass transfer is governed by the mass transfer relaxation function ν , which is described by the equation below. However, the exact magnitude of ν is not well established. Consequently, a correlation inspired by previous studies has been adopted [Downar-Zapolski et al. \(1996\)](#), [Pelanti \(2022\)](#).

$$\nu = \Lambda \alpha_v^{1.2} \left(\frac{p_{\text{sat}} - p}{p_{\text{crit}} - p_{\text{sat}}} \right)^{0.36}, \quad \Lambda = 4 \text{ Pa} \cdot \text{kg}^2 / (\text{s} \cdot \text{J}^2), \quad (6.89)$$

where p_{crit} is the pressure of the critical point.

The results revealed that the vapor generation rate within the first millisecond was relatively slow, with the numerical results slightly underestimating the experimental observations. Subsequently, it was observed that around 100 ms, the void fraction was higher in the simulations compared to the experimental data, a trend that persisted until the conclusion of the experiment.

Notably, the computational model predicted an earlier onset of vaporization than what was documented in the experiments (approximately 50 ms before). Furthermore, the model does not account for head losses or pipe deformation, both of which are known to slow down wave propagation. This limitation may explain the early prediction of vaporization. The model shows good agreement with the RELAP5 results, which have been selected as a reference for comparison in the literature [Sun et al. \(2021\)](#). Absolute and mean absolute error analyses were conducted for both the G5 and G7 locations, comparing the models with the RELAP5 results. The RELAP5 results produced the lowest mean absolute error, performing slightly better than the pTg-finite result (see Appendix C).

Case 4:

The test case proposed by [Riegel \(1978\)](#), which also known as the Canon experiment, as explained before. This experiment involves inducing a complete system breach to rapidly depressurize a horizontal pipe. As depicted in Figure 6.23, the pipe used in this study is 4.389 meters long with an internal diameter of 102.3 millimeters. One end of the pipe is sealed with a membrane, while the other end is closed. In the Canon experiments, the void fraction is measured at a specific point, while pressure readings are recorded at various locations along the pipe.

For the experiment, the initial pressure and temperature of the pipe were set to 32 bar and 220°C, while the pressure and temperature of the experimental environment were 1 bar and ambient temperature. However, in the numerical simulation, the environment was filled with steam at 1 bar and 220°C instead of air. The numerical simulations were conducted using a 1D simplified geometry with a mesh of 1000 cells, with one side closed and the other

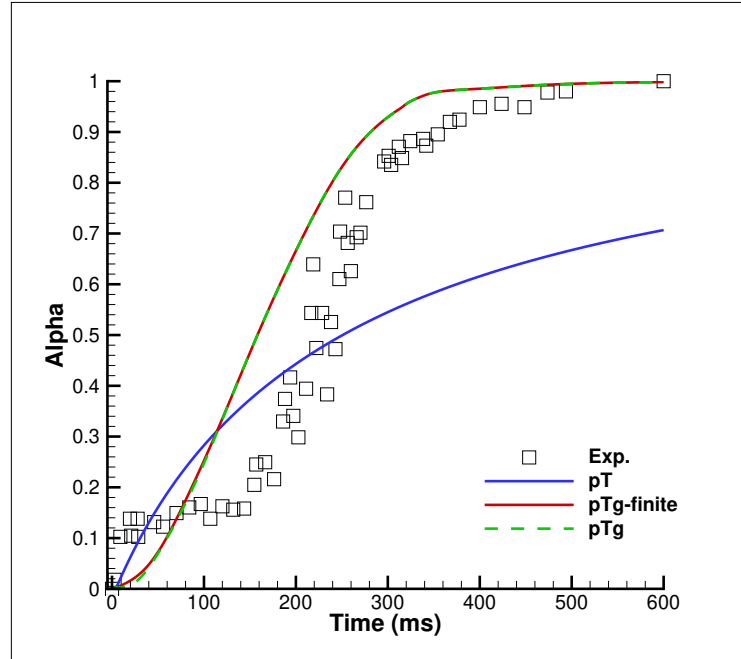


Figure 6.17: Comparison of void ratio profiles at location G5 (2.627 m upstream from the breach) from the Edwards O'Brien experiment: experimental results (Exp., black square markers), instantaneous mechanical and thermal relaxation (pT, blue solid line), instantaneous mechanical, thermal, and finite-rate chemical relaxation (pTg-finite, red solid line), and instantaneous mechanical, thermal, and chemical relaxation (pTg, green dashed line), case 3.

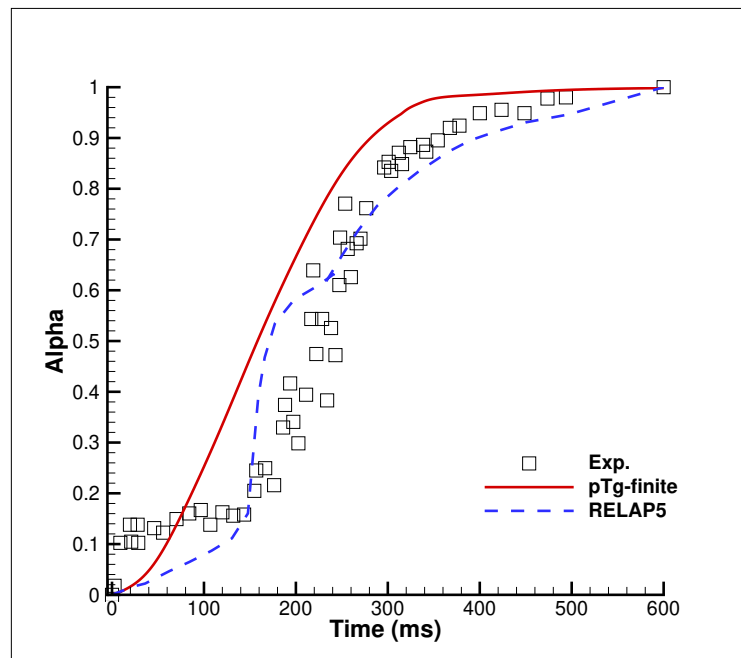


Figure 6.18: Comparison of void ratio profiles at location G5 (2.627 m upstream from the breach) from the Edwards O'Brien experiment: experimental results (Exp., black square markers), pTg-finite results (pTg-finite, red solid line) from the solver, and RELAP5 results (RELAP5, blue dashed line) obtained from the literature by [Sun et al. \(2021\)](#), case 3.

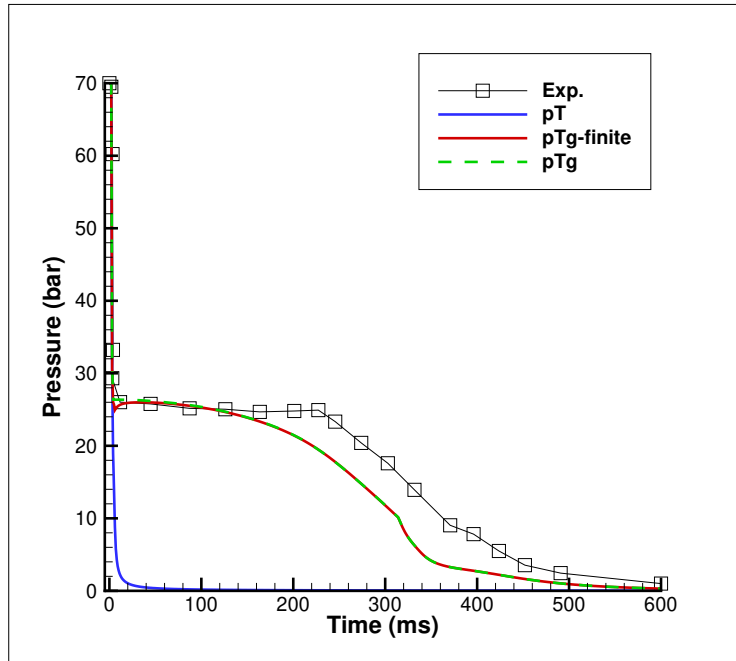


Figure 6.19: Comparison of pressure profiles at location G5 (2.627 m upstream from the breach) from the Edwards O’Brien experiment: experimental results (Exp., black square markers), instantaneous mechanical and thermal relaxation (pT, blue solid line), instantaneous mechanical, thermal, and finite-rate chemical relaxation (pTg-finite, red solid line), and instantaneous mechanical, thermal, and chemical relaxation (pTg, green dashed line), case 3.

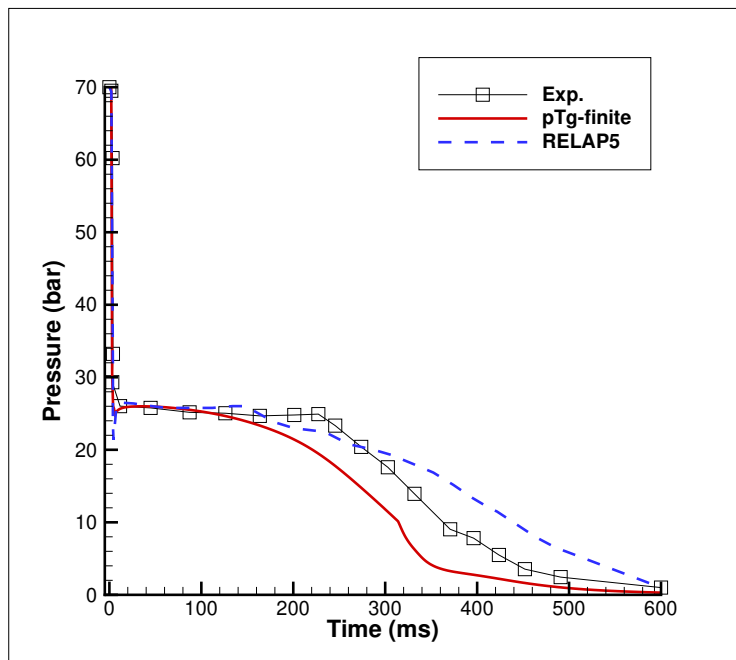


Figure 6.20: Comparison of pressure profiles at location G5 (2.627 m upstream from the breach) from the Edwards O’Brien experiment: experimental results (Exp., black square markers), pTg-finite results (pTg-finite, red solid line) from the solver, and RELAP5 results (RELAP5, blue dashed line) obtained from the literature by Sun et al. (2021), case 3.

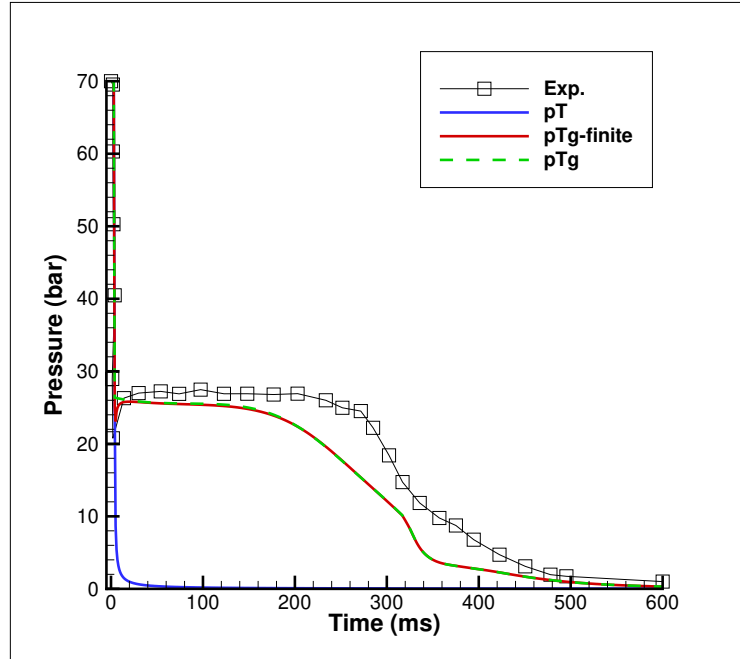


Figure 6.21: Comparison of pressure profiles at location G7 (4.017 m upstream from the breach) from the Edwards O'Brien experiment: experimental results (Exp., black square markers), instantaneous mechanical and thermal relaxation (pT, blue solid line), instantaneous mechanical, thermal, and finite-rate chemical relaxation (pTg-finite, red solid line), and instantaneous mechanical, thermal, and chemical relaxation (pTg, green dashed line), case 3.

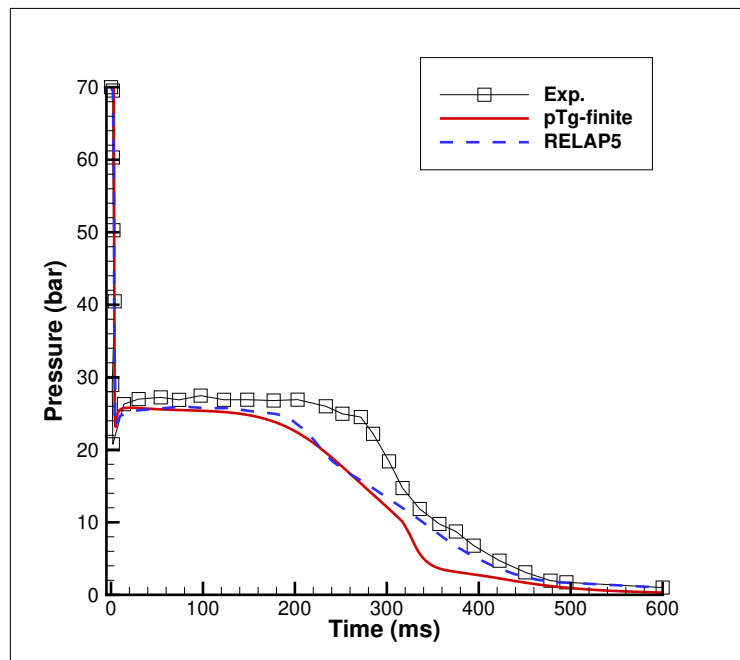


Figure 6.22: Comparison of pressure profiles at location G7 (4.017 m upstream from the breach) from the Edwards O'Brien experiment: experimental results (Exp., black square markers), pTg-finite results (pTg-finite, red solid line) from the solver, and RELAP5 results (RELAP5, blue dashed line) obtained from the literature by [Sun et al. \(2021\)](#), case 3.

connected to an atmospheric pressure tank. The stiffened gas equation of state and initial conditions are detailed in Table 6.5 and Table 6.6.

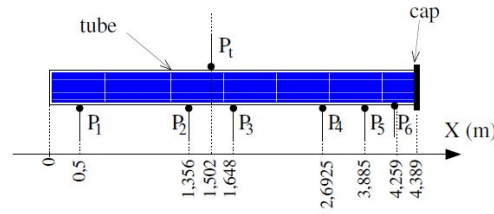


Figure 6.23: Schematic of experiment facility for the Canon.

Table 6.5: EoS parameters for liquid and vapor phases for the case 4.

	Liquid	Vapor
γ	1.66	1.34
P_∞ (Pa)	769317123.86	0.00
q (J.kg ⁻¹)	-1359570.00	2032350.00
C_v (J.kg ⁻¹ .K ⁻¹)	2807.61	1162.00
q' (J.kg ⁻¹ .K ⁻¹)	11671.61	2351.11

Table 6.6: Initial conditions for the case 4.

	Pipe	Tank
α_l	$1 - 10^{-3}$	10^{-3}
α_v	10^{-3}	$1 - 10^{-3}$
ρ_l (kg.m ⁻³)	841.12	837.74
ρ_v (kg.m ⁻³)	16.72	0.52
P_l (bar)	32	1
P_v (bar)	32	1

The results, shown at 800 ms, are presented in Figures 6.24 through 6.29. Specifically, Figure 6.24 illustrates the void ratio profiles obtained using different relaxation models from the solver and compares these results with the HRM Tabulated EoS results from the literature [Lepareux \(1994\)](#). To address the substantial discrepancies between the initial numerical results and the experimental data, reference results from the literature were incorporated to enable a more meaningful comparison and improve the evaluation of the solver's performance. Also, Figure 6.25 and Figure 6.29 illustrate the pressure profiles at P1 and P5, respectively, obtained using different relaxation models from the solver, and compare these results with the HRM Tabulated EoS results from the literature. Finally, Figure 6.26, Figure 6.27, and Figure 6.28 show the results for the P2, P3, and P4 locations using different relaxation models.

The finite-rate mass transfer is controlled by the mass transfer relaxation function ν , described by the following equation. However, the precise value of ν remains uncertain. Therefore, a correlation inspired by previous research has been employed [Downar-Zapolski](#)

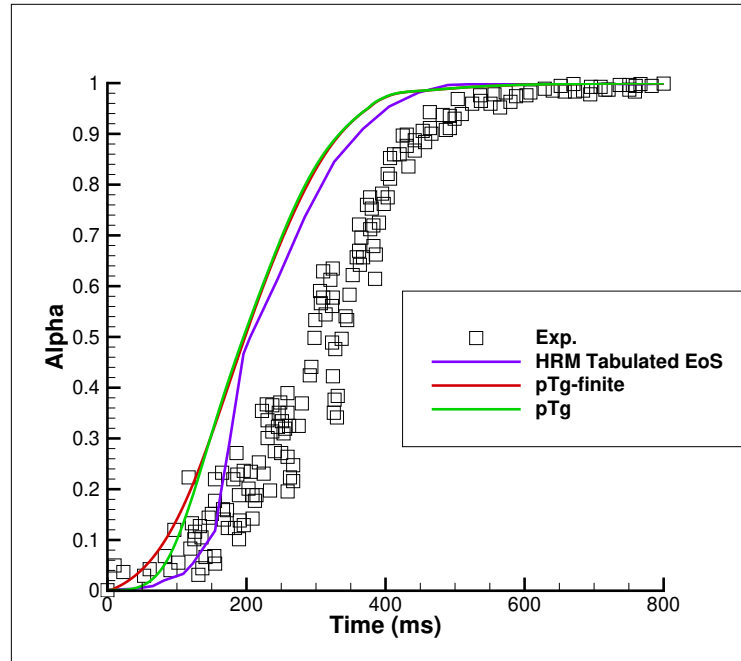


Figure 6.24: Comparison of void ratio profiles at location PT (2.887 m upstream from the breach) from the Canon experiment: experimental results (Exp., black square markers), instantaneous mechanical, thermal, and finite-rate chemical relaxation (pTg-finite, red solid line), and instantaneous mechanical, thermal, and chemical relaxation (pTg, green solid line) from the solver, and HRM Tabulated EoS results (HRM Tabulated EoS, purple solid line) obtained from the literature by [Lepareux \(1994\)](#) case 4.

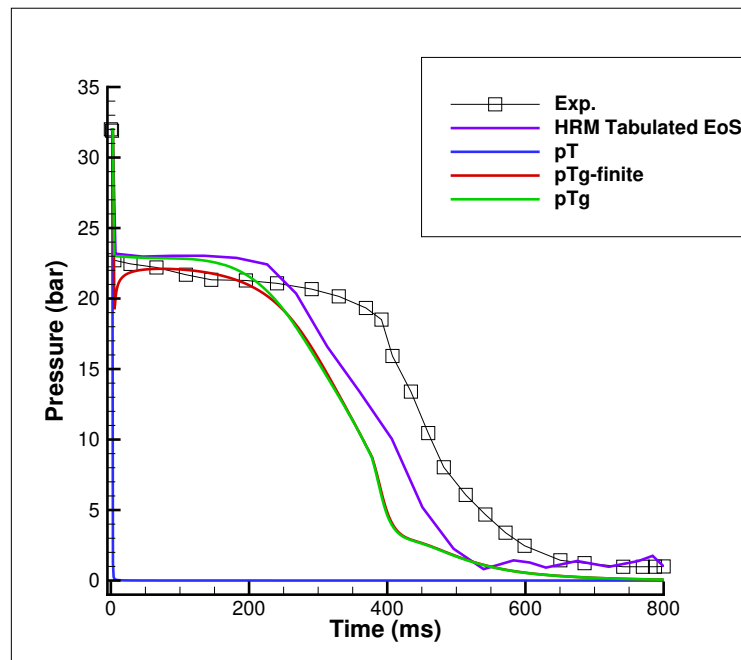


Figure 6.25: Comparison of pressure profiles at location P1 (3.899 m upstream from the breach) from the Canon experiment: experimental results (Exp., black square markers), instantaneous mechanical and thermal relaxation (pT, blue solid line), instantaneous mechanical, thermal, and finite-rate chemical relaxation (pTg-finite, red solid line), and instantaneous mechanical, thermal, and chemical relaxation (pTg, green solid line) from the solver, and HRM Tabulated EoS results (HRM Tabulated EoS, purple solid line) obtained from the literature by [Lepareux \(1994\)](#) case 4.

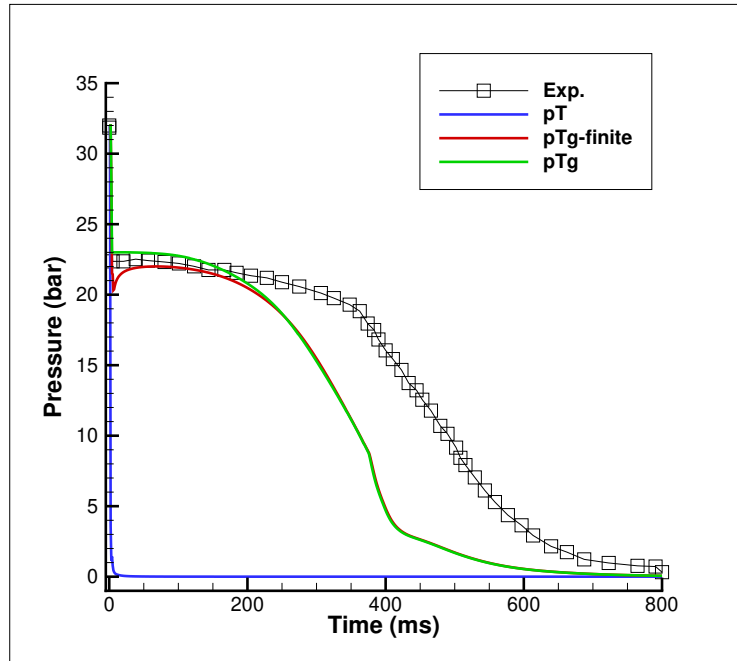


Figure 6.26: Comparison of pressure profiles at location P2 (3.033 m upstream from the breach) from the Canon experiment: experimental results (Exp., black square markers), instantaneous mechanical and thermal relaxation (pT, blue solid line), instantaneous mechanical, thermal, and finite-rate chemical relaxation (pTg-finite, red solid line), and instantaneous mechanical, thermal, and chemical relaxation (pTg, green solid line), case 4.

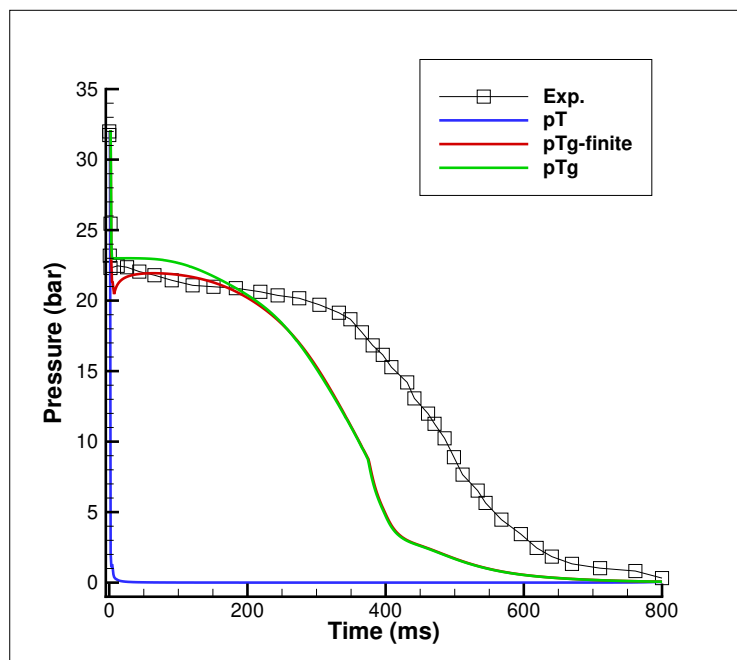


Figure 6.27: Comparison of pressure profiles at location P3 (2.471 m upstream from the breach) from the Canon experiment: experimental results (Exp., black square markers), instantaneous mechanical and thermal relaxation (pT, blue solid line), instantaneous mechanical, thermal, and finite-rate chemical relaxation (pTg-finite, red solid line), and instantaneous mechanical, thermal, and chemical relaxation (pTg, green solid line), case 4.

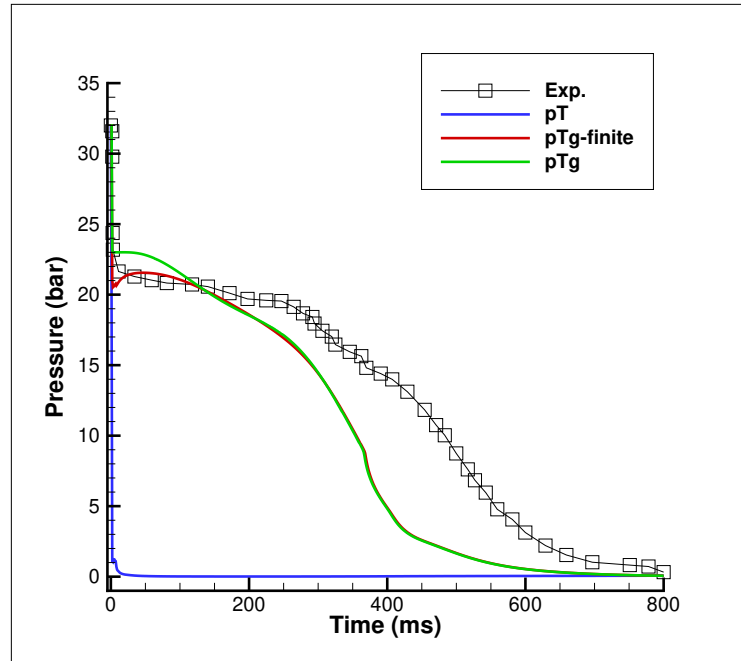


Figure 6.28: Comparison of pressure profiles at location P4 (1.6965 m upstream from the breach) from the Canon experiment: experimental results (Exp., black square markers), instantaneous mechanical and thermal relaxation (pT, blue solid line), instantaneous mechanical, thermal, and finite-rate chemical relaxation (pTg-finite, red solid line), and instantaneous mechanical, thermal, and chemical relaxation (pTg, green solid line), case 4.

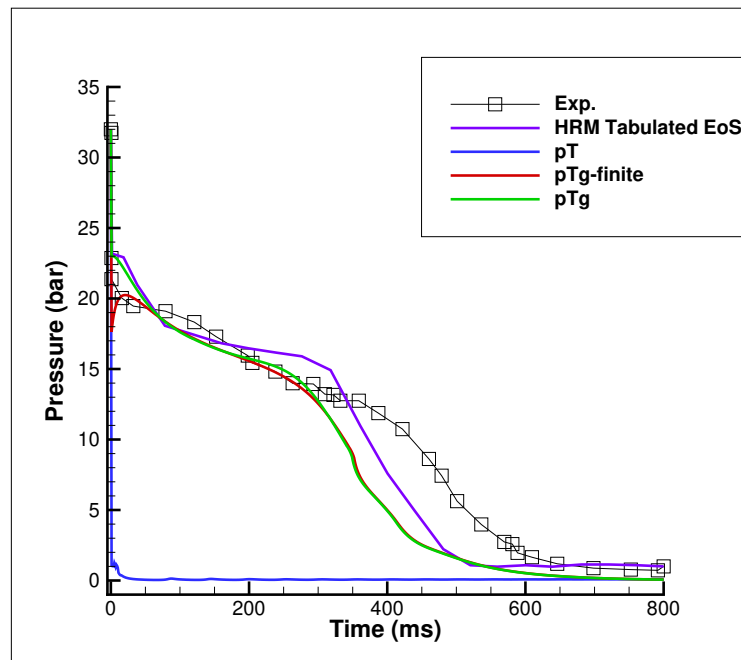


Figure 6.29: Comparison of pressure profiles at location P5 (0.504 m upstream from the breach) from the Canon experiment: experimental results (Exp., black square markers), instantaneous mechanical and thermal relaxation (pT, blue solid line), instantaneous mechanical, thermal, and finite-rate chemical relaxation (pTg-finite, red solid line), and instantaneous mechanical, thermal, and chemical relaxation (pTg, green solid line) from the solver, and HRM Tabulated EoS results (HRM Tabulated EoS, purple solid line) obtained from the literature by [Lepareux \(1994\)](#) case 4.

et al. (1996), Pelanti (2022).

$$\nu = \Lambda \alpha_v^{0.9} \left(\frac{p_{\text{sat}} - p}{p_{\text{crit}} - p_{\text{sat}}} \right)^{0.66}, \quad \Lambda = 1 \text{ Pa} \cdot \text{kg}^2 / (\text{s} \cdot \text{J}^2), \quad (6.90)$$

where p_{crit} is the pressure of the critical point.

At the beginning of the transient, a rarefaction wave forms at the open end of the pipe and propagates along its length, causing a rapid decrease in liquid water pressure and triggering vaporization. The pressure then continues to decline until it reaches the asymptotic value corresponding to the external atmospheric pressure. The models predict vaporization to occur earlier than observed in the experiments, although they perform slightly better than the HRM in capturing this process. As previously discussed, the model does not consider head losses or pipe deformation, both of which are known to slow wave propagation. This limitation could be responsible for the early prediction of vaporization.

Case 5:

The Bartak experiment, as presented by Barták (1990), investigates the rapid depressurization of superheated water and the dynamic formation of vapor bubbles within it. This study is particularly relevant for understanding scenarios such as large break loss-of-coolant accidents in pressurized water nuclear reactors. These events are characterized by the sudden rupture of primary coolant piping, resulting in a depressurization wave that propagates through the system. The pressure within this wave can drop significantly below the saturation pressure corresponding to the initial temperature of the coolant, leading to a metastable state before nucleation and vapor bubble formation occur.

The experimental setup involved a scaled model of a VVER-type PWR vessel, including internal structures and a horizontal pipe attached to the system. The pipe, measuring 1700 mm in length with an inner diameter of 88 mm, was equipped with a rupture-disc assembly to simulate the sudden pipe break. The system was pressurized and heated to a range of initial conditions, with pressures between 8 and 12.5 MPa and temperatures from 130 to 300°C. The present study focuses on an experimental scenario initiated with initial conditions of 125 bar and 563.15 K. The primary focus of this experiment was to analyze the pressure undershoot phenomenon, where the pressure drops below the saturation level, and to model the subsequent wave propagation and vapor bubble dynamics.

Throughout the experiment, pressure and temperature were measured at various locations along the discharge channel using piezoelectric transducers and thermocouples. The measurements aimed to capture the rapid changes in pressure and void fraction that occur during depressurization. The study provides valuable insights into the behavior of superheated liquids under rapid depressurization, including the critical role of nucleation in halting the depressurization process and initiating vapor generation.

The results from this study are crucial for validating computational models that simulate such phenomena in nuclear reactors. The experimental findings emphasize the importance of considering both the initial temperature and the depressurization rate, as these factors significantly influence the pressure to undershoot and the subsequent vapor bubble formation.

To model this experiment numerically, a simplified one-dimensional geometry was used, and the computational domain was discretized with a mesh of 1000 cells. Boundary conditions were chosen to reflect the experimental setup, with one end of the pipe sealed and the other end connected to an atmospheric pressure tank.

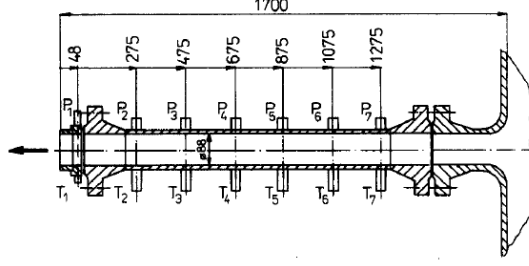


Figure 6.30: Schematic of experiment facility for the Bartak experiment.

Table 6.7: EoS parameters for liquid and vapor phases for the Bartak experiment.

	Liquid	Vapor
γ	1.387	1.954
P_∞ (Pa)	8899×10^5	0
q (J.kg ⁻¹)	-1244191	2287484
q' (J.kg ⁻¹ .K ⁻¹)	0	6417
C_v (J.kg ⁻¹ .K ⁻¹)	3202	462

The experimental setup for the Bartak experiment is illustrated in Figure 6.30, and the equation of state (EoS) parameters used in the simulations are provided in Table 6.7.

The result, displayed after 16 ms, is presented in Figure 6.31. This figure compares the pressure profiles at the P1 location (0.048 m upstream from the breach) obtained from different relaxation models with the experimental data. The models include pT (instantaneous mechanical and thermal relaxation), pTg-finite (instantaneous mechanical, thermal, and finite-rate chemical relaxation), and pTg (instantaneous mechanical, thermal, and chemical relaxation). The experimental data is also plotted for comparison.

Finite-rate mass transfer is governed by the mass transfer relaxation function ν , which is described by the equation below. However, the exact magnitude of ν is not well established. Consequently, a correlation inspired by previous studies has been adopted [Downar-Zapolski et al. \(1996\)](#), [Pelanti \(2022\)](#).

$$\nu = \Lambda \alpha_v^{0.9} \left(\frac{p_{\text{sat}} - p}{p_{\text{crit}} - p_{\text{sat}}} \right)^{0.66}, \quad \Lambda = 1 \text{ Pa} \cdot \text{kg}^2 / (\text{s} \cdot \text{J}^2), \quad (6.91)$$

where p_{crit} is the pressure of the critical point.

This test case is specifically designed to capture and analyze the initial phase of transient flow behavior, providing insights into the early dynamics of such phenomena. The experiment begins with the abrupt rupture of a disc at one end of the pipe, which generates a rarefaction wave that travels backward from the rupture point. This causes an immediate and rapid drop in pressure, bringing it under the saturation pressure associated with the initial stagnation temperature. The sudden depressurization forces the liquid into a metastable state, pushing the fluid from thermodynamic disequilibrium toward stability. The process is eventually stopped by rapid vaporization, commonly referred to as explosion-like nucleation (For further discussions, see [Barták \(1990\)](#), [Debenedetti \(1996\)](#), and [Carey \(2020\)](#)). As shown in Figure 6.31, the result qualitatively agrees with the experimental data, particularly aligning with the pTg-finite model. This demonstrates the numerical model's capability to accurately estimate the formation of a metastable superheated state, where the pressure drops under the saturation pressure associated with the temperature, followed

by subsequent vaporization.

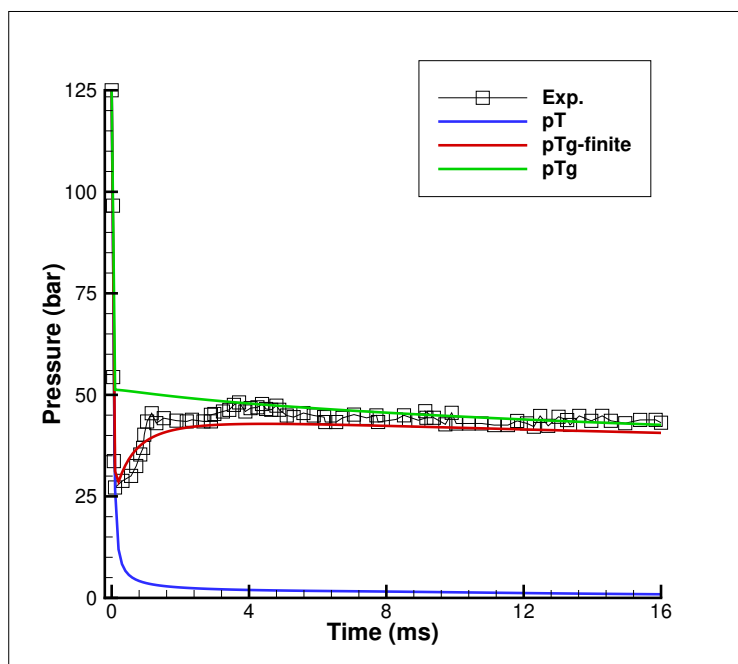


Figure 6.31: Comparison of pressure profiles at location P1 (0.048 m upstream from the breach) from the Bartak experiment: experimental results (Exp., black square markers), instantaneous mechanical and thermal relaxation (pT, blue solid line), instantaneous mechanical, thermal, and finite-rate chemical relaxation (pTg-finite, red solid line), and instantaneous mechanical, thermal, and chemical relaxation (pTg, green solid line), case 5.

6.5 Summary

In this chapter, the six-equation model with arbitrary-rate relaxation for compressible two-phase flow is explored in detail. The governing equations are presented along with the stiffened gas equation of state, which is employed to describe the thermodynamic behavior of the phases. Key transfer terms, including volume, heat, and mass exchange between phases, are modeled as relaxation processes.

The numerical solution of the system is performed using a fractional step method, with distinct steps for solving the hyperbolic system and the relaxation source terms. Relaxation procedures, including mechanical, thermal, and chemical relaxations, are presented, with non-instantaneous versions provided specifically for the thermal and chemical relaxation processes.

Validation test cases, such as the shock tube and double rarefaction tube experiments, were implemented. Through these test cases, the model's capability to handle liquid-to-vapor and vapor-to-liquid transitions was demonstrated. Additionally, convergence studies and results from the higher-order extension of the HLLC scheme were provided. Along with the validation test cases, different relaxation procedure scenarios were also tested, such as instantaneous mechanical relaxation with finite-rate thermal relaxation, instantaneous mechanical and thermal relaxation, and instantaneous mechanical and thermal relaxation with finite-rate chemical relaxation. Furthermore, different test cases, such as the Edwards O'Brien and Canon experiments, were also tested using the model. Similar to previous results, numerical vaporization was predicted earlier than in the experiments. The model does not include head losses or pipe deformation, both of which are known to slow down

wave propagation, which may explain the early prediction of vaporization. However, for both test cases, the results were compared with those from the literature (RELAP5 and HRM), and good agreement was observed. Finally, the model was tested on the Bartak experiment, which simulates scenarios like large break loss-of-coolant accidents in pressurized water reactors. These events involve a sudden rupture of primary coolant piping, causing a depressurization wave that drives the coolant into a metastable state before nucleation and vapor bubble formation. The experiment focuses on capturing the initial phase of transient flow behavior, where the abrupt rupture generates a rarefaction wave, leading to rapid pressure drop below the saturation point. Results with non-instantaneous mass transfer showed close alignment with experimental results, demonstrating the model's ability to precisely estimate the formation of a metastable superheated state.

Chapter 7

General conclusion and perspectives

7.1 General conclusion

This thesis has explored the complex phenomena of gas-liquid multiphase flows, with a particular focus on their behavior in critical industrial contexts, such as nuclear power plant operations during accidents like the Loss of Coolant Accident. The study has successfully implemented and analyzed numerical models based on the Baer–Nunziato framework, comparing both 4-equation and 6-equation models.

In this context, the Harten-Lax-van Leer Contact scheme was implemented as a core numerical method to solve the hyperbolic systems of conservation laws that govern multiphase flows. The HLLC scheme is especially capable of dealing with phenomena such as shock waves and contact discontinuity, thus making it successful to describe advanced flow phenomena in gas-liquid flows. Its ability to resolve shocks and rarefaction waves with minimal numerical diffusion ensures that key features of the flow are accurately captured. Additionally, various types of relaxation processes were used in the models to deal with non-equilibrium conditions. Mechanical, thermal and chemical relaxations were modeled from instantaneous up to arbitrary-rate relaxation. This feature allowed a most flexible description also for phase transition as well as interaction dynamics between gas and liquid especially under the presence of rapid depressurization scenarios.

In the initial part of this study, two distinct models were implemented in the custom-built numerical solver: a six-equation model with a single velocity and a four-equation model. The six-equation model, based on relaxed velocity equilibrium, is derived from the Baer-Nunziato seven-equation model under the assumption of instantaneous kinetic equilibrium. The four-equation model represents two-phase flow in kinetic, mechanical, and thermal equilibrium. Both models were first implemented in the custom-built solver and then validated using various test cases.

First, the depressurization process in a pipe containing CO₂ was tested using these two models. The test was conducted with two different scenarios: in the first scenario, mass transfer was not activated, while in the second, mass transfer was activated. In both scenarios, both models were consistent with the reference results. While the scenario without mass transfer could also be captured by the four-equation model discussed in Chapter 4, only the new models were able to produce accurate results in the mass transfer scenario. Additionally, extensive convergence studies were performed to ensure numerical stability and accuracy across different grid resolutions.

The models were further validated against nuclear-specific test cases, such as the Canon and Super-Canon experiments. These experiments are crucial for simulating nuclear reactor scenarios like LOCA, where rapid depressurization leads to vaporization and complex

multiphase flow dynamics. For these experiments, numerical analyses were performed for three different chemical relaxation procedures. The results obtained with the solver were compared to those from various models in the literature (HRM), and good agreement was observed. However, both in the obtained results and in those from the literature, the calculations predicted earlier vaporization than observed in the experiments. This discrepancy, while present, is consistent with other numerical approaches in the literature and highlights the challenges of capturing the precise timing of phase transitions under extreme conditions. The early prediction of vaporization can be attributed to the model's exclusion of head losses and pipe deformation, both of which are known to slow the propagation of pressure waves. Without accounting for these effects, the models predict a faster pressure drop, leading to the early onset of vaporization.

In the Super-Canon experiment, unlike the previous experiment, the temperature and pressure values were higher to represent the conditions in the primary loop of a Pressurized Water Reactor. Numerical analyses were conducted for three different chemical relaxation procedures, and the results obtained were compared to those from other models in the literature (the five-equation model). Similar to the previous case, earlier vaporization was predicted by the numerical models. Given the wide range of pressures and temperatures in this scenario, the stiffened gas equation of state appears too simplistic to accurately capture the thermodynamic behavior of water. However, the close alignment of the results with those from the literature indicates that the current models are capable of simulating flash vaporization, even in complex and challenging numerical scenarios.

In the final section of the study, the single-velocity six-equation model with arbitrary-rate relaxation was analyzed and implemented in a custom-built solver. Unlike the previous six-equation model, this new version allows thermal and chemical relaxation processes to be handled either instantaneously or arbitrarily. Specifically, thermal relaxation is considered under pressure equilibrium conditions, while chemical relaxation is addressed under both pressure and temperature equilibrium conditions. It should also be noted that the model can account for chemical relaxation under thermal constraints. As a result, the model utilizes the five-equation model with pressure relaxation (p-relaxed) and the four-equation model with pressure and temperature relaxation (pT-relaxed) to carry out the relaxation process. Furthermore, by applying certain simplifying assumptions, semi-exact analytical solutions of an exponential nature were derived to describe the relaxation processes. In terms of computational efficiency, this model offers advantages over the previous six-equation model because it does not require an iterative procedure to determine equilibrium properties.

The model was validated using various test cases, including the shock tube and double rarefaction tests under different scenarios. The results showed good agreement with reference solutions. Additionally, the model was tested on the Bartak experiment, which examines the rapid depressurization of superheated water and the dynamic formation of vapor bubbles within it. This study is particularly relevant for understanding scenarios such as LOCA in pressurized water reactors. These events are characterized by the sudden rupture of primary coolant pipes, resulting in a depressurization wave propagating through the system. The pressure within this wave can drop significantly below the saturation pressure corresponding to the initial temperature of the coolant, leading to a metastable state before nucleation and vapor bubble formation occur. The results were qualitatively consistent with experimental data in the case of arbitrary mass transfer, demonstrating the numerical model's ability to accurately predict the formation of a superheated metastable state, where the pressure drops below the saturation pressure, followed by subsequent vaporization.

7.2 Perspectives

There are several ways for future work to enhance the precision and applicability of the models presented in this thesis. Firstly, a major improvement can be achieved by implementing more advanced equations of state to describe the thermodynamic properties of the fluid at extreme conditions, where both high pressure and high temperature effects become significant. Although the EoS model used in this work is sufficiently accurate for some test cases, with more advanced EoS it can guarantee accurate prediction of phase transitions as well as metastable states.

Moreover, implementing the simulations in three dimensions (3D) would offer a more accurate and detailed representation of the experiments. While the current 1D simulations are effective for initial validation, they may miss important spatial effects and flow dynamics that only become apparent in a full 3D analysis, especially in scenarios involving complex geometries and interactions.

To improve the predictions of the models further, some loss mechanisms such as head losses and losses due to pipe deformation should be taken into account in the simulations. These mechanisms are known to slow down wave propagations and likely lead to later vaporization predictions than those obtained with present models. Especially for fast depressurizations and rapid pressure transients they will then play a major role, so that a model that accounts for them should produce even more accurate results.

Finally, an important next step is to integrate these models into the NSMB (Navier-Stokes Multi-Block) solver. So far, the models have been executed in a solver developed in-house and made exclusively for this work. Implementing the models to the NSMB environment will allow to benefit of more advanced features and be directly applicable on a larger set of cases and topics, thus increasing realism and usability.

Appendix A

Error Analysis for Canon Experiment

This appendix covers the fundamental concepts of *Absolute Error* and *Mean Absolute Error (MAE)*, which are essential in quantifying the discrepancies between measured or predicted values and their corresponding true values. These metrics are widely used in error analysis to assess the accuracy of models or experimental results.

1. Absolute Error

The Absolute Error is described as the absolute difference between a measured value and the true value of the quantity being measured. It quantifies the magnitude of the deviation, disregarding the sign of the error, and is expressed as:

$$\text{Absolute Error} = |\text{Measured Value} - \text{True Value}|$$

Where:

- Measured Value refers to the experimentally obtained or predicted value.
- True Value is the exact or accepted value of the quantity.

The absolute error enables a direct comparison of the error magnitude for each measurement, giving insight into the specific variances between the true and measured values.

2. Mean Absolute Error (MAE)

The Mean Absolute Error (MAE) is a commonly used statistical metric that measures the average of the absolute errors across a set of observations. It offers an overall assessment of the accuracy of a model or experimental procedure by considering the average magnitude of the errors, independent of their direction. The MAE is calculated as follows:

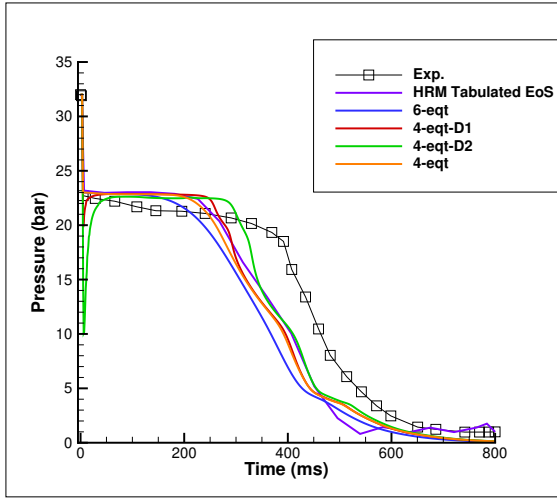
$$\text{MAE} = \frac{1}{n} \sum_{i=1}^n |\text{Measured Value}_i - \text{True Value}_i|$$

Where:

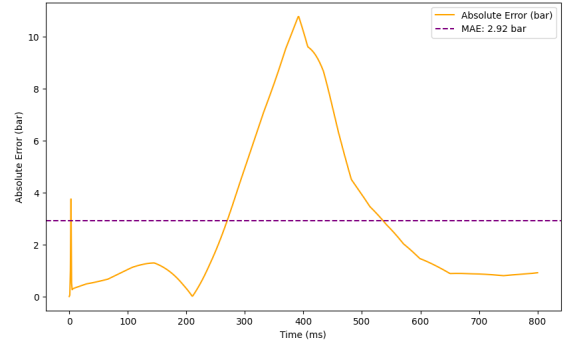
- n is the total number of observations or data points.
- Measured Value i is the i -th measured or predicted value.
- True Value i is the i -th true or accepted value.

The MAE provides a summary measure of prediction measurement accuracy by averaging the absolute differences between the measured and true values. It is a robust measure of error that avoids the issue of error cancellation, as it does not consider the direction of the error.

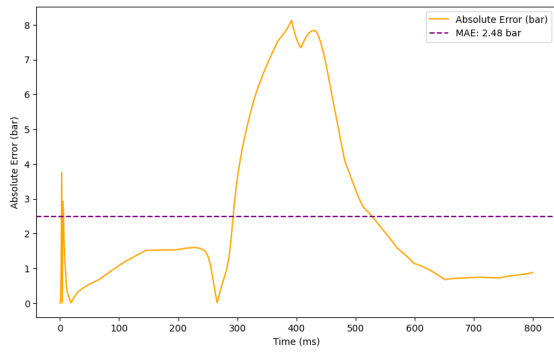
Both absolute error and MAE play crucial roles in assessing the performance of computational models and experimental measurements. While absolute error highlights the deviation for individual measurements, the MAE provides a more general overview of the accuracy across a dataset, making it a widely used metric in error analysis. In this analysis, uncertainties are not explicitly considered because the primary focus is on the comparison of the absolute and mean absolute errors between measured and true values, with any uncertainty being negligible relative to the scale of the errors analyzed.



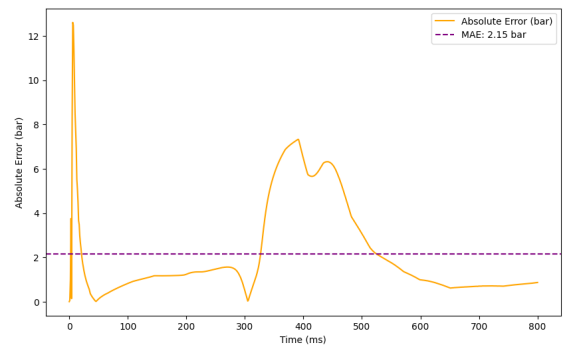
(a) Pressure evaluation at P1 location.



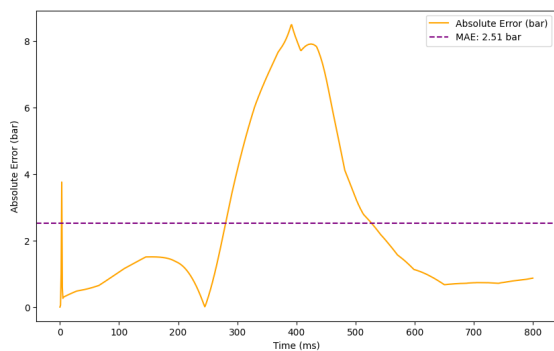
(b) Error analysis for 6-eqt.



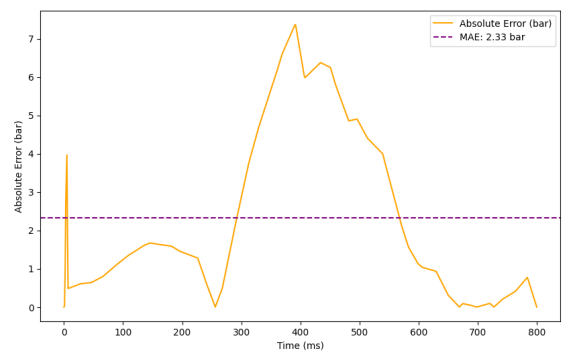
(c) Error analysis for 4-eqt-D1.



(d) Error analysis for 4-eqt-D2.

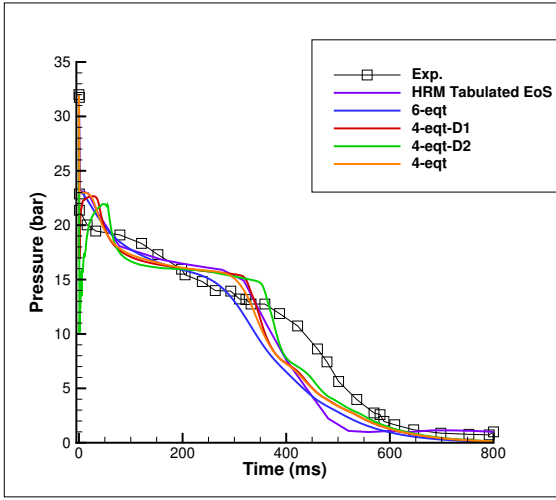


(e) Error analysis for 4-eqt.

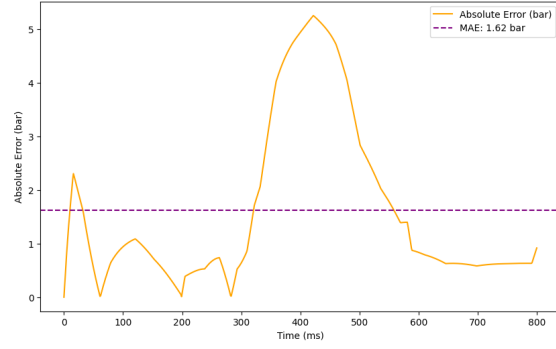


(f) Error analysis for HRM.

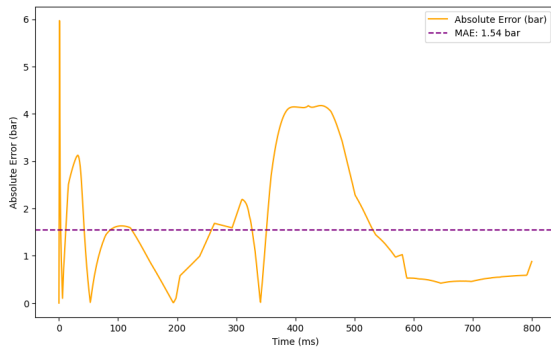
Figure A.1: Overview of the error analysis for the Canon experiment across various numerical models at the P1 location.



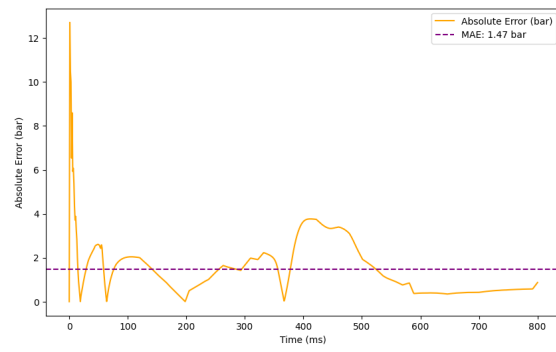
(a) Pressure evaluation at P5 location.



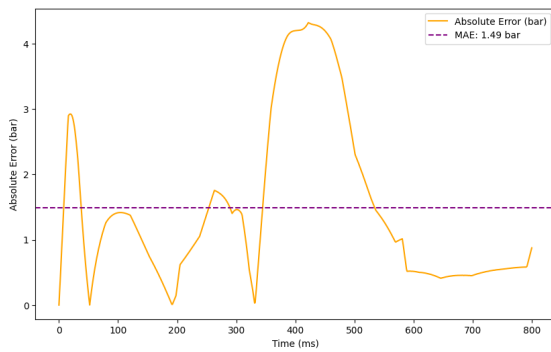
(b) Error analysis for 6-eqt.



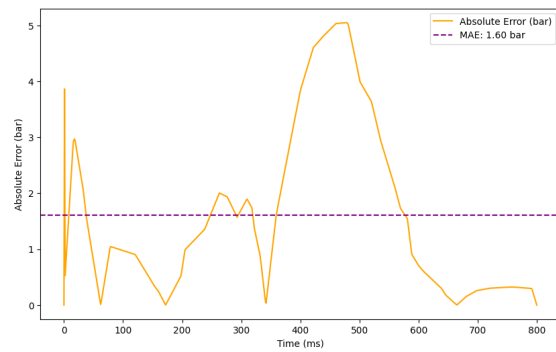
(c) Error analysis for 4-eqt-D1.



(d) Error analysis for 4-eqt-D2.



(e) Error analysis for 4-eqt.

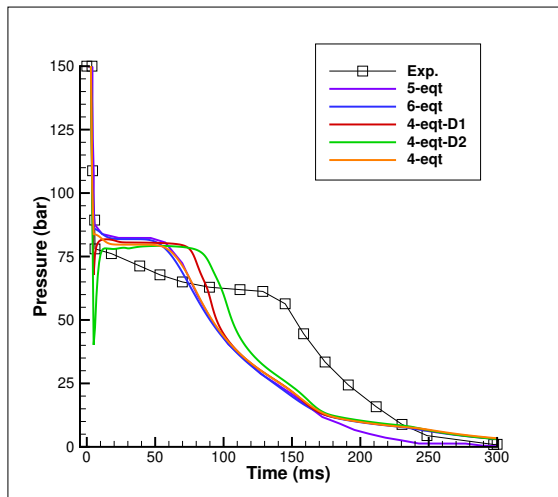


(f) Error analysis for HRM.

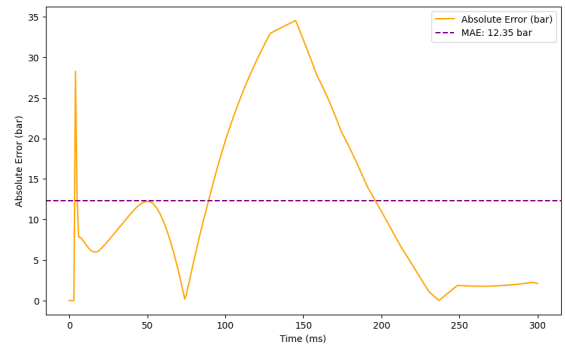
Figure A.2: Overview of the error analysis for the Canon experiment across various numerical models at the P5 location.

Appendix B

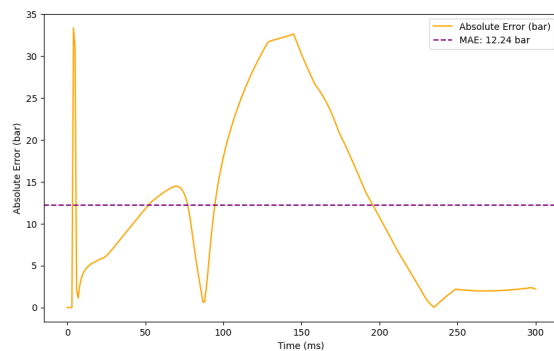
Error Analysis for Super-Canon Experiment



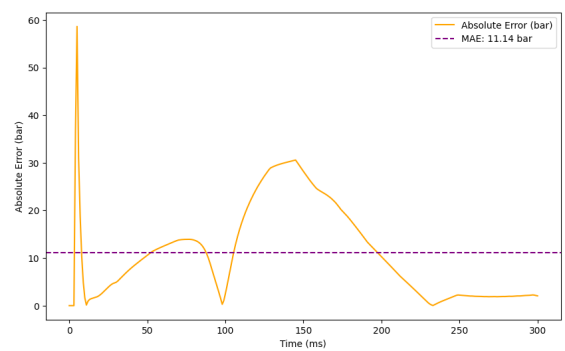
(a) Pressure evaluation at P1 location.



(b) Error analysis for 6-eqt.

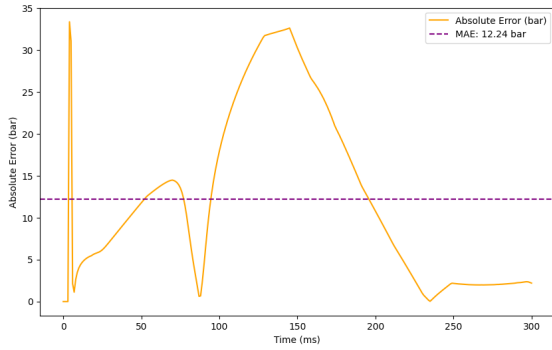


(c) Error analysis for 4-eqt-D1.

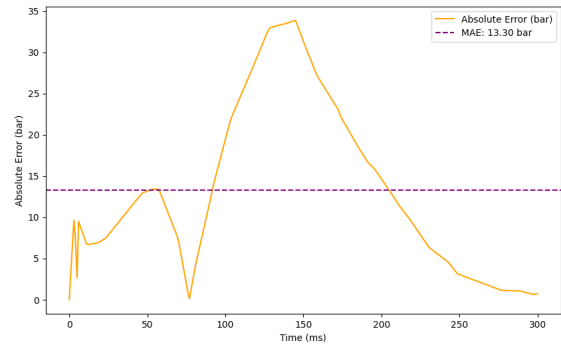


(d) Error analysis for 4-eqt-D2.

Figure B.1: Overview of the error analysis for the Super-Canon experiment across various numerical models at the P1 location.

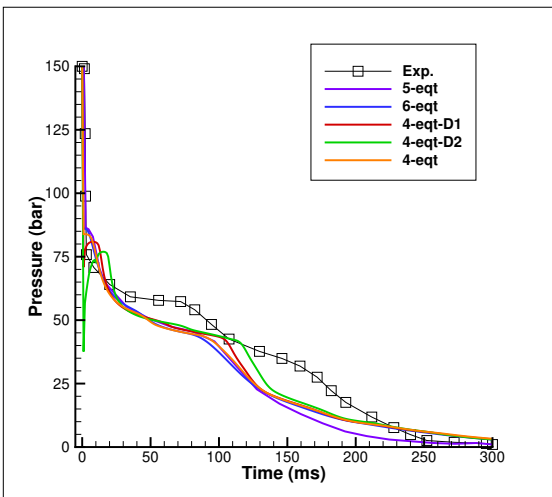


(e) Error analysis for 4-eqt.

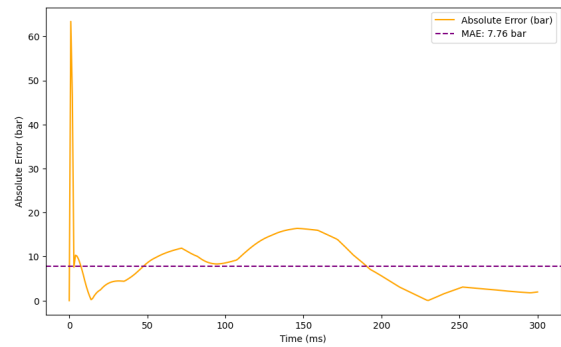


(f) Error analysis for 5-eqt.

Figure B.1: Overview of the error analysis for the Super-Canon experiment across various numerical models at the P1 location (continued).

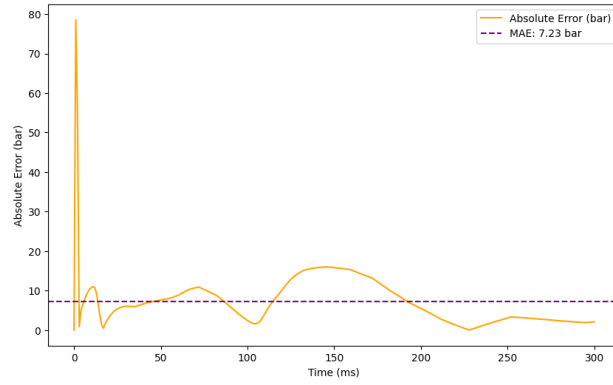


(a) Pressure evaluation at P5 location.

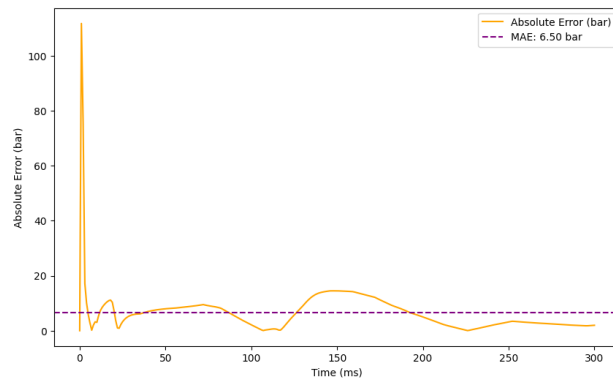


(b) Error analysis for 6-eqt.

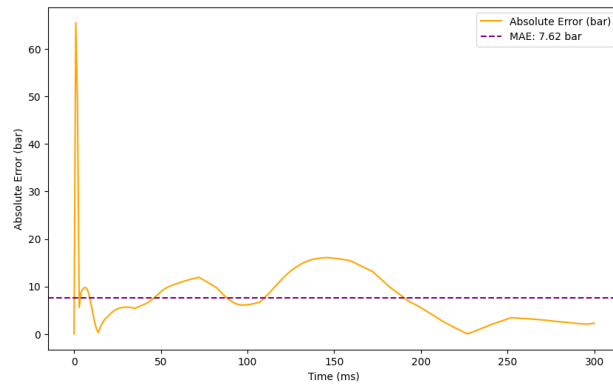
Figure B.2: Overview of the error analysis for the Super-Canon experiment across various numerical models at the P5 location.



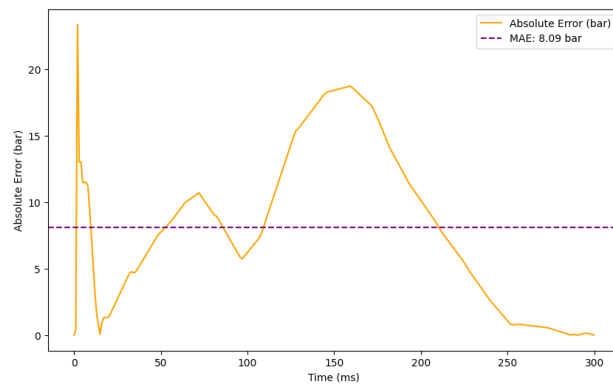
(c) Error analysis for 4-eqt-D1.



(d) Error analysis for 4-eqt-D2.



(e) Error analysis for 4-eqt.

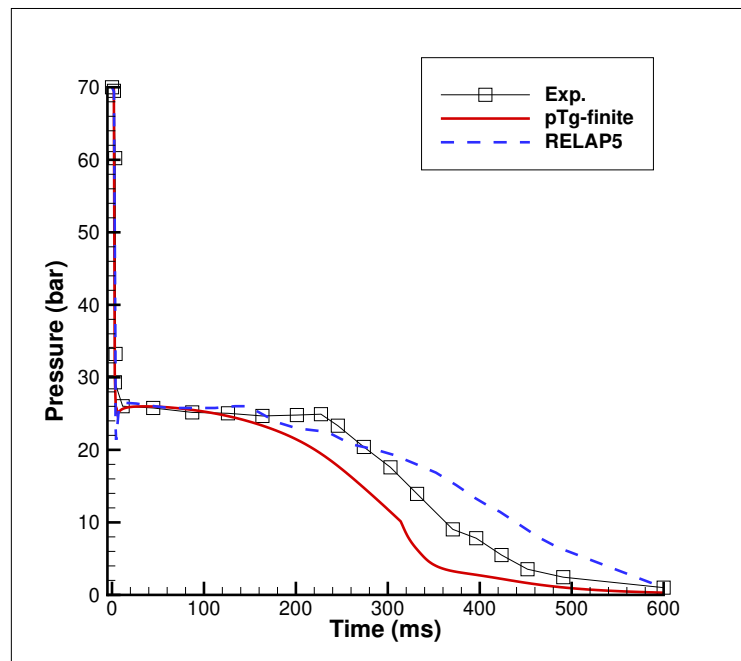


(f) Error analysis for 5-eqt.

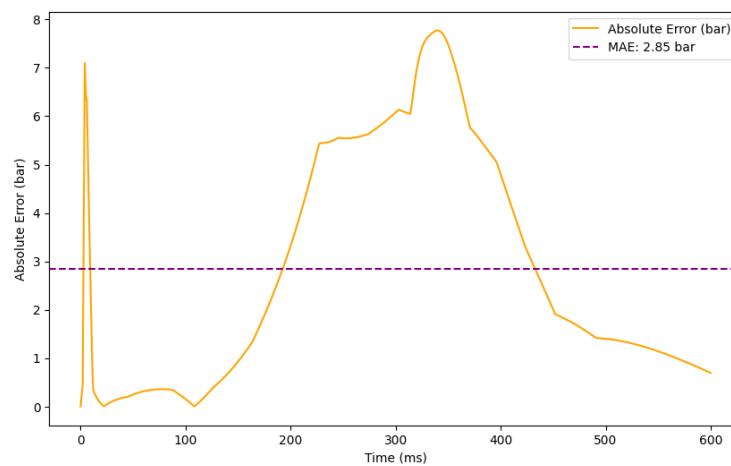
Figure B.2: Overview of the error analysis for the Super-Canon experiment across various numerical models at the P5 location (continued).

Appendix C

Error Analysis for Edwards O'Brien Experiment

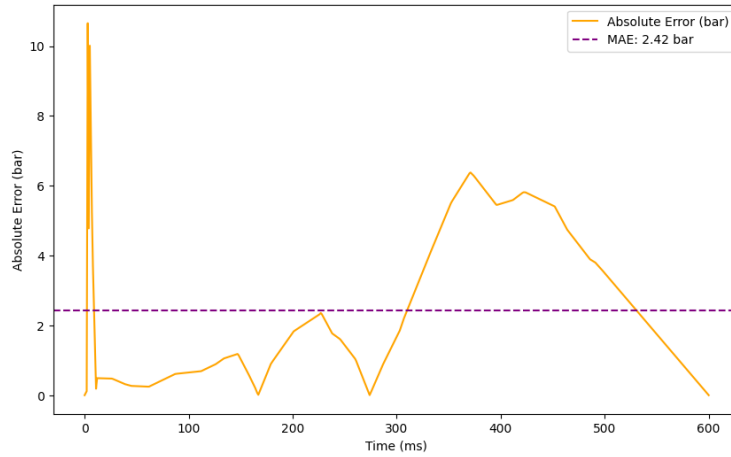


(a) Pressure evaluation at G5 location.



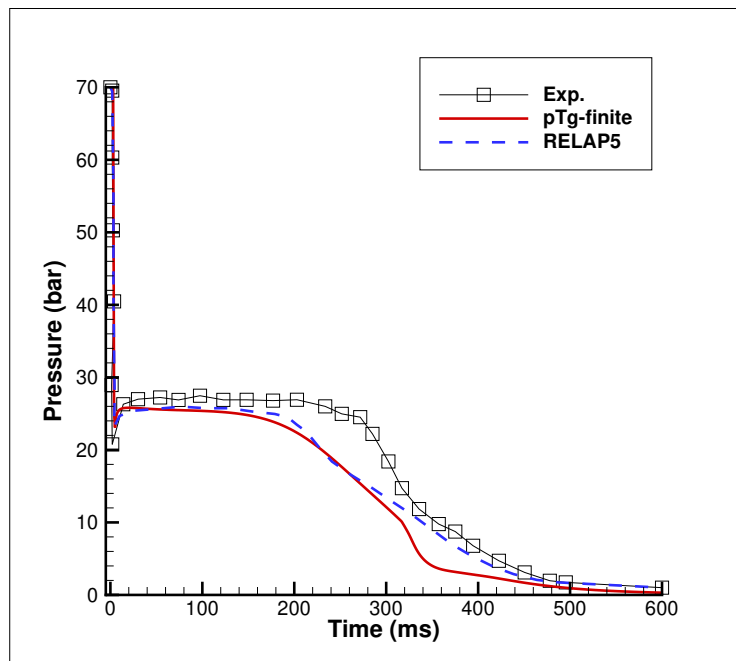
(b) Error analysis for pTg-finite.

Figure C.1: Overview of the error analysis for the Edwards O'Brien experiment at the G5 location.



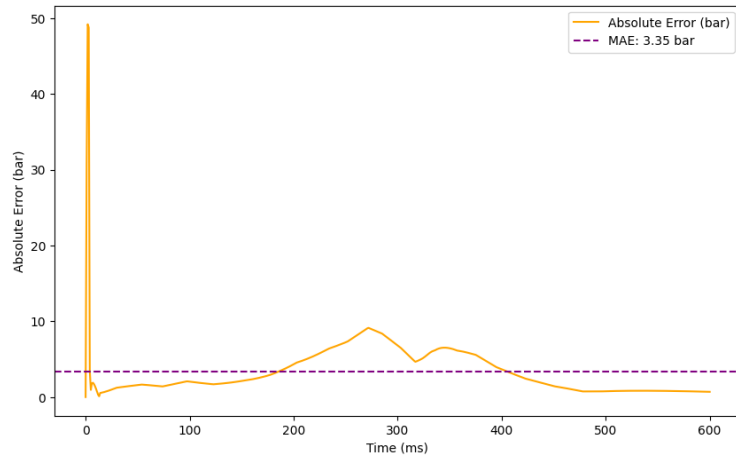
(c) Error analysis for RELAP.

Figure C.1: Overview of the error analysis for the Edwards O'Brien experiment at the G5 location (continued).

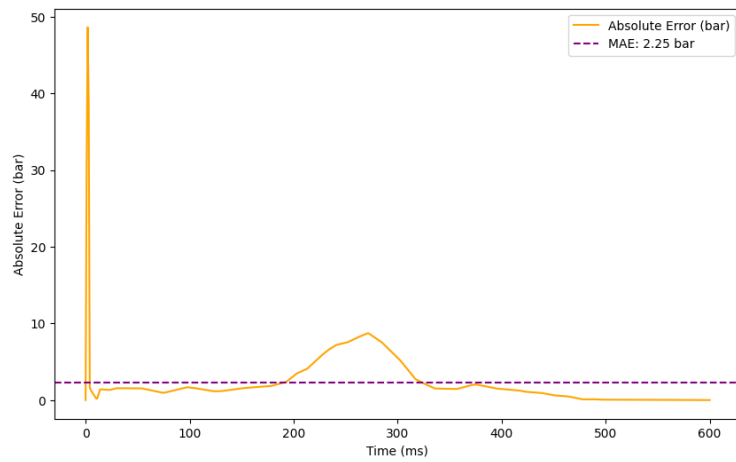


(a) Pressure evaluation at G7 location.

Figure C.2: Overview of the error analysis for the Edwards O'Brien experiment at the G7 location.



(b) Error analysis for pTg-finite.



(c) Error analysis for RELAP.

Figure C.2: Overview of the error analysis for the Edwards O'Brien experiment at the G7 location (continued).

References

- 5 Fast Facts About Nuclear Energy. <https://www.energy.gov/ne/articles/5-fast-facts-about-nuclear-energy>.
- IAEA PRIS (Power Reactor Information System). <https://pris.iaea.org/PRIS/WorldStatistics/NuclearShareofElectricityGeneration.aspx>.
- Nuclear Power Reactors - World Nuclear Association. <https://world-nuclear.org/information-library/nuclear-fuel-cycle/nuclear-power-reactors/nuclear-power-reactors>.
- Physical aspects of the relaxation model in two-phase flow. *Proceedings of the Royal Society of London. A. Mathematical and Physical Sciences*, 428(1875):379–397, April 1990. ISSN 0080-4630. doi: 10.1098/rspa.1990.0040.
- Probabilistic Safety Assessment: A Report*. Number 6 = 75 [d. Gesamtw.] in Safety Series INSAG / International Atomic Energy Agency, Vienna. International Atomic Energy Agency, Vienna, 1992. ISBN 978-92-0-102492-3.
- Two-Phase Flow: Theory and Applications*. Routledge, November 2017. ISBN 978-0-203-73486-5. doi: 10.1201/9780203734865.
- NSMB. <https://cfse.ch/about/our-tools/nsmb/>, December 2018.
- R. Abgrall, B. Nkonga, and R. Saurel. Efficient numerical approximation of compressible multi-material flow for unstructured meshes. *Computers & Fluids*, 32(4):571–605, May 2003. ISSN 00457930. doi: 10.1016/S0045-7930(02)00012-9.
- Rémi Abgrall. How to Prevent Pressure Oscillations in Multicomponent Flow Calculations: A Quasi Conservative Approach. *Journal of Computational Physics*, 125(1):150–160, April 1996. ISSN 00219991. doi: 10.1006/jcph.1996.0085.
- Rémi Abgrall and Smadar Karni. A comment on the computation of non-conservative products. *Journal of Computational Physics*, 229(8):2759–2763, April 2010. ISSN 00219991. doi: 10.1016/j.jcp.2009.12.015.
- M. Achuthan. *Engineering Thermodynamics*. PHI Learning, New Delhi, 2nd ed edition, 2009. ISBN 978-81-203-3845-6.
- Md. Alamgir and J. H. Lienhard. Correlation of Pressure Undershoot During Hot-Water Depressurization. *Journal of Heat Transfer*, 103(1):52–55, February 1981. ISSN 0022-1481, 1528-8943. doi: 10.1115/1.3244429.
- Robert A. Alberty. Use of Legendre transforms in chemical thermodynamics (IUPAC Technical Report). *Pure and Applied Chemistry*, 73(8):1349–1380, August 2001. ISSN 1365-3075, 0033-4545. doi: 10.1351/pac200173081349.

- Serge Alinhac. *Hyperbolic Partial Differential Equations*. Springer New York, New York, NY, 2009. ISBN 978-0-387-87822-5 978-0-387-87823-2. doi: 10.1007/978-0-387-87823-2.
- Grégoire Allaire, Sébastien Clerc, and Samuel Kokh. A Five-Equation Model for the Simulation of Interfaces between Compressible Fluids. *Journal of Computational Physics*, 181(2):577–616, September 2002. ISSN 00219991. doi: 10.1006/jcph.2002.7143.
- Andrianov. *Analytical and Numerical Investigation of Two-Phase Flows*. PhD thesis, 2003.
- Wojciech Angielczyk, Yann Bartosiewicz, and Dariusz Butrymowicz. Development of Delayed Equilibrium Model for CO₂ convergent-divergent nozzle transonic flashing flow. *International Journal of Multiphase Flow*, 131:103351, October 2020. ISSN 03019322. doi: 10.1016/j.ijmultiphaseflow.2020.103351.
- Robert E. Apfel. Water Superheated to 279.5° C at Atmospheric Pressure. *Nature Physical Science*, 238(82):63–64, July 1972. ISSN 0300-8746, 2058-1106. doi: 10.1038/physci238063a0.
- Abderraouf Arabi, Yacine Salhi, Youcef Zenati, El-Khider Si-Ahmed, and Jack Legrand. Analysis of Horizontal Gas-liquid Intermittent Flow Sub-Regimes Transitions: Physical Mechanisms and Flow Maps, November 2023.
- Paola Bacigaluppi, Julien Carlier, Marica Pelanti, Pietro Marco Congedo, and Rémi Abgrall. Assessment of a non-conservative four-equation multiphase system with phase transition. 2021. doi: 10.48550/ARXIV.2105.12874.
- M.R. Baer and J.W. Nunziato. A two-phase mixture theory for the deflagration-to-detonation transition (ddt) in reactive granular materials. *International Journal of Multiphase Flow*, 12(6):861–889, November 1986. ISSN 03019322. doi: 10.1016/0301-9322(86)90033-9.
- D. Barnea, Y. Luninski, and Y. Taitel. Flow pattern in horizontal and vertical two phase flow in small diameter pipes. *The Canadian Journal of Chemical Engineering*, 61(5): 617–620, October 1983. ISSN 0008-4034, 1939-019X. doi: 10.1002/cjce.5450610501.
- J. Barták. A study of the rapid depressurization of hot water and the dynamics of vapour bubble generation in superheated water. *International Journal of Multiphase Flow*, 16(5):789–798, September 1990. ISSN 03019322. doi: 10.1016/0301-9322(90)90004-3.
- Yann Bartosiewicz and Jean-Marie Seynhaeve. DELAYED EQUILIBRIUM MODEL (DEM) OF FLASHING CHOKED FLOWS RELEVANT TO LOCA. *Multiphase Science and Technology*, 25(2-4):117–131, 2013. ISSN 0276-1459. doi: 10.1615/MultScienTechn.v25.i2-4.50.
- Yann Bartosiewicz and Jean-Marie Seynhaeve. Delayed Equilibrium Model (DEM) of Flashing Choked Flows Relevant to LOCA and Implementation in System Codes. In *Volume 2B: Thermal Hydraulics*, page V02BT09A040, Prague, Czech Republic, July 2014. American Society of Mechanical Engineers. ISBN 978-0-7918-4591-2. doi: 10.1115/ICONE22-30957.
- R. Becker and W. Döring. Kinetische Behandlung der Keimbildung in übersättigten Dämpfen. *Annalen der Physik*, 416(8):719–752, January 1935. ISSN 0003-3804, 1521-3889. doi: 10.1002/andp.19354160806.

- David J. Benson. Computational methods in Lagrangian and Eulerian hydrocodes. *Computer Methods in Applied Mechanics and Engineering*, 99(2-3):235–394, September 1992. ISSN 00457825. doi: 10.1016/0045-7825(92)90042-I.
- David Bodansky. *Nuclear Energy: Principles, Practices, and Prospects*. Springer, New York, 2nd ed edition, 2004. ISBN 978-0-387-20778-0.
- E. Boucker, E. Quémerais, and J. Laviéville. Neptune cfd version 1.0 -verification against numerical and physical test cases. Technical report, June 2005.
- Christopher E. Brennen. *Fundamentals of Multiphase Flow*. Cambridge University Press, Cambridge [England] ; New York, 2005. ISBN 978-0-521-84804-6.
- H Bruce Stewart and Burton Wendroff. Two-phase flow: Models and methods. *Journal of Computational Physics*, 56(3):363–409, December 1984. ISSN 00219991. doi: 10.1016/0021-9991(84)90103-7.
- Van P. Carey. *Liquid-Vapor Phase-Change Phenomena: An Introduction to the Thermophysics of Vaporization and Condensation Processes in Heat Transfer Equipment*. CRC Press, 3 edition, February 2020. ISBN 978-0-429-08222-1. doi: 10.1201/9780429082221.
- J. Carlier. *Schémas Aux Résidus Distribués et Méthodes à Propagation Des Ondes Pour La Simulation d'écoulements Compressibles Diphasiques Avec Transfert de Chaleur et de Masse*. PhD thesis, Université Paris-Saclay (ComUE), 2019.
- Yunus A. Çengel, Michael A. Boles, and Mehmet Kanoglu. *Thermodynamics: An Engineering Approach*. McGraw-Hill Education, New York, NY, ninth edition edition, 2019. ISBN 978-1-259-82267-4.
- Ramesh Chandra. *Nuclear Medicine Physics: The Basics*. Wolters Kluwer Health/Lippincott Williams & Wilkins, Philadelphia, 7th ed edition, 2011. ISBN 978-1-4511-0941-2.
- Alexandre Chiapolino. Some contributions to the theoretical modeling and numerical simulation of compressible two-phase flows.
- Alexandre Chiapolino and Richard Saurel. Extended Noble–Abel Stiffened-Gas Equation of State for Sub-and-Supercritical Liquid-Gas Systems Far from the Critical Point. *Fluids*, 3(3):48, July 2018. ISSN 2311-5521. doi: 10.3390/fluids3030048.
- Alexandre Chiapolino, Pierre Boivin, and Richard Saurel. A simple phase transition relaxation solver for liquid–vapor flows. *International Journal for Numerical Methods in Fluids*, 83(7):583–605, March 2017. ISSN 0271-2091, 1097-0363. doi: 10.1002/flid.4282.
- S. Clerc. Numerical Simulation of the Homogeneous Equilibrium Model for Two-Phase Flows. *Journal of Computational Physics*, 161(1):354–375, June 2000. ISSN 00219991. doi: 10.1006/jcph.2000.6515.
- Clayton T. Crowe, John D. Schwarzkopf, Martin Sommerfeld, and Yutaka Tsuji. *Multiphase Flows with Droplets and Particles*. CRC Press, 0 edition, August 2011. ISBN 978-0-429-10639-2. doi: 10.1201/b11103.
- Marco Jose da Silva. *Impedance Sensors for Fast Multiphase Flow Measurement and Imaging*. Number 33 in Dresdner Beiträge Zur Sensorik. TUDpress, Verl. der Wiss, Dresden, 2008. ISBN 978-3-940046-99-4.

- Luca d'Agostino and Maria Vittoria Salvetti, editors. *Cavitation Instabilities and Rotor-dynamic Effects in Turbopumps and Hydroturbines: Turbopump and Inducer Cavitation, Experiments and Design*, volume 575 of *CISM International Centre for Mechanical Sciences*. Springer International Publishing, Cham, 2017. ISBN 978-3-319-49717-4 978-3-319-49719-8. doi: 10.1007/978-3-319-49719-8.
- F. Daude, P. Galon, Z. Gao, and E. Blaud. Numerical experiments using a HLLC-type scheme with ALE formulation for compressible two-phase flows five-equation models with phase transition. *Computers & Fluids*, 94:112–138, May 2014. ISSN 00457930. doi: 10.1016/j.compfluid.2014.02.008.
- S. F. Davis. Simplified Second-Order Godunov-Type Methods. *SIAM Journal on Scientific and Statistical Computing*, 9(3):445–473, May 1988. ISSN 0196-5204, 2168-3417. doi: 10.1137/0909030.
- M. De Lorenzo, Ph. Lafon, M. Di Matteo, M. Pelanti, J.-M. Seynhaeve, and Y. Bartosiewicz. Homogeneous two-phase flow models and accurate steam-water table look-up method for fast transient simulations. *International Journal of Multiphase Flow*, 95:199–219, October 2017a. ISSN 03019322. doi: 10.1016/j.ijmultiphaseflow.2017.06.001.
- M. De Lorenzo, Ph. Lafon, J.-M. Seynhaeve, and Y. Bartosiewicz. Benchmark of Delayed Equilibrium Model (DEM) and classic two-phase critical flow models against experimental data. *International Journal of Multiphase Flow*, 92:112–130, June 2017b. ISSN 03019322. doi: 10.1016/j.ijmultiphaseflow.2017.03.004.
- M. De Lorenzo, M. Pelanti, and Ph. Lafon. HLLC-type and path-conservative schemes for a single-velocity six-equation two-phase flow model: A comparative study. *Applied Mathematics and Computation*, 333:95–117, September 2018. ISSN 00963003. doi: 10.1016/j.amc.2018.03.092.
- M. De Lorenzo, Ph. Lafon, M. Pelanti, A. Pantano, M. Di Matteo, Y. Bartosiewicz, and J.-M. Seynhaeve. A hyperbolic phase-transition model coupled to tabulated EoS for two-phase flows in fast depressurizations. *Nuclear Engineering and Design*, 371:110954, January 2021. ISSN 00295493. doi: 10.1016/j.nucengdes.2020.110954.
- Marco de Lorenzo. *Modelling and Numerical Simulation of Metastable Two-Phase Flows*. PhD thesis, Université Paris Saclay (COMUE), May 2018.
- Pablo G. Debenedetti. *Metastable Liquids: Concepts and Principles*. Physical Chemistry. Princeton University Press, Princeton, N.J, 1996. ISBN 978-0-691-08595-1.
- R. Decker, United States. National Aeronautics, Space Administration, United States. National Aeronautics, Space Administration. Office of Management, United States. National Aeronautics, Space Administration. Scientific, and Technical Information Division. *Constitutive Relationships and Models in Continuum Theories of Multiphase Flows*. NASA Conference Publication. National Aeronautics and Space Administration, Office of Management, Scientific and Technical Information Division, 1989.
- Y. Delannoy and J.L. Kueny. Two-phase flow approach in unsteady cavitation modelling. *FED ASME*, (98):153–158, 1990.
- Andreas D. Demou, Nicolò Scapin, Marica Pelanti, and Luca Brandt. A pressure-based diffuse interface method for low-Mach multiphase flows with mass transfer. *Journal of*

- Computational Physics*, 448:110730, January 2022. ISSN 00219991. doi: 10.1016/j.jcp.2021.110730.
- Ricardo Dias, Antonio A. Martins, Rui Lima, and Teresa M. Mata, editors. *Single and Two-Phase Flows on Chemical and Biomedical Engineering*. BENTHAM SCIENCE PUBLISHERS, July 2012. ISBN 978-1-60805-295-0. doi: 10.2174/97816080529501120101.
- Jean Donea, Antonio Huerta, J.-Ph. Ponthot, and A. Rodríguez-Ferran. Arbitrary L agrangian– E ulerian Methods. In Erwin Stein, René Borst, and Thomas J. R. Hughes, editors, *Encyclopedia of Computational Mechanics*. Wiley, 1 edition, August 2004. ISBN 978-0-470-84699-5 978-0-470-09135-7. doi: 10.1002/0470091355.ecm009.
- P. Downar-Zapolski, Z. Bilicki, L. Bolle, and J. Franco. The non-equilibrium relaxation model for one-dimensional flashing liquid flow. *International Journal of Multiphase Flow*, 22(3):473–483, June 1996. ISSN 03019322. doi: 10.1016/0301-9322(95)00078-X.
- Donald A. Drew. ANALYTICAL MODELING OF MULTIPHASE FLOWS. In *Boiling Heat Transfer*, pages 31–84. Elsevier, 1992. ISBN 978-0-444-89499-1. doi: 10.1016/B978-0-444-89499-1.50005-8.
- Donald A. Drew and Stephen L. Passman. *Theory of Multicomponent Fluids*. Springer, New York, 1999. ISBN 978-0-387-22637-8.
- F. R. Edwards and T. P. O'Brien. Studies of phenomena connected with depressurization of water reactor. *J. Br. Nucl. Energy Soc.*, (No. 9):125–135, 1970.
- E. Elias and P. L. Chambre´. Flashing Inception in Water During Rapid Decompression. *Journal of Heat Transfer*, 115(1):231–238, February 1993. ISSN 0022-1481, 1528-8943. doi: 10.1115/1.2910654.
- Gloria Faccanoni, Samuel Kokh, and Grégoire Allaire. Modelling and simulation of liquid-vapor phase transition in compressible flows based on thermodynamical equilibrium. *ESAIM: Mathematical Modelling and Numerical Analysis*, 46(5):1029–1054, September 2012. ISSN 0764-583X, 1290-3841. doi: 10.1051/m2an/2011069.
- Ronald P Fedkiw, Tariq Aslam, Barry Merriman, and Stanley Osher. A Non-oscillatory Eulerian Approach to Interfaces in Multimaterial Flows (the Ghost Fluid Method). *Journal of Computational Physics*, 152(2):457–492, July 1999. ISSN 00219991. doi: 10.1006/jcph.1999.6236.
- Tore Flåtten and Halvor Lund. RELAXATION TWO-PHASE FLOW MODELS AND THE SUBCHARACTERISTIC CONDITION. *Mathematical Models and Methods in Applied Sciences*, 21(12):2379–2407, December 2011. ISSN 0218-2025, 1793-6314. doi: 10.1142/S0218202511005775.
- Thierry Gallouët, Jean-Marc Hérard, and Nicolas Seguin. NUMERICAL MODELING OF TWO-PHASE FLOWS USING THE TWO-FLUID TWO-PRESSURE APPROACH. *Mathematical Models and Methods in Applied Sciences*, 14(05):663–700, May 2004. ISSN 0218-2025, 1793-6314. doi: 10.1142/S0218202504003404.
- R.W Garner. Comparative Analysis of Standard Problems, Standard Problem 1. *Aerojet Nuclear Company Report, Interim Report*, 1973.

- J. W. Gibbs. On the equilibrium of heterogeneous substances. *American Journal of Science*, s3-16(96):441–458, December 1878. ISSN 0002-9599. doi: 10.2475/ajs.s3-16.96.441.
- James Glimm, John W. Grove, Xiao Lin Li, Keh-ming Shyue, Yanni Zeng, and Qiang Zhang. Three-Dimensional Front Tracking. *SIAM Journal on Scientific Computing*, 19(3):703–727, May 1998. ISSN 1064-8275, 1095-7197. doi: 10.1137/S1064827595293600.
- Sergei K Godunov. Finite difference method for numerical computation of discontinuous solutions of the equations of fluid dynamics. 1959.
- E. Goncalves and Y. Hoarau. Mass transfer modelling for compressible two-phase flows. *20th International Conference of Numerical Analysis and Applied Mathematics (ICNAAM 2022)*, 2022.
- E. Goncalves, Y. Hoarau, and D. Zeidan. Simulation of shock-induced bubble collapse using a four-equation model. *Shock Waves*, 29(1):221–234, January 2019. ISSN 0938-1287, 1432-2153. doi: 10.1007/s00193-018-0809-1.
- Eric Goncalvès. Numerical study of expansion tube problems: Toward the simulation of cavitation. *Computers & Fluids*, 72:1–19, February 2013. ISSN 00457930. doi: 10.1016/j.compfluid.2012.11.019.
- Eric Goncalvès. Modeling for non isothermal cavitation using 4-equation models. *International Journal of Heat and Mass Transfer*, 76:247–262, September 2014. ISSN 00179310. doi: 10.1016/j.ijheatmasstransfer.2014.04.065.
- Eric Goncalvès and Boris Charrière. Modelling for isothermal cavitation with a four-equation model. *International Journal of Multiphase Flow*, 59:54–72, February 2014. ISSN 03019322. doi: 10.1016/j.ijmultiphaseflow.2013.10.015.
- Eric Goncalves and Regiane Fortes Patella. Numerical simulation of cavitating flows with homogeneous models. *Computers & Fluids*, 38(9):1682–1696, October 2009. ISSN 00457930. doi: 10.1016/j.compfluid.2009.03.001.
- Eric Goncalves and Dia Zeidan. Simulation of Compressible Two-Phase Flows Using a Void Ratio Transport Equation. *Communications in Computational Physics*, 24(1), 2018. ISSN 18152406. doi: 10.4208/cicp.OA-2017-0024.
- E. Grüneisen. Theorie des festen Zustandes einatomiger Elemente. *Annalen der Physik*, 344(12):257–306, January 1912. ISSN 0003-3804, 1521-3889. doi: 10.1002/andp.19123441202.
- Ami Harten. High resolution schemes for hyperbolic conservation laws. *Journal of Computational Physics*, 49(3):357–393, March 1983. ISSN 00219991. doi: 10.1016/0021-9991(83)90136-5.
- J.J. Heijnen and K. Van’t Riet. Mass transfer, mixing and heat transfer phenomena in low viscosity bubble column reactors. *The Chemical Engineering Journal*, 28(2):B21–B42, April 1984. ISSN 03009467. doi: 10.1016/0300-9467(84)85025-X.
- Olivier Heuzé. General form of the Mie–Grüneisen equation of state. *Comptes Rendus. Mécanique*, 340(10):679–687, October 2012. ISSN 1873-7234. doi: 10.1016/j.crme.2012.10.044.

- C.W Hirt and B.D Nichols. Volume of fluid (VOF) method for the dynamics of free boundaries. *Journal of Computational Physics*, 39(1):201–225, January 1981. ISSN 00219991. doi: 10.1016/0021-9991(81)90145-5.
- C.W. Hirt, A.A. Amsden, and J.L. Cook. An Arbitrary Lagrangian–Eulerian Computing Method for All Flow Speeds. *Journal of Computational Physics*, 135(2):203–216, August 1997. ISSN 00219991. doi: 10.1006/jcph.1997.5702.
- Yannick Hoarau, Dorian Pena, Jan B. Vos, Dominique Charbonier, Alain Gehri, Marianna Braza, Thibaut Deloze, and Eric Laurendeau. Recent Developments of the Navier Stokes Multi Block (NSMB) CFD solver. In *54th AIAA Aerospace Sciences Meeting*, San Diego, California, USA, January 2016. American Institute of Aeronautics and Astronautics. ISBN 978-1-62410-393-3. doi: 10.2514/6.2016-2056.
- Olivier Hurisse. Numerical simulations of steady and unsteady two-phase flows using a homogeneous model. *Computers & Fluids*, 152:88–103, July 2017. ISSN 00457930. doi: 10.1016/j.compfluid.2017.04.007.
- Olivier Hurisse and Lucie Quibel. Simulations of water-vapor two-phase flows with non-condensable gas using a Noble-Able-Chemkin stiffened gas equation of state. *Computers & Fluids*, 239:105399, May 2022. ISSN 00457930. doi: 10.1016/j.compfluid.2022.105399.
- Internationale Atomenergie-Organisation. *Safety of Nuclear Power Plants: Design: Specific Safety Requirements; This Publication Includes a CD-ROM Containing the IAEA Safety Glossary 2007 Edition (2007) and the Fundamental Safety Principles (2006)*. Number SSR-2/1 in IAEA Safety Standards Series Specific Safety Requirements. IAEA, Vienna, 2012. ISBN 978-92-0-121510-9.
- J. M. Irvine. *Nuclear Power: A Very Short Introduction*. Number 268 in Very Short Introductions. Oxford University Press, Oxford ; New York, 2011. ISBN 978-0-19-958497-0.
- Mamoru Ishii and Takashi Hibiki. *Thermo-Fluid Dynamics of Two-Phase Flow*. Springer New York, New York, NY, 2011. ISBN 978-1-4419-7984-1 978-1-4419-7985-8. doi: 10.1007/978-1-4419-7985-8.
- A. Jameson, Wolfgang Schmidt, and Eli Turkel. Numerical solution of the Euler equations by finite volume methods using Runge Kutta time stepping schemes. In *14th Fluid and Plasma Dynamics Conference*, Palo Alto, CA, U.S.A., June 1981. American Institute of Aeronautics and Astronautics. doi: 10.2514/6.1981-1259.
- Ian A Johnston. Noble-Abel Equation of State. *Defence Science and Technology Organisation PO Box 1500 Edinburgh, South Australia 5111, Australia*, 2005.
- H. Kamerlingh Onnes. Expression of the equation of state of gases and liquids by means of series. *Koninklijke Nederlandse Akademie van Wetenschappen Proceedings Series B Physical Sciences*, 4:125–147, June 1902.
- A K Kapila, R Menikoff, J B Bdzil, and S F Son. Two-Phase Modeling of DDT in Granular Materials: Reduced Equations.
- Smadar Karni. Hybrid Multifluid Algorithms. *SIAM Journal on Scientific Computing*, 17(5):1019–1039, September 1996. ISSN 1064-8275, 1095-7197. doi: 10.1137/S106482759528003X.

- Yeon-Sik Kim, Jong-Hwan Kim, and Tae-Soon Kwon. A review of meta-stable aspects on a subcooled critical flow in nozzles and orifices. *Annals of Nuclear Energy*, 159:108328, September 2021. ISSN 03064549. doi: 10.1016/j.anucene.2021.108328.
- Jasper J. Kreeft and Barry Koren. A new formulation of Kapila’s five-equation model for compressible two-fluid flow, and its numerical treatment. *Journal of Computational Physics*, 229(18):6220–6242, September 2010. ISSN 00219991. doi: 10.1016/j.jcp.2010.04.025.
- A. Kumbaro, I. Toumi, and V. Seignole. Flux Schemes for the Numerical Simulation of Two Phase Flows. In Nobuyuki Satofuka, editor, *Computational Fluid Dynamics 2000*, pages 621–626. Springer Berlin Heidelberg, Berlin, Heidelberg, 2001. ISBN 978-3-642-62560-2 978-3-642-56535-9. doi: 10.1007/978-3-642-56535-9_94.
- Mathieu Labois. *Modélisation des déséquilibres mécaniques pour les écoulements diphasiques : approches par relaxation et par modèle réduit*. PhD thesis, Université de Provence - Aix-Marseille I, October 2008.
- R.T. Lahey, L.Y. Cheng, D.A. Drew, and J.E. Flaherty. The effect of virtual mass on the numerical stability of accelerating two-phase flows. *International Journal of Multiphase Flow*, 6(4):281–294, August 1980. ISSN 03019322. doi: 10.1016/0301-9322(80)90021-X.
- M.-H. Lallemand, A. Chinnayya, and O. Le Métayer. Pressure relaxation procedures for multiphase compressible flows. *International Journal for Numerical Methods in Fluids*, 49(1):1–56, September 2005. ISSN 0271-2091, 1097-0363. doi: 10.1002/fld.967.
- Rihui Lan and Pengtao Sun. A novel arbitrary Lagrangian–Eulerian finite element method for a parabolic/mixed parabolic moving interface problem. *Journal of Computational and Applied Mathematics*, 383:113125, February 2021. ISSN 03770427. doi: 10.1016/j.cam.2020.113125.
- O Le Métayer, J Massoni, and R Saurel. Élaboration des lois d’état d’un liquide et de sa vapeur pour les modèles d’écoulements diphasiques. *International Journal of Thermal Sciences*, 43(3):265–276, March 2004. ISSN 12900729. doi: 10.1016/j.ijthermalsci.2003.09.002.
- Olivier Le Métayer and Richard Saurel. The Noble-Abel Stiffened-Gas equation of state. *Physics of Fluids*, 28(4):046102, April 2016. ISSN 1070-6631, 1089-7666. doi: 10.1063/1.4945981.
- M. Lepareux. Programme PLEXUS matériau eau modèle homogène équilibre. Technical report, Un: Rapport DMT, 1994.
- Randall J. LeVeque. *Numerical Methods for Conservation Laws*. Lectures in Mathematics ETH Zürich. Birkhäuser Verlag, Basel ; Boston, 2nd ed edition, 1992. ISBN 978-3-7643-2723-1 978-0-8176-2723-2.
- Randall J. LeVeque and Keh-Ming Shyue. Two-Dimensional Front Tracking Based on High Resolution Wave Propagation Methods. *Journal of Computational Physics*, 123(2):354–368, February 1996. ISSN 00219991. doi: 10.1006/jcph.1996.0029.
- Yixiang Liao and Dirk Lucas. Computational modelling of flash boiling flows: A literature survey. *International Journal of Heat and Mass Transfer*, 111:246–265, August 2017. ISSN 00179310. doi: 10.1016/j.ijheatmasstransfer.2017.03.121.

- J. H. Lienhard and Amir Karimi. Homogeneous Nucleation and the Spinodal Line. *Journal of Heat Transfer*, 103(1):61–64, February 1981. ISSN 0022-1481, 1528-8943. doi: 10.1115/1.3244431.
- J. H. Lienhard, Md. Alamgir, and M. Trela. Early Response of Hot Water to Sudden Release from High Pressure. *Journal of Heat Transfer*, 100(3):473–479, August 1978. ISSN 0022-1481, 1528-8943. doi: 10.1115/1.3450833.
- Gaute Linga and Tore Flåtten. A hierarchy of non-equilibrium two-phase flow models. *ESAIM: Proceedings and Surveys*, 66:109–143, 2019. ISSN 2267-3059. doi: 10.1051/proc/201966006.
- Meng-Sing Liou and Christopher J. Steffen. A New Flux Splitting Scheme. *Journal of Computational Physics*, 107(1):23–39, July 1993. ISSN 00219991. doi: 10.1006/jcph.1993.1122.
- H. Lochon. *Modélisation et Simulation d'écoulements Transitoires Eau-Vapeur En Approche Bifluide*. PhD thesis, Université Aix-Marseille, 2016.
- Alexandra Metallinou Log. *Depressurization of CO₂ in Pipes: Analysis of Experiments and Non-Equilibrium Flashing Flow Models*. Doctoral thesis, NTNU, 2023.
- Halvor Lund. A Hierarchy of Relaxation Models for Two-Phase Flow. *SIAM Journal on Applied Mathematics*, 72(6):1713–1741, January 2012. ISSN 0036-1399, 1095-712X. doi: 10.1137/12086368X.
- Halvor Lund and Peder Aursand. Two-Phase Flow of CO₂ with Phase Transfer. *Energy Procedia*, 23:246–255, 2012. ISSN 18766102. doi: 10.1016/j.egypro.2012.06.034.
- Jorge Pérez Mañes, Victor Hugo Sánchez Espinoza, Sergio Chiva Vicent, Michael Böttcher, and Robert Stieglitz. Validation of NEPTUNE-CFD Two-Phase Flow Models Using Experimental Data. *Science and Technology of Nuclear Installations*, 2014:1–19, 2014. ISSN 1687-6075, 1687-6083. doi: 10.1155/2014/185950.
- Amit Mangal, Vikas Jain, and A.K. Nayak. Capability of the RELAP5 code to simulate natural circulation behavior in test facilities. *Progress in Nuclear Energy*, 61:1–16, November 2012. ISSN 01491970. doi: 10.1016/j.pnucene.2012.06.005.
- Robert E. Masterson. *Nuclear Reactor Thermal Hydraulics: An Introduction to Nuclear Heat Transfer and Fluid Flow*. CRC Press, Boca Raton : CRC Press, [2019], 1 edition, August 2019. ISBN 978-1-315-22623-1. doi: 10.1201/b22067.
- T. Ménard, S. Tanguy, and A. Berlemont. Coupling level set/VOF/ghost fluid methods: Validation and application to 3D simulation of the primary break-up of a liquid jet. *International Journal of Multiphase Flow*, 33(5):510–524, May 2007. ISSN 03019322. doi: 10.1016/j.ijmultiphaseflow.2006.11.001.
- Ralph Menikoff and Bradley J. Plohr. The Riemann problem for fluid flow of real materials. *Reviews of Modern Physics*, 61(1):75–130, January 1989. ISSN 0034-6861. doi: 10.1103/RevModPhys.61.75.
- J. Michael Doster and Mark A. Holmes. Numerical Stability of the Six-Equation, Single-Pressure Model with Viscous Terms. *Nuclear Science and Engineering*, 124(1):125–144, September 1996. ISSN 0029-5639, 1943-748X. doi: 10.13182/NSE96-A24229.

- Gustav Mie. Zur kinetischen Theorie der einatomigen Körper. *Annalen der Physik*, 316(8): 657–697, January 1903. ISSN 0003-3804, 1521-3889. doi: 10.1002/andp.19033160802.
- Abdalellah O. Mohammed, Hussain H. Al-Kayiem, and A.B. Osman. Investigations on the slug two-phase flow in horizontal pipes: Past, presents, and future directives. *Chemical Engineering Science*, 238:116611, July 2021. ISSN 00092509. doi: 10.1016/j.ces.2021.116611.
- Ricardo A. Molins, editor. *Food Irradiation: Principles and Applications*. Wiley, New York, 2001. ISBN 978-0-471-35634-9.
- S C Mossop. The Freezing of Supercooled Water. *Proceedings of the Physical Society. Section B*, 68(4):193–208, April 1955. ISSN 0370-1301. doi: 10.1088/0370-1301/68/4/301.
- Andreas L. Muhlbauer and J. David Raal. *Phase Equilibria: Measurement & Computation*. Routledge, Boca Raton, 1 edition, February 2023. ISBN 978-0-203-74362-1. doi: 10.1201/9780203743621.
- Ingo Müller and Ingo Müller. *Thermodynamics. Interaction of Mechanics and Mathematics Series*. Pitman Advanced Publ. Program, Boston, 1985. ISBN 978-0-273-08577-5.
- Angelo Murrone and Hervé Guillard. A five equation reduced model for compressible two phase flow problems. *Journal of Computational Physics*, 202(2):664–698, January 2005. ISSN 00219991. doi: 10.1016/j.jcp.2004.07.019.
- Loann Neron and Richard Saurel. Noble–Abel/first-order virial equations of state for gas mixtures resulting from multiple condensed reactive materials combustion. *Physics of Fluids*, 34(1):016107, January 2022. ISSN 1070-6631, 1089-7666. doi: 10.1063/5.0079187.
- Jonatan Núñez-De La Rosa. High-order methods for computational astrophysics, 2015.
- OECD and Nuclear Energy Agency. *Risks and Benefits of Nuclear Energy*. Nuclear Development. OECD, June 2007. ISBN 978-92-64-03551-5 978-92-64-03552-2. doi: 10.1787/9789264035522-en.
- Stanley Osher and James A Sethian. Fronts propagating with curvature-dependent speed: Algorithms based on Hamilton-Jacobi formulations. *Journal of Computational Physics*, 79(1):12–49, November 1988. ISSN 00219991. doi: 10.1016/0021-9991(88)90002-2.
- S. Pascal-Ribot and Y. Blanchet. Buffeting lift forces and local air–water flow aspects around a rigid cylinder. *International Journal of Multiphase Flow*, 33(11):1237–1254, November 2007. ISSN 03019322. doi: 10.1016/j.ijmultiphaseflow.2007.05.007.
- Marica Pelanti. Arbitrary-rate relaxation techniques for the numerical modeling of compressible two-phase flows with heat and mass transfer. *International Journal of Multiphase Flow*, 153:104097, August 2022. ISSN 03019322. doi: 10.1016/j.ijmultiphaseflow.2022.104097.
- Marica Pelanti and Keh-Ming Shyue. A mixture-energy-consistent six-equation two-phase numerical model for fluids with interfaces, cavitation and evaporation waves. *Journal of Computational Physics*, 259:331–357, February 2014. ISSN 00219991. doi: 10.1016/j.jcp.2013.12.003.

- Marica Pelanti and Keh-Ming Shyue. A numerical model for multiphase liquid–vapor–gas flows with interfaces and cavitation. *International Journal of Multiphase Flow*, 113:208–230, April 2019. ISSN 03019322. doi: 10.1016/j.ijmultiphaseflow.2019.01.010.
- S. Peluchon, G. Gallice, and L. Mieussens. A robust implicit–explicit acoustic-transport splitting scheme for two-phase flows. *Journal of Computational Physics*, 339:328–355, June 2017. ISSN 00219991. doi: 10.1016/j.jcp.2017.03.019.
- Ding-Yu Peng and Donald B. Robinson. A New Two-Constant Equation of State. *Industrial & Engineering Chemistry Fundamentals*, 15(1):59–64, February 1976. ISSN 0196-4313, 1541-4833. doi: 10.1021/i160057a011.
- Fabien Petitpas, Erwin Franquet, Richard Saurel, and Olivier Le Metayer. A relaxation-projection method for compressible flows. Part II: Artificial heat exchanges for multiphase shocks. *Journal of Computational Physics*, 225(2):2214–2248, August 2007. ISSN 00219991. doi: 10.1016/j.jcp.2007.03.014.
- Gad A. Pinhasi, A. Ullmann, and A. Dayan. MODELING OF FLASHING TWO-PHASE FLOW. *Reviews in Chemical Engineering*, 21(3-4), January 2005. ISSN 2191-0235, 0167-8299. doi: 10.1515/REVCE.2005.21.3-4.133.
- T. A. Porsching. A Finite Difference Method for Thermally Expandable Fluid Transients. *Nuclear Science and Engineering*, 64(1):177–186, September 1977. ISSN 0029-5639, 1943-748X. doi: 10.13182/NSE77-A27088.
- Andrea Prosperetti and Grétar Tryggvason, editors. *Computational Methods for Multiphase Flow*. Cambridge University Press, 1 edition, March 2007. ISBN 978-0-521-84764-3 978-0-521-13861-1 978-0-511-60748-6. doi: 10.1017/CBO9780511607486.
- R. A. Berry, R. Saurel, F. Petitpas, E. Daniel, O. Le Metayer, S. Gavriluk, and N. Dovetta. Progress in the Development of Compressible, Multiphase Flow Modeling Capability for Nuclear Reactor Flow Applications. Technical Report INL/EXT-08-15002, 946849, October 2008.
- Michel Reocreux. *Contribution to the Study of Critical Flow Rates in a Water-Vapour Two-Phase Flow*. PhD thesis, Universite Grenoble Alpes, 1974.
- Richard Saurel, Fabien Petitpas, and Ray A. Berry. Simple and efficient relaxation methods for interfaces separating compressible fluids, cavitating flows and shocks in multiphase mixtures. *Journal of Computational Physics*, 228(5):1678–1712, March 2009. ISSN 00219991. doi: 10.1016/j.jcp.2008.11.002.
- William Rider, Douglas Kothe, S Mosso, John Cerutti, and John Hochstein. Accurate solution algorithms for incompressible multiphase flows. In *33rd Aerospace Sciences Meeting and Exhibit*, Reno, NV, U.S.A., January 1995. American Institute of Aeronautics and Astronautics. doi: 10.2514/6.1995-699.
- Bernd Riegel. *CONTRIBUTION A L’ETUDE DE LA DÉCOMPRESSION D’UNE CAPACITÉ EN RÉGIME DIPHASIQUE*. PhD thesis, L’INSTITUT NATIONAL POLYTECHNIQUE DE GRENOBLE, 1978.
- Marguerite Robinson, A. C. Fowler, A. J. Alexander, and S. B. G. O’Brien. Waves in Guinness. *Physics of Fluids*, 20(6):067101, June 2008. ISSN 1070-6631, 1089-7666. doi: 10.1063/1.2929369.

- P.L. Roe. Approximate Riemann solvers, parameter vectors, and difference schemes. *Journal of Computational Physics*, 43(2):357–372, October 1981. ISSN 00219991. doi: 10.1016/0021-9991(81)90128-5.
- V.V. Rusanov. The calculation of the interaction of non-stationary shock waves and obstacles. *USSR Computational Mathematics and Mathematical Physics*, 1(2):304–320, January 1962. ISSN 00415553. doi: 10.1016/0041-5553(62)90062-9.
- Scott D. Sagan. The Causes of Nuclear Weapons Proliferation. *Annual Review of Political Science*, 14(1):225–244, June 2011. ISSN 1094-2939, 1545-1577. doi: 10.1146/annurev-polisci-052209-131042.
- Richard Saurel. Interfaces, Detonation Waves, Cavitation and the Multiphase Godunov Method. In E. F. Toro, editor, *Godunov Methods*, pages 785–807. Springer US, New York, NY, 2001. ISBN 978-1-4613-5183-2 978-1-4615-0663-8. doi: 10.1007/978-1-4615-0663-8_77.
- Richard Saurel and Rémi Abgrall. A Multiphase Godunov Method for Compressible Multifluid and Multiphase Flows. *Journal of Computational Physics*, 150(2):425–467, April 1999. ISSN 00219991. doi: 10.1006/jcph.1999.6187.
- Richard Saurel and Olivier Lemetayer. A multiphase model for compressible flows with interfaces, shocks, detonation waves and cavitation. *Journal of Fluid Mechanics*, 431: 239–271, March 2001. ISSN 0022-1120, 1469-7645. doi: 10.1017/S0022112000003098.
- Richard Saurel, Fabien Petitpas, and Remi Abgrall. Modelling phase transition in metastable liquids: Application to cavitating and flashing flows. *Journal of Fluid Mechanics*, 607:313–350, July 2008. ISSN 0022-1120, 1469-7645. doi: 10.1017/S0022112008002061.
- Richard Saurel, Pierre Boivin, and Olivier Le Métayer. A general formulation for cavitating, boiling and evaporating flows. *Computers & Fluids*, 128:53–64, April 2016. ISSN 00457930. doi: 10.1016/j.compfluid.2016.01.004.
- Denis Serre. *Systems of Conservation Laws 1: Hyperbolicity, Entropies, Shock Waves*. Cambridge University Press, 1 edition, May 1999. ISBN 978-0-521-58233-9 978-0-511-61237-4. doi: 10.1017/CBO9780511612374.
- H. Städtke, G. Franchello, and B. Worth. Numerical simulation of multi-dimensional two-phase flow based on flux vector splitting. *Nuclear Engineering and Design*, 177(1-3): 199–213, December 1997. ISSN 00295493. doi: 10.1016/S0029-5493(97)00194-5.
- Frank H. Stillinger. Water Revisited. *Science*, 209(4455):451–457, July 1980. ISSN 0036-8075, 1095-9203. doi: 10.1126/science.209.4455.451.
- Gilbert Strang. On the Construction and Comparison of Difference Schemes. *SIAM Journal on Numerical Analysis*, 5(3):506–517, September 1968. ISSN 0036-1429, 1095-7170. doi: 10.1137/0705041.
- Lin Sun, Minjun Peng, Genglei Xia, Xuesong Wang, and Mingyu Wu. Development and Validation of Multiscale Coupled Thermal-Hydraulic Code Combining RELAP5 and Fluent Code. *Frontiers in Energy Research*, 8:613852, February 2021. ISSN 2296-598X. doi: 10.3389/fenrg.2020.613852.

- Yehuda Taitel, Dvora Barnea, and A. E. Dukler. Modelling flow pattern transitions for steady upward gas-liquid flow in vertical tubes. *AIChE Journal*, 26(3):345–354, May 1980. ISSN 0001-1541, 1547-5905. doi: 10.1002/aic.690260304.
- I. Tiselj and C. Samuel Martin. Slug modeling with 1D two-fluid model. *Kerntechnik*, 77(2):101–107, May 2012. ISSN 2195-8580, 0932-3902. doi: 10.3139/124.110238.
- Iztok Tiselj and Stojan Petelin. Modelling of Two-Phase Flow with Second-Order Accurate Scheme. *Journal of Computational Physics*, 136(2):503–521, September 1997. ISSN 00219991. doi: 10.1006/jcph.1997.5778.
- Yi Han Toh. Efficient non-iterative multi-point method for solving the Riemann problem. *Nonlinear Dynamics*, 112(7):5439–5451, April 2024. ISSN 0924-090X, 1573-269X. doi: 10.1007/s11071-023-09229-5.
- E. F. Toro. Riemann-problem-based techniques for computing reactive two-phased flows. In Alain Dervieux and Bernard Larrouturou, editors, *Numerical Combustion*, volume 351, pages 472–481. Springer Berlin Heidelberg, Berlin, Heidelberg, 1989. ISBN 978-3-540-51968-3 978-3-540-46866-0. doi: 10.1007/3-540-51968-8_108.
- E. F. Toro. *Riemann Solvers and Numerical Methods for Fluid Dynamics: A Practical Introduction*. Springer, Berlin, 1997. ISBN 978-3-662-03490-3.
- E. F. Toro, M. Spruce, and W. Speares. Restoration of the contact surface in the HLL-Riemann solver. *Shock Waves*, 4(1):25–34, July 1994. ISSN 0938-1287, 1432-2153. doi: 10.1007/BF01414629.
- I Toumi. A weak formulation of roe’s approximate riemann solver. *Journal of Computational Physics*, 102(2):360–373, October 1992. ISSN 00219991. doi: 10.1016/0021-9991(92)90378-C.
- G. Tryggvason, B. Bunner, A. Esmaeeli, D. Juric, N. Al-Rawahi, W. Tauber, J. Han, S. Nas, and Y.-J. Jan. A Front-Tracking Method for the Computations of Multiphase Flow. *Journal of Computational Physics*, 169(2):708–759, May 2001. ISSN 00219991. doi: 10.1006/jcph.2001.6726.
- Salih Ozen Unverdi and Grétar Tryggvason. A front-tracking method for viscous, incompressible, multi-fluid flows. *Journal of Computational Physics*, 100(1):25–37, May 1992. ISSN 00219991. doi: 10.1016/0021-9991(92)90307-K.
- J. D. van der Waals. *Over de continuïteit van den gas- en vloeistoestand*. Sijthoff, 1873.
- Bram Van Leer. Towards the ultimate conservative difference scheme III. Upstream-centered finite-difference schemes for ideal compressible flow. *Journal of Computational Physics*, 23(3):263–275, March 1977. ISSN 00219991. doi: 10.1016/0021-9991(77)90094-8.
- M. Volmer and A. Weber. Keimbildung in übersättigten Gebilden. *Zeitschrift für Physikalische Chemie*, 119U(1):277–301, January 1926. ISSN 2196-7156, 0942-9352. doi: 10.1515/zpch-1926-11927.
- J.B Vos, P Leyland, V. van Kemenade, C. Gacherieu, N Duquesne, and P Lötstedt. NSMB Handbook 6.07. Technical report, Lausanne, EPFL, 2014.

- Graham B. Wallis. *One-Dimensional Two-Phase Flow*. Dover Books on Engineering. Dover Publications, Inc, Garden City, New York, 2020. ISBN 978-0-486-84282-0.
- Lin Wang, Yiren Yang, Yuxing Li, and Yating Wang. Dynamic behaviours of horizontal gas-liquid pipes subjected to hydrodynamic slug flow: Modelling and experiments. *International Journal of Pressure Vessels and Piping*, 161:50–57, March 2018. ISSN 03080161. doi: 10.1016/j.ijpvp.2018.02.005.
- B. Wealer, S. Bauer, C.v. Hirschhausen, C. Kemfert, and L. Göke. Investing into third generation nuclear power plants - Review of recent trends and analysis of future investments using Monte Carlo Simulation. *Renewable and Sustainable Energy Reviews*, 143:110836, June 2021. ISSN 13640321. doi: 10.1016/j.rser.2021.110836.
- Stephen Whitaker. *The Method of Volume Averaging*, volume 13 of *Theory and Applications of Transport in Porous Media*. Springer Netherlands, Dordrecht, 1999. ISBN 978-90-481-5142-4 978-94-017-3389-2. doi: 10.1007/978-94-017-3389-2.
- Zein. *Numerical Methods for Multiphase Mixture Conservation Laws with Phase Transition*. PhD thesis, Otto-von-Guericke-Universität at Magdeburg, 2010.
- Ali Zein, Maren Hantke, and Gerald Warnecke. Modeling phase transition for compressible two-phase flows applied to metastable liquids. *Journal of Computational Physics*, 229(8): 2964–2998, April 2010. ISSN 00219991. doi: 10.1016/j.jcp.2009.12.026.
- Ju Zhang. A simple and effective five-equation two-phase numerical model for liquid-vapor phase transition in cavitating flows. *International Journal of Multiphase Flow*, 132:103417, November 2020. ISSN 03019322. doi: 10.1016/j.ijmultiphaseflow.2020.103417.
- Taiyang Zhang and Caleb S. Brooks. Linear stability analysis of flashing instability based on the homogeneous equilibrium model. *Nuclear Engineering and Design*, 373:110994, March 2021. ISSN 00295493. doi: 10.1016/j.nucengdes.2020.110994.
- Ling Zou, Haihua Zhao, and Hongbin Zhang. Implicitly solving phase appearance and disappearance problems using two-fluid six-equation model. *Progress in Nuclear Energy*, 88:198–210, April 2016. ISSN 01491970. doi: 10.1016/j.pnucene.2015.12.006.

Two-phase flow modeling for the simulation of loss-of-coolant accidents in nuclear reactors

Résumé

Cette thèse étudie la dynamique des écoulements gaz-liquide, en se concentrant spécifiquement sur les accidents de perte de réfrigérant dans les réacteurs à eau pressurisée. Ces accidents représentent des défis de sécurité majeurs, car ils entraînent une perte rapide de réfrigérant, pouvant potentiellement causer des accidents graves du réacteur. L'étude met en avant le rôle crucial des états métastables, qui surviennent lorsque l'eau, généralement maintenue à haute pression pour rester sous forme liquide, subit une dépressurisation rapide.

Pour aborder ces phénomènes complexes, cette recherche implémente et valide différents modèles d'écoulement diphasique dans un solveur numérique personnalisé. Deux modèles spécifiques sont examinés : un modèle à six équations intégrant un équilibre de vitesse relâché et un modèle à quatre équations basé sur des hypothèses d'équilibre cinétique, mécanique et thermique. De plus, le modèle à six équations avec une méthode de relaxation à taux arbitraire est étudié pour mettre en évidence le transfert de masse non instantané, qui est crucial pour prédire avec précision l'état métastable lors des transitions de phase. Les modèles sont validés à l'aide d'une gamme de cas tests, comprenant à la fois des cas standard trouvés dans la littérature et des cas spécifiques liés aux accidents de perte de réfrigérant.

Mots clés : écoulement diphasique, analyse numérique, état métastable, sûreté nucléaire

Résumé en anglais

This thesis investigates the dynamics of gas-liquid flows, focusing specifically on Loss of Coolant Accidents (LOCAs) in Pressurized Water Reactors (PWRs). LOCAs present significant safety challenges, as they lead to rapid coolant loss, potentially causing severe reactor accidents. The study emphasizes the critical role of metastable states, which occur when water, typically maintained at high pressure to remain in liquid form, experiences rapid depressurization.

To address these complex phenomena, this research implements and validates different two-phase flow models within a custom-built numerical solver. Two specific models are examined: a six-equation model incorporating a relaxed velocity equilibrium and a four-equation model based on kinetic, mechanical, and thermal equilibrium assumptions. Additionally, the six-equation model with an arbitrary-rate relaxation method is investigated to emphasize the non-instantaneous mass transfer, which is critical for accurately predicting the metastable state during phase transitions. The models are validated using a range of test cases, including both standard cases found in the literature and specific test cases related to loss-of-coolant accidents.

Keywords : two-phase flow, numerical analysis, metastable state, nuclear safety